Design of a Polarization Adaptive Beamforming Transmitter Sub-Array for Beyond Line of Sight Satellite Communications in Unmanned Aircraft Systems

by

Enrique M. Alvelo - Rivera

A thesis submitted in partial fulfillment of the requirements for the degree of

MASTER OF SCIENCE
in
ELECTRICAL ENGINEERING

UNIVERSITY OF PUERTO RICO
MAYAGÜEZ CAMPUS
2018

Approved by:

Rafael H. Medina - Sánchez, Ph.D. President, Graduate Committee	Date
José Colom - Ustáriz, Ph.D. Co-President, Graduate Committee	Date
Sandra Cruz - Pol , Ph.D. Member, Graduate Committee	Date
Rafael A. Rodríguez - Solís , Ph.D. Member, Graduate Committee	Date
Ingrid Y. Padilla, Ph.D. Representative of Graduate Studies Office	Date
José Colom - Ustáriz, Ph.D. Chairperson of the Department	Date

ABSTRACT

The market outlook for upgrade, expansion and new acquisition of military UAS equipment exhibits substantial potential to grow during the 10 year period extending from year 2016 to year 2025. Some of the mission characteristics and requirements that will drive future UAS development include: continuing microminiaturization, sensor fusion, command, control & communications standardization, and infrastructure integration to achieve smaller, less costly and more capable UAVs. Hence, an increased market demand for research & development of UAS antenna systems is also expected during the same 10 year period.

The University of Puerto Rico at Mayagüez is currently developing a "Hybrid Mechanical/ Electronic Steerable Antenna Array for SATCOM Terminals" to help enable significant efficiency and endurance improvements in future UAS platforms. The thesis "Design of a Polarization Adaptive Beamforming Transmitter Sub-Array for Beyond Line of Sight Satellite Communications in Unmanned Aircraft Systems" presented in this document complements the development project of the "Hybrid Mechanical/ Electronic Steerable Antenna Array for $SATCOM$ Terminals" that will operate in the extended Ku – band frequency range. Furthermore, the "Design of a Polarization Adaptive Beamforming Transmitter Sub-Array for Beyond Line of Sight Satellite Communications in Unmanned Aircraft Systems" provides a fundamental unit cell that enables the development of a Tx beamformer network module that minimizes risks of fabrication errors, simplifies

operation & maintenance tasks and provides roll-out flexibility for future antenna system expansions.

The microwave circuit included in the "Design of a Polarization Adaptive Beamforming Transmitter Sub-Array for Beyond Line of Sight Satellite Communications in Unmanned Aircraft Systems" consists of one driver amplifier, one 1:2 coupler, two variable phase shifters, one $90°$ hybrid coupler and two power amplifiers interconnected by microstrip line structures. Simultaneous one dimensional electronic beam steering and polarization tilt rotation might be achieved by electronically adapting the phase shifts provided by both transmission paths to help mitigate the effects of adjacent satellite interference.

According to simulation results the overall performance of the "Design of a Polarization Adaptive Beamforming Transmitter Sub-Array for Beyond Line of Sight Satellite Communications in Unmanned Aircraft Systems" meets relevant requirements of key commercial, military and industrial standard specifications available to the general public as unclassified or declassified information. However, it was observed that the predicted polarization axial ratio performance partially complies with MIL-STD-188-164B standard specifications regarding amplitude variations of the transmission uplink function and linear polarization axial ratio for Ku-band systems using antennas with diameters smaller or equal to $2.5\ m$. The highest extent of polarization axial ratio degradation was observed at the interconnection between the output ports of the phase shifters and the input ports of the hybrid coupler. The theoretical model developed as part of this research project confirmed that the polarization axial ratio performance suffers severe degradation mainly caused by the introduction of amplitude errors. Hence, variable attenuators were presented as the most practical solution to enable the required amplitude compensation to mitigate the effects of amplitude errors on gain ripple and polarization axial ratio performance.

RESUMEN

La perspectiva del mercado para la mejora, ampliación y nueva adquisición de equipo militar de sistemas de aeronaves no tripuladas exhibe un potencial de crecimiento substancial durante el período de 10 años que se extiende desde el año 2016 hasta el año 2025. Algunas de las características y requisitos de las misiones que impulsarán el desarrollo futuro de sistemas de aeronaves no tripuladas incluyen: microminiaturización continua, fusión de sensores, estandarización de plataformas de comando, control y comunicaciones, en adición a la integración de infraestructura para lograr vehículos aéreos no tripulados con menores tamaños, menores costos y mayores capacidades. Por lo tanto, también se espera un incremento en la demanda del mercado para la investigación y desarrollo de sistemas de antenas para sistemas de aeronaves no tripuladas durante el mismo período de 10 años.

Actualmente, la Universidad de Puerto Rico en Mayagüez está desarrollando el proyecto "Hybrid Mechanical/ Electronic Steerable Antenna Array for SATCOM Terminals" para permitir mejoras significativas en el rendimiento y la resistencia de futuras plataformas de sistemas de aeronaves no tripuladas. La tesis "Design of a Polarization Adaptive Beamforming Transmitter Sub-Array for Beyond Line of Sight Satellite Communications in Unmanned Aircraft Systems" presentada en este documento complementa el desarrollo del proyecto "Hybrid Mechanical/ Electronic Steerable Antenna Array for SATCOM Terminals" que operará en la gama de frecuencias de la banda Ku extendida. Además, la tesis "Design of a Polarization Adaptive Beamforming

Transmitter Sub-Array for Beyond Line of Sight Satellite Communications in Unmanned Aircraft Systems" proporciona una celda unitaria fundamental que permite el desarrollo de un módulo de red de formación del haz de transmisión que reduce al mínimo los riesgos de errores de fabricación, simplifica las tareas de operación y mantenimiento, en adición a proporcionar flexibilidad en el despliegue de expansiones futuras del sistema de antenas.

El circuito de microondas incluido en la tesis "Design of a Polarization Adaptive Beamforming Transmitter Sub-Array for Beyond Line of Sight Satellite Communications in Unmanned Aircraft Systems" consta de un amplificador de mediana potencia, dos desfasadores variables, un acoplador de potencia 1:2, un acoplador híbrido de 90° y dos amplificadores de alta potencia interconectados por estructuras compuestas de líneas de transmisión de tipo microcinta. El direccionamiento electrónico, unidimensional, del haz de radiación y la rotación de la inclinación de la polarización de la onda pueden lograrse simultáneamente adaptando electrónicamente los cambios de fase proporcionados en ambos pasos de transmisión para ayudar a mitigar los efectos de interferencia de satélites adyacentes.

De acuerdo a los resultados de simulaciones, el rendimiento global de la tesis "Design of a Polarization Adaptive Beamforming Transmitter Sub-Array for Beyond Line of Sight Satellite Communications in Unmanned Aircraft Systems" cumple con los requisitos pertinentes de especificaciones claves de estándares comerciales, militares e industriales disponibles al público en general como información no clasificada o desclasificada. Sin embargo, se observó que el rendimiento de la razón axial de polarización prevista cumple parcialmente con especificaciones de estándar MIL-STD-188-164B con respecto a las variaciones de amplitud de la función de transmisión del enlace ascendente y la razón axial de polarización lineal para sistemas de banda Ku que utilizan antenas de diámetro menor o igual a 2.5 m. El más alto grado de degradación de la razón axial de polarización se observó en la interconexión entre los puertos de salida de los desfasadores y los puertos de entrada del acoplador híbrido. El modelo teórico desarrollado como parte de este proyecto de investigación confirmó que el rendimiento de la razón axial de polarización sufre una degradación severa causada principalmente por la introducción de errores de amplitud. Por lo tanto, la implementación de atenuadores variables fue presentada como la solución más práctica para permitir la compensación de amplitud necesaria para mitigar los efectos de los errores de amplitud en el rendimiento de la ondulación en la ganancia y la razón axial de polarización.

ACKNOWLEDGEMENTS

Thanks to my parents, Mrs. Elba I. Rivera and Mr. Miguel A. Alvelo, for their unconditional love, dedication and support through all these years.

Thanks to my brother, Dr. Miguel F. Alvelo-Rivera, for believing always in me and for being a source of inspiration during my entire life.

Thanks to the *Puerto Rico Science, Technology and Research Trust* for providing the required funding to make this project possible.

Special thanks to Dr. Sandra Cruz-Pol, Dr. José Colom-Ustáriz, Dr. Rafael Rodríguez Solís and Dr. Rafael H. Medina for this unique opportunity to grow up my personal, academic and professional skills at *UPRM*.

TABLE OF CONTENTS

LIST OF FIGURES

LIST OF TABLES

LIST OF ABBREVIATIONS

ASI	Adjacent Satellite Interference
ACPR	Adjacent Channel Power Ratio
ADC	Analog to Digital Converter
AR	Axial Ratio
ATTEN	Attenuator
ATS	Air Traffic Services
BER	Bit Error Rate
BFN	Beamforming Network
BLOS	Beyond Line of Sight
BOM	Bill of Materials
BUSD	Billion of United States Dollars
C3	Command, Control and Communications
C4I	Command, Control, Communications, Computers and Intelligence
CAD	Computer Aided Design
CDL	Common Data Link
CP	Circular Polarization
COTS	Commercial Off the Shelf
DA	Driver Amplifier
DAC	Digital to Analog Converter
dB	Decibel
dBm	Decibel referenced to 1 milliwatt
dBW	Decibel referenced to 1 watt
DL	Downlink or Forward Link
DoD	Department of Defense
DSP	Digital Signal Processing
$\mathbf{E_b/N_o}$	Bit Energy to Noise Power Density Ratio
$\mathbf{E_s/N_o}$	Symbol Energy to Noise Power Density Ratio
EIRP	Effective Isotropic Radiated Power
EO	Electro-Optic
EW	Electronic Warfare
EVM	Error Vector Magnitude
FEC	Forward Error Correction
FEM	Finite Element Method
FMV	Full Motion Video
FPGA	Field Programmable Gate Array
G/T	Gain Over NoiseTemperature Ratio
HB	Harmonic Balance
HD	High Definition
IC	Integrated Circuit
IF	Intermediate frequency
IIP3	Input Third Order Intercept Point
IL	Insertion Loss
IM	Intermodulation

IMD	Intermodulation Distortion
IMD3	Third Order Intermodulation Distortion
IMD5	Fifth Order Intermodulation Distortion
IP3	Third Order Intercept Point
IR	Infrared
ISR	Intelligence, Surveillance and Reconnaissance
ISI	Inter-Symbol Interference
ITU	International Telecommunications Union
ITU-R	ITU Radiocommunication Sector
Ku	K under frequency
Ka	K above frequency
LHCP	Left Handed Circular Polarization
LO	Local Oscillator
LOS	Line of Sight
Mbps	Mega bits per second
ML	Mismatch Loss
MMIC	Monolithic Microwave Integrated Circuit
MoM	Method of Moments
NASA	National Aeronautics and Space Administration
NATO	North Atlantic Treaty Organization
NOAA	National Oceanic and Atmospheric Administration
NRZ	Non-return to zero
O&M	Operations and Maintenance
OIP3	Output Third Order Intercept Point
OoB	Out of Band
Op Amp	Operational Amplifier
OQPSK	Offset Quadrature Phase Shift Keying
P1dB	1 dB Compression Point
PA	Power Amplifier
PAPR	Peak to Average Power Ratio
PCB	Printed Circuit Board
PHEMT	Pseudomorphic High Electron Mobility Transistor
PN	Pseudo Noise
PS	Phase Shifter
PSK	Phase Shift Keying
PTFE	Polytetrafluoroethylene
PWT	Precision Targeting Workstation
QPSK	Quadrature Phase Shift Keying
R&D	Research and Development
RDT&E	Research, Development,Testing and Evaluation
RF	Radio Frequency
RHCP	Right Handed Circular Polarization
RL	Return Loss
RMS	Root Mean Square
RR	ITU Radio Regulation
RRC	Root Raised Cosine
Rx	Receive mode

S	Scattering Matrix
SAR	Synthetic Aperture Radar
SATCOM	Satellite Communications
SDL	SATCOM Data Link
SIGINT	Signals Intelligence
SMPM	Sub-Miniature Push-On Micro Interface
SNR	Signal to Noise Ratio
SSPA	Solid State Power Amplifier
STANAG	NATO Standardization Agreement
STARS	Space Based Telemetry and Range Safety
TCDL	Tactical Common Data Link
TCO	Total Cost of Ownership
TDRSS	Tracking and Data Relay Satellite System
TEM	Transverse Electromagnetic
Tx	Transmit mode
UAV	Unmanned Aerial Vehicle
UAS	Unmanned Aircraft System
UL	Uplink or Reverse Link
UPRM	University of Puerto Rico at Mayaguez
USAF	United States Air Force
XPOL	Cross Polarized
W	Watt

1 INTRODUCTION

1.1 Motivation

The global defense industry is currently investing heavily in research and development, which has led to the development of technologies to enhance the endurance, survivability and usability of unmanned aircraft systems. The actual number of UAS operations is expected to surpass manned aircraft operations, for both military and commercial domains, by 2035 [1]. Figure 1.1 shows the DoD′s UAS forecast for the 20 year period from 2015 to 2035.

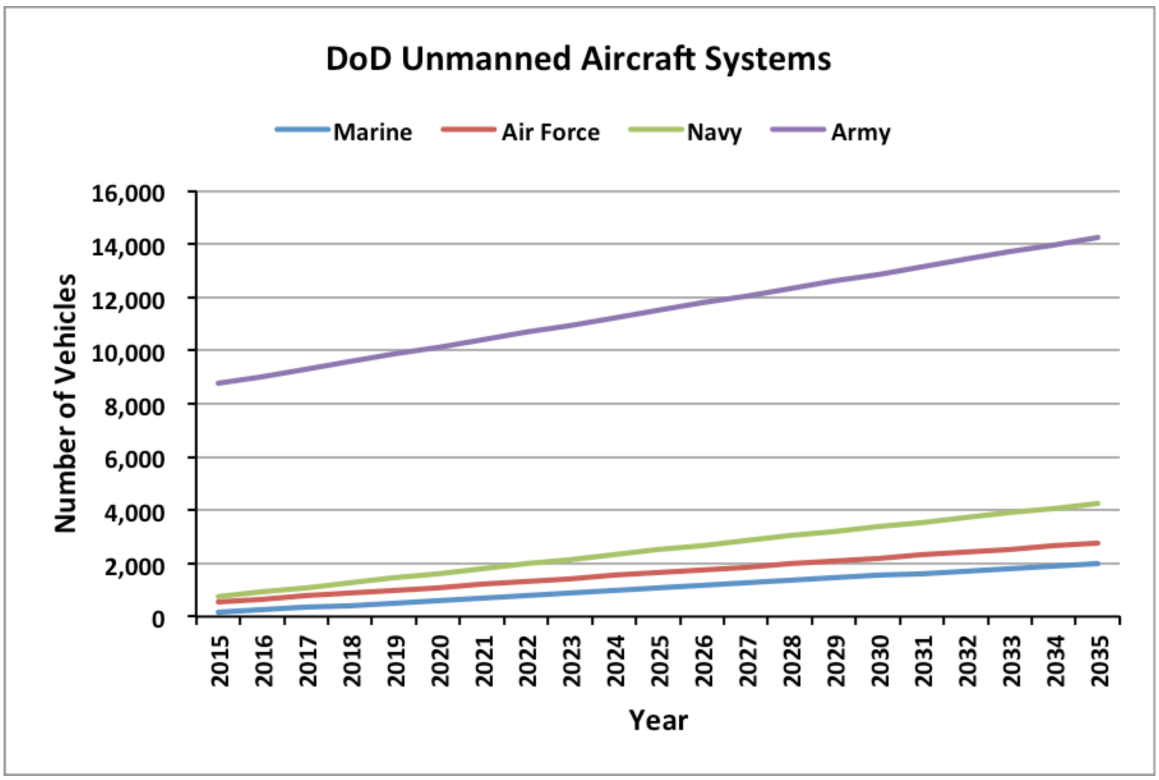

Figure 1.1 – U.S. Department of Defense UAS Forecast for Years 2015 – 2035 [1].

According to [1] the U.S. DoD projected an increase in the percentage of unmanned vehicles from the actual 25% up to 70% by the end of year 2035. Also, a more aggressive forecast in [2] predicts that the U.S. will account for 77% of the total worldwide spending on military UAS research, development, testing and evaluation for the 10 year period from 2016 to 2025. This corresponds to 69.7 $BUSD$ for the 10 year period from 2016 to 2025, half of the time projected in [1].

Mission need is tightly coupled with technology, meaning that technological developments are mission enablers in the same way that mission requirements drive technological changes. Some of the many mission characteristics and requirements that will drive future UAS development include: light weight (composite structures), long endurance, high payload carrying capacity, and interchangeability between standardized payload modules [1]. Likewise, continuing microminiaturization, sensor fusion, command, control & communications standardization, and infrastructure integration will result in smaller, less costly and more capable $UAVs$ [1]. Hence, an increased market demand for research & development of Ku-band antenna systems considering UAS applications might also be expected.

According to [3] the U.S. DoD Tier III and IV UAS employ mechanically steerable dish reflector antennas with diameters of 30cm to 1.2 m to achieve higher gain and faster Ku-band data rates. For instance, Predator/Reaper $(MQ-1/9)$ $UAVs$ are typically equipped with 76 cm antennas to provide EIRP of 53.5 dBW and G/T of 12 dB/K. Likewise, Global Hawk $UAVs$ are equipped with 1.2 m antennas to provide EIRP of 64.7 dBW and G/T of 14 dB/K [4]. Figure 1.2 shows the Ku-band $SATCOM$ Data Link $(KuSDL)$ Predator Reconnaissance Antenna System by L3 Communications in NOAA\NASA Predator B-001 UAV.

Figure 1.2 – KuSDL Predator Reconnaissance Antenna System by L3 Communications [5].

The mechanically steerable dish reflector antennas currently used in Global Hawk and Predator/ Reaper UAVs have proven to do the work but at the same time they have limited the endurance and capabilities of legacy UAS. The large sizes of these antennas require the implementation of radome structures with higher profiles that increase the aerodynamic drag, total weight, fuel consumption and radar cross section of these $UAVs$.

Obviously, the implementation of a more compact antenna type is required to solve most of the issues introduced by the implementation of mechanically steerable dish reflector antennas in legacy UAS. Phased arrays are directive antennas made up of a number of radiating elements that typically resembles planar or conformal structures with significantly lower profile than mechanically steered dish reflector antennas [6]. The lower profile of phased array antennas enables the implementation of smaller and more aerodynamic radomes in future UAV designs. The implementation of smaller radomes results in a reduced UAV radar cross section, minimizing the probability of UAV detection during ISR missions and military theaters. Furthermore, phased array antennas are capable of performing fast and accurate beam scanning, allowing the implementation of multiple functions either interlaced in time or simultaneously [7]. This particular feature could be exploited to enable beam switching capabilities in next generation SATCOM systems in order to extend UAS endurance and communication capabilities. Figure 1.3 illustrates the one dimensional phased array antenna beam steering concept.

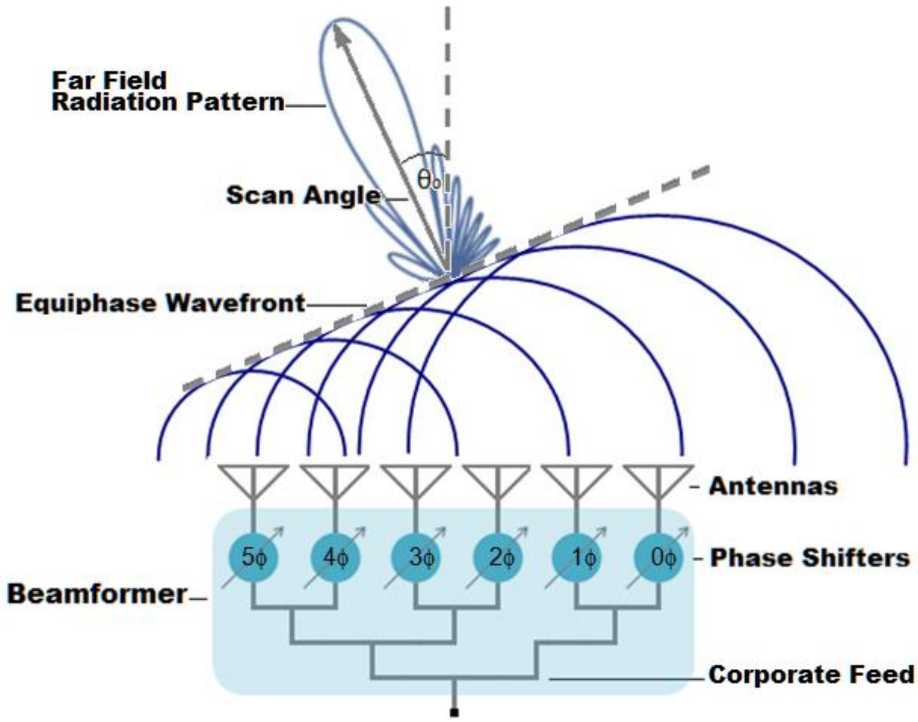

Figure 1.3 – One Dimensional Phased Array Antenna Beam Steering [7].

The relative amplitudes of constructive and destructive interference effects, among the waves radiated by its radiating elements, determine the shape of the phased array's effective far field radiation pattern [6]. The required phase shift at the n^{th} element (ϕ_n) of a linear array composed of N radiating elements is set in terms of the phase difference between excitation signals of adjacent elements (ϕ).

The most common phased array antenna types implement either hybrid mechanical/electronic one dimensional steering of a single beam, or fully electronic two dimensional steering of a single beam. One dimensional beam steering can be achieved by combining electronic beam steering in one specific orientation (i.e. elevation) and mechanical beam steering in other orientation (i.e. azimuth). Two dimensional beam steering can be achieved by implementation of independent electronic beam steering in two directions (i.e. elevation and azimuth). The implementation of phased array antennas using two dimensional beam steering might result in higher total cost of ownership when analog beamformers are considered since they require twice as many phase shifters than hybrid electronic/mechanical one dimensional beam steering phased array antennas.

The University of Puerto Rico at Mayagüez is currently developing a "Hybrid Mechanical/ Electronic Steerable Antenna Array for $SATCOM$ Terminals". A one dimensional scanning approach is implemented to electronically steer the main beam in elevation and a single-axis servo actuator to mechanically steer the main beam in azimuth by rotating the phased array assembly. Also, both, Tx and Rx, phased arrays are meant to coexist in a single antenna aperture assembly with a physical area of $30.48\ cm \times 30.48\ cm$. It is expected that this unique capability will help to enable significant efficiency and endurance improvements for future UAV developments. Figure 1.4 shows the system architecture of the hybrid mechanical/electronic steerable antenna array.

The Tx antenna system will operate in the extended Ku-band frequency range from 13.75 GHz to 14.5 GHz. Its design is comprised of twenty eight Tx antenna sub-arrays. A Tx antenna sub-array employs a total of twenty dual polarized Tx antenna elements to build up the required Tx antenna gain. Each Tx antenna sub-array will be connected to a Tx Sub-Array via SMPM connectors. The purpose of the Tx Sub-Array is to provide microwave signal power amplification, electronic beam steering and dynamic "linear" polarization tracking functionality.

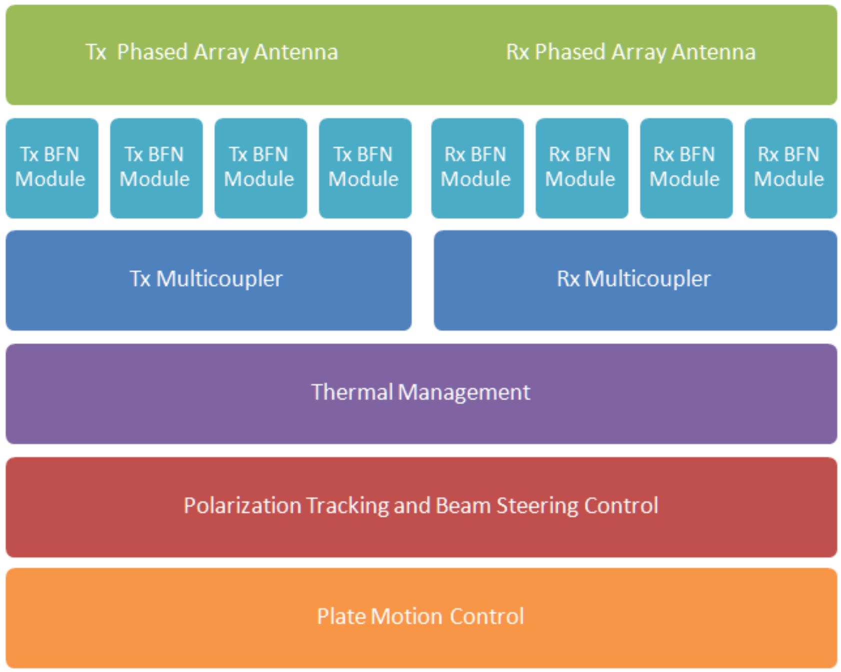

Figure 1.4 – System Architecture of the Hybrid Mechanical/Electronic Steerable Antenna Array.

The "Design of a Polarization Adaptive Beamforming Transmitter Sub-Array for Beyond Line of Sight Satellite Communications in Unmanned Aircraft Systems" complements the "Hybrid Mechanical/ Electronic Steerable Antenna Array for $SATCOM$ Terminals" development since currently there aren't any Tx Sub-Array solutions available, covering all possible Ku-band antenna scenarios, as commercial off the shelf components in the market. Figure 1.5 shows the microwave circuit schematic of the proposed Tx Sub-Array design.

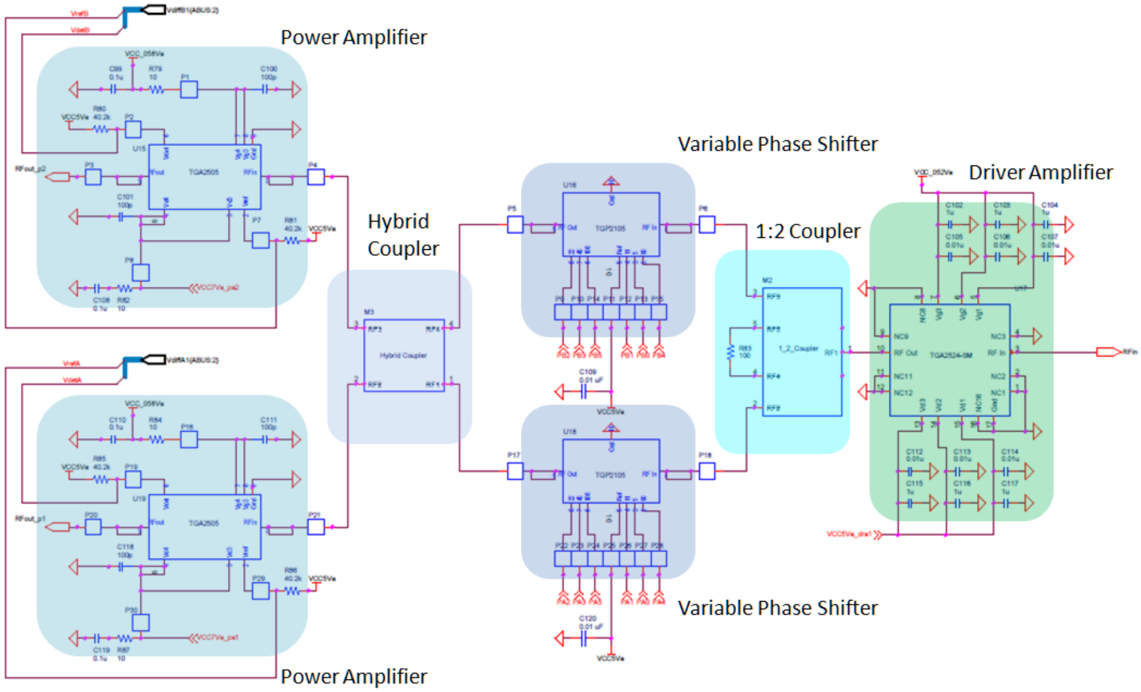

Figure 1.5 –Microwave Circuit Schematic of the Proposed Tx Sub-Array Design.

The microwave circuit of the proposed Tx Sub-Array design consists of one driver amplifier, one 1:2 coupler, two variable phase shifters, one 90° hybrid coupler and two power amplifiers connected by microstrip line structures to achieve two independent transmission paths. Simultaneous one dimensional electronic beam steering and polarization tilt rotation might be achieved by electronically adapting the phase shifts provided by both Tx Sub-Array transmission paths.

The proposed Tx Sub-Array design provides a fundamental unit cell that enables the development of a Tx BFN Module that minimizes risks of fabrication errors, simplifies operation & maintenance $(O\&M)$ tasks and provides roll-out flexibility for future antenna system expansions. Each Tx BFN Module is comprised of seven Tx Sub-

Arrays. In this case, the implementation of the Tx antenna system considers only four Tx BFN Modules. Figure 1.6 shows the hierarchical circuit schematic of the Tx BFN Module for implementation of the hybrid mechanical/electronic steerable antenna array system.

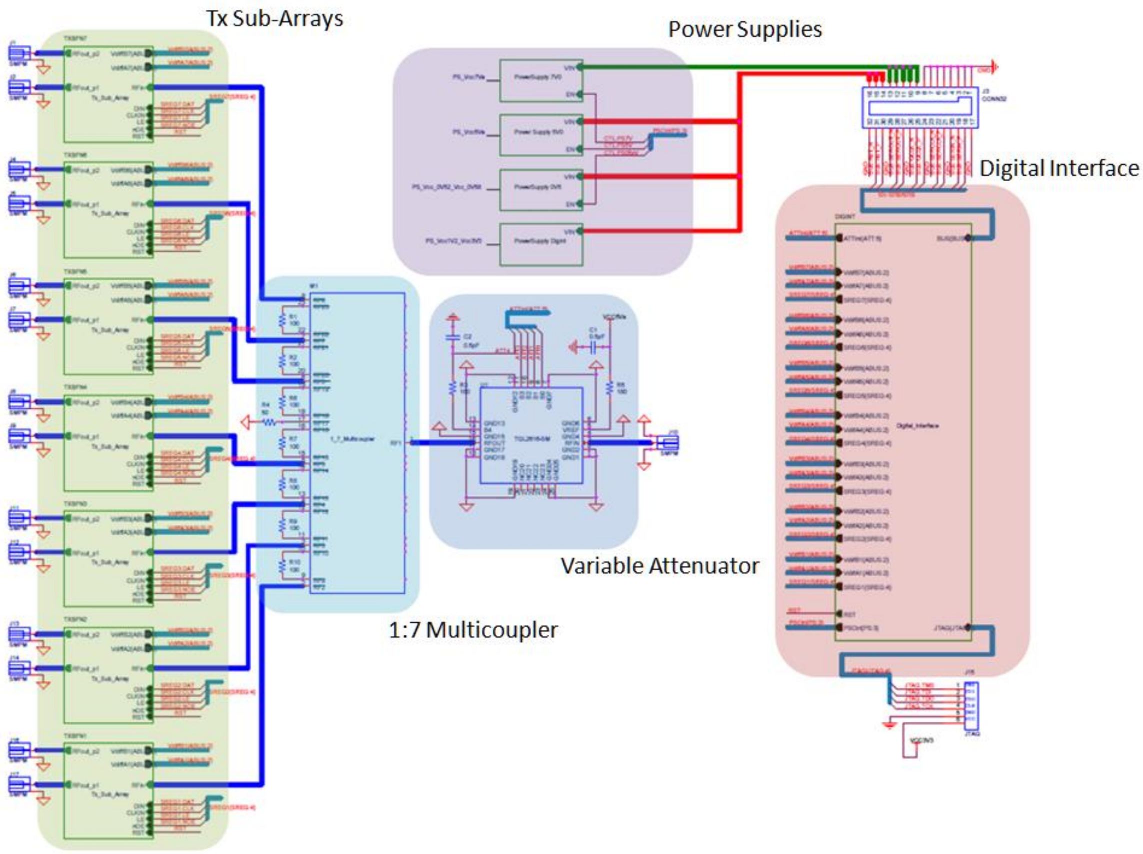

Figure 1.6 – Hierarchical Circuit Schematic of the Tx BFN Module.

Figure 1.7 shows the microwave circuit layout for the Tx BFN Module. The microwave circuit layout of one Tx BFN Module fits in a printed circuit board (PCB) area measuring approx. $5.35\ cm \times 7.24\ cm$.

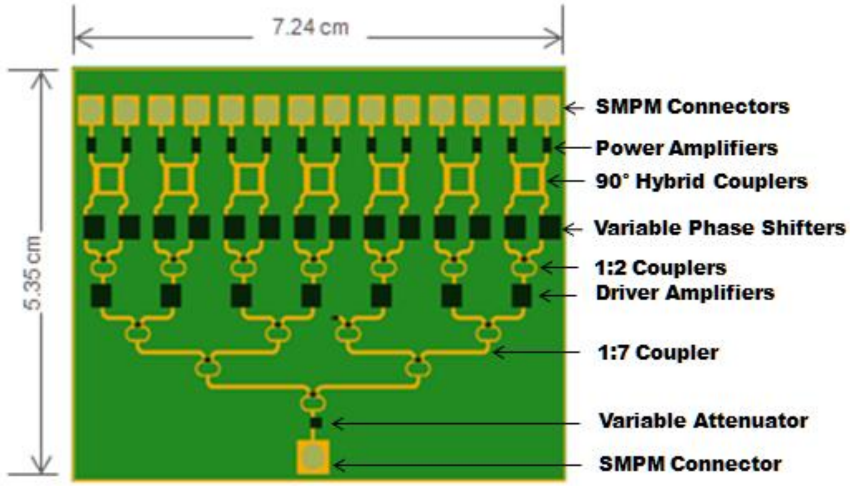

Figure 1.7 – Microwave Circuit Layout of the Tx BFN Module.

Hence, the "Design of a Polarization Adaptive Beamforming Transmitter Sub-Array for Beyond Line of Sight Satellite Communications in Unmanned Aircraft Systems" becomes an essential element to complement the "Hybrid Mechanical/ Electronic Steerable Antenna Array for $SATCOM$ Terminals" currently developed by the University of Puerto Rico at Mayagüez.

1.2 Objectives

The objectives of the "Design of a Polarization Adaptive Beamforming Transmitter Sub-Array for Beyond Line of Sight Satellite Communications in Unmanned Aircraft Systems" project are aligned with the following of the "Hybrid Mechanical/ Electronic Steerable Antenna Array for $SATCOM$ Terminals" project:

- Replace mechanical steered dish antenna with a single aperture hybrid steered phased array antenna in existing UAS .

- Impact aerodynamics, radar cross section and endurance of future UAS.
- Mitigate adjacent satellite interference of Ku-band beyond line of sight ($BLOS$) links in UAS.

Also, the following objectives are specific to the "Design of a Polarization Adaptive Beamforming Transmitter Sub-Array for Beyond Line of Sight Satellite Communications in Unmanned Aircraft Systems" project:

- Design a Tx Sub-Array circuit that complies with the given set of technical requirements presented in Section 3.1.
- Predict the performance of the proposed Tx Sub-Array design using computer aided design (CAD) methods and tools.
- Compare the predicted Tx Sub-Array performance against key commercial, industrial and military standard specifications.
- Identify potential solutions to the predicted Tx Sub-Array performance issues.
- Generate a hierarchical schematic diagram, the bill of quantities and the microwave circuit layout of the proposed Tx Sub-Array design.

1.3 Methodology

The following processes and procedures were performed during the design of the proposed Tx Sub-Array circuit (Chapter 3):

- Determine the architecture of the Tx Sub-Array's microwave circuit (Section 3.2.1).

- Define the antenna inter-element spacing in the X and Y directions.
- Estimate the required number of antenna sub-arrays and antenna elements per antenna sub-array considering the given antenna aperture dimensions.

- Define the nominal microwave circuit architecture of the Tx Sub-Array (Section 3.2.2).
  - Estimate the directivity and realized gain of the antenna.
  - Estimate the Tx output power that satisfies the given EIRP requirement.
  - Estimate the required power amplifier's gain.
  - Modify the Tx Sub-Array's nominal microwave circuit architecture to meet the estimated Tx output power requirements.
- Determine the linearity requirements of the Tx Sub-Array's microwave circuit (Section 3.3).
  - Estimate the peak to average power ratio of the transmitted waveform.
  - Specify the required 1dB compression point performance.
  - Estimate the required output third order intermodulation performance.
- Design or select the Tx Sub-Array's microwave circuit components (Section 3.4).
  - Estimate the transmission and impedance mismatch losses of microstrip line planar structures.
  - Select "commercial off the shelf" power amplifiers and variable phase shifters.

- Perform link budget calculations to determine the Tx Sub-Array's output power, 1dB compression point and output third order intermodulation point.

The following processes and procedures were performed during the simulation of the proposed Tx Sub-Array circuit performance (Chapter 4):

- Predict the performance of the Tx Sub-Array's microwave circuit.
  - Estimate the frequency response of the proposed Tx Sub-Array circuit design (Section 4.1).
  - Estimate the linearity of the proposed Tx Sub-Array circuit design (Section 4.2).
  - Predict the spurious domain emissions of the proposed Tx Sub-Array circuit design (Section 4.3).
  - Predict the out of band domain emissions of the proposed Tx Sub-Array circuit design (Sections 4.4).
  - Predict the modulation accuracy of the proposed Tx Sub-Array circuit design (Section 4.5).
  - Predict the polarization accuracy of the proposed Tx Sub-Array circuit design (Section 4.6).
- Identify key commercial, industrial and military standard performance specifications applying to proposed Tx Sub-Array design (Chapter 4 and Chapter 5).

- Compare the simulation outcomes against key commercial, military and industrial standard specifications (Chapter 5).
- Test potential solutions to the predicted Tx Sub-Array performance issues. (Section 5.6.1).
- Summarize the most relevant findings and conclusions of this research project (Chapter 6).

1.4 Tools and Equipment

The following CAD tools and laboratory equipment were used to perform the design and simulation of the proposed Tx Sub-Array circuit:

- E4419B EPM Series Power Meter by Agilent Technologies
- Allegro Design Entry CIS by Cadence
- Allegro PCB Editor by Cadence
- Electronic Desktop (HFSS) by AnSys
- Excel by Microsoft
- LTspice IV by Linear Technology
- LTpowerCAD II by Linear Technology
- Matlab by Mathworks
- N5227A PNA Network Analyzer by Agilent Technologies
- R-Tools by Mersen

1.5 Scope, Organization and Audience

This document presents the most relevant microwave engineering aspects of the proposed “Design of a Polarization Adaptive Beamforming Transmitter Sub-Array for Beyond Line of Sight Satellite Communications in Unmanned Aircraft Systems”. Other engineering aspects regarding design of power supplies, digital controllers, calibration & optimization algorithms, instrumentation, mechanical sub-assemblies and thermal management solutions have been considered during the design process but they are beyond the scope of this document.

Chapter 2 provides background information regarding payload service demand, communications protocol, data link throughputs and antenna system solutions implemented in UAS applications.

Chapter 3 presents the technical requirements, microwave circuit architecture and microwave circuit components regarding the proposed Tx Sub-Array design.

Chapter 4 presents the simulations results for the proposed Tx Sub-Array design. The outcomes of these simulations are further analyzed and discussed in Chapter 5.

Chapter 5 presents the analyses of simulations results from Chapter 4. The outcomes from these analyses are compared against relevant commercial, military and industrial standard specifications.

Chapter 6 summarizes the most relevant findings resulting from the analyses performed in Chapter 5.

Due to the complex nature of phase array antenna technology this document is intended for those readers that have an intermediate to advanced background in electromagnetics and telecommunications engineering. Examples of this are undergraduate students, graduate students, professors and professionals that have taken at least two courses in microwave engineering, communications engineering, and antenna engineering.

2 BACKGROUND

2.1 Service Demand

UAS are comprised of an unmanned aircraft and other supporting elements required for their operation as shown in. Figure 2.1. The unmanned aircraft element, better known as UAV, is typically a rotary, fixed winged, or lighter than air aircraft that is operated remotely, programmed and/or autonomous, and can be capable of flight beyond visual range. UAS are operated under direct human oversight or control. The human element includes trained personnel and certified pilot/operator, maintainer, mission commander, and mission analyst, depending on the concept. The UAV pilot/operator is located within the UAS control element. While the control element is typically on the ground, it may also be on another aircraft, ground vehicle or maritime vessel. The support equipment element is necessary to transport, maintain, launch, and recover the UAV. The communications element includes all communications internally and between the UAS and ATS. Communication links may be either LOS or $BLOS$. The payload element is the equipment allowing the UAS to accomplish its tactical mission. UAS payloads can generally be categorized into the following four sub-elements: sensors, communication relay, weapons, and cargo [8].

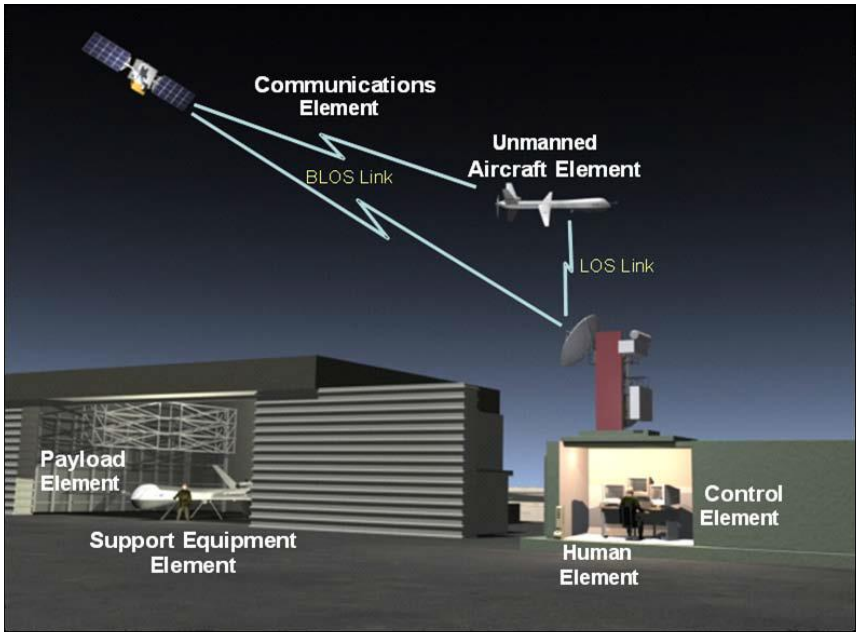

Figure 2.1 – Unmanned Aircraft System Elements by U.S. Department of Defense [8].

The large volumes of data that can be gathered by airborne sensors provide unique challenges and opportunities. For instance, the Teal Group, an independent business consulting firm, predicts a rise from 3.5 $BUSD$ in 2016 to 6.3 $BUSD$ in 2025 for a wide range of UAV payloads including: Electro-Optic/Infrared (EO/IR) sensors, Synthetic Aperture Radars $(SARs)$, SIGINT and EW Systems, and C4I Systems [2]. Furthermore, the Teal Group also predicts a sudden near-term rise from 985 $MUSD$ in 2016 to 1.7 $BUSD$ in 2021 for the "default sensor" EO/IR market led by early availability of funding to transfer manned U-2 intelligence surveillance and reconnaissance (ISR) aircraft sensors to Global Hawk, and by major HD upgrade programs for both Reapers and Gray Eagles [2].

Airborne ISR satellite networks are typically characterized by high throughput return links and lower throughput forward links. Figure 2.2 shows the U.S. DoD target data rate evolution for Ku-band terminals on Predator/Reapers and Global Hawks $UAVs$. Return link data rates of interest range from 0.2 to 45 Mbps for most systems, with 10.71 Mbps being of particular interest as it allows transport of high-definition full motion video (FMV), HD $720p$, along with other platform/mission traffic.

Intelsat's next-generation constellation of high-throughput satellites, Epic$^{\mathrm{NG}}$, employs C-, Ku- and Ka-bands, wide beams, spot beams, and frequency re-use technology to provide a host of customer-centric benefits. According to [3] each Epic$^{\mathrm{NG}}$ satellite provides a bandwidth capacity that is 5 to 8 times the bandwidth capacity of a conventional satellite, and 2 to 3 times the capacity of each of the WGS satellites operated by the U.S. Air Force. Likewise, [1] predicts that commercial satellite service providers will also continue to increase their global satellite communications capabilities for both the military and commercial users of the UAS. For instance, Inmarsat's 1.3 $BUSD$ deployment of its Global Xpress Ka-band satellite service is in fact in anticipation of the future increase in ISR data from all UAS markets.

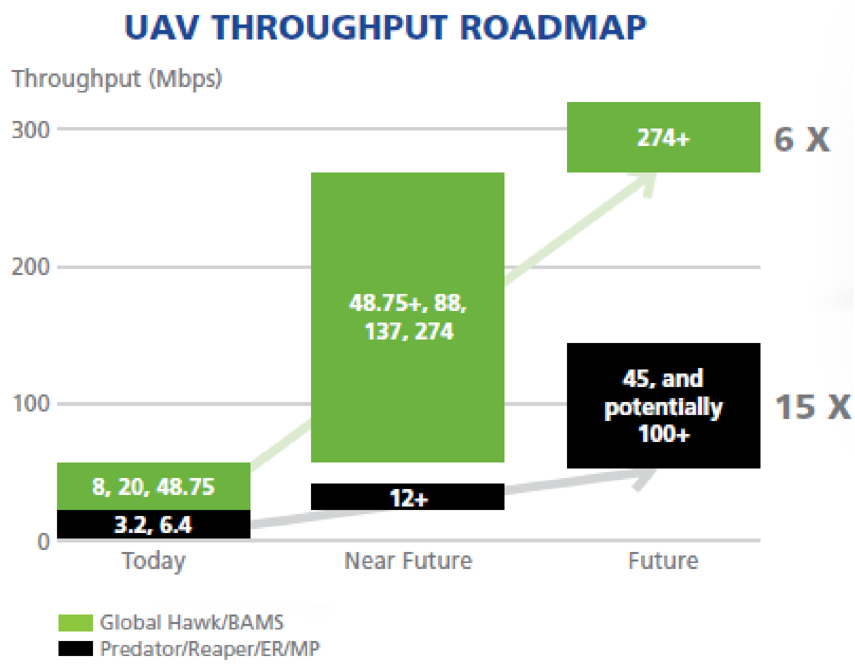

Figure 2.2 – U.S. DoD Throughput Roadmap for Ku-Band Terminals on UAVs [9].

2.2 Common Data Link

The U.S. $DoD's$ "Common Data Link Waveform Specification 7681990 Rev. F" and the first implementation of NATO's "$STANAG$ 7085 Interoperable Data Links for Imaging Systems" specification provides general requirements and directives for the implementation of the Common Data Link (CDL) communications protocol [10], [11]. The CDL communications protocol allows the remote operation and exploitation of sensors (i.e EO/IR and SAR) carried by CDL capable platforms from $BLOS$ locations via satellite. CDL provides a full-duplex, jam resistant, spread spectrum, point-to-point digital microwave communications link between the ISR sensor, the sensor platform, and the surface terminals. The CDL uplink operates at data rates from 200 kbps to 45 Mbps. The

CDL downlink can operate at data rates from 10.71 Mbps, 45 Mbps, 137 Mbps, or 274 Mbps [12].

Likewise, the Tactical Common Data Link ($TCDL$) program provides a family of interoperable, secure, digital data links for use with both manned and unmanned airborne reconnaissance platforms. It provides ISR data at rates from 1.544 Mbps to at least 10.7 Mbps over ranges of 200 kilometers. Furthermore, it will soon support the required higher CDL data rates at 45 Mbps, 137 Mbps and 274 Mbps [12]

2.3 Ku-Band Phased Array Antennas for BLOS Links

According to [12] in August and November 1999, the U.S. Navy demonstrated a phased array antenna that can handle $SATCOM$ and CDL operation. Frequencies utilized were in the EF/S band (2.2-2.3 GHz) and I/X band (7.25-8.4 GHz) both for military$SATCOM$, plus I/X band (9.7-10.5 GHz) and Ku-band (14.5-15.35 GHz) for CDL and Ku-band (10.95-14.5 GHz) for commercial $SATCOM$. The U.S. Air Force's UAV, Global Hawk, participated in the exercise Linked Seas 00 demonstrating transmission of radar imagery to both the US Army's Tactical Exploitation System and to the USS George Washington, and subsequently to the Joint Analysis Center at Molesworth in the United Kingdom. In the following Joint Task Force Exercise 00-02, CDL was utilized to pass re-tasking requests to Global Hawk from ship and land-based terminals. Previously the U.S. Navy sponsored a demonstration of Synthetic Radar Imagery transmission from the UAV via CDL into the Joint Services Imagery Processor Navy, passed through the

Common Imagery Processor to the Precision Targeting Workstation (PWT) for analysis. Imagery was then provided to an airborne F/A-18.

Furthermore, [13] describes NASA's plan to deploy a Ku-band phase array antenna on a F15-B aircraft to test a 5-Mbps Ku-band telemetry link with the Tracking and Data Relay Satellite System ($TDRSS$) as part of Phase 2 of the Space-Based Telemetry and Range Safety ($STARS$) study. The selected antenna is a 184 element phased array, electronically steerable in elevation and mechanically steerable in azimuth, designed and manufactured by EMS Technologies. Figure 2.3 shows the Darkstar UAV Ku-Band SATCOM Antenna by EMS Technologies. The Darkstar UAV Ku-Band $SATCOM$ antenna employs resonant slot apertures fed by ferrite phase shifters through microwave network and performs mechanically tracked linear polarization. The antenna dimensions are 74.955 cm diameter, 33.02 cm depth, and total weight of 119 lb. According to [14] and [15] the implementation of the Darkstar UAV Ku-Band $SATCOM$ phased array antenna achieved Phase 2 performance expectations in terms of tracking and telemetry data rates but it isn't still clear the reason why NASA decided to implement mechanical steerable dish reflector antennas in most of its $UAVs$.

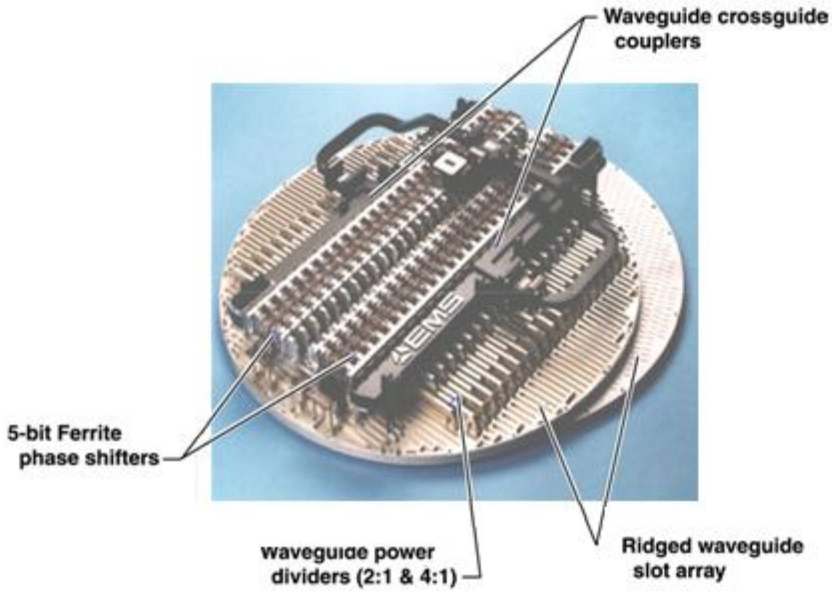

Figure 2.3 – Darkstar UAV Ku-Band SATCOM Antenna by EMS Technologies [13].

Conversely, newer phase array antenna solutions are becoming available in the market. For instance, Gilat's BlackRay 71 Ku Enhanced antenna system is a hybrid mechanical/electrical flat panel phase array antenna terminal that can provide IP based $BLOS$ communications with throughputs over 1.5 $Mbps$ for Ku-Band uplink applications in UAS. Figure 2.4 shows the BlackRay 71 Ku Enhanced Antenna System by Gilat Satellite Networks. Gilat's BlackRay 71 Ku Enhanced flat panel antenna system employs a passive array of microstrip patches and a Ku band solid stated power amplifier ($SSPA$) to provide an effective isotropic radiated power ($EIRP$) of approximately 41 dBW across the 13.75 GHz – 14.5 GHz spectrum. The antenna swept volume dimensions are 34.5 cm diameter, 18.5 cm depth, and combined weight of 19.7 lb.

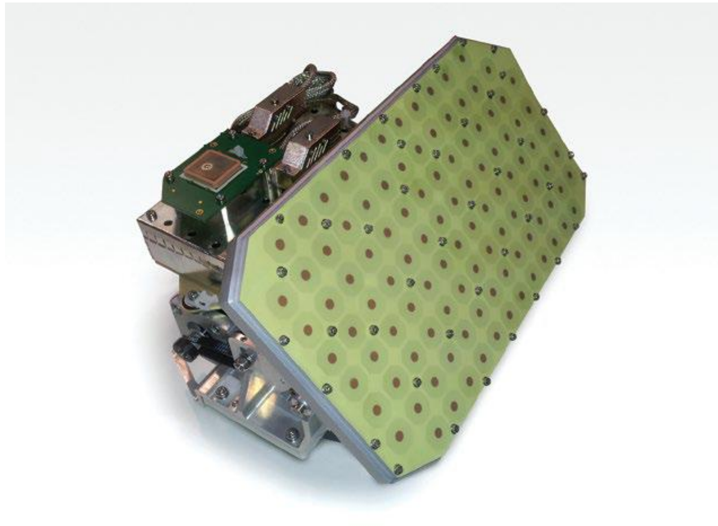

Figure 2.4 – BlackRay 71 Ku Enhanced Antenna System by Gilat Satellite Networks

2.4 Mitigation of Adjacent Satellite Interference

The drive toward smaller antennas in UAVs increases the probability of higher adjacent satellite interference(ASI) levels. Uplink ASI might be caused by the off-axis interference emissions from other satellite communication systems served by satellites in adjacent orbital slots. Increased levels of ASI are observable at orbital slot spacing of less than 2.0° in the United States or less than 3.0° in Europe when adjacent satellites have overlapping beams and frequency ranges [16]. Hence, ITU-R-S.1323-2 recommends users and satellite operators to allow for at least 20% of total noise power (~1.0 dB) allocated to ASI [16].

The implementation of polarization diversity techniques provides an alternative solution to mitigate the ASI generated by transmissions to and from satellites operating in equal frequency ranges. The polarization of a transverse electromagnetic plane wave describes the locus traced by the tip of its time - harmonic electrical field vector at a plane in space that is orthogonal to its direction of propagation. Different polarization schemes can be assigned to the antenna beams of adjacent satellites and/or user terminals. In this way the electrical isolation between adjacent satellites can be increased to improve the retainability and signal integrity of SATCOM links in UAVs. Polarization diversity, synthesized from two orthogonal signals, might be achieved by electronically re-configuring the amplitude and phase difference between cross-polarized antenna feeding ports as described in [17], [18], [19] and/or by alternating the polarizations of interleaved array elements within the same antenna aperture as described in [20].

3 DESIGN

3.1 TECHNICAL REQUIREMENTS

The following requirements were previously defined during the preparation of the project proposal regarding the “Hybrid Mechanical/ Electronic Steerable Antenna Array for $SATCOM$ Terminals” currently being developed by the University of Puerto Rico at Mayagüez:

- The Tx phased array antenna must operate in the Ku-band uplink frequency range from 13.75 GHz to 14.50 GHz.
- The $EIRP$ must be larger than 43 dBW when the main beam is pointed at ± 30° elevation angle.
- The Tx phased array antenna must provide linear polarization diversity.
- The maximum input power must be smaller than 30 dBm.
- The nominal power supply voltage is equal to +28 Vdc.
- The antenna aperture occupies a maximum area of $30.48\ cm \times 30.48\ cm$.
- The entire beamformer circuit must fit in a printed circuit board area measuring less than $15.24\ cm \times 30.48\ cm$.

It is also assumed that the impedances of all input and output ports must be referenced to 50 Ω.

3.2 MICROWAVE CIRCUIT DESIGN

3.2.1 PHASED ARRAY INTER-ELEMENT SPACING

The “Hybrid Mechanical/ Electronic Steerable Antenna Array for $SATCOM$ Terminals” will resemble a planar multilayer array structure made of a number of cross polarized stacked microstrip patch antennas. Both, Tx and Rx, phased array antennas will be interleaved together into one single aperture with a physical area of $30.48\ cm \times 30.48\ cm$. Figure 3.1 shows the hybrid mechanical/electronic steerable antenna array planar structure.

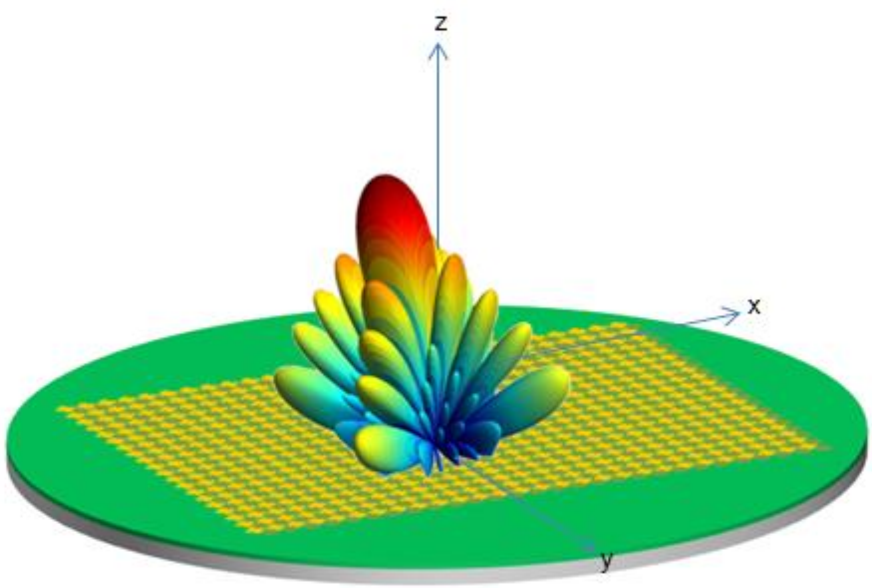

Figure 3.1 – Hybrid Mechanical/Electronic Steerable Antenna Array.

To avoid the formation of grating lobes the inter-element spacing in the direction of the x axis for adjacent radiating elements with similar polarizations (d_x) can be determined using the expression in Eq. 3.1

Eq. 3.1

$$d_x = \frac{\lambda}{2}$$

where λ is wavelength of the transmitted microwave signal with frequency of operation equal to f_0.

The inter-element spacing in the direction of the x axis for adjacent radiating elements with orthogonal polarizations $\left(d_{x_0}\right)$ can be determined using the expression in Eq. 3.2.

Eq. 3.2

$$d_{x_0} = \frac{\lambda}{4}$$

To provide enough board space to interleave Tx and Rx radiating elements in the same antenna aperture a larger inter-element spacing in the direction of the y axis $\left(d_y\right)$ must be implemented. The required d_y value can be determined using the expression in Eq. 3.3.

Eq. 3.3

$$d_y = \frac{\lambda}{1.5}$$

The minimum inter-element spacing values can be achieved by using the highest frequency of the required Tx frequency range, $f_0 = 14.5\ GHz$. Based on this frequency value the transmitted wavelength $\lambda = 2.07\ cm$ and the required inter-element spacing values are $d_x = 10.34\ mm$, $d_{x_0} = 5.17\ mm$ and $d_y = 13.79\ mm$.

The required number of antenna sub-arrays (N_x) and the required number of radiating elements per antenna sub-array $\left(N_y\right)$ can be determined using the expression in Eq. 3.4 and Eq. 3.5

Eq. 3.4

$$N_x = \frac{L_x}{d_x}$$

Eq. 3.5

$$N_y = \frac{L_y}{d_y}$$

where L_x represents the physical length of the phased array antenna aperture in the direction of the x axis, L_y represents the physical length of the phased array antenna aperture in the direction of the y axis. Based on the given antenna aperture physical dimensions $L_x = L_y = 30.84\ cm$ then $N_x = 28$ antenna sub-arrays and $N_y = 20$ radiating elements per antenna sub-array. Hence, the required number of Tx Sub-Arrays is also equal to twenty eight.

3.2.2 MICROWAVE CIRCUIT ARCHITECTURE

The fundamental Tx Sub-Array microwave circuit architecture employs one 1:2 coupler in order to split the transmitted Ku-band signal into two symmetric transmission paths with equal power and phase. Two variable phase shifters are used to control the difference in phase shifts between the signals of both transmission paths while one 90° hybrid coupler enables complex quadrature modulation at is output ports by combining the signal power of both transmission paths. Figure 3.2 shows the fundamental microwave circuit architecture for the Tx Sub-Array.

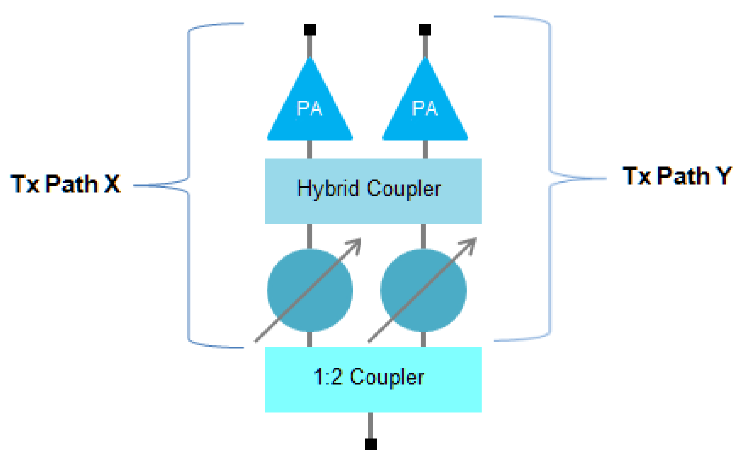

Figure 3.2 – Fundamental Microwave Circuit Architecture for the Tx Sub-Array.

Simultaneous one dimensional electronic beam steering and polarization tilt rotation might be achieved by electronically adapting the phase shifts provided by both Tx Sub-Array transmission paths. The phase shift of transmission path x at the n^{th} sub-array $\left(\phi_{x_n}\right)$ is set in terms of the phase difference between excitation signals of adjacent sub-arrays (ϕ) using the expression in Eq. 3.6

Eq. 3.6

$$\phi_{x_n} = \left(\frac{2 \cdot n \cdot \pi \cdot f_0}{c}\right) \cdot d_x \cdot sin(\theta_0) \qquad n = 0, 1, 2 \ldots N_x - 1$$

where c is the speed of light in vacuum in m/s [6].

According to the analysis in Appendix F the phase shift of the transmission path y at the n^{th} sub-array (ϕ_n) can be set in terms of the target polarization tilt angle as shown in Eq. 3.7

Eq. 3.7

$$\phi_{y_n} = \phi_{x_n} + \frac{\pi}{2} - 2 \cdot \psi_0$$

were ψ_0 is the target polarization tilt angle in $radians$.

Conversely, placing the PAs at the end of both transmission paths provides additional gain to achieve the required signal power levels at the antenna-sub-array ports and minimizes the connection losses between the PAs and the antenna sub-arrays. Moreover, this also relaxes linearity requirements of the PAs.

According to [21] the effective isotropic radiated power $(EIRP)$ of a two dimensional active phased array antenna can be determined using the expression in Eq. 3.8

Eq. 3.8

$$EIRP = N^2 \cdot P_{mod} \cdot D_{cell} \cdot (1 - |\Gamma|^2)$$

where N represents the required number of radiating elements $\left(N = N_x \cdot N_y = 560\right)$, P_{mod} represents the required PA output power, Γ represents the active reflection coefficient of the array input terminals. The active reflection coefficient Γ varies as a complex function of the scan angle because of the impedance mismatch that results from inter-element coupling, sometimes called mutual impedance. The directivity of a single radiating element (D_{cell}) is the defined as shown in Eq. 3.9

Eq. 3.9

$$D_{cell} = \frac{4 \cdot \pi \cdot d_x \cdot d_y}{\lambda^2} \cdot \cos(\theta_0)$$

where θ_0 represents the scan angle of the main lobe of the Tx phased array antenna. Choosing $\mathrm{f}_0 = 14.0$ GHz due to availability of S-parameter data provided by MMIC vendors at the center of the Tx frequency range, with $\theta_0 = 30°$ according EiRP requirement in Section 3.1 and the previously calculated inter-element spacing values the resulting directivity value is $D_{cell} = 3.97$.

Conversely, P_{mod} can be determined in terms of the given EIRP specification for a one dimensional active phased array antenna using the expression in Eq. 3.10

Eq. 3.10

$$P_{mod_{dBW}} = 10 \cdot \log_{10}\left(\frac{EIRP}{N_x \cdot N \cdot \epsilon_A \cdot D_{cell} \cdot (1 - |\Gamma|^2)}\right)$$

where ϵ_A represents the aperture efficiency [21]. Considering $\Gamma = 0.1$ and $\epsilon_A = 0.7$ as typical values then $P_{mod_{dBW}} = -2.65\ dBW$.

According to Eq. 3.9 the value of D_{cell} might be significantly reduced for operating scenarios with large scan angles. Therefore, the addition of a 3 dB margin is a design trade off that guarantees the required $EIRP$ level for operation scenarios with scan angles as large as $\pm 60°$. The expression in Eq. 3.11 can be used to account for this effect

Eq. 3.11

$$P_{out_{dBm}} = P_{mod_{dBW}} + \ 33\ dB$$

where $P_{out_{dBm}}$ represents the required output power per Tx Sub-Array in dBm. Hence, for design purposes $P_{out_{dBm}} = 30.35\ dBm$.

To provide the required input signal power to each Tx Sub-Array a $1:28$ corporate feed architecture is implemented. The 1:28 corporate feed architecture can be achieved by connecting the input ports of four $1:7$ multicouplers to the four output ports of an external 1:4 multicoupler.

The total gain (loss) introduced by the $1:28$ corporate feed $\left(G_{feed_{dB}}\right)$ can be determined using parameter values in Figure 3.26 and the expression in Eq. 3.12

Eq. 3.12

$$G_{feed_{dB}} = 10 \cdot \log_{10}\left(\frac{\epsilon_{L_1}\epsilon_{L_2}}{N_x}\right)$$

where ϵ_{L_1} represents the loss efficiency of the 1:4 multicoupler and ϵ_{L_2} represents the loss efficiency of the 1:7 multicoupler network. Considering that $\epsilon_{L_1} = 0.6$ and $\epsilon_{L_2} = 0.7$ then $G_{feed_{dB}} = -18.24\ dB$.

The available power per Tx Sub-Array $\left(P_{out\_feed_{dBm}}\right)$ can be determined using the expression in Eq 3.13

Eq. 3.13

$$P_{out\_feed_{dBm}} = P_{in\_feed_{dBm}} + 10 \cdot \log_{10}\left(1 - \left|\Gamma_{feed}\right|^2\right) + G_{feed_{dB}}$$

where $P_{in\_feed_{dBm}}$ represents the signal power level provided by the external Ku-band Mini CDL transceiver and Γ_{feed} represents the effective reflection coefficient at the 1:28 corporate feed's input terminal. Assuming $\mathrm{P_{in\_feed_{dBm}}} = 30$ dBm and $\Gamma_{\mathrm{feed}} = 0$ then the available power $\mathrm{P_{out\_feed_{dBm}}} = 9.68$ dBm.

Conversely, the required power amplifier gain $\left(G_{pa_{dB}}\right)$ can be determined using parameter values in Figure 3.26 and Eq. 3.14

Eq. 3.14

$$G_{pa_{dB}} = P_{out_{dBm}} - \left(P_{out\_feed_{dBm}} + 10 \cdot \log_{10}(1 - |\Gamma_{in}|^2) + G_{wc_{dB}} + G_{ps_{dB}} + G_{hc_{dB}}\right)$$

where Γ_{in} represents the effective reflection coefficient at the Tx Sub-Array's input terminal, $G_{wc_{dB}}$ represents the gain (loss) introduced by the 1:2 coupler in dB, $G_{ps_{dB}}$ represents the gain (loss) introduced by the phase shifter in dB, $G_{hc_{dB}}$ represents the gain introduced by the 90° hybrid coupler in dB and $G_{pa_{dB}}$ represents the gain introduced by the power amplifier in dB. From previous simulations and MMIC data sheet information it has been observed that $\mathrm{G_{wc_{dB}}} = -3.20$ dB and $\mathrm{G_{ps_{dB}}} = -10.00$ dB are reasonable values for this design. Also, it has been observed that for a Tx Sub-Array polarization state with $\psi_0 = 0°$ the gain of the hybrid coupler used as a power combiner $\mathrm{G}_{\mathrm{hc}_{\mathrm{dB}}} = 6$ dB. In this case, assuming that $\Gamma_{\mathrm{in}} = 0$ then $\mathrm{G}_{\mathrm{pa}_{\mathrm{dB}}} = 25.93$ dB.

However, the effects of impedance mismatch losses must be considered to prevent a negative impact on the expected communications range. The relation between the effective mismatch losses and the effective reflection coefficients at the inputs of the Tx Sub Array and the 1:28 corporate feed are shown in Eq. 3.15 and Eq. 3.16

Eq. 3.15

$$ML_{in_{dB}} = -10\log_{10}(1 - |\Gamma_{in}|^2)$$

Eq. 3.16

$$ML_{feed_{dB}} = -10\log_{10}\left(1 - \left|\Gamma_{feed}\right|^2\right)$$

where the $ML_{in_{dB}}$ accounts for all mismatch losses in the Tx Sub - Array and $ML_{feed_{dB}}$ accounts for all mismatch losses in the 1:28 corporate feed. From previous simulations it has been observed that $ML_{in_{dB}} = 1.94\ dB$ and $ML_{feed_{dB}} = 1.94\ dB$. Hence, Eq. 3.13 and Eq. 3.14 can be re-calculated considering that $\Gamma_{feed} = 0.6$ and $\Gamma_{in} = 0.6$. Now the resulting $G_{pa_{dB}}$ value is 3.88 dB higher than the previous value. This clearly indicates that the proposed Tx Sub-Array design must include a driver amplifier in its microwave circuit architecture if $G_{pa_{dB}} \leq 25.93\ dB$. Figure 3.3 shows the proposed microwave circuit architecture for the Tx Sub-Array including the driver amplifier.

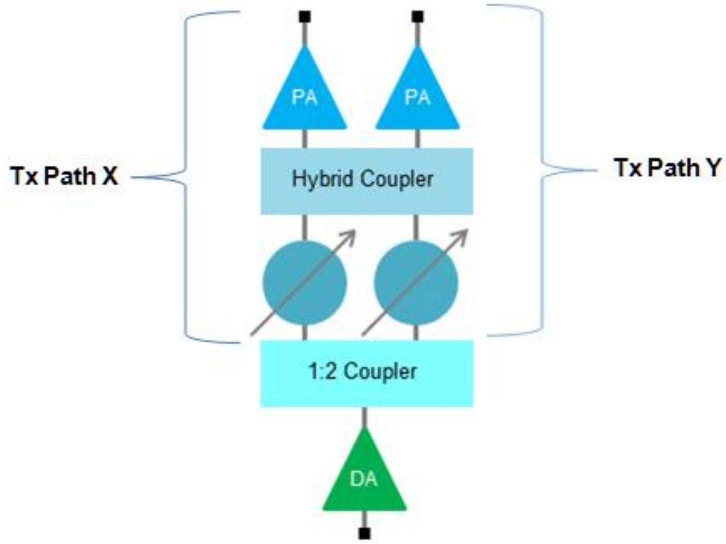

Figure 3.3 – Proposed Microwave Circuit Architecture for the Tx Sub-Array.

The required input power per Tx Sub-Array $\left(P_{in_{dBm}}\right)$ can be determined using Eq. 3.17.

Eq. 3.17

$$P_{in_{dBm}} = P_{out_{dBm}} - \left(\left(10 \cdot log_{10}(1 - |\Gamma_{in}|^2\right) + G_{da_{dB}} + G_{wc_{dB}} + G_{ps_{dB}} + G_{hc_{dB}} + G_{pa_{dB}}\right)\right)$$

where $G_{da_{dB}}$represents the gain introduced by the driver amplifier in dB. For instance, if a driver amplifier with $\mathrm{G}_{\mathrm{da}_{\mathrm{dB}}} = 23.25$ dB is chosen due to Tx Sub-Array linearity requirements (Section 3.3) then $\mathrm{P}_{\mathrm{in}_{\mathrm{dBm}}} = -9.69$ dBm. This value is significantly lower than $\mathrm{P}_{\mathrm{out\_feed}_{\mathrm{dBm}}}$. Hence, the recommended Tx BFN Module design must include a variable attenuator in its microwave circuit architecture in order to achieve the required $\mathrm{P}_{\mathrm{in}_{\mathrm{dBm}}}$ value. Figure 3.4 shows the microwave circuit architecture for the Tx BFN Module.

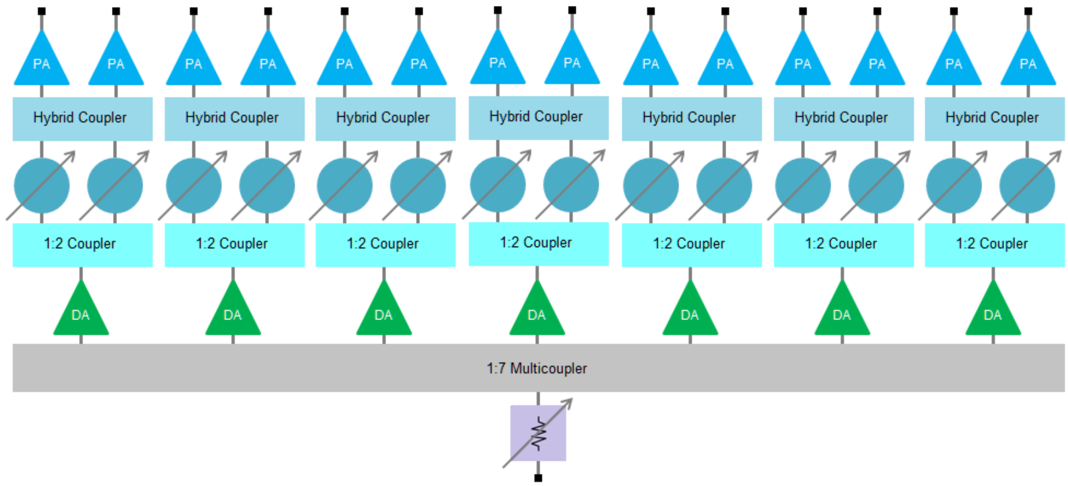

Figure 3.4 – Microwave Circuit Architecture for the Tx BFN Module.

The required attenuation value $\left(G_{atten_{dB}}\right)$ can be determined using Eq. 3.18

Eq. 3.18

$$G_{atten_{dB}} = P_{in_{dBm}} - P_{out\_feed_{dBm}}$$

Based on previously calculated values $P_{out\_feed_{dBm}} = 9.68\ dBm$, $P_{in_{dBm}} = -9.69\ dBm$ and $G_{atten_{dB}} = -19.37\ dB$. This value is the required gain reduction to guarantee to avoid the non-linear behavior of the amplifiers in the Tx Sub-Arrays when operating at the required $EiRP$ level in Section 3.1.

3.3 MICROWAVE CIRCUIT LINEARITY

The most common types of modulation waveforms implemented in satellite communications links are derived from complex quadrature modulation schemes where the modulated signal has simultaneous in-phase (I) and quadrature (Q) components in the I-Q plane. A signal with a complex quadrature modulation scheme might be modeled using the expression in Eq.3.19

Eq. 3.19

$$s(t) = \sqrt{\frac{2E_s}{T_s}}[h(t)\,\mathrm{I(t)}\cos(2\pi f_0 t) - h(t)Q(t-\delta)\sin(2\pi f_0 t)]$$

where E_s is the symbol energy, T_s is the symbol duration, f_0 is the carrier frequency, δ is the time offset, $h(t)$ is the baseband shaping filter, $\mathrm{I(t)}$ is the non-return to zero (NRZ) pseudorandom bit sequence associated to the in-phase component and $\mathrm{Q(t)}$ is the non-return to zero (NRZ) pseudorandom bit sequence associated to the quadrature component [22].

Since the peak power of $s(t)$ is limited by the saturation level of the PA, it follows that the higher its peak to average power ratio $(PAPR)$, the lower its average power, and thus the shorter it gets its transmission range [23]. Hence, it is of critical importance to consider the $PAPR$ during the design of the Tx Sub-Array.

According to [23] the $PAPR$ is defined as the ratio between the highest possible value of the instantaneous transmitted power that may occur in a given system (P_{Peak}) and the value obtained by averaging the transmitted power over a long (ideally infinite) period of time$\left(P_{Avg}\right)$ as shown in Eq. 3.20.

Eq. 3.20

$$PAPR = 10 \cdot \log_{10}\left(\frac{P_{Peak}}{P_{Avg}}\right) = 10 \cdot \log_{10}\left(\frac{\max\limits_{t_p} \frac{1}{\tau}\int_{t_p}^{t_p+\tau} s^2(t)\ dt}{\frac{1}{T}\int_{t_0}^{t_0+T} s^2(t)\ dt}\right)$$

where t_0 is the instant when the modulation waveform begins, T is the period of the modulation waveform, t_p is the instant within the time interval $[t_0,\ t_0 + T]$ where the modulation waveform reaches its maximum value and τ is the duration of the interval where the modulation waveform sustains its maximum value.

The $PAPR$ of the modulation waveform can be estimated using the envelope analysis methods described in [24]. For instance, a modulated signal with the same characteristics to those of the $OQPSK$ waveform described by Eq. 4.13, Eq.4.16 and Table 4.2 has an estimated $PAPR = 2.11\ dB$ assuming that spread spectrum is not being used. The required peak output power per Tx Sub-Array can be calculated using the expression in Eq. 3.21.

Eq. 3.21

$$P_{Peak_{dBm}} = P_{Avg_{dBm}} + PAPR$$

From previous calculations in Section 3.2.2 it can be considered that ${P_{Avg}}_{dBm} = {P_{out}}_{dBm}$. Hence, ${P_{Peak}}_{dBm} = 32.46\ dBm$ and for practical reasons it is also assumed that the required output 1 dB compression point of each Tx Sub-Array $\left(P_{1dB_{dBm}}\right)$ transmission path is equal or higher than $32.46\ dBm$.

According to the nominal microwave circuit architecture in Figure 3.2 the power amplifier's output 1 dB compression point $\left(P_{1dB_{pa}}\right)$ can be estimated using the expression in Eq. 3.22 that was derived from the set of equations in [25]

Eq. 3.22

$$P_{1dB_{pa}} = \frac{1}{\left(\frac{1}{P_{1dB}} - \left(\frac{1}{P_{1dB_{wc}} G_{ps} G_{hc} G_{pa}} + \frac{1}{P_{1dB_{ps}} G_{hc} G_{pa}} + \frac{1}{P_{1dB_{hc}} G_{pa}}\right)\right)}$$

where P_{1dB} represents the required output 1 dB compression point per Tx Sub-Array in mW, $P_{1dB_{wc}}$ represents the 1:2 coupler's output 1 dB compression point in mW, G_{ps} represents the gain (loss) introduced by the phase shifter, G_{hc} represents the gain introduced by the 90° hybrid coupler,G_{pa} represents the gain introduced by the power amplifier, $P_{1dB_{ps}}$ represents the phase shifter's output 1 dB compression point in mW and $P_{1dB_{hc}}$ represents the 90° hybrid coupler's output 1 dB compression point in mW. Since the use of this equation requires dimensionless gain values and/or absolute power levels expressed in mW units then the values considered in Section 3.2.2 calculations must be converted first. Hence, for a Tx Sub-Array polarization state with $\psi_0 = 0°$,

$\mathrm{P_{1dB}} = 1{,}761.98\ mW$, $\mathrm{P_{1dB_{wc}}} = 10^6\ mW$, $\mathrm{G_{ps}} = 0.10$, $\mathrm{G_{hc}} = 3.98$, $\mathrm{G_{pa}} = 391.74$, $\mathrm{P_{1dB_{ps}}} = 25.12$ mW and $\mathrm{P_{1dB_{hc}}} = 10^6\ mW$ then the resulting $\mathrm{P_{1dB_{pa}}} = 1{,}845.02\ mW$ or $\mathrm{P_{1dB_{pa_{dBm}}}} = 32.66$ dBm.

Likewise, according to the proposed microwave circuit architecture in Figure 3.3 the driver amplifier's output 1 dB compression point $\left(P_{1dB_{da}}\right)$ can be estimated using the expression in Eq. 3.23 that was derived from the set of equations in [25]

Eq. 3.23

$$P_{1dB_{da}} = \frac{1}{G_{wc}G_{ps}G_{hc}G_{pa}\left(\frac{1}{P_{1dB}} - \left(\frac{1}{P_{1dB_{wc}}G_{ps}G_{hc}G_{pa}} + \frac{1}{P_{1dB_{ps}}G_{hc}G_{pa}} + \frac{1}{P_{1dB_{hc}}G_{pa}} + \frac{1}{P_{1dB_{pa}}}\right)\right)}$$

where G_{wc} represents the gain (loss) introduced by the 1:2 coupler. Since the use of this equation requires dimensionless gain values and/or absolute power levels expressed in mW units then the values considered in Section 3.2.2 calculations must be converted first. Hence, with $\mathrm{G_{wc}} = 0.48$, $\mathrm{G_{ps}} = 0.10$, $\mathrm{G_{hc}} = 3.98$, $\mathrm{G_{pa}} = 391.74$, $\mathrm{P_{1dB_{ps}}} = 25.11\ mW$, $\mathrm{P_{1dB_{hc}}} = 10^6\ mW$ and $\mathrm{P_{1dB_{pa}}} = 1{,}845.02\ mW$ then $\mathrm{P_{1dB_{da}}} = 630.96\ mW$ or $\mathrm{P_{1dB_{da_{dBm}}}} = 28$ dBm.

According to [26] the output third order intercept point of a non-linear device is approximately 9.66 dB above its output 1 dB compression point. Hence, the power amplifier's output third order intercept point in dBm $\left(OIP_{3_{pa_{dBm}}}\right)$ can be estimated using the expression in Eq. 3.24

Eq. 3.24

$$OIP_{3_{pa_{dBm}}} = P_{1dB_{pa_{dBm}}} + 9.66\ dB$$

Considering that $P_{1dB_{pa_{dBm}}} = 32.66\ dBm$ then $OIP_{3_{pa_{dBm}}} = 42.32\ dBm.$

Likewise, the driver amplifier's output third order intercept point in dBm $\left(OIP_{3_{da_{dBm}}}\right)$ can be estimated using the expression in Eq. 3.25

Eq. 3.25

$$OIP_{3_{da_{dBm}}} = P_{1dB_{da_{dBm}}} + 9.66\ dB$$

Considering that $P_{1dB_{da_{dBm}}} = 28\ dBm$ then $OIP_{3_{da_{dBm}}} = 37.66\ dBm.$

Likewise, according to the proposed microwave circuit architecture in Figure 3.3 the required output third order intercept point per Tx Sub-Array (OIP_3) can be estimated using the expression in Eq. 3.26 that was derived from the set of equations in [25]

Eq. 3.26

$$OIP_3 = \frac{1}{\frac{1}{OIP_{3_{da}} G_{wc} G_{ps} G_{hc} G_{pa}} + \frac{1}{OIP_{3_{wc}} G_{ps} G_{hc} G_{pa}} + \frac{1}{OIP_{3_{ps}} G_{hc} G_{pa}} + \frac{1}{OIP_{3_{hc}} G_{pa}} + \frac{1}{OIP_{3_{pa}}}}$$

where $OIP_{3_{da}}$ represents the driver amplifier's output third order intercept point in mW, $OIP_{3_{wc}}$ represents the 1:2 coupler's output third order intercept point in mW, $OIP_{3_{ps}}$ represents the phase shifter's output third order intercept point in mW, $OIP_{3_{pa}}$ represents the power amplifier's output third order intercept point in mW. Considering $G_{wc} = 0.48$,

$G_{ps} = 0.10$, $G_{hc} = 3.98$, $G_{pa} = 391.74$, $OIP_{3_{da}} = 4{,}634.47 \ \ mW$, $OIP_{3_{wc}} = 10^6 \, mW$, $OIP_{3_{ps}} = 1{,}258.93 \, mW$, $OIP_{3_{hc}} = 10^6 \, mW$ and $OIP_{3_{pa}} = 17{,}061.82 \, mW$ then $OIP_3 = 16{,}292.96 \ mW$ or $OIP_{3_{dBm}} = \ 42.12 \ dBm$.

3.4 MICROWAVE CIRCUIT COMPONENTS

3.4.1 PASSIVE COMPONENTS

The design of all passive circuit components included in Figure 1.7 considers the implementation of interconnected microstrip line structures on Roger's RO4350B™ laminate. A microstrip line is a type of electrical transmission line fabricated using PCB technology, and is typically used to convey microwave-frequency signals from an excitation source to a load circuit. The microstrip line structure in Figure 3.5 consists of a conducting strip separated from a ground plane by a dielectric layer known as the substrate. The design equations used for estimation of the physical dimensions regarding microstrip lines can be found in [27].

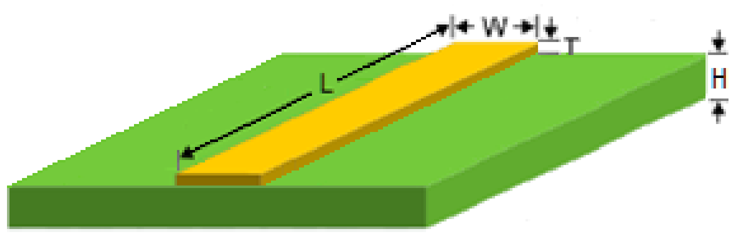

Figure 3.5 – Microstrip Line Structure.

In this case, the proposed RO4350B™ laminate has dielectric thickness of 0.254 mm, copper thickness of 17 μm and copper surface roughness of 2.8 μm. Roger's RO4350B™ materials are proprietary woven glass reinforced hydrocarbon/ceramics with electrical performance close to PTFE/woven glass and the manufacturability of epoxy/ glass. Roger's RO4350B™ is available at a fraction of the cost of conventional microwave laminates and no special through-hole treatments or handling procedures are required as with PTFE based microwave materials. Furthermore, Roger's RO4350B™ laminates are less likely to experience dielectric breakdown than other typical laminates based on FR-4. This characteristic is of critical importance since the proposed microwave circuits will operate in aerial environments where there is a much higher probability of building electrostatic charge [28].

3.4.1.1 90° Hybrid Coupler

The 90° hybrid coupler included in Figure 1.7 is a four port circuit that produces equal amplitude signals with a phase difference of 90° between the through and coupled ports. This unique characteristic enables complex quadrature modulation at its output ports when used as a power combiner. Figure 3.6 shows the microstrip line structure layout for the proposed 90° hybrid coupler.

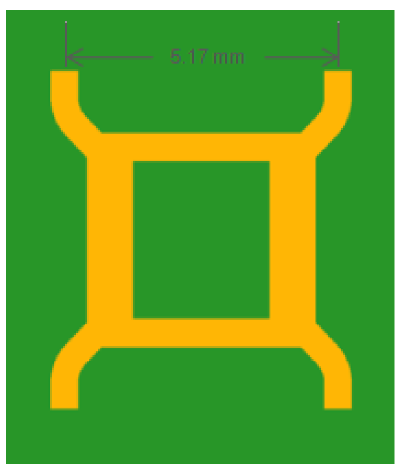

Figure 3.6 – 90° Hybrid Coupler Layout.

A symmetric power distribution is implemented assuming that all ports are matched to 50 Ω impedances. The series microstrip line branches are λ/4 transformers, each with characteristic impedance of 35.55 Ω. The width of these microstrip lines is approximately 0.92 mm. The shunt microstrip line branches are λ/4 transformers, each with characteristic impedance of 50 Ω. The width of these microstrip lines is approximately 0.540 mm.

The slanted (±45°) microstrip lines at each port are included to improve the match and to achieve a port to port separation of 5.17 mm, half the required array element spacing in the horizontal direction. These are also microstrip lines with characteristic impedance of 50 Ω.

The frequency response of the 90° hybrid coupler can be characterized by the scattering parameter matrix shown in Eq. 3.27

Eq. 3.27

$$\mathbf{S} = \begin{bmatrix} S_{11} & S_{12} & S_{13} & S_{14} \\ S_{21} & S_{22} & S_{23} & S_{24} \\ S_{31} & S_{32} & S_{33} & S_{34} \\ S_{41} & S_{42} & S_{43} & S_{44} \end{bmatrix}$$

where S_{ii} represents the voltage reflection coefficient of the ith port when all other ports are terminated with matched loads and S_{ij} represents the voltage transmission coefficient from the jth port to the ith port when all other ports are terminated with matched loads.

According to [29] the diagonal elements of the scattering matrix can be determined using the expression in Eq. 3.28

Eq. 3.28

$$S_{ii} = \left. \frac{v_i^-}{v_i^+} \right|_{v_k^+ = 0 \; for \; k \neq i}$$

where v_i^- represents the outgoing wave voltage amplitude at the ith port and v_i^+ represents the incident wave voltage amplitude at the ith port.

Likewise, the off-diagonal elements of the scattering matrix can be determined by using the expression in Eq. 3.29

Eq. 3.29

$$S_{ij} = \left. \frac{v_i^-}{v_j^+} \right|_{v_k^+ = 0 \; for \; k \neq j}$$

where v_i^- represents the outgoing wave voltage amplitude at the ith port and v_j^+ represents the incident wave voltage amplitude at the jth port [29].

For instance, the scattering parameter matrix for an ideal 90° hybrid coupler is shown in Eq. 3.30 below.

Eq. 3.30

$$\mathbf{S} = \frac{-1}{\sqrt{2}} \begin{bmatrix} 0 & j & 1 & 0 \\ j & 0 & 0 & 1 \\ 1 & 0 & 0 & j \\ 0 & 1 & j & 0 \end{bmatrix}$$

The actual scattering parameters of the 90° hybrid coupler can be estimated using a commercial CAD tool that implements similar mathematical procedures as the method of moments (MoM) described in [30] and [31].

Figure 3.7 shows the predicted transmission coefficient magnitudes for the proposed 90° hybrid coupler design. The average gain predicted within the required Tx frequency range is approx. -3.18 dB. The predicted gain imbalance average within the required Tx frequency range is approx. 0.32 dB.

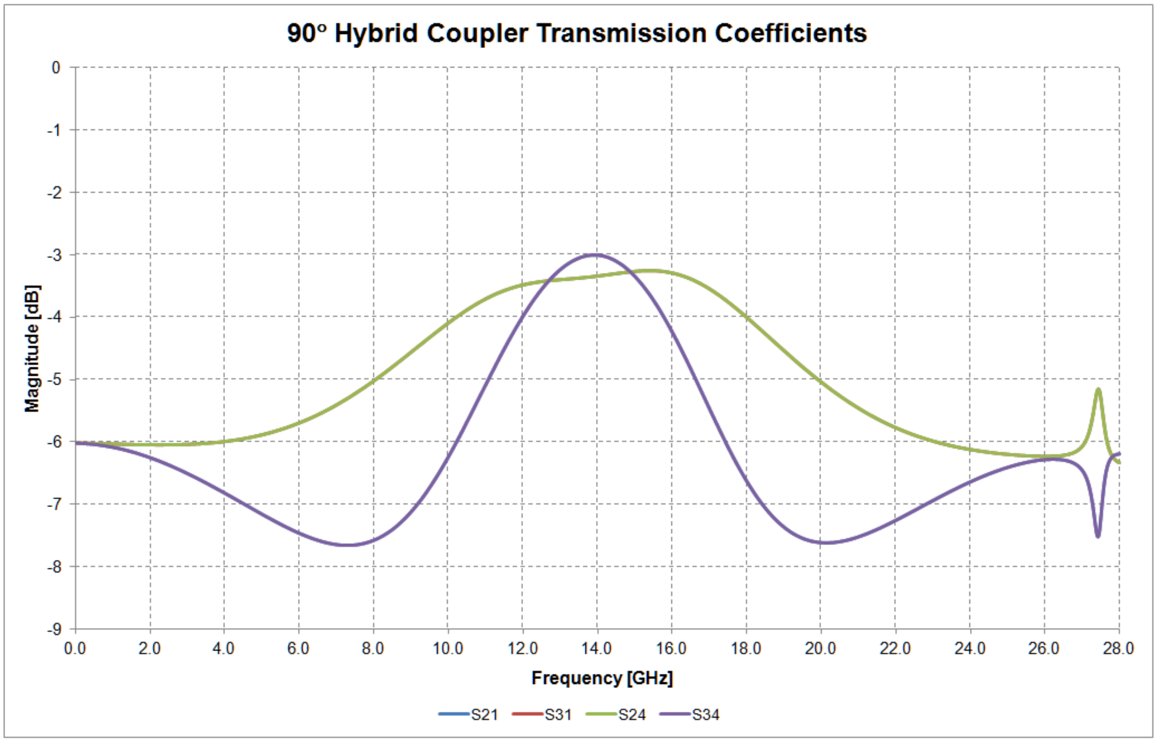

Figure 3.7 – 90° Hybrid Coupler Transmission Coefficient Magnitudes.

Figure 3.8 shows the predicted transmission coefficient phases for the proposed 90° hybrid coupler design. The predicted phase difference average within the required Tx frequency range is approx. 89.77°. This implies an average phase imbalance of only 0.23° from the theoretical phase difference of 90°.

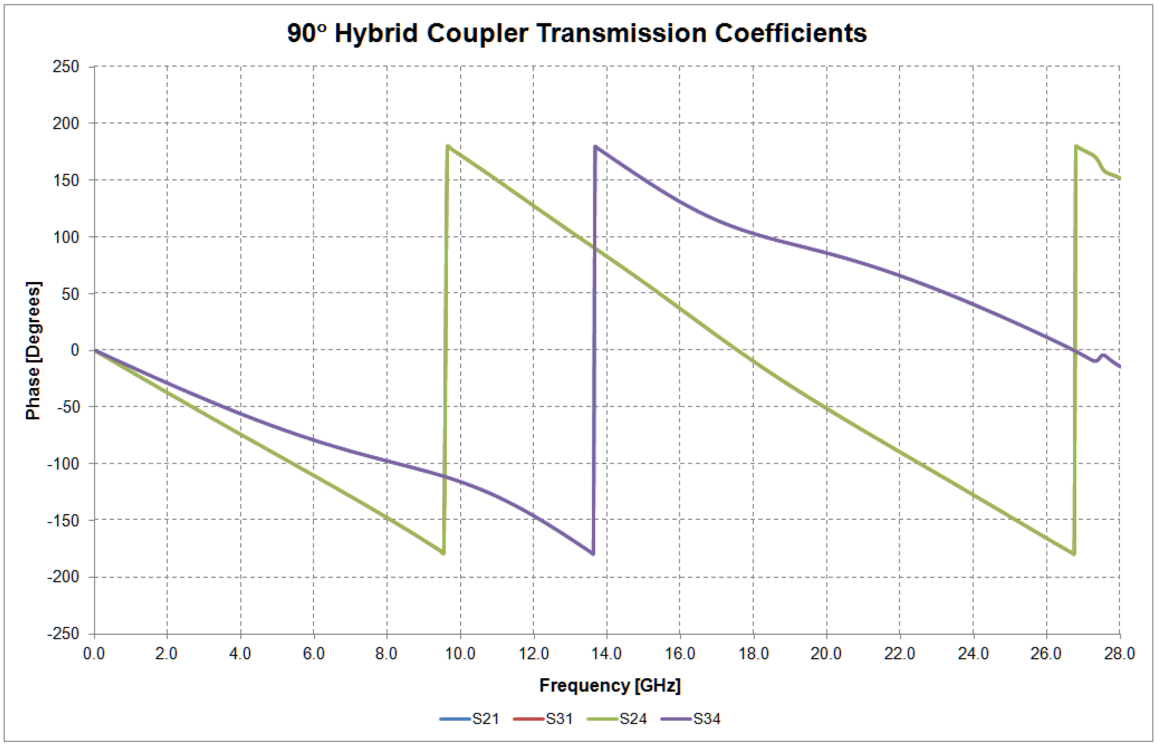

Figure 3.8 – 90° Hybrid Coupler Transmission Coefficient Phases.

Figure 3.9 shows the predicted reflection coefficient magnitudes for the proposed 90° hybrid coupler design. The predicted minimum return loss within the required Tx frequency range is approx. 25.041 dB at the input ports and approx. 25.040 dB at the output ports.

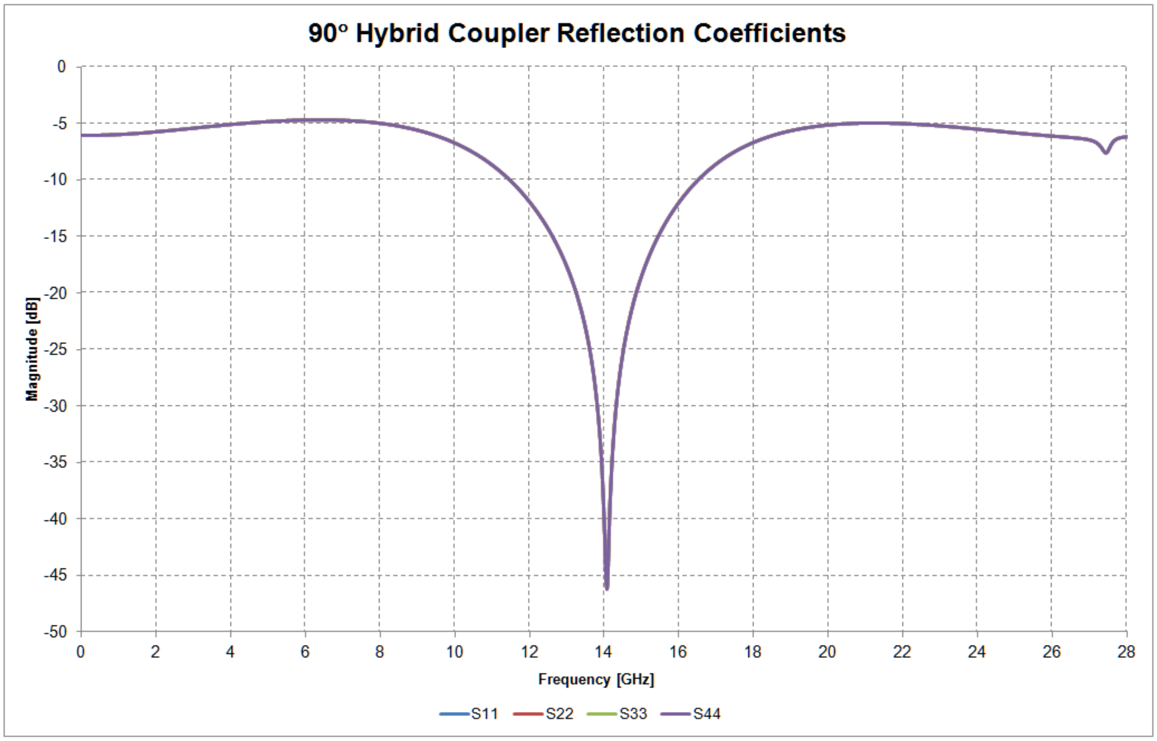

Figure 3.9 – 90° Hybrid Coupler Reflection Coefficient Magnitudes.

Figure 3.10 shows the predicted isolation coefficient magnitudes for the proposed 90° hybrid coupler design. The predicted minimum isolation within the required Tx frequency range is approx. 24.20 dB.

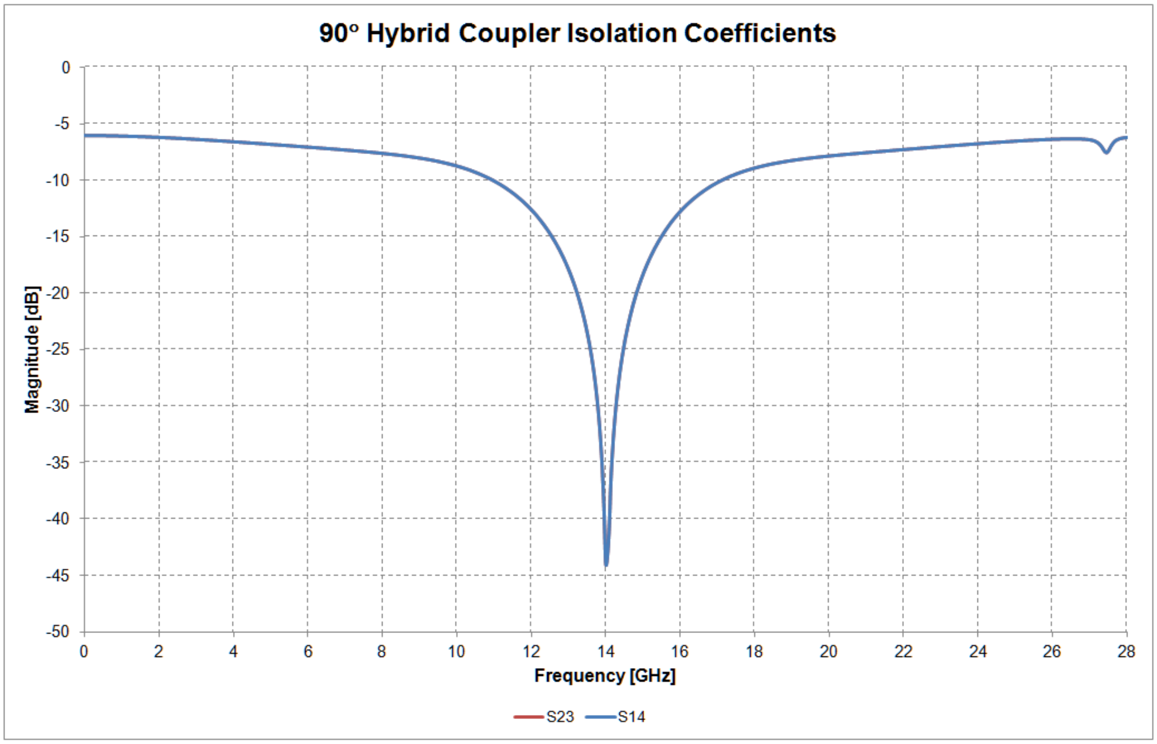

Figure 3.10 – 90° Hybrid Coupler Isolation Coefficient Magnitudes.

3.4.1.2 1:2 Coupler

The 1:2 coupler included in Figure 1.7, in this case a Wilkinson power divider, provides equal amplitude power splitting with equal phase when its output ports are matched. This unique characteristic enables the basic structure for the implementation of the multicouplers composing the corporate architecture of the proposed beamformer design. Figure 3.11 shows the microstrip line structure layout for the proposed 1:2 coupler.

Figure 3.11 – 1:2 Coupler Layout.

A symmetric power distribution is implemented assuming that all ports are matched to 50 Ω impedances. The C shaped microstrip lines connected to the input port (port 1) are $\lambda/4$ transformers each with characteristic impedance of 70.71 Ω. The width of these microstrip lines is approximately 0.302 mm. The S shaped microstrip lines have characteristic impedance of 50 Ω. The width of these microstrip lines is approximately 0.540 mm. The separation between output ports (ports 2 and 3) is 5.17 mm.

Conversely, power reflections from the output ports are dissipated in the 100 Ω resistor that is connected between the ends of the C shaped λ/4 impedance transformers. The size of the gap between the ends of the C shaped λ/4 impedance transformers is. 0.5588 mm.

The frequency response of the 1:2 coupler can be characterized by the scattering parameter matrix shown in Eq. 3.31.

Eq. 3.31

$$\mathbf{S} = \begin{bmatrix} S_{11} & S_{12} & S_{13} \\ S_{21} & S_{22} & S_{23} \\ S_{31} & S_{32} & S_{33} \end{bmatrix}$$

For instance, the scattering parameter matrix for an ideal 1:2 coupler is shown in Eq. 3.32 below.

Eq. 3.32

$$\mathbf{S} = \frac{-j}{\sqrt{2}} \begin{bmatrix} 0 & 1 & 1 \\ 1 & 0 & 0 \\ 1 & 0 & 0 \end{bmatrix}$$

The actual scattering parameters of the 1:2 coupler can be estimated using a commercial CAD tool that implements similar mathematical procedures as the method of moments (MoM) described in [30] and [31].

Figure 3.12 shows the predicted transmission coefficient magnitudes for the proposed 1:2 coupler design. The predicted gain average within the required Tx frequency range is approx. -3.31 dB. The predicted gain imbalance average within the required Tx frequency range is approx. 0.0002 dB.

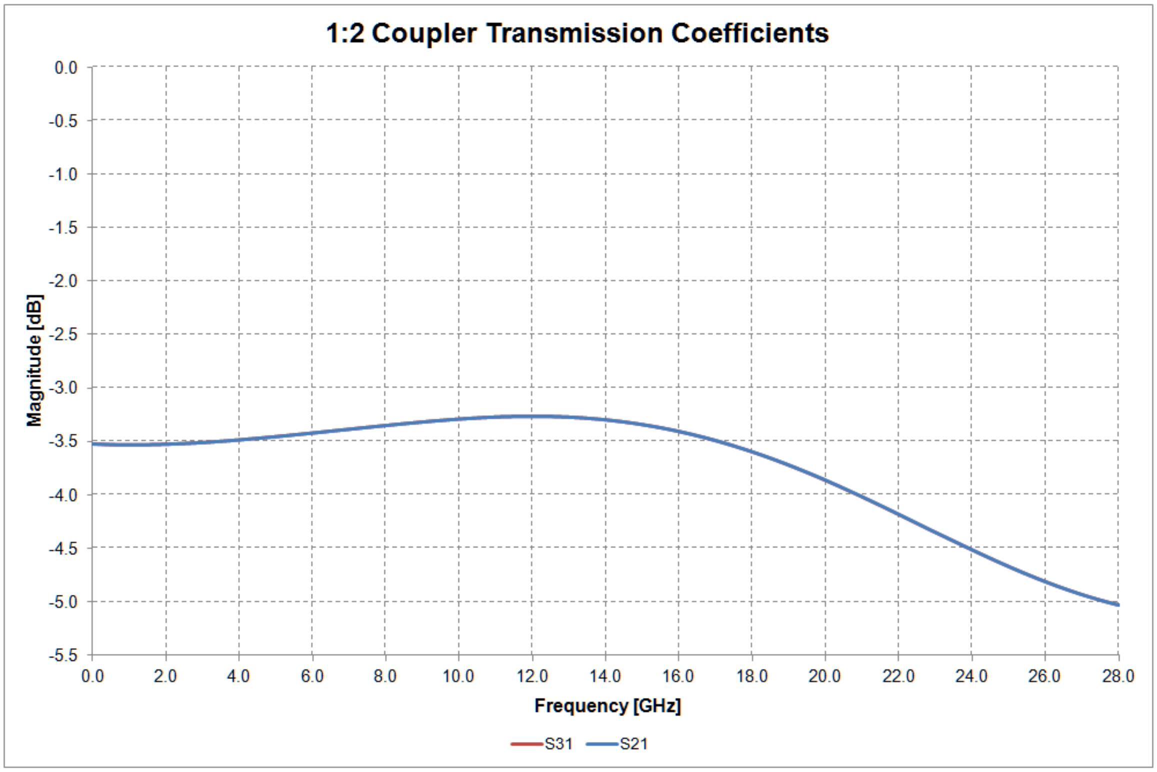

Figure 3.12 – 1:2 Coupler Transmission Coefficient Magnitudes.

Figure 3.13 shows the predicted transmission coefficient phases for the proposed 1:2 coupler design. The predicted phase difference average within the required Tx frequency range is approx. 0.0038°.

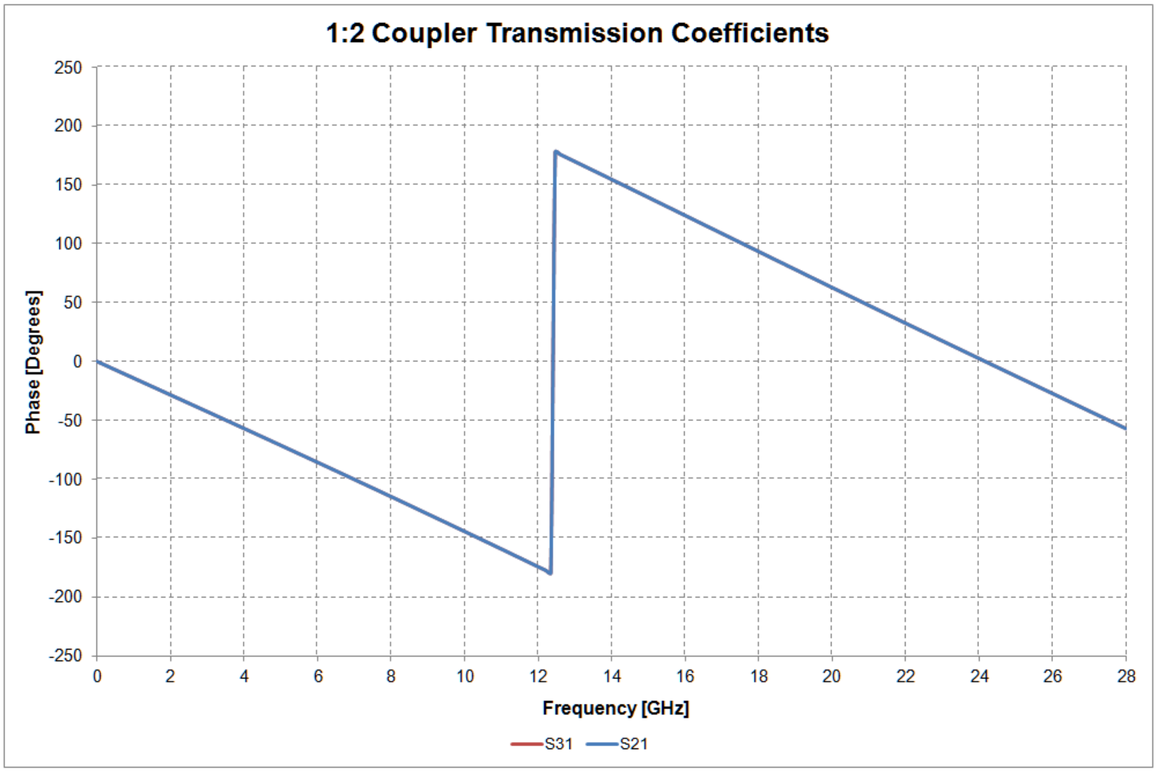

Figure 3.13 – 1:2 Coupler Transmission Coefficient Phases.

Figure 3.14 shows the predicted reflected coefficient magnitudes for the proposed 1:2 coupler design. The predicted minimum return loss within the required Tx frequency range is approx. 29.83 dB at the input port and approx. 18.07 dB at the output ports.

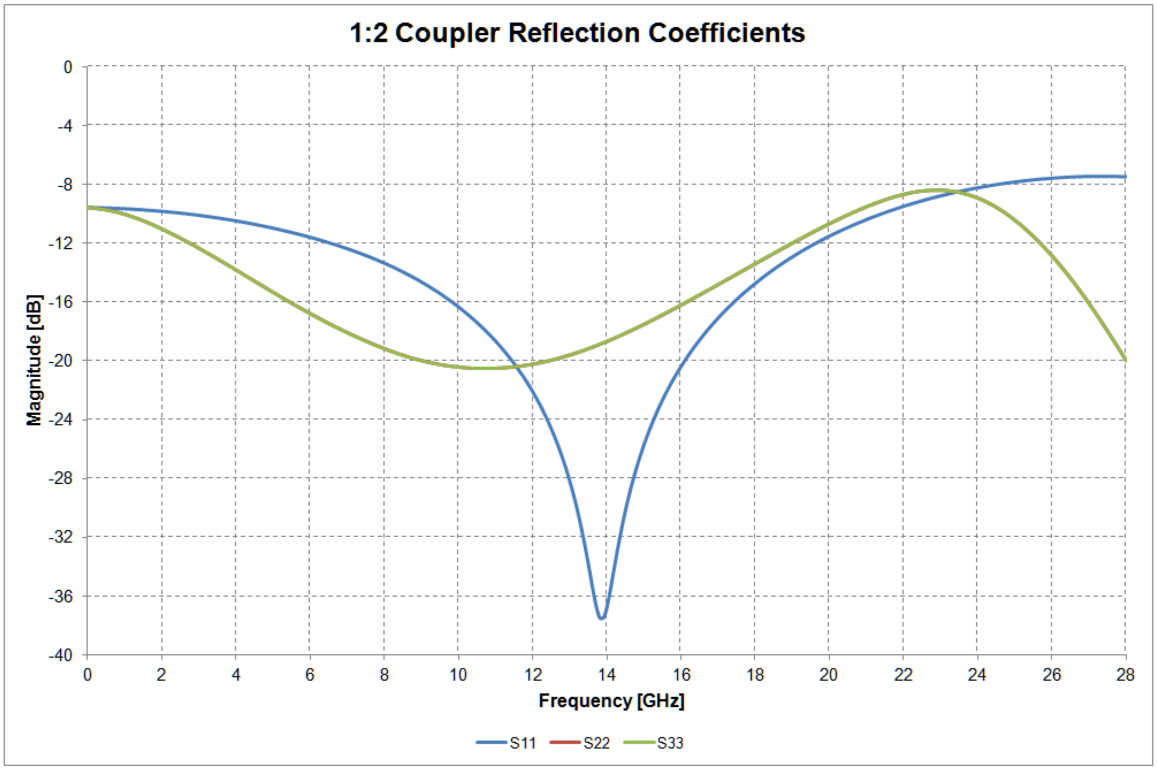

Figure 3.14 – 1:2 Coupler Reflection Coefficient Magnitudes.

Figure 3.15 shows the predicted isolation coefficient magnitudes for the proposed 1:2 coupler design. The predicted minimum isolation within the required Tx frequency range is approx. 19.01 dB.

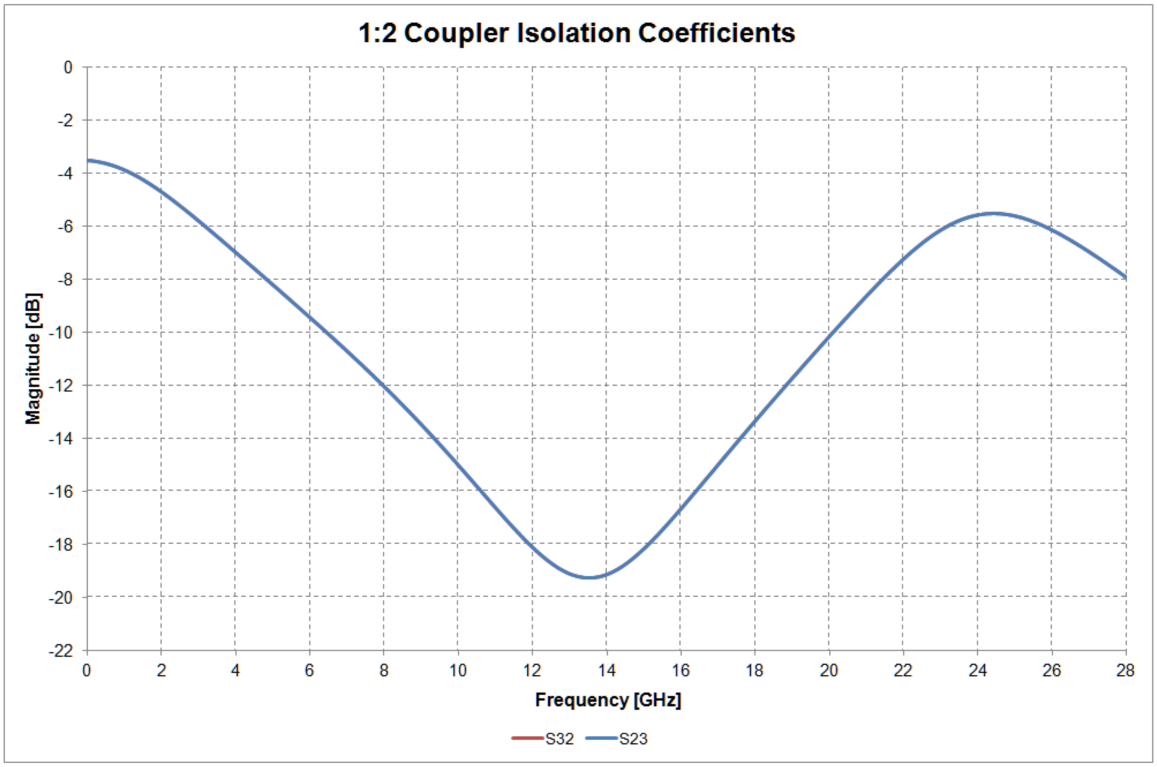

Figure 3.15 – 1:2 Coupler Isolation Coefficient Magnitudes.

3.4.1.3 1:7 Multicoupler

The design of the 1:7 multicoupler included in Figure 1.7 is based on re-use, modification and interconnection of the 1:2 coupler microstrip line structure described in the previous section. The interconnections are implemented by microstrip lines with characteristic impedance of 50 Ω. The width of these microstrip lines is approximately 0.540 mm. Figure 3.16 shows the microstrip line structure layout for the proposed 1:7 multicoupler design.

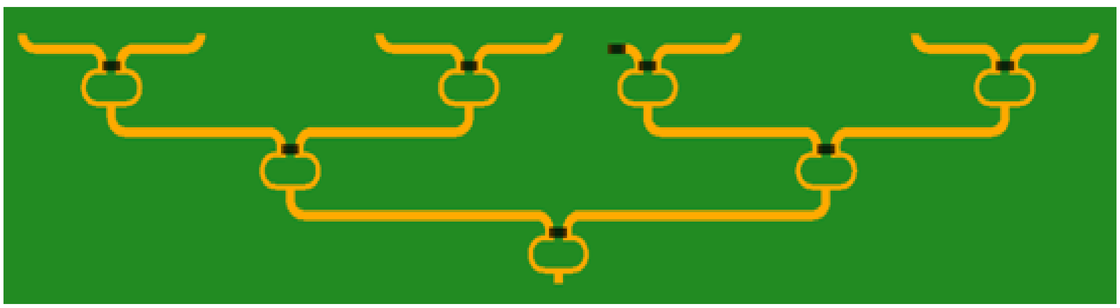

Figure 3.16 - 1:7 Multicoupler Layout.

A basic 1:8 multicoupler architecture is implemented and modified by terminating one of its output ports with a 50 Ω resistor. The remaining output ports are repositioned to achieve a separation of 10.34 mm between adjacent output ports. Uniform phase and even power distribution are achieved by this simple approach.

The frequency response of the 1:7 multicoupler can be characterized by the scattering parameter matrix shown in Eq. 3.33.

Eq. 3.33

$$\mathbf{S} = \begin{bmatrix} S_{11} & S_{12} & S_{13} & S_{14} & S_{15} & S_{16} & S_{17} & S_{18} \\ S_{21} & S_{22} & S_{23} & S_{24} & S_{25} & S_{26} & S_{27} & S_{28} \\ S_{31} & S_{32} & S_{33} & S_{34} & S_{35} & S_{36} & S_{37} & S_{38} \\ S_{41} & S_{42} & S_{43} & S_{44} & S_{45} & S_{46} & S_{47} & S_{48} \\ S_{51} & S_{52} & S_{53} & S_{54} & S_{55} & S_{56} & S_{57} & S_{58} \\ S_{61} & S_{62} & S_{63} & S_{64} & S_{65} & S_{66} & S_{67} & S_{68} \\ S_{71} & S_{72} & S_{73} & S_{74} & S_{75} & S_{76} & S_{77} & S_{78} \\ S_{81} & S_{82} & S_{83} & S_{84} & S_{85} & S_{86} & S_{87} & S_{88} \end{bmatrix}$$

For instance, the scattering parameter matrix for an ideal 1:7 multicoupler is shown in Eq. 3.34 below.

Eq. 3.34

$$\mathbf{S} = \frac{e^{j\left(\pi/2\,+\,\beta(\ell_1+\ell_2+\ell_3)\right)}}{2\sqrt{2}} \cdot \begin{bmatrix} 0 & 1 & 1 & 1 & 1 & 1 & 1 & 1 \\ 1 & 0 & 0 & 0 & 0 & 0 & 0 & 0 \\ 1 & 0 & 0 & 0 & 0 & 0 & 0 & 0 \\ 1 & 0 & 0 & 0 & 0 & 0 & 0 & 0 \\ 1 & 0 & 0 & 0 & 0 & 0 & 0 & 0 \\ 1 & 0 & 0 & 0 & 0 & 0 & 0 & 0 \\ 1 & 0 & 0 & 0 & 0 & 0 & 0 & 0 \\ 1 & 0 & 0 & 0 & 0 & 0 & 0 & 0 \end{bmatrix}$$

where ℓ_1 is the length of the microstrip lines connected to the output ports of the first 1:2 coupler structure, ℓ_2 is the length of the microstrip lines connected to the output ports of the second and third 1:2 coupler structures and ℓ_3 is the length of the microstrip lines connected to the output ports of the fourth, fifth, sixth and seventh 1:2 coupler structures.

The actual scattering parameters of the 1:7 multicoupler can be estimated using a commercial CAD tool that implements similar mathematical procedures as the method of moments (MoM) described in [30] and [31].

Figure 3.17 shows the predicted transmission coefficient magnitudes for the proposed 1:7 multicoupler design. The predicted gain average within the required Tx frequency range is approx. -10.4 dB. The average gain imbalance predicted within the required Tx frequency range is approx. 0.13 dB.

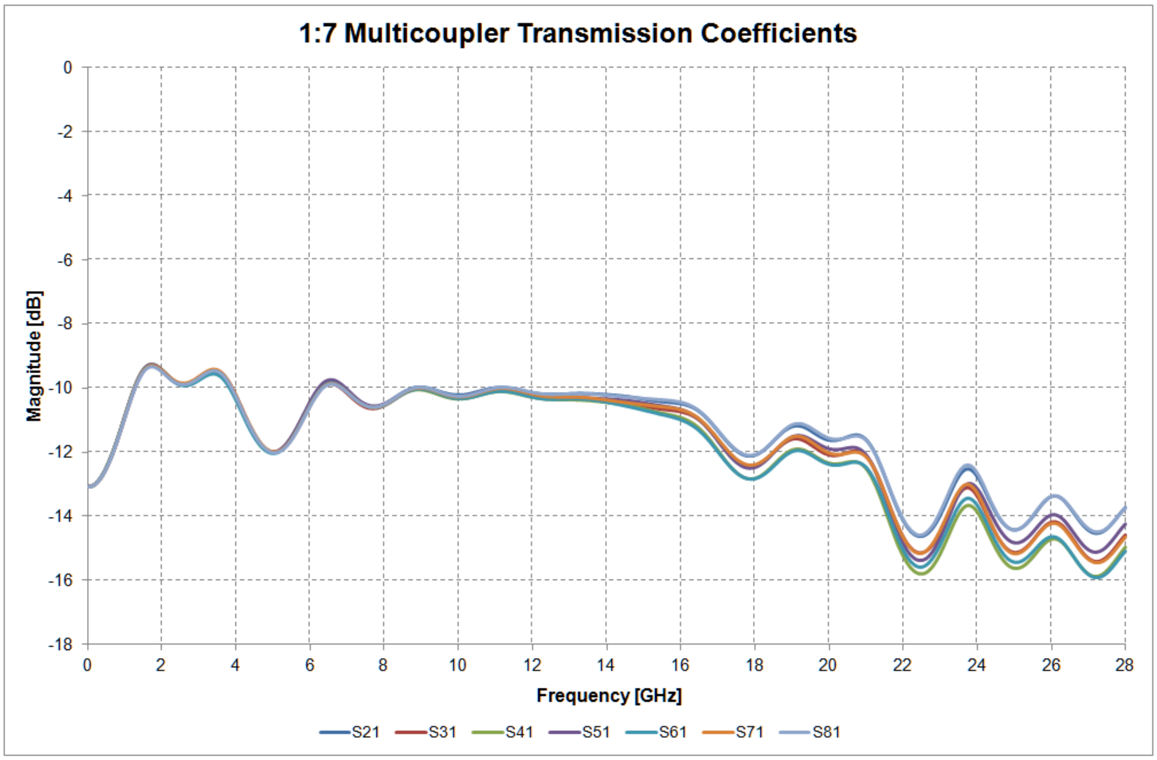

Figure 3.17 - 1:7 Multicoupler Transmission Coefficient Magnitudes.

Figure 3.18 shows the predicted transmission coefficient phases for the proposed 1:7 multicoupler design. The predicted phase difference average within the required Tx frequency range is approx. 0.23°.

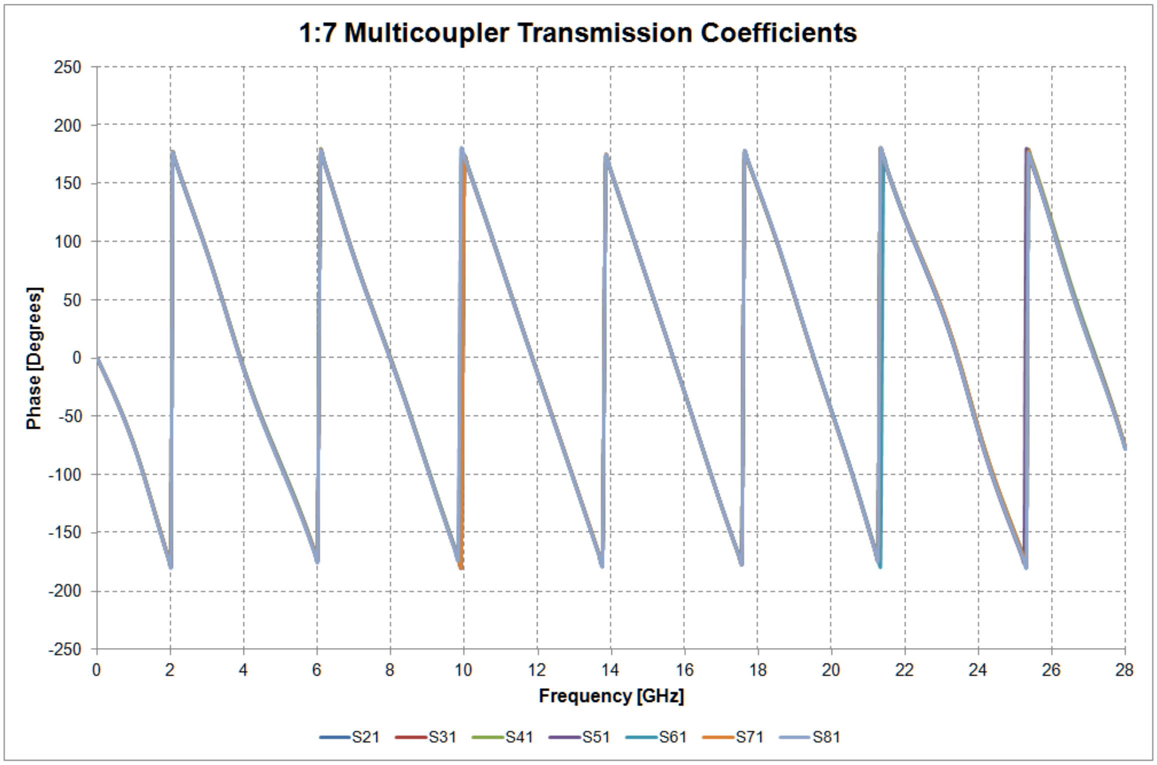

Figure 3.18 - 1:7 Multicoupler Transmission Coefficient Phases.

Figure 3.19 shows the predicted reflection coefficient magnitudes for the proposed 1:7 multicoupler design. The predicted minimum return loss within the required Tx frequency range is approx. 27.9 dB at the input port and approx. 18.2 dB at the output ports.

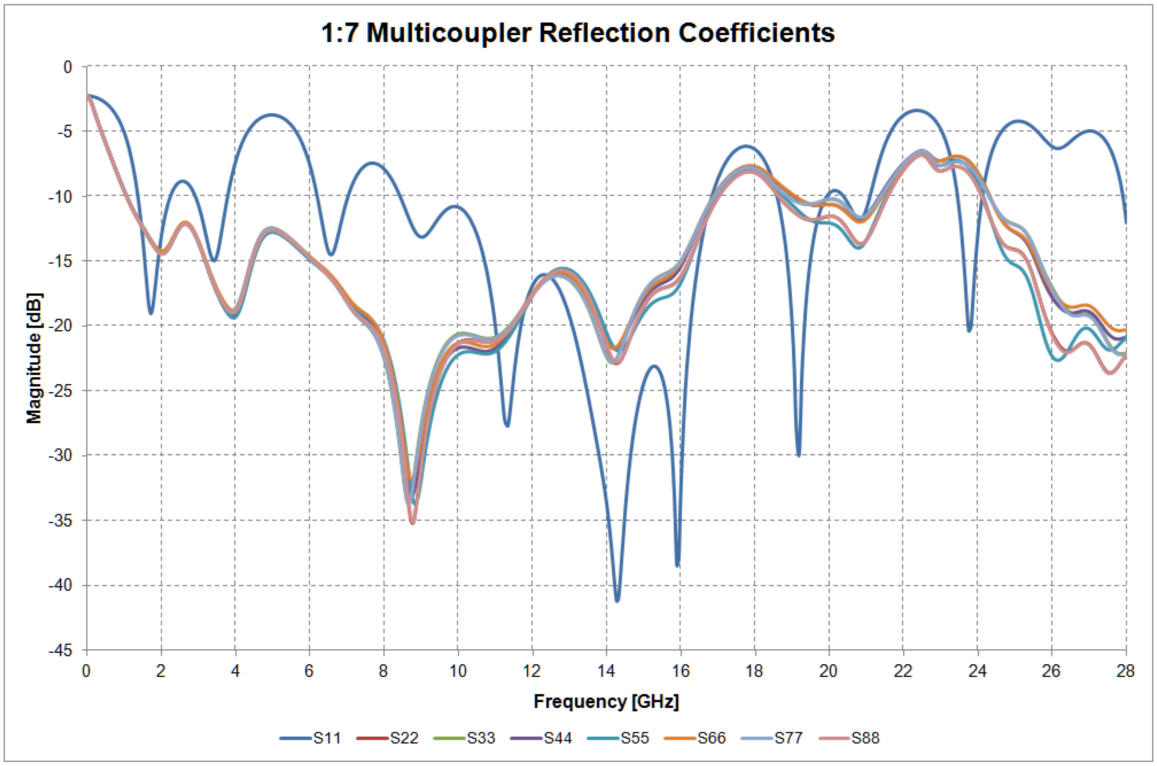

Figure 3.19 - 1:7 Multicoupler Reflection Coefficient Magnitudes.

Figure 3.20 shows the predicted isolation coefficient magnitudes for the proposed 1:7 multicoupler design. The predicted minimum isolation within the required Tx frequency range is approx. 15.64 dB.

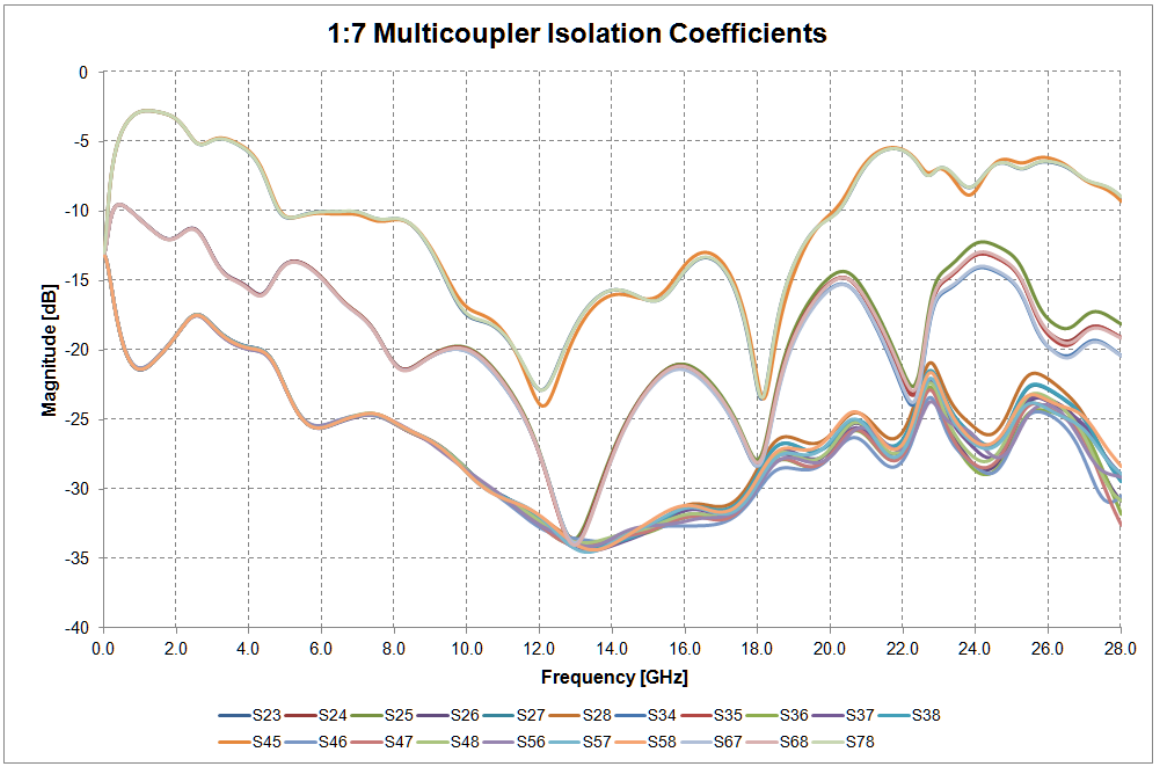

Figure 3.20 - 1:7 Multicoupler Isolation Coefficient Magnitudes.

3.4.1.4 1:4 Multicoupler

The design of the 1:4 multicoupler that interconnects to four Tx BFN Modules is based on re-use, modification and interconnection of the 1:2 coupler microstrip line structure described in the previous section. The interconnections are implemented by microstrip lines with characteristic impedance of 50 Ω. The width of these microstrip lines is approximately 0.540 mm. Figure 3.21 shows the microstrip line structure layout for the proposed 1:7 multicoupler design.

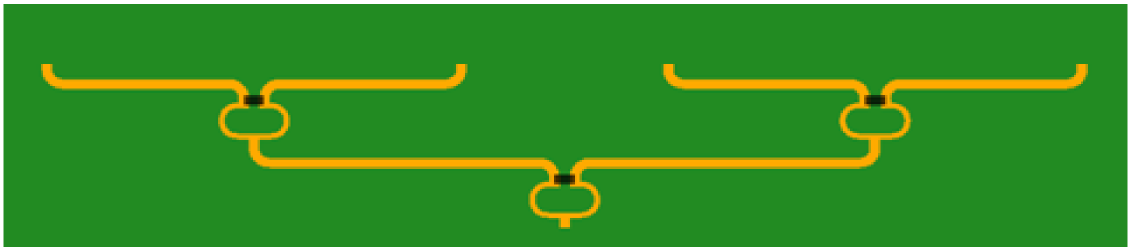

Figure 3.21 - 1:4 Multicoupler Layout.

A symmetric 1:4 multicoupler power distribution is implemented assuming that all ports are matched to 50 Ω impedances. The separation between adjacent output ports is 72.38 mm.

For instance, the frequency response of the 1:4 multicoupler can be characterized by the scattering parameter matrix shown in Eq. 3.35.

Eq. 3.35

$$\mathbf{S} = \begin{bmatrix} S_{11} & S_{12} & S_{13} & S_{14} & S_{15} \\ S_{21} & S_{22} & S_{23} & S_{24} & S_{25} \\ S_{31} & S_{32} & S_{33} & S_{34} & S_{35} \\ S_{41} & S_{42} & S_{43} & S_{44} & S_{45} \\ S_{51} & S_{52} & S_{53} & S_{54} & S_{55} \end{bmatrix}$$

The scattering parameter matrix for an ideal 1:7 multicoupler is shown in Eq. 3.36 below.

Eq. 3.36

$$\mathbf{S} = \frac{e^{j(\pi + \beta(\ell_1 + \ell_2))}}{2} \cdot \begin{bmatrix} 0 & 1 & 1 & 1 & 1 \\ 1 & 0 & 0 & 0 & 0 \\ 1 & 0 & 0 & 0 & 0 \\ 1 & 0 & 0 & 0 & 0 \\ 1 & 0 & 0 & 0 & 0 \end{bmatrix}$$

where ℓ_1 is the length of the microstrip lines connected to the output ports of the first 1:2 coupler structure and ℓ_2 is the length of the microstrip lines connected to the output ports of the second and third 1:2 coupler structures.

The actual scattering parameters of the 1:4 multicoupler can be estimated using a commercial CAD tool that implements similar mathematical procedures as the method of moments (MoM) described in [30] and [31].

Figure 3.22 shows the predicted transmission coefficient magnitudes for the proposed 1:4 multicoupler design. The predicted gain average within the required Tx frequency range is approx. -8.18 dB. The predicted average gain imbalance within the required Tx frequency range is approx. 0.02 dB.

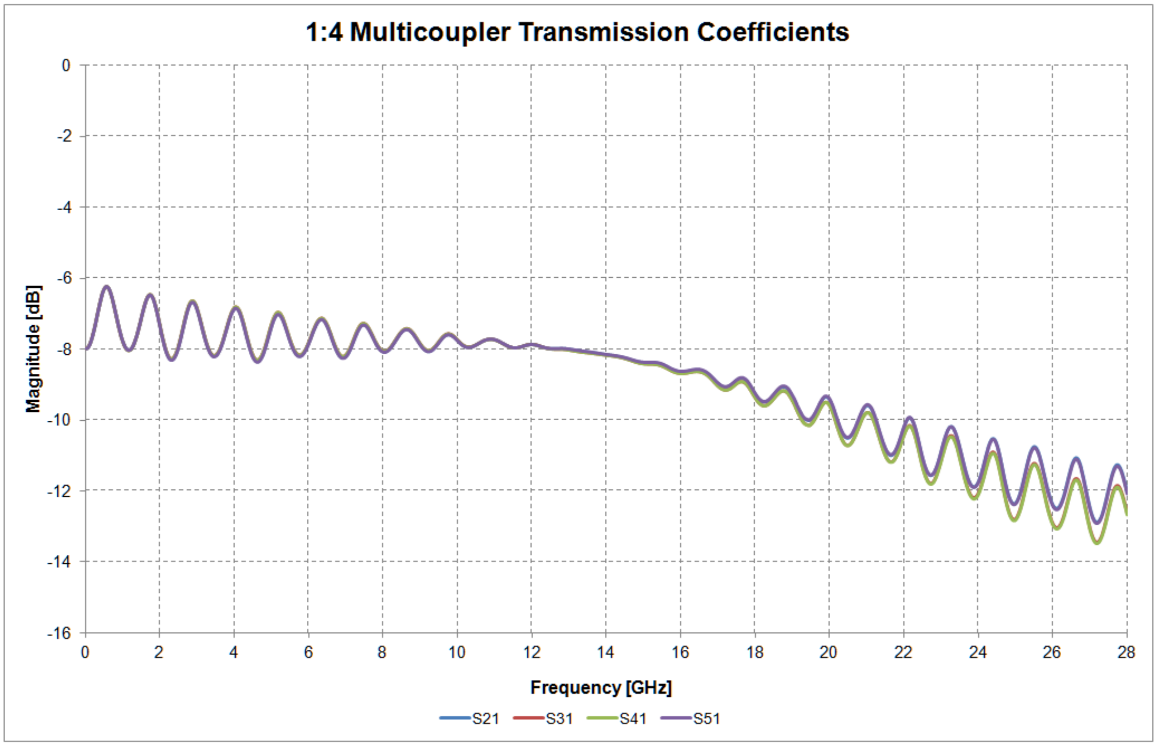

Figure 3.22 - 1:4 Multicoupler Transmission Coefficient Magnitudes.

Figure 3.23 shows the predicted transmission coefficient phases for the proposed 1:4 multicoupler design. The predicted phase difference average within the required Tx frequency range is approx. 0.22°.

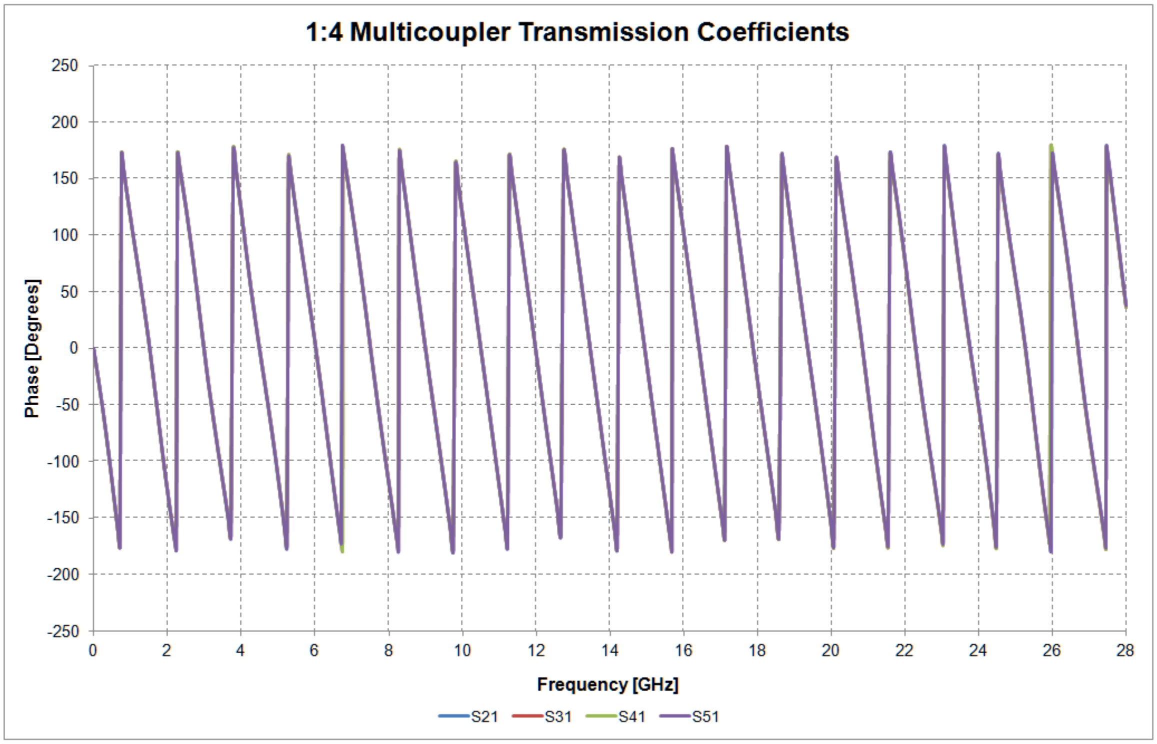

Figure 3.23 - 1:4 Multicoupler Transmission Coefficient Phases.

Figure 3.24 shows the predicted reflection coefficient magnitudes for the proposed 1:4 multicoupler design. The predicted minimum return loss within the required Tx frequency range is approx. 25.49 dB at the input port and approx. 16.98 dB at the output ports.

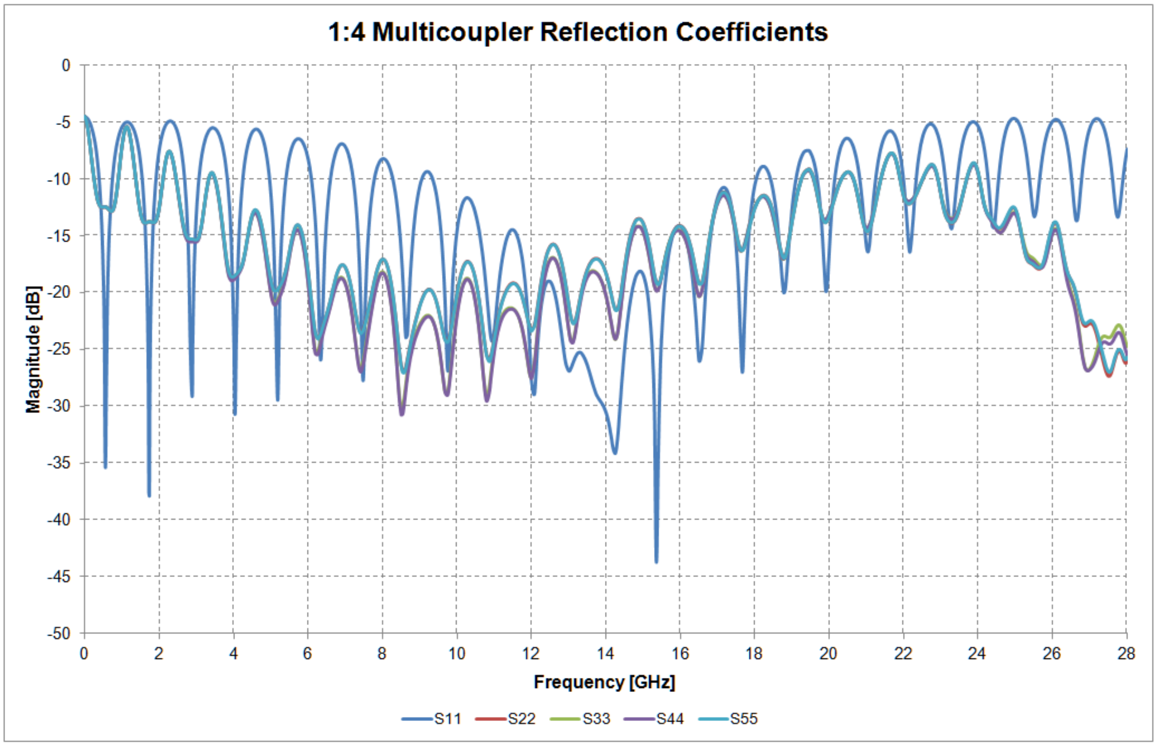

Figure 3.24 - 1:4 Multicoupler Reflection Coefficient Magnitudes.

Figure 3.25 shows the predicted isolation coefficient magnitudes for the proposed 1:4 multicoupler design. The predicted minimum isolation within the required Tx frequency range is approx. 16.82 dB.

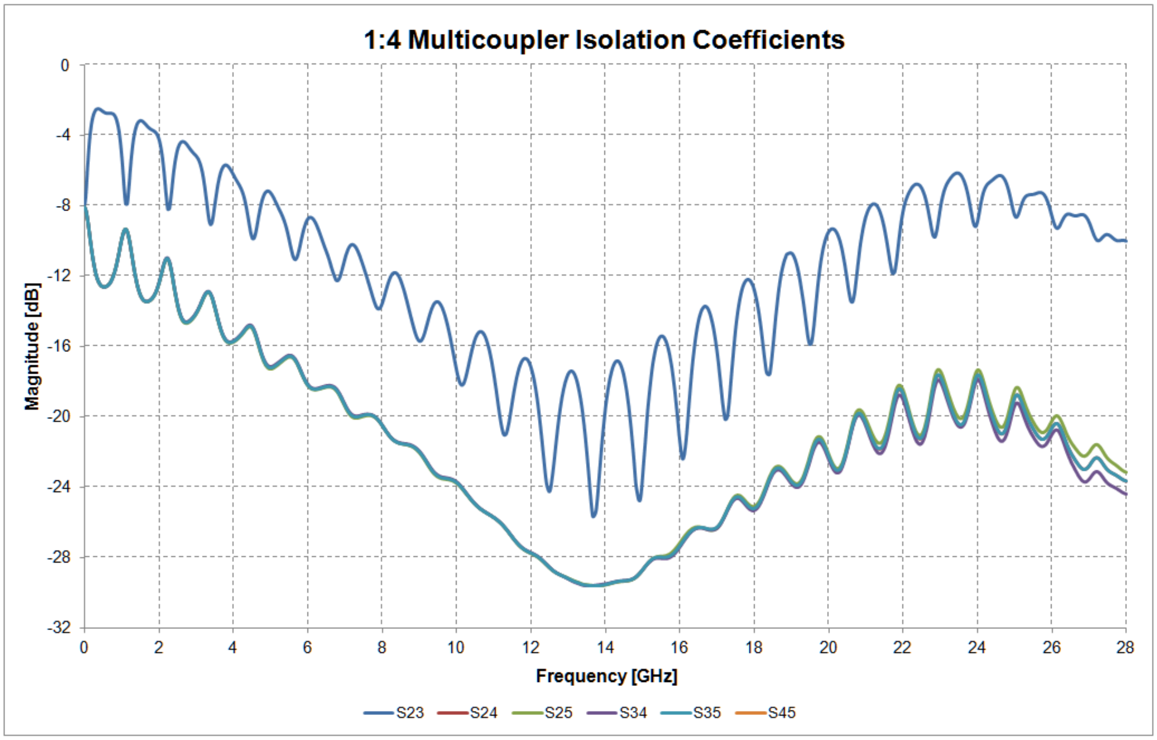

Figure 3.25 - 1:4 Multicoupler Isolation Coefficient Magnitudes.

3.4.2 ACTIVE COMPONENTS

Only commercial off the shelf microwave integrated circuits are considered in the proposed Tx Sub-Array design in order to accelerate project schedule and to allow more efficient use of existing project funds. The following set of components was found to be the optimum solution considering performance requirements, PCB space constraints, power consumption, thermal management, life cycle, lead time and project cost. The selection of these components is based on the results of the analyses performed in Section 3.2 and Section 3.3. Figure 3.26 shows the link budget parameters of the proposed Tx Sub-Array design.

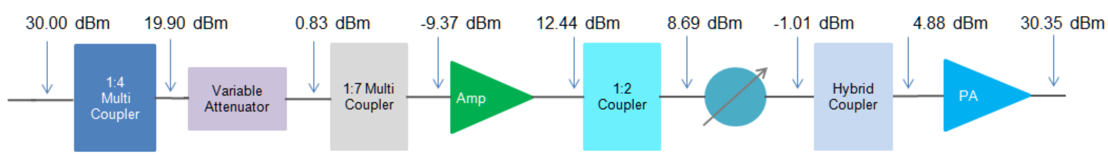

Vendor			Triquint				Triquint				Triquint				Triquint	
Part Num.	-		TGL2616		-		TGA2524		-		TGP2105		-		TGA2505	
Pin_max			35	dBm			19	dBm	-		30	dBm	-		24	dBm
Gain	-8.16	dB	-19.07	dB	-10.21	dB	23.75	dB	-3.30	dB	-9.70	dB	5.89	dB	25.47	dB
P1dB	-		-		-		26.4	dBm	-		14.30	dBm	-		33.23	dBm
IP3	-		16.93	dBm	-		36.4	dBm	-		31.302	dBm	-		39.1	dBm
ML	-1.94	dB					-1.94	dB								

Figure 3.26– Link Budget Parameters of the Proposed Tx Sub-Array Design.

The performance parameters regarding the power amplifiers, variable phase shifters, driver amplifiers and variable attenuators were obtained from measurement data provided by Qorvo in data sheets, spreadsheets and/or .s2p data files. The performance parameters regarding the hybrid couplers, 1:2 couplers, 1:7 couplers and 1:4 couplers were obtained from simulations performed in Section 3.4.1.1, Section 3.4.1.2, Section

3.4.1.3 and Section 3.4.1.4. The effective mismatch loss (ML) margins were included to account for the effects of reflections in the Tx Sub-Array and the devices forming the corporate feed structure.

3.4.2.1 Power Amplifier

The PA is the most critical part in modern microwave transmitter circuits. The output power, linearity and efficiency provided by a PA have direct influence on the reliability and the signal integrity of modern microwave transmitters.

A small power amplifier solution like Triquint TGA2505, shown in Figure 3.27, allows a modular transmitter architecture and helps to minimize project impact in case of PCB fabrication issues.

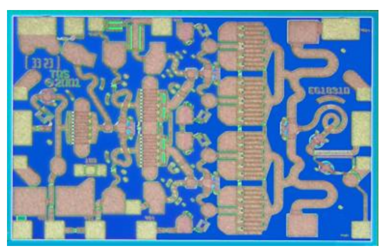

Figure 3.27 – Triquint TGA2505 Power Amplifier Die Package by Qorvo.

Some of the key features regarding the TGA2505 Power Amplifier are listed below:

- Frequency range: 13 to 17 GHz
- 34 dBm midband Pout
- 25 dB nominal Gain

- 39 dBm midband IP3
- 7 dB typical input return loss
- 12 dB typical output return loss
- Built-in directional power detector with reference
- 0.25um pHEMT technology
- Bias conditions: 7 V, 640 mA
- Chip dimensions: 2.03 mm x 1.39 mm x 0.10 mm

The small-signal linear frequency response of a PA can be characterized by the scattering parameter matrix in Eq. 3.37

Eq. 3.37

$$\mathbf{S} = \begin{bmatrix} S_{11} & S_{12} \\ S_{21} & S_{22} \end{bmatrix}$$

For instance, the scattering parameter matrix for an ideal PA is shown in Eq. 3.38

Eq. 3.38

$$\mathbf{S} = \begin{bmatrix} 0 & 0 \\ \sqrt{G} & 0 \end{bmatrix}$$

where G is the power gain of the PA.

Figure 3.28 shows the measured transmission coefficient magnitudes for the Triquint TGA2505 PA.

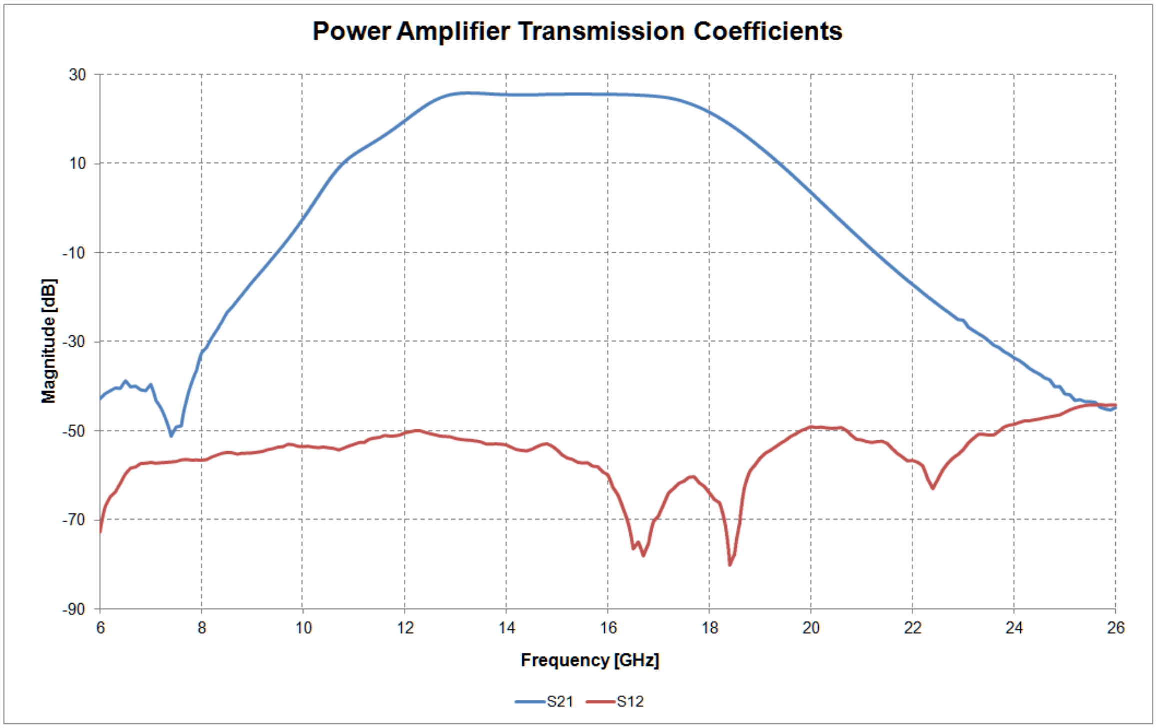

Figure 3.28 – Power Amplifier Transmission Coefficient Magnitudes.

Figure 3.29 shows the measured reflection coefficient magnitudes for the Triquint TGA2505 PA.

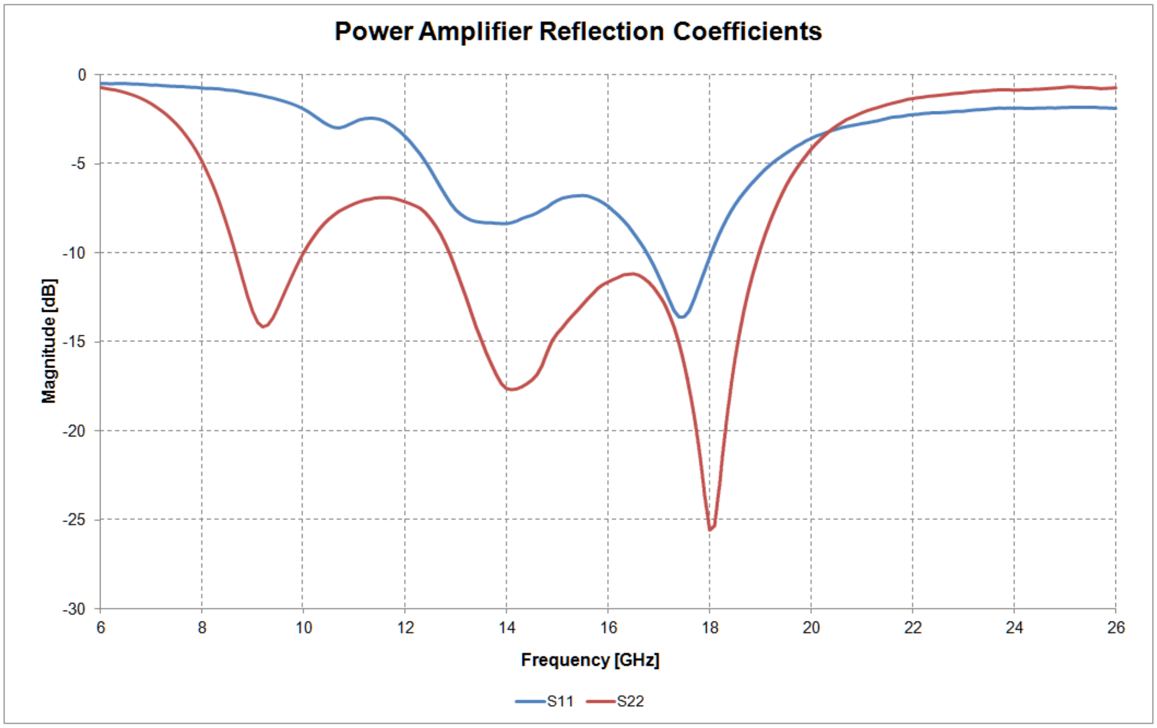

Figure 3.29 – Power Amplifier Reflection Coefficient Magnitudes.

The non-linear response of a PA can be characterized by its gain compression curve. Figure 3.30 shows the measured gain compression curve for Triquint TGA2505 PA.

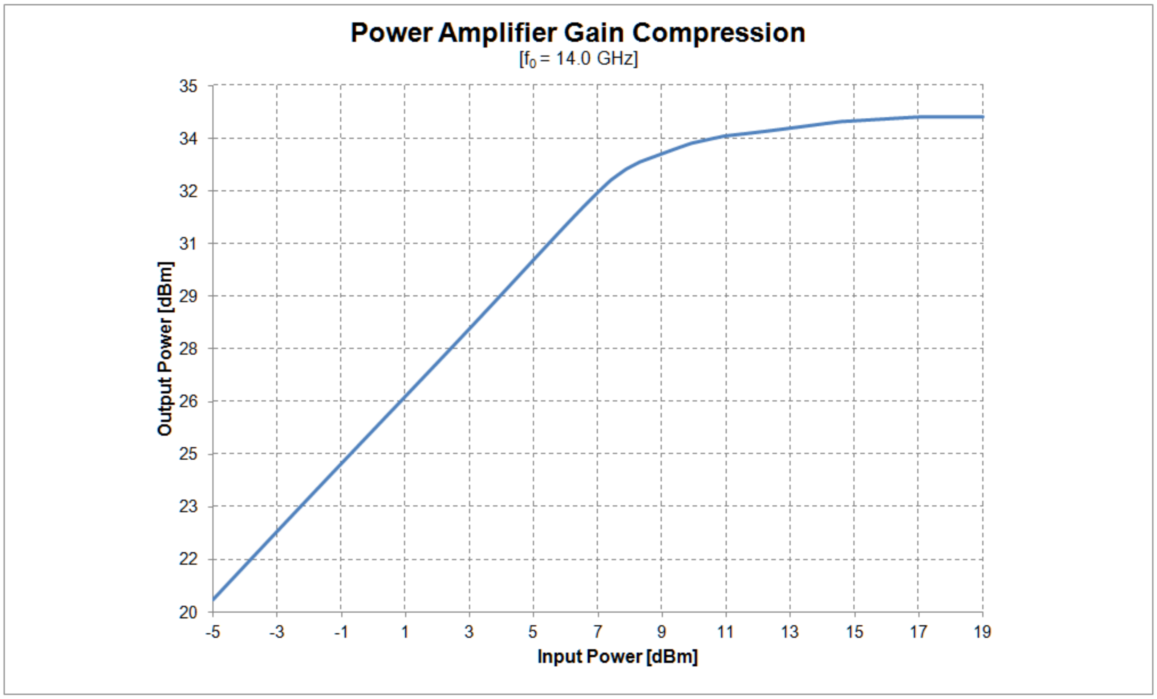

Figure 3.30 – Power Amplifier Gain Compression Curve.

Figure 3.31 shows the predicted power amplifier two tone third order intermodulation distortion for a two tone test case with first fundamental frequency (f_1) equal to 13.98929 GHz, second fundamental frequency (f_2) equal to 14.01071 GHz and input power level (P_{in}) equal to 4.11 dBm per tone that corresponds to the $1dB$ compression point.

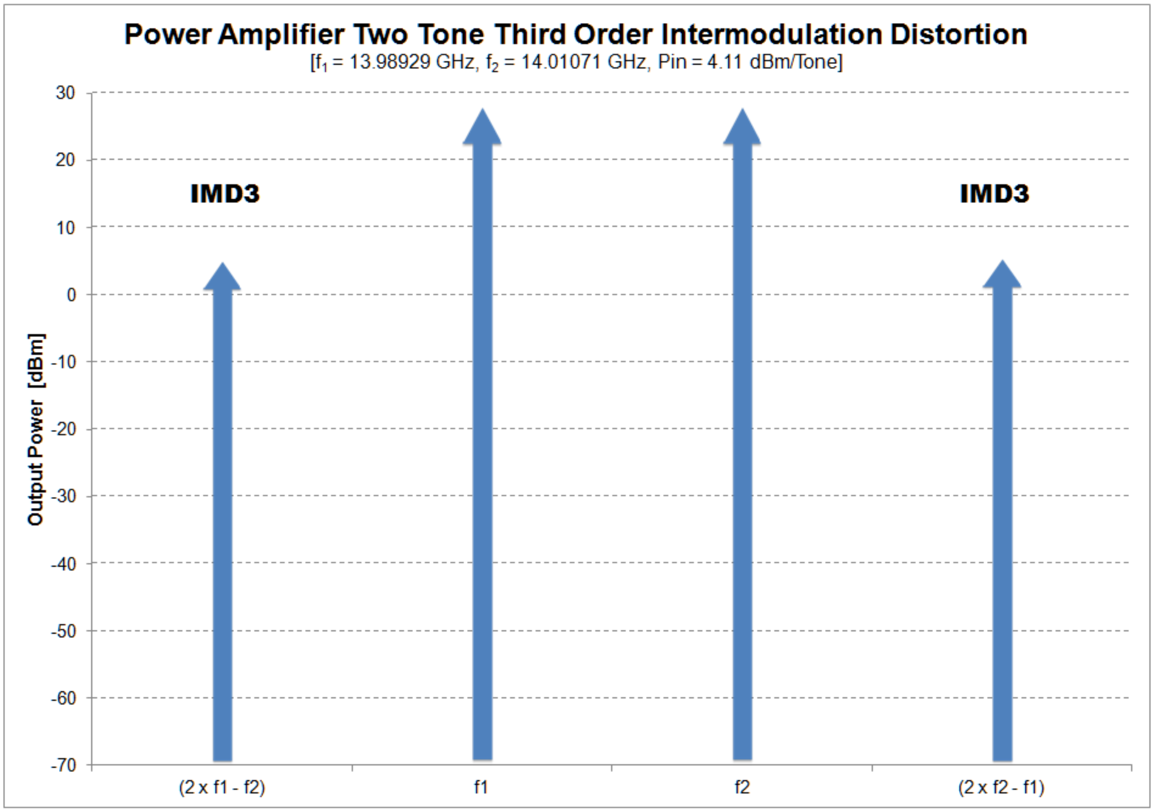

Figure 3.31 – Power Amplifier Two Tone Third Order Intermodulation Distortion.

3.4.2.2 Variable Phase Shifter

Variable phase shifters (PS) are microwave integrated circuits that produce controllable phase delays in their input signals. The most common application of variable phase shifters is electronic beam steering in phased array antennas.

Triquint TGP2105, shown in Figure 3.32, is the only digital phase shifter solution in the market that provides variable phase shifts from 0° to 360° over the entire Ku Band spectrum.

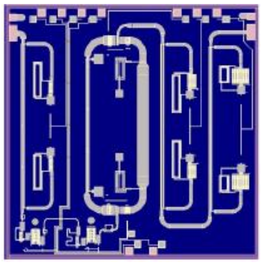

Figure 3.32 – Triquint TGP2105 Digital Phase Shifter Die Package by Qorvo.

Some of the key features regarding the TGP2105 digital phase shifter are listed below:

- Frequency range: 6 - 18 GHz
- 6-bit digital phase shifter
- 360 degree coverage, LSB = 5.625 degrees
- RMS phase error: 4 degrees
- RMS amplitude error: 0.45 dB
- Insertion loss: < 10 dB

- Return loss: > 12 dB
- Input P1dB: > 25 dBm
- Input IP3: > 41 dBm
- Control voltage: 0/+5 V
- Chip dimensions: 3.15 mm x 3.15 mm x 0.10 mm

The small-signal linear response of a PS can be characterized by the scattering parameter matrix shown in Eq. 3.39.

Eq. 3.39

$$\mathbf{S} = \begin{bmatrix} S_{11} & S_{12} \\ S_{21} & S_{22} \end{bmatrix}$$

For instance, the scattering parameter matrix for an ideal PS is shown in Eq. 3.40 below

Eq. 3.40

$$\mathbf{S} = \begin{bmatrix} 0 & e^{-j\phi} \\ e^{-j\phi} & 0 \end{bmatrix}$$

where ϕ is the phase shift of the device.

Figure 3.33 shows the transmission coefficient magnitudes for Triquint TGP2105 digital phase shifter.

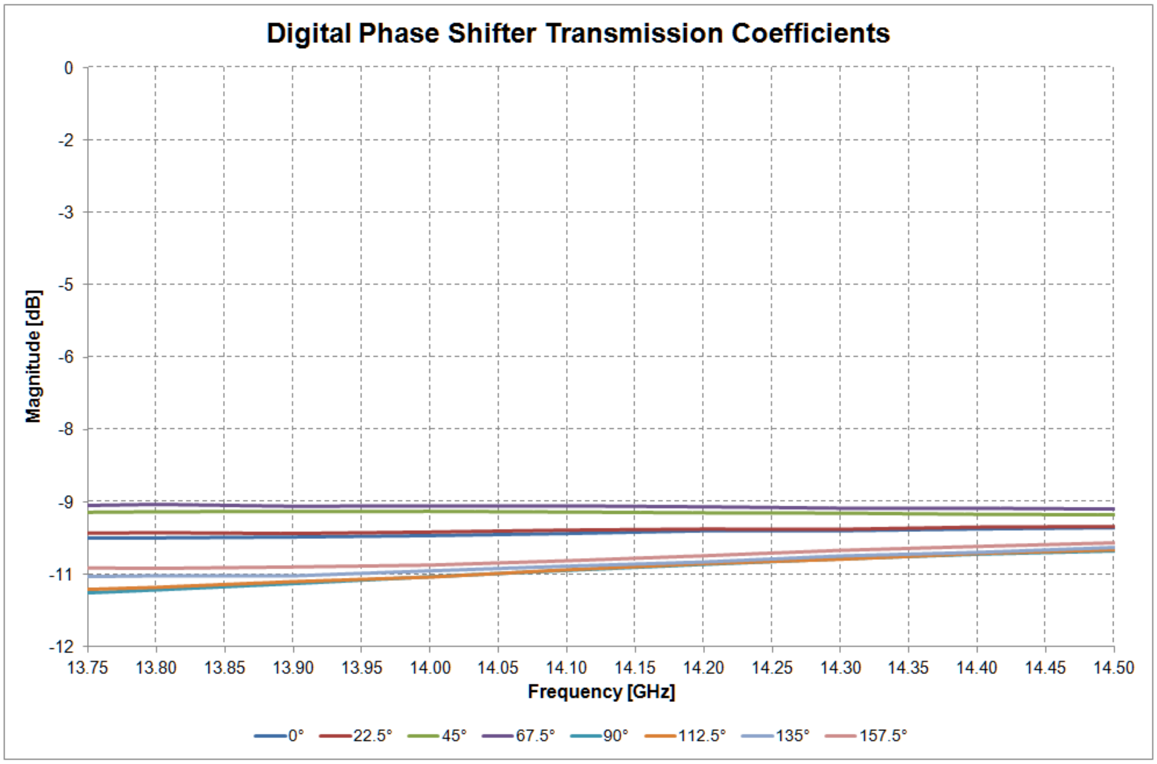

Figure 3.33 – Digital Phase Shifter Transmission Coefficient Magnitudes

Figure 3.34 shows the transmission coefficient phases for Triquint TGP2105 digital phase shifter.

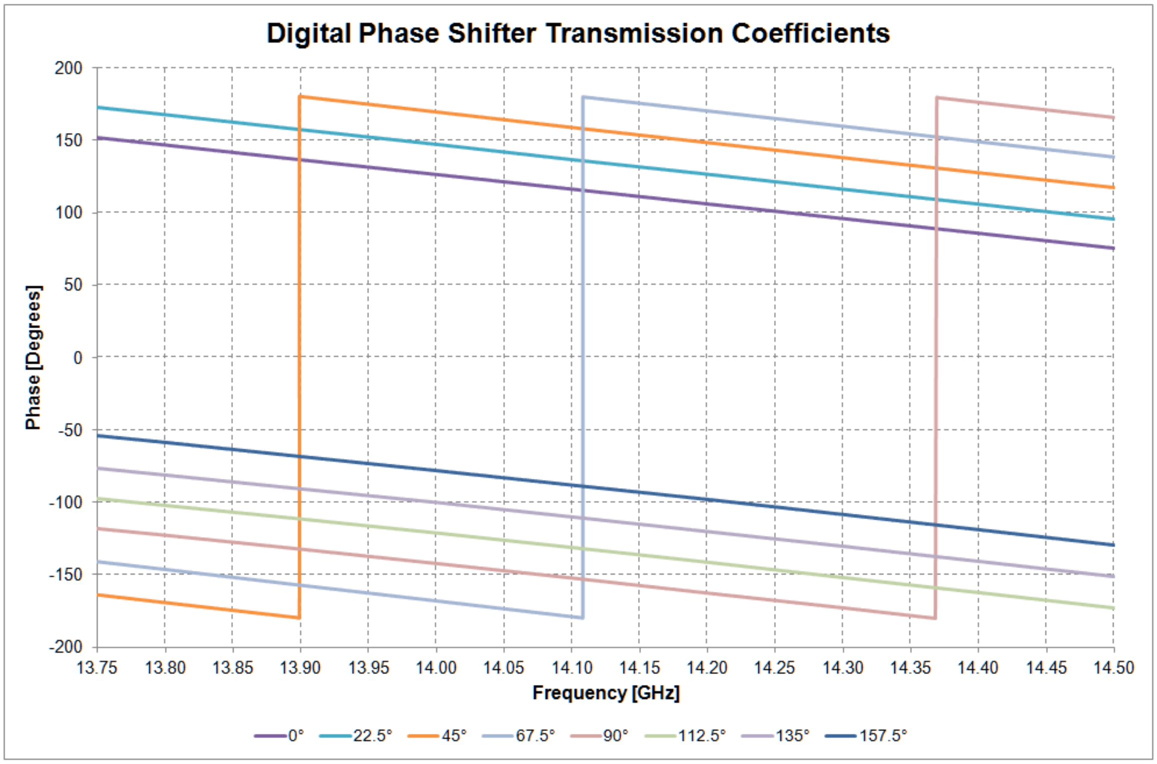

Figure 3.34 – Digital Phase Shifter Transmission Coefficient Phases.

Figure 3.35 shows the reflection coefficient magnitudes for Triquint TGP2105 digital phase shifter.

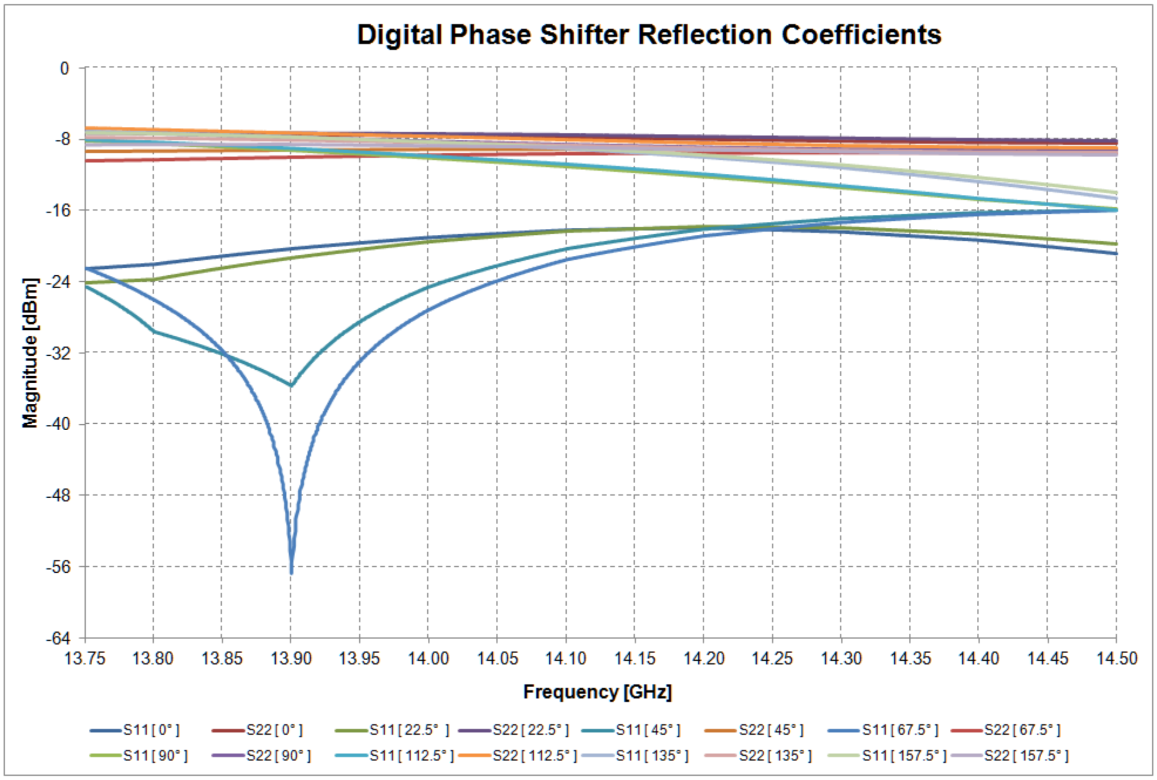

Figure 3.35 – Digital Phase Shifter Reflection Coefficient Magnitudes.

3.4.2.3 Driver Amplifier

Triquint TGA2524-SM driver amplifier (DA), shown in Figure 3.36, provides enough gain with good linearity, low cost and a small footprint.

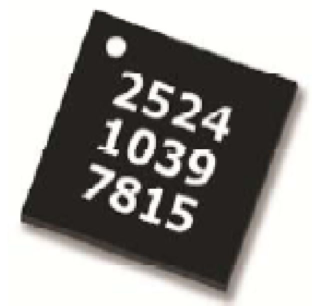

Figure 3.36 – Triquint TGA2524-SM Driver Amplifier QFN Package by Qorvo.

Some of the key features regarding the TGA2524-SM Driver Amplifier are listed below:

- Frequency range: 12 to 16 GHz
- Power: 26.5 dBm Psat, 26 dBm P1dB
- Gain: 23 dB, good gain flatness with regulation
- OTOI: 37 dBm at 8 dBm Pout/tone
- NF: 7 dB
- Bias: Vd = 5 V, Idq = 320 mA, Vg = -0.52 V Typical
- Package dimensions: 3.0 x 3.0 x 0.85 mm

The small-signal linear response of a DA can be characterized by the scattering parameter matrix shown in Eq. 3.41

Eq. 3.41

$$\mathbf{S} = \begin{bmatrix} S_{11} & S_{12} \\ S_{21} & S_{22} \end{bmatrix}$$

For instance, the scattering parameter matrix for an ideal driver amplifier are shown in Eq. 3.42 below

Eq. 3.42

$$\mathbf{S} = \begin{bmatrix} 0 & 0 \\ \sqrt{G} & 0 \end{bmatrix}$$

where G is the power gain of the DA.

Figure 3.37 shows the measured transmission coefficient magnitudes for the Triquint TGA2524-SM driver amplifier.

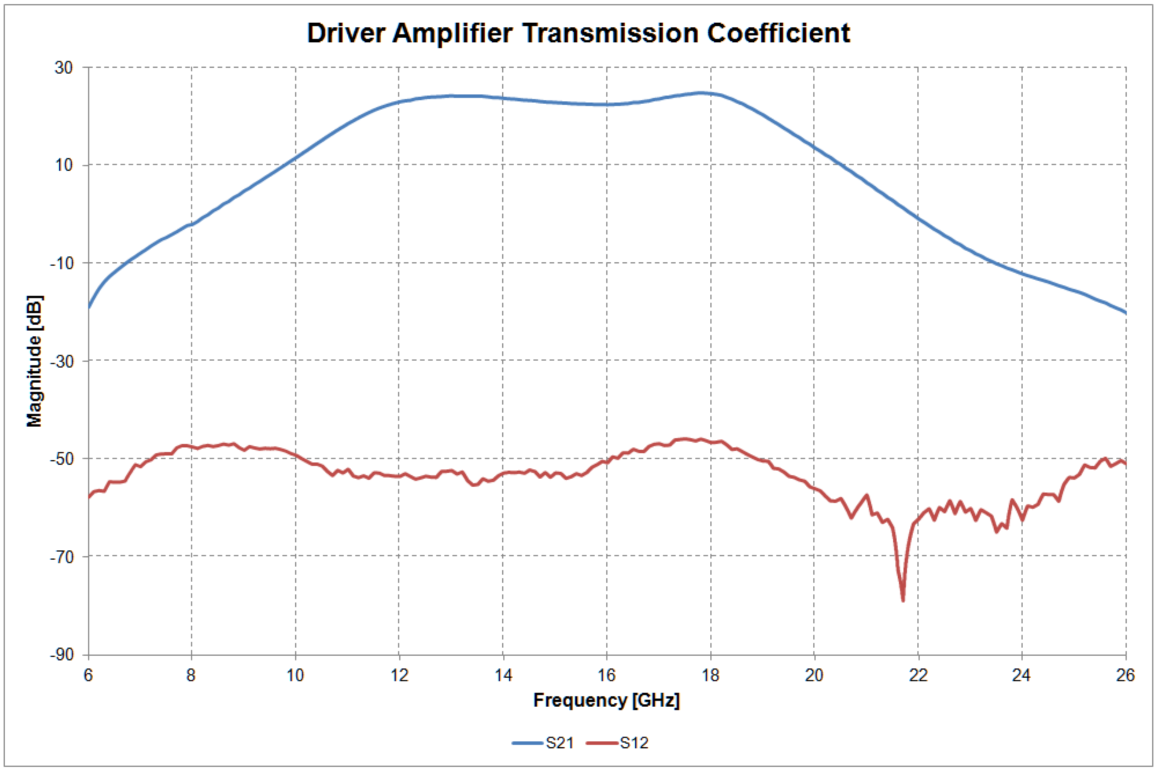

Figure 3.37 – Driver Amplifier Transmission Coefficient Magnitudes.

Figure 3.38 shows the measured reflection coefficient magnitudes for the Triquint TGA2524-SM driver amplifier.

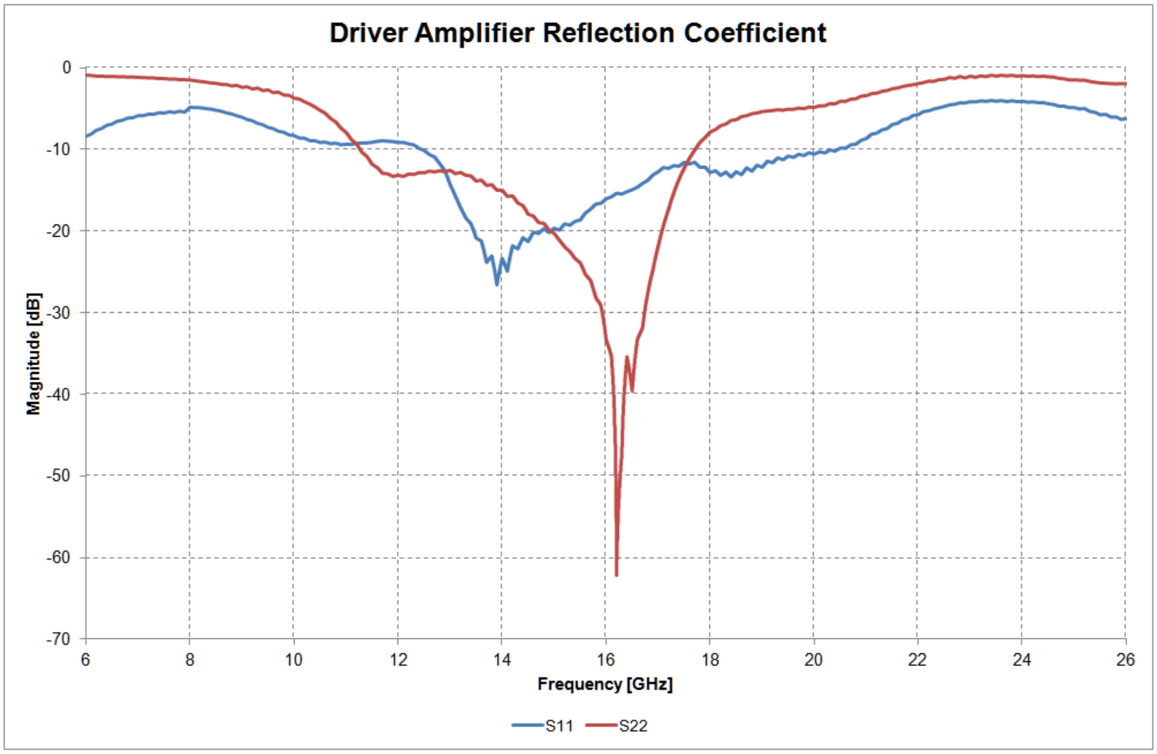

Figure 3.38 – Driver Amplifier Reflection Coefficient Magnitudes.

Figure 3.39 shows the measured gain compression curve for Triquint TGA2524-SM driver amplifier.

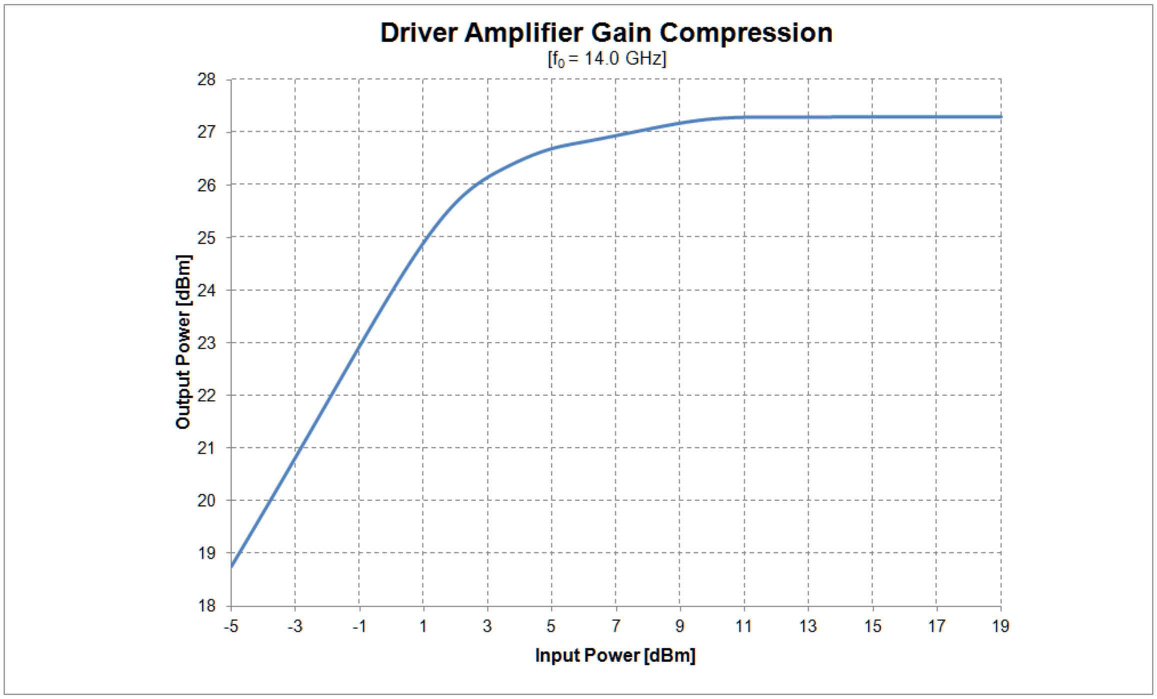

Figure 3.39 - Driver Amplifier Gain Compression Curve.

Figure 3.40 shows the predicted driver amplifier two tone third order intermodulation distortion for a two tone test case with first fundamental frequency (f_1) equal to 13.98929 GHz, second fundamental frequency (f_2) equal to 14.01071 GHz and input power level (P_{in}) equal to 1.3 dBm per tone that corresponds to its $1dB$ compression point.

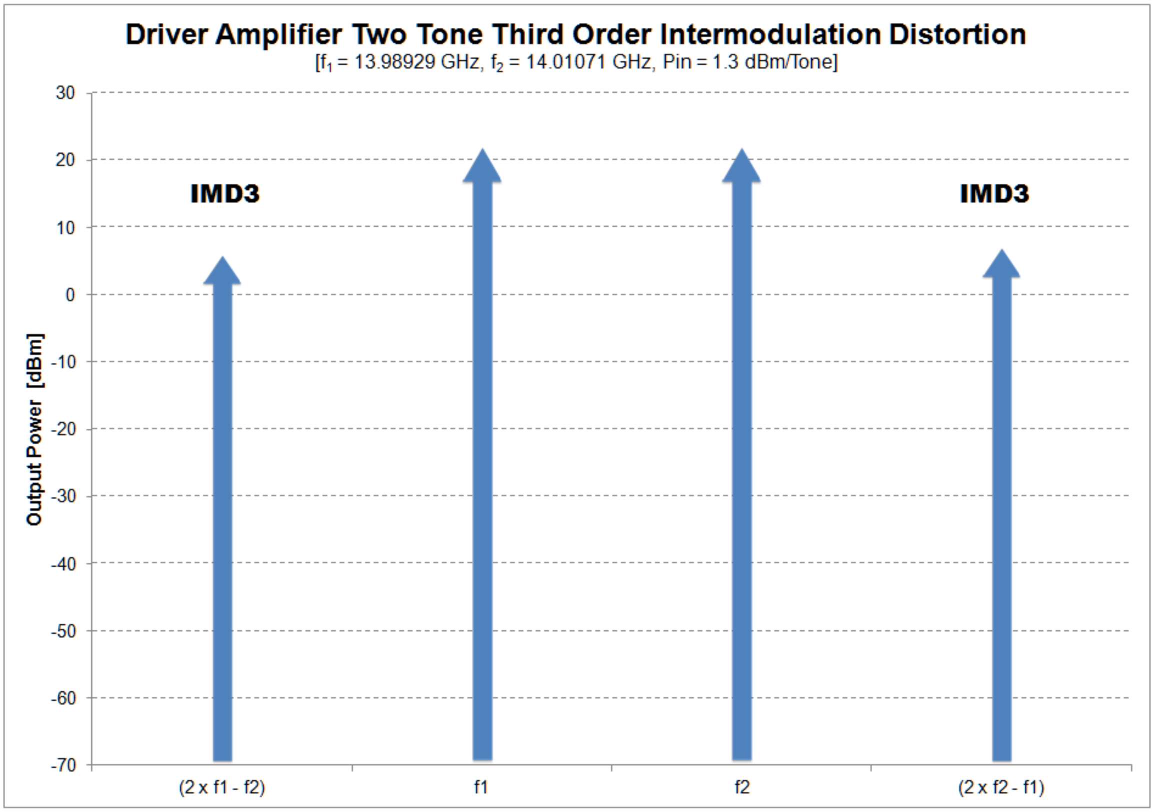

Figure 3.40 – Driver Amplifier Two Tone Third Order Intermodulation Distortion.

3.4.2.4 Variable Attenuator

Variable attenuators are microwave integrated circuits that produce controllable amplitude reductions in their input signals. The most common applications of variable attenuators are power control, impedance matching, amplitude compensation and side lobe reduction in phased array antennas.

Triquint TGL2616-SM Digital Attenuator, shown in Figure 3.41, enables control of input power levels of each transmitter sub-array.

Figure 3.41 – Triquint TGL2616-SM Digital Attenuator Package by Qorvo.

Some of the key features regarding the TGL2616-SM Digital Attenuator are listed below:

- Frequency Range: 10-20 GHz
- 5-Bit Digital Attenuator
- Attenuation Range: 23.25 dB
- Attenuation Step Size (LSB): 0.75 dB
- Insertion Loss (Ref. State): 4.8 dB

- RMS Amplitude Error: < 0.6 dB
- RMS Step Error: < 0.3 dB
- Control Voltage: 3.3-5.0 V
- Positive logic
- Size: 4.0 mm x 4.0 mm x 0.10 mm

The small-signal linear response of an attenuator can be characterized by the scattering parameter matrix shown in Eq. 3.43.

Eq. 3.43

$$\mathbf{S} = \begin{bmatrix} S_{11} & S_{12} \\ S_{21} & S_{22} \end{bmatrix}$$

For instance, the scattering parameter matrix for an ideal attenuator is shown in Eq. 3.44 below

Eq. 3.44

$$\mathbf{S} = \begin{bmatrix} 0 & e^{-\alpha} \\ e^{-\alpha} & 0 \end{bmatrix}$$

where α is the attenuation of the device.

Figure 3.42 shows the transmission coefficient magnitudes for Triquint TGL2616-SM digital attenuator.

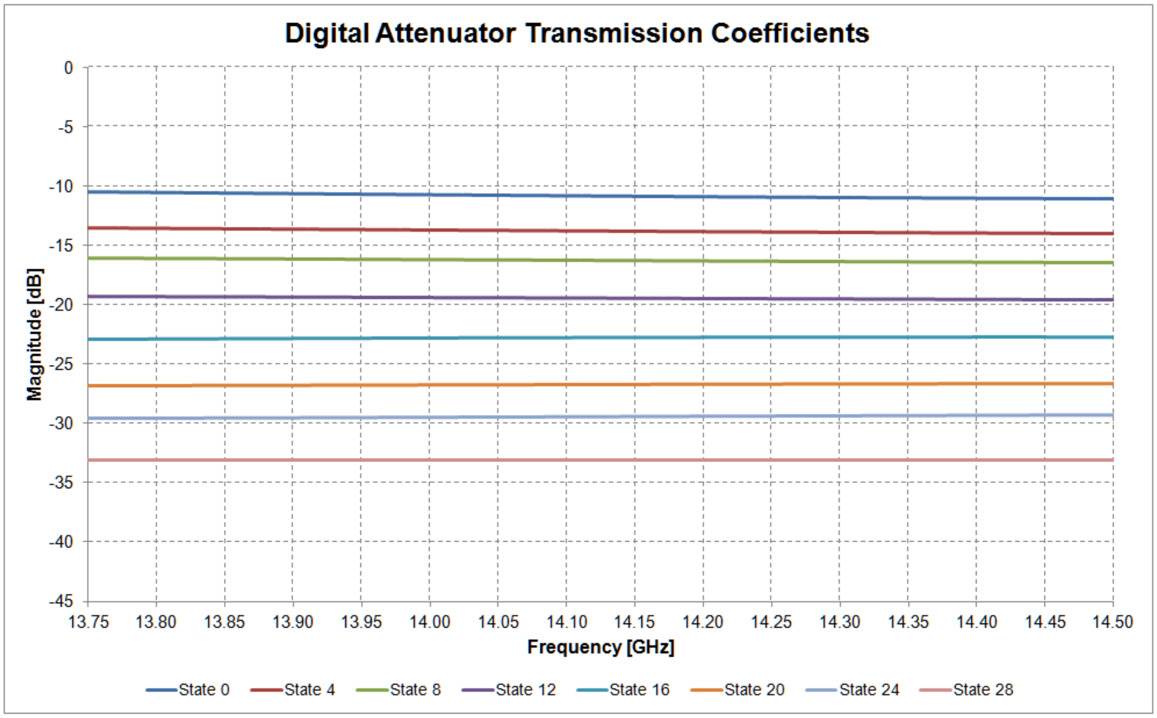

Figure 3.42 – Digital Attenuator Transmission Coefficient Magnitudes.

Figure 3.43 shows the transmission coefficient phases for Triquint TGL2616-SM digital attenuator.

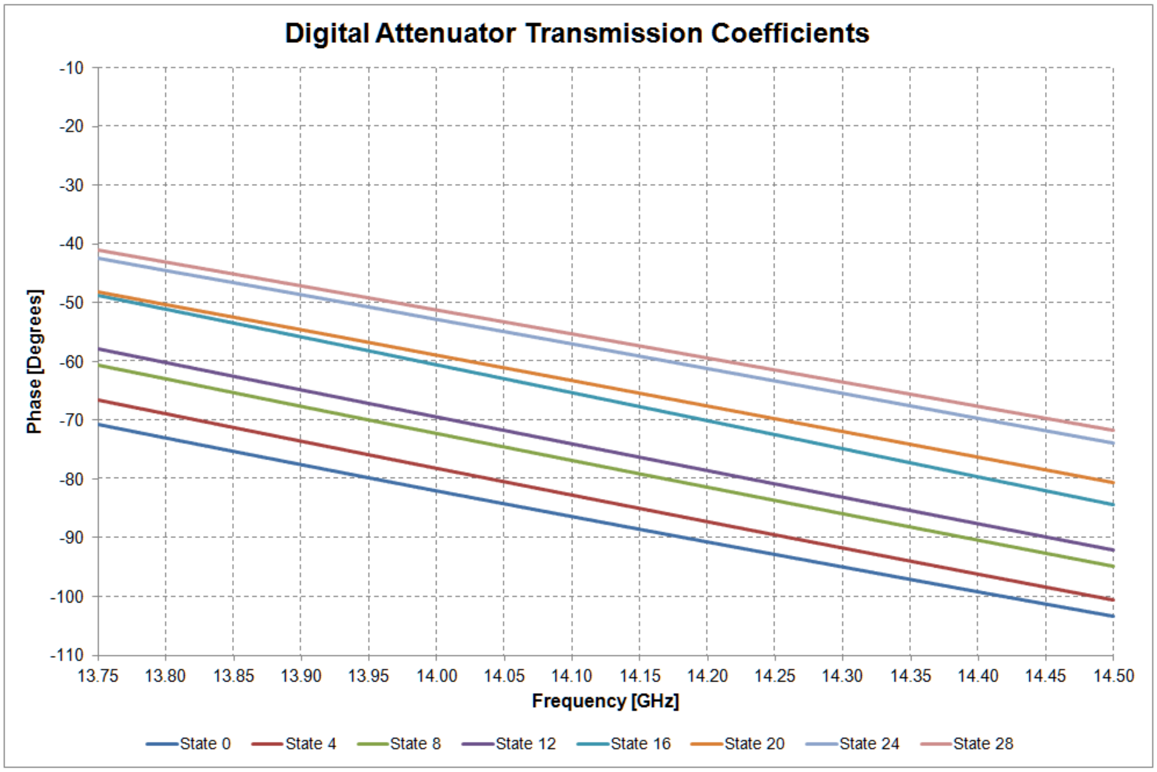

Figure 3.43 – Digital Attenuator Transmission Coefficient Phases.

Figure 3.44 shows the reflection coefficient magnitudes for Triquint TGL2616-SM digital attenuator.

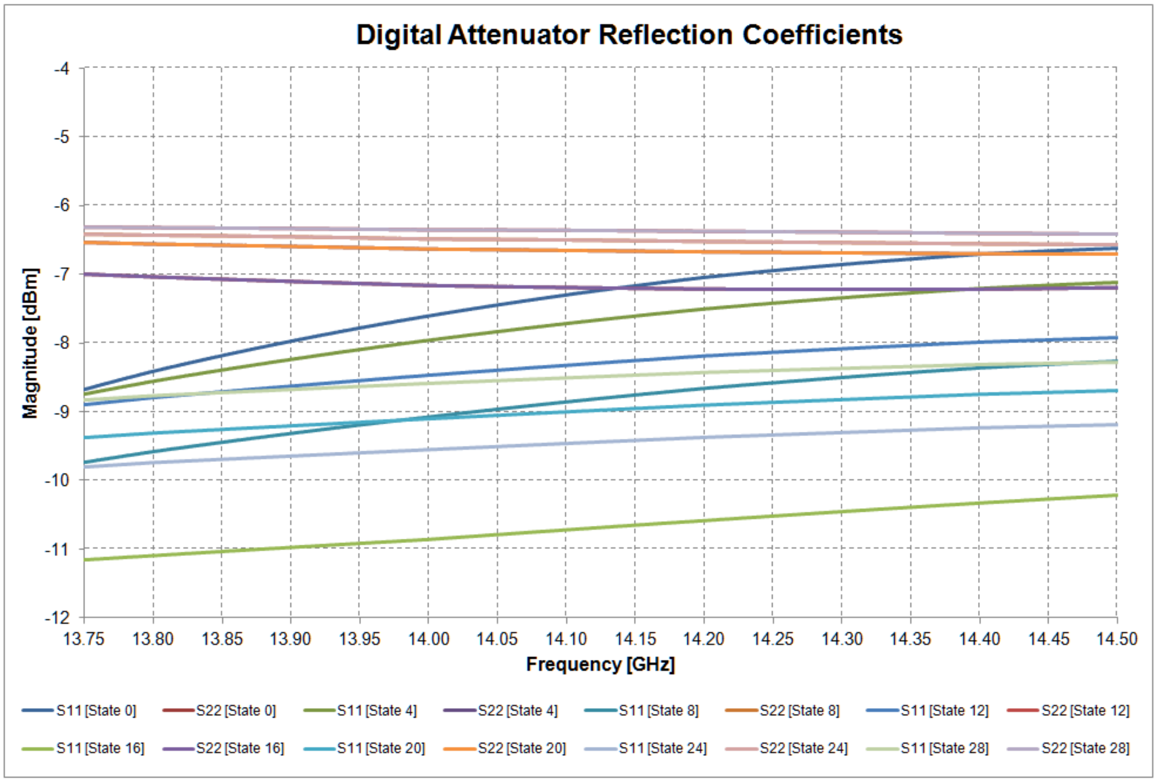

Figure 3.44 – Digital Attenuator Reflection Coefficient Magnitudes.

4 SIMULATION

4.1 FREQUENCY RESPONSE

Linear networks and non-linear networks operating with sufficiently small signals can be fully characterized by scattering parameter matrices measured at their connection ports. Once the S-parameter matrices have been determined, the behavior of the networks can be predicted, regardless of their internal circuit configuration. Figure 4.1 shows the simplified Tx Sub-Array model for multi-port S parameter analysis.

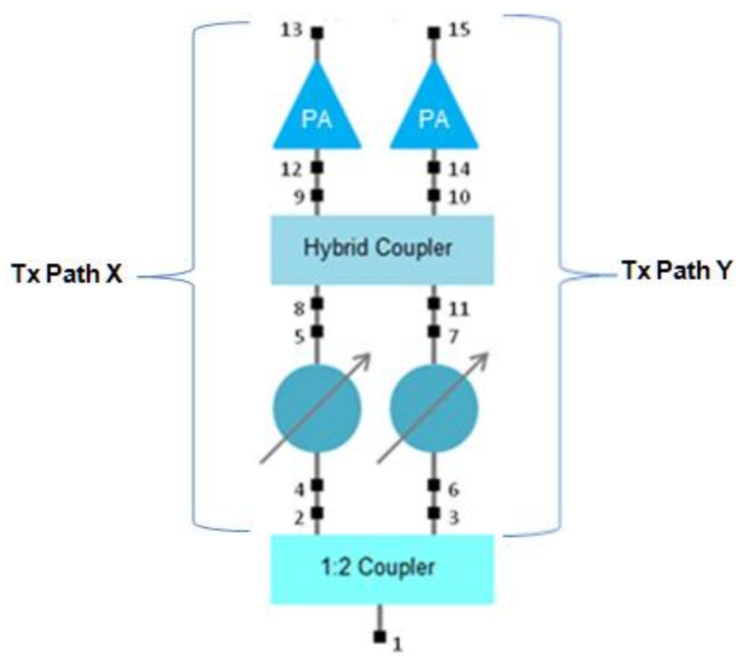

Figure 4.1 – Tx Sub-Array Model for Multi-port S-Parameter Analysis.

According to [32] the signal flow of the cascaded multi-port microwave circuit shown in Figure 4.1 can be expressed in terms of the scattering parameter matrix ($\boldsymbol{S}$) defined in Eq. 4.1

Eq. 4.1

$$\mathbf{S} = \begin{bmatrix} \mathbf{S}_{\boldsymbol{ee}} & \mathbf{S}_{\boldsymbol{ei}} \\ \mathbf{S}_{\boldsymbol{ie}} & \mathbf{S}_{\boldsymbol{ii}} \end{bmatrix}$$

and the connection matrix ($\boldsymbol{\Gamma_c}$) defined in Eq. 4.2

Eq. 4.2

$$\boldsymbol{\Gamma_c} = \begin{bmatrix} \boldsymbol{\Gamma_{ee}} & \boldsymbol{\Gamma_{ei}} \\ \boldsymbol{\Gamma_{ie}} & \boldsymbol{\Gamma_{ii}} \end{bmatrix}$$

where the scattering parameter matrix that groups the signal flows of externally connected ports ($\mathbf{S}_{\boldsymbol{ee}}$) is defined in Eq. 4.3

Eq. 4.3

$$\mathbf{S}_{\boldsymbol{ee}} = \begin{bmatrix} S_{11} & 0 & 0 \\ 0 & S_{1313} & 0 \\ 0 & 0 & S_{1515} \end{bmatrix}$$

the scattering parameter matrix that groups the signal flows between internally connected ports and externally connected ports ($\mathbf{S}_{\boldsymbol{ei}}$) is defined in Eq. 4.4

Eq. 4.4

$$\mathbf{S}_{\boldsymbol{ei}} = \begin{bmatrix} S_{12} & S_{13} & 0 & 0 & 0 & 0 & 0 & 0 & 0 & 0 & 0 & 0 \\ 0 & 0 & 0 & 0 & 0 & 0 & 0 & 0 & 0 & 0 & S_{1312} & 0 \\ 0 & 0 & 0 & 0 & 0 & 0 & 0 & 0 & 0 & 0 & 0 & S_{1514} \end{bmatrix}$$

the scattering parameter matrix that groups the signal flows between externally connected ports and internally connected ports ($\mathbf{S}_{\boldsymbol{ie}}$) is defined in Eq. 4.5

Eq. 4.5

$$\mathbf{S}_{ie} = \begin{bmatrix} S_{21} & 0 & 0 \\ S_{31} & 0 & 0 \\ 0 & 0 & 0 \\ 0 & 0 & 0 \\ 0 & 0 & 0 \\ 0 & 0 & 0 \\ 0 & 0 & 0 \\ 0 & 0 & 0 \\ 0 & 0 & 0 \\ 0 & 0 & 0 \\ 0 & S_{1213} & 0 \\ 0 & 0 & S_{1415} \end{bmatrix}$$

the scattering parameter matrix that groups the signal flows between internally connected ports ($\mathbf{S}_{ii}$) is defined in Eq. 4.6

Eq. 4.6

$$\mathbf{S}_{ii} = \begin{bmatrix} S_{22} & S_{23} & 0 & 0 & 0 & 0 & 0 & 0 & 0 & 0 & 0 & 0 \\ S_{32} & S_{33} & 0 & 0 & 0 & 0 & 0 & 0 & 0 & 0 & 0 & 0 \\ 0 & 0 & S_{44} & S_{45} & 0 & 0 & 0 & 0 & 0 & 0 & 0 & 0 \\ 0 & 0 & S_{54} & S_{55} & 0 & 0 & 0 & 0 & 0 & 0 & 0 & 0 \\ 0 & 0 & 0 & 0 & S_{66} & S_{67} & 0 & 0 & 0 & 0 & 0 & 0 \\ 0 & 0 & 0 & 0 & S_{76} & S_{77} & 0 & 0 & 0 & 0 & 0 & 0 \\ 0 & 0 & 0 & 0 & 0 & 0 & S_{88} & S_{89} & S_{810} & S_{811} & 0 & 0 \\ 0 & 0 & 0 & 0 & 0 & 0 & S_{98} & S_{99} & S_{910} & S_{911} & 0 & 0 \\ 0 & 0 & 0 & 0 & 0 & 0 & S_{108} & S_{109} & S_{1010} & S_{1011} & 0 & 0 \\ 0 & 0 & 0 & 0 & 0 & 0 & S_{118} & S_{119} & S_{1110} & S_{1111} & 0 & 0 \\ 0 & 0 & 0 & 0 & 0 & 0 & 0 & 0 & 0 & 0 & S_{1212} & 0 \\ 0 & 0 & 0 & 0 & 0 & 0 & 0 & 0 & 0 & 0 & 0 & S_{1414} \end{bmatrix}$$

and the connection matrix that groups the internally connected ports ($\mathbf{\Gamma}_{ii}$) is defined in Eq. 4.7.

Eq. 4.7

$$\boldsymbol{\Gamma_{ii}} = \begin{bmatrix} 0 & 0 & 1 & 0 & 0 & 0 & 0 & 0 & 0 & 0 & 0 & 0 \\ 0 & 0 & 0 & 0 & 1 & 0 & 0 & 0 & 0 & 0 & 0 & 0 \\ 1 & 0 & 0 & 0 & 0 & 0 & 0 & 0 & 0 & 0 & 0 & 0 \\ 0 & 0 & 0 & 0 & 0 & 0 & 1 & 0 & 0 & 0 & 0 & 0 \\ 0 & 1 & 0 & 0 & 0 & 0 & 0 & 0 & 0 & 0 & 0 & 0 \\ 0 & 0 & 0 & 0 & 0 & 0 & 0 & 0 & 0 & 1 & 0 & 0 \\ 0 & 0 & 0 & 1 & 0 & 0 & 0 & 0 & 0 & 0 & 0 & 0 \\ 0 & 0 & 0 & 0 & 0 & 0 & 0 & 0 & 0 & 0 & 1 & 0 \\ 0 & 0 & 0 & 0 & 0 & 0 & 0 & 0 & 0 & 0 & 0 & 1 \\ 0 & 0 & 0 & 0 & 0 & 1 & 0 & 0 & 0 & 0 & 0 & 0 \\ 0 & 0 & 0 & 0 & 0 & 0 & 0 & 1 & 0 & 0 & 0 & 0 \\ 0 & 0 & 0 & 0 & 0 & 0 & 0 & 0 & 1 & 0 & 0 & 0 \end{bmatrix}$$

The resulting scattering parameter matrix with respect to the external ports $(\boldsymbol{S_e})$ can be obtained using the expression in Eq. 4.8.

Eq. 4.8

$$\boldsymbol{S_e} = \boldsymbol{S_{ee}} + \boldsymbol{S_{ei}}(\boldsymbol{\Gamma_{ii}} - \boldsymbol{S_{ii}})^{-1}\boldsymbol{S_{ie}} = \begin{bmatrix} S_{e11} & S_{e12} & S_{e13} \\ S_{e21} & S_{e22} & S_{e23} \\ S_{e31} & S_{e32} & S_{e33} \end{bmatrix}$$

The frequency response of cascaded multi-port microwave circuits can be predicted by scattering parameter analysis at a specific range of frequencies. Figure 4.2 shows the Tx Sub-Array configuration for simulation of the frequency response.

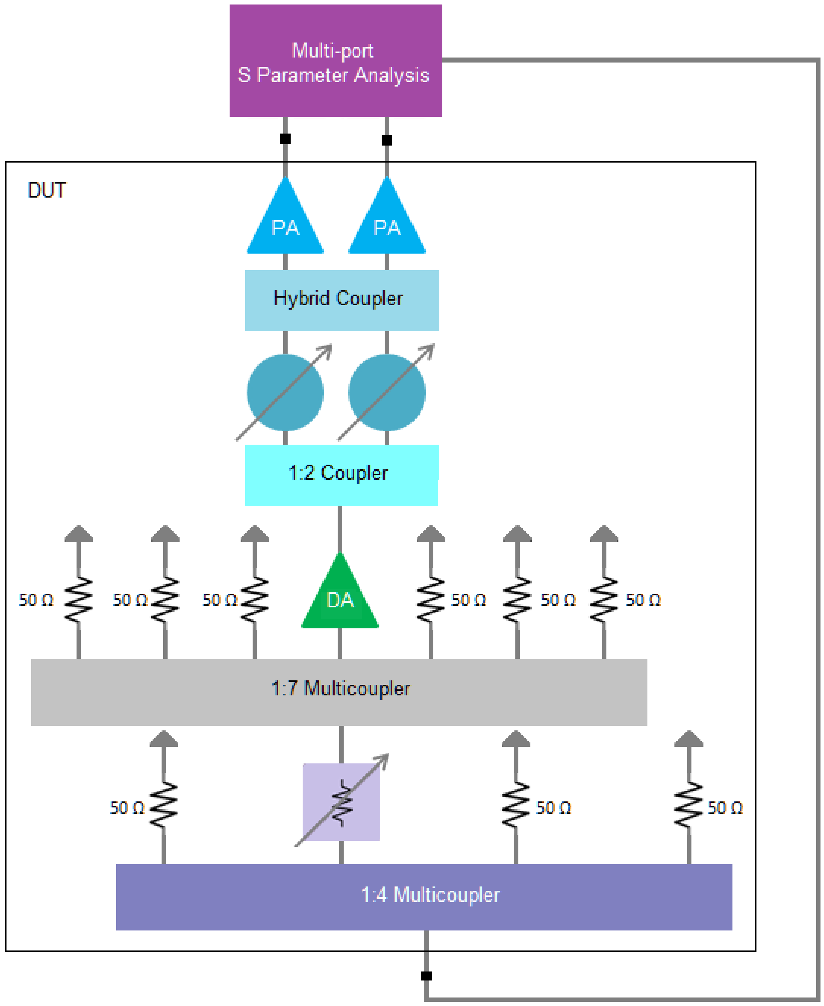

Figure 4.2 – Tx Sub-Array Configuration for Simulation of the Frequency Response.

Figure 4.3 shows the predicted Tx Sub-Array transmission coefficient magnitudes at a polarization state with elevation scan angle equal to 0° and polarization tilt angle equal to 0°.

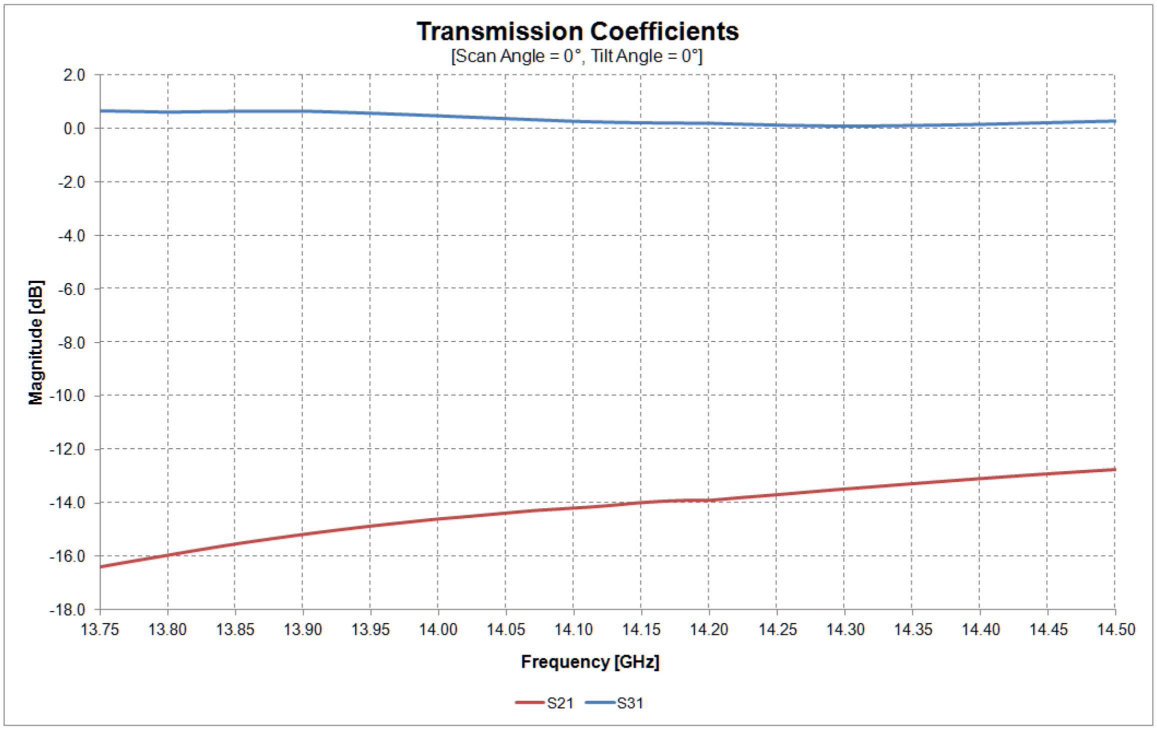

Figure 4.3 – Tx Sub-Array Transmission Coefficient Magnitudes for a Test Case with Elevation Scan Angle Equal to 0° and Polarization Tilt Angle Equal to 0°.

Figure 4.4 shows the predicted Tx Sub-Array transmission coefficient phases at a polarization state with elevation scan angle equal to 0° and polarization tilt angle equal to 0°.

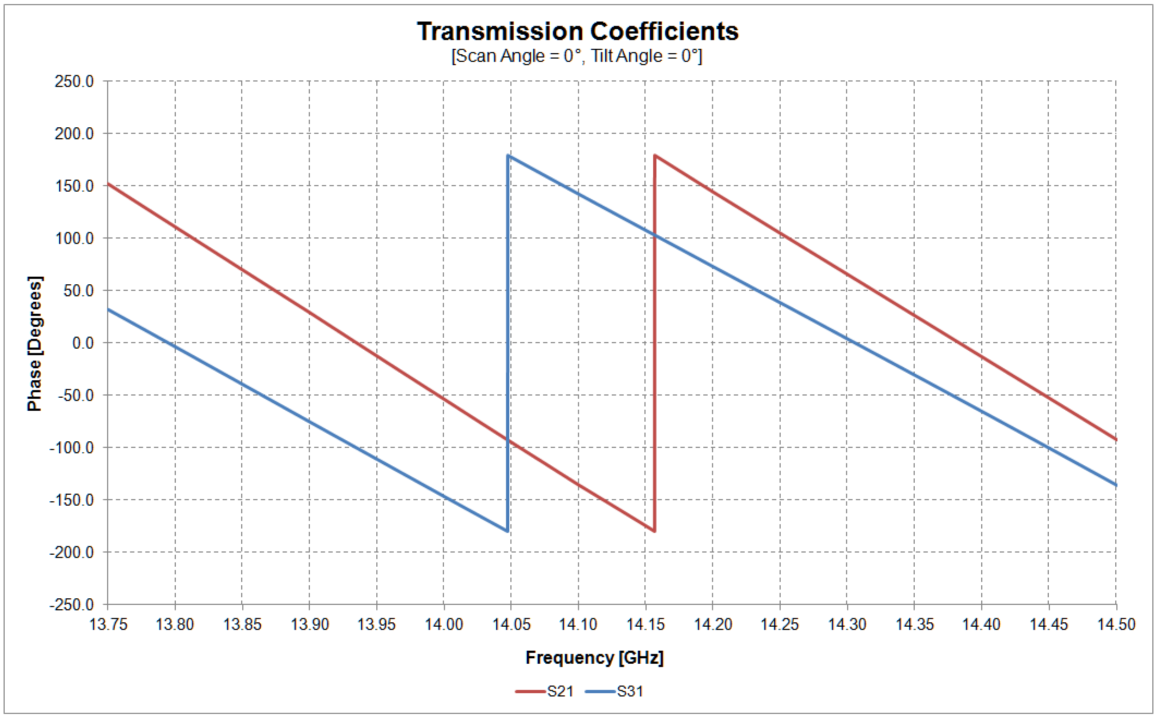

Figure 4.4– Tx Sub-ArrayTransmission Coefficient Phases for a Test Case with Elevation Scan Angle Equal to 0° and Polarization Tilt Angle Equal to 0°.

Figure 4.5 shows the predicted Tx Sub-Array reflection coefficient magnitudes at a polarization state with elevation scan angle equal to 0° and polarization tilt angle equal to 0°.

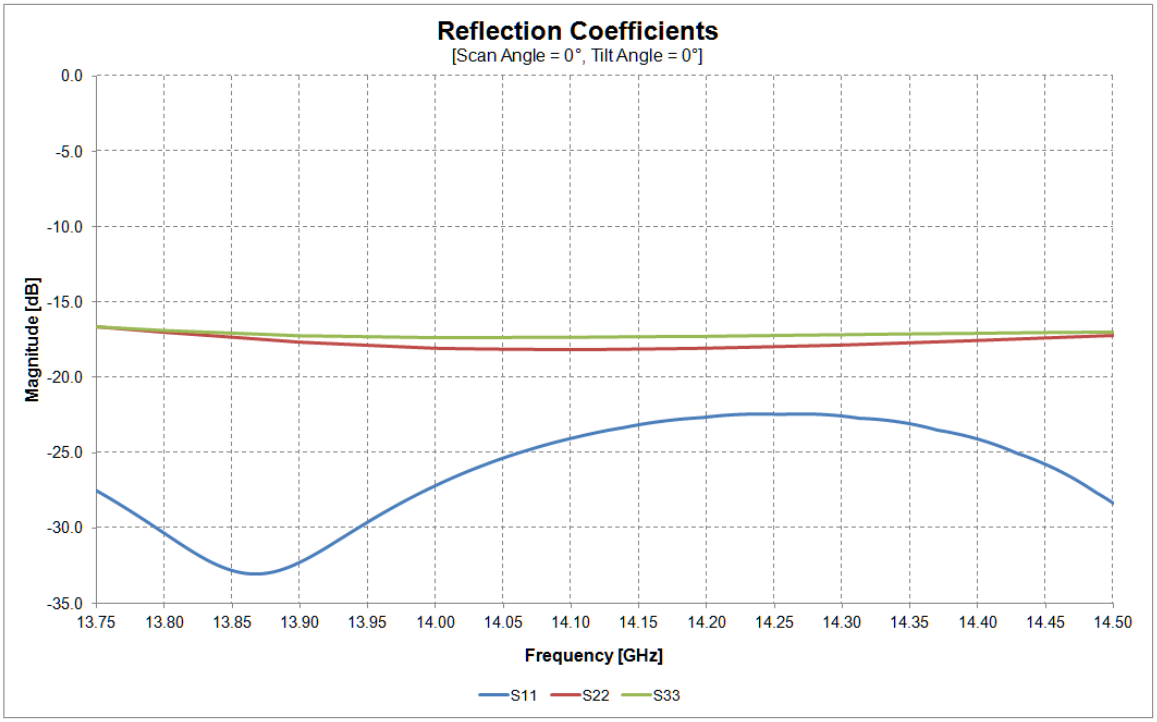

Figure 4.5 – Tx Sub-Array Reflection Coefficient Magnitudes for a Test Case with Elevation Scan Angle Equal to 0° and Polarization Tilt Angle Equal to 0°.

Figure 4.6 shows the predicted Tx Sub-Array isolation coefficient magnitudes at a polarization state with elevation scan angle equal to 0° and polarization tilt angle equal to 0°.

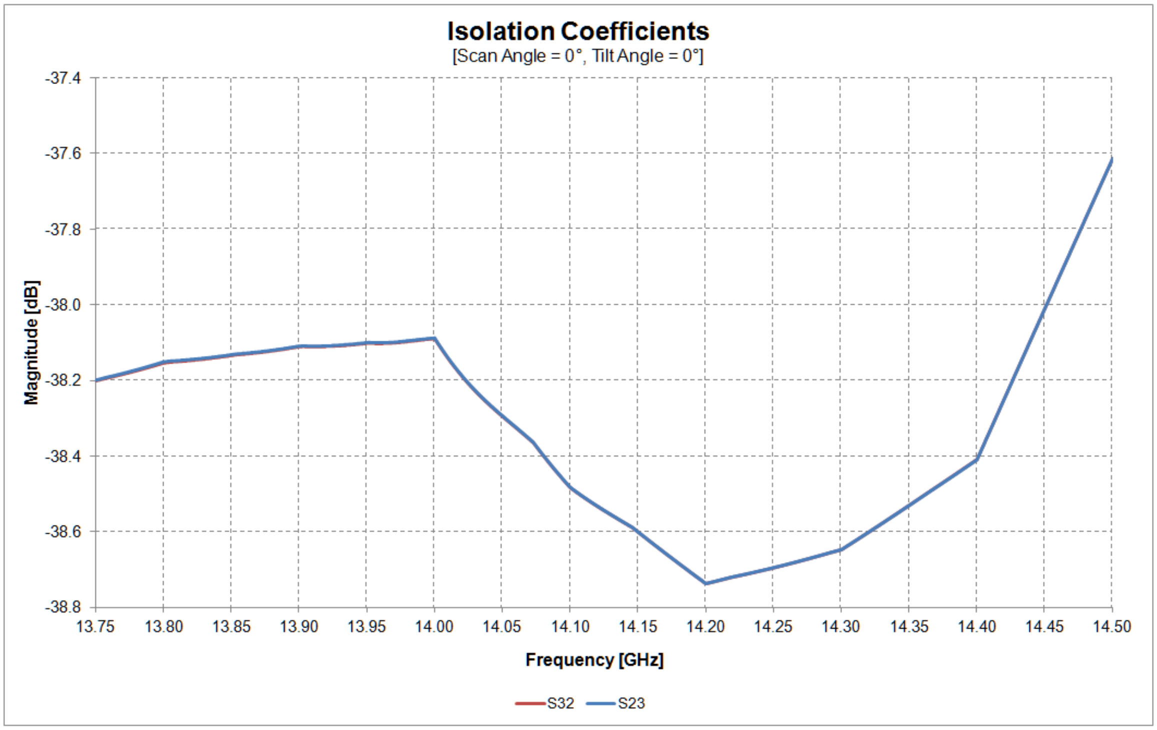

Figure 4.6 – Tx Sub-Array Isolation Coefficient Magnitudes for a Test Case with Elevation Scan Angle Equal to 0° and Polarization Tilt Angle Equal to 0°.

4.2 LINEARITY

Non-linear characteristics of microwave devices (i.e. power amplifier) can cause gain compression issues leading to lower output power levels and the appearance of inter-modulation distortion products. Spurious and spectral re-growth emissions are both manifestations of inter-modulation distortion in microwave devices.

The non-linearity of a device can be described by measureable characteristics like its 1 dB compression point (P_{1dB}) and/or its third order intercept point (IP_3), shown in Figure 4.7.

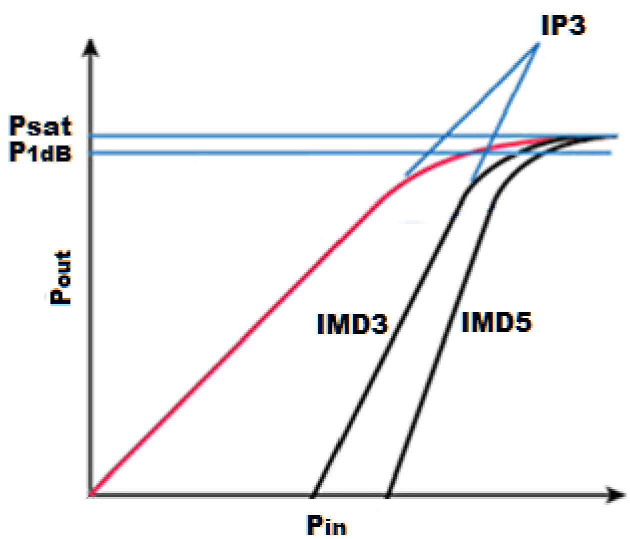

Figure 4.7 – Gain Compression of a Non-Linear Device [33].

The 1 dB compression point of a non-linear device is the power level where the output power is 1 dB lower than the expected out of an ideally linear device. This point is easier to measure than the third order intercept point and requires only one tone at the input of the device. For instance, [34] shows that the output signal (v_o) of a non-linear microwave device can be estimated using the expression in Eq. 4.9

Eq. 4.9

$$v_o = k_1 v_i + \frac{3}{4} k_3 {v_i}^3$$

where the k_n variables are real and the input signal (v_i) assumes the form of the single tone shown in Eq. 4.10.

Eq. 4.10

$$v_i = a \cos(2\pi f_0 t)$$

Furthermore, [34] shows that when the non-linear microwave device is operating at its 1 dB compression point (P_{1dB}) the variable k_3 might be expressed in terms of the linear gain variable k_1 using Eq. 4.11.

Eq. 4.11

$$k_3 = -0.145 \frac{k_1}{a^2}$$

The 1 dB compression point can be predicted using a commercial CAD tool that implements RF source power sweeping and similar harmonic balance analysis methods as described in [24]. Figure 4.8 shows the Tx Sub-Array configuration and excitation source parameters for simulation of gain compression.

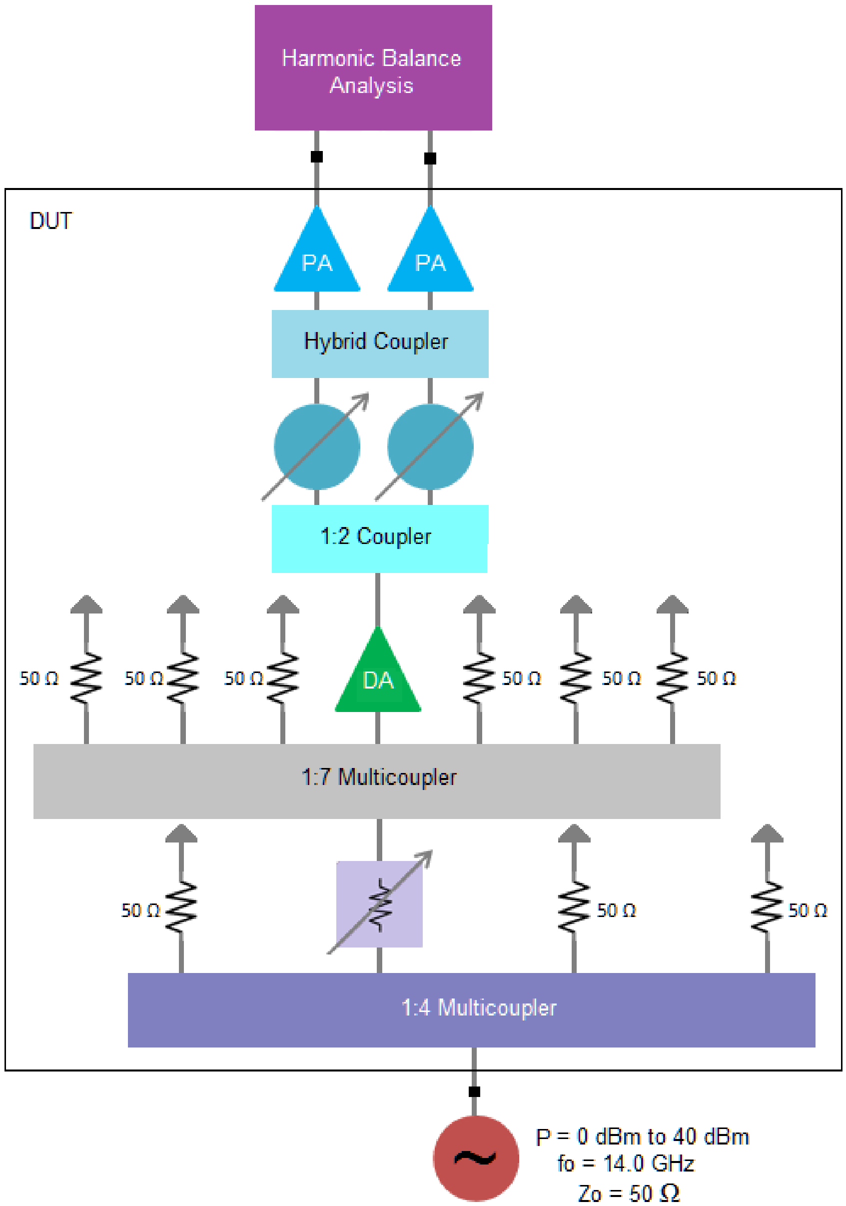

Figure 4.8 – Tx Sub-Array Configuration for Simulation of Gain Compression.

Figure 4.9 shows the predicted Tx Sub-Array gain compression for a test case with frequency of operation equal to 14.0 GHz, elevation scan angle equal to 0° and polarization tilt angle equal to 0°. The predicted 1 dB compression point can be calculated once the transfer function of the fundamental frequency has been determined. The predicted average 1 dB compression point value is approximately 32.86 dBm.

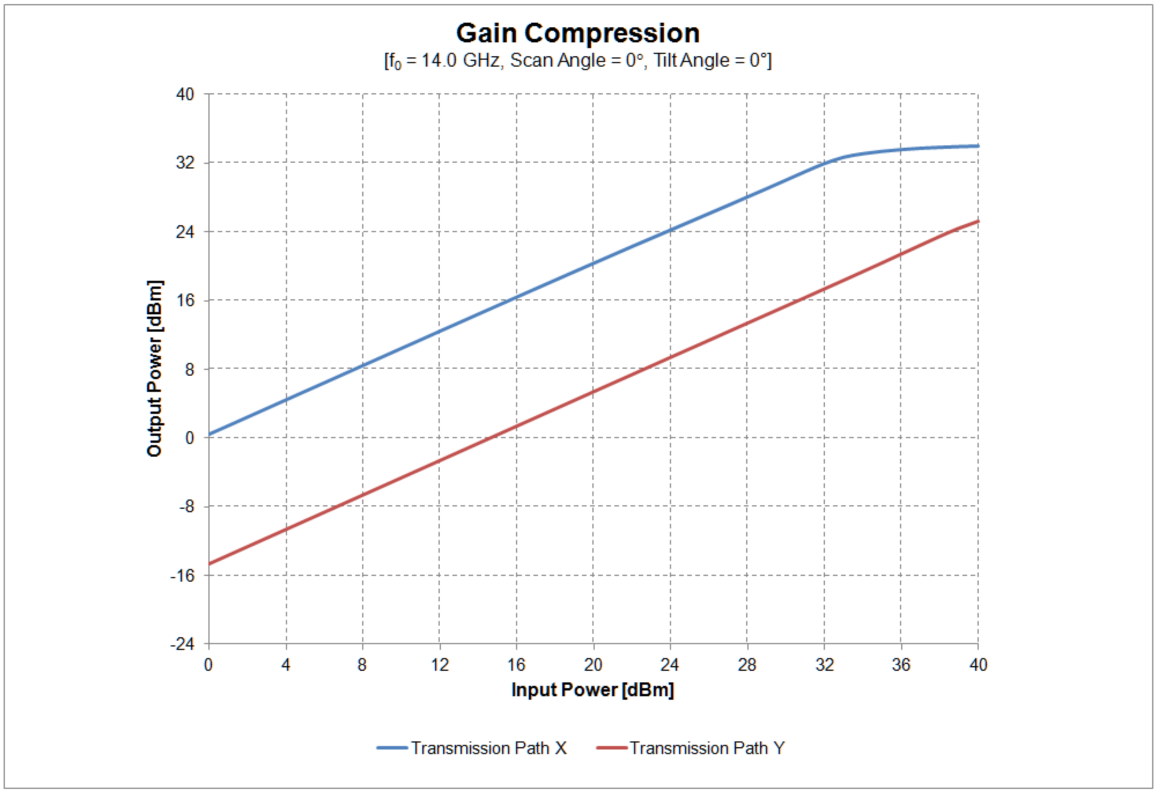

Figure 4.9 – Tx Sub-Array Gain Compression for a Test Case with Frequency of Operation Equal to 14.0 GHz, Elevation Scan Angle Equal to 0° and Polarization Tilt Angle Equal to 0°.

Conversely, it is often preferred to quantify the transmitter distortion by means of the output third order intercept point since it might be computed directly from the third order intermodulation distortion ($IMD3$) for any arbitrary value of output power as shown in Eq. 4.12.

Eq. 4.12

$$OIP_3 = P_{out} + \frac{P_{out} - P_{IMD3}}{2}$$

where P_{out} represents the output power level of the fundamental frequency, expressed in dBm units, and P_{IMD3} represents the output power level of the third order intermodulation distortion, also expressed in dBm units.

In telecommunications, a third-order intercept point $(IP3)$ is a measure for weakly nonlinear systems and devices, for example receivers, linear amplifiers and mixers. It is based on the idea that the device nonlinearity can be modeled using a low-order polynomial, derived by means of Taylor series expansion. The third-order intercept point relates nonlinear products caused by the third-order nonlinear term to the linearly amplified signal, in contrast to the second-order intercept point that uses second-order terms. The intercept point is a purely mathematical concept and does not correspond to a practically occurring physical power level. In many cases, it lies far beyond the damage threshold of the device. The output third order intercept point can be predicted using commercial CAD tools that implement similar two tone harmonic balance analysis methods as described in [24] and [23]. Figure 4.10 shows the Tx Sub-Array configuration and excitation source parameters for simulation of third order intermodulation distortion.

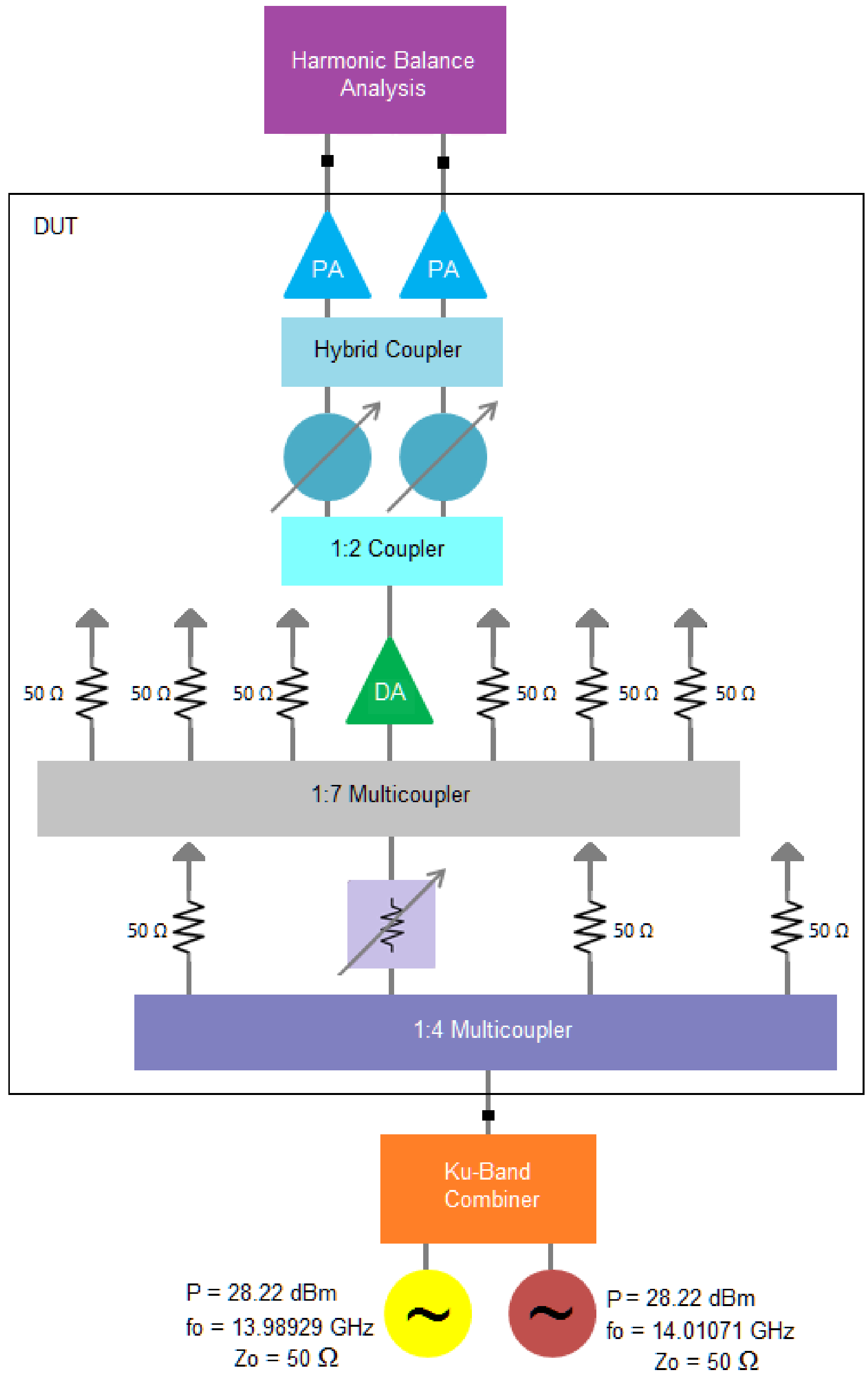

Figure 4.10 – Tx Sub-Array Configuration for Simulation of Third Order Intermodulation Distortion.

Figure 4.11 shows the predicted Tx Sub-Array two tone third order intermodulation distortion for a test case with first fundamental frequency (f_1) equal to 13.98929 GHz, second fundamental frequency (f_2) equal to 14.01071 GHz, elevation scan angle equal to 0°, polarization tilt angle equal to 0° and input power level (P_{in}) equal to 28.22 dBm per tone that corresponds to its 1 dB compression point. The predicted average output third order intercept point is approximately 42.07 dBm.

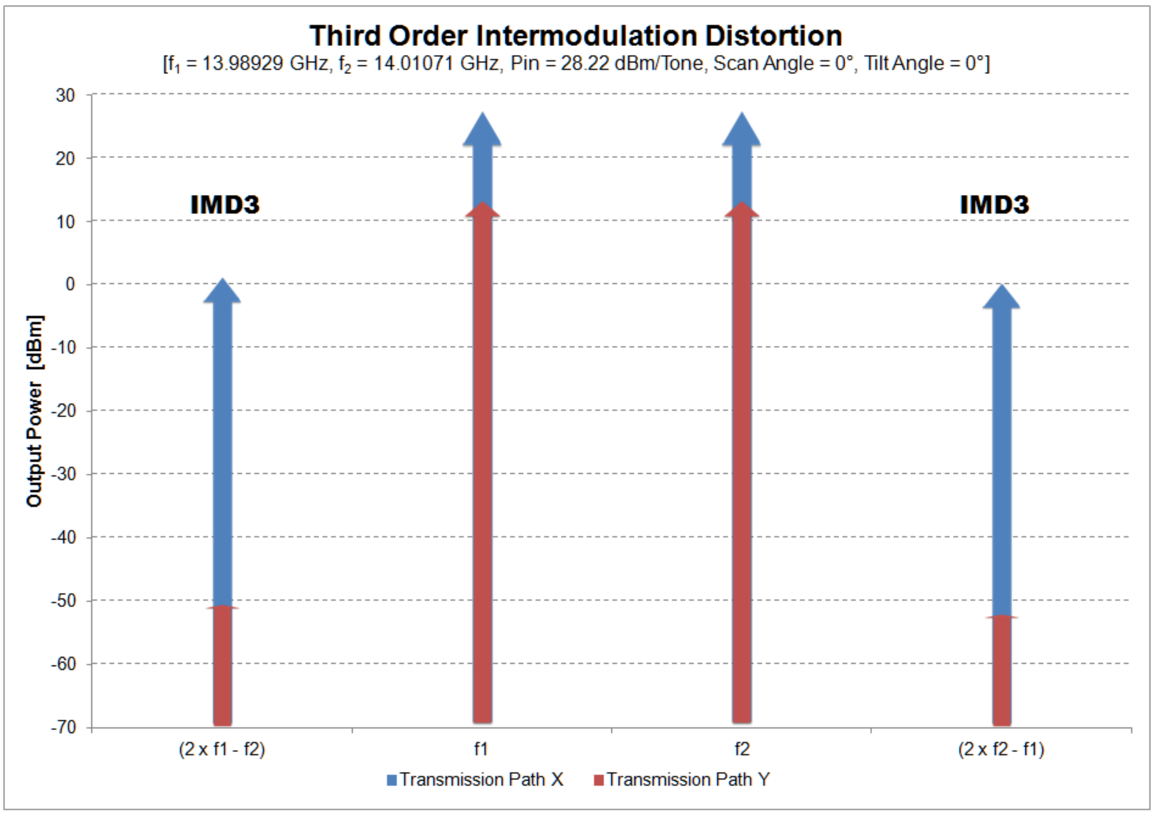

Figure 4.11 – Tx Sub-Array Two ToneThird Order Intermodulation Distortion for a Test Case with First Fundamental frequency f_1 Equal to 13.98929 GHz, Second Fundamental Frequency (f_2) Equal to 14.01071 GHz , Elevation Scan Angle Equal to 0°, Polarization Tilt Angle Equal to 0° and Input Power Level (P_{in}) Equal to 28.22 dBm per Tone.

.

4.3 SPURIOUS DOMAIN EMISSIONS

Spurious domain emissions are radio frequency emissions on a frequency, or frequencies, which are outside the necessary bandwidth and the level of which may be reduced without affecting the corresponding transmission of information. Spurious domain emissions include harmonic emissions, parasitic emissions, inter-modulation products and frequency conversion products as shown in Figure 4.12, but exclude out-of-band emissions [35].

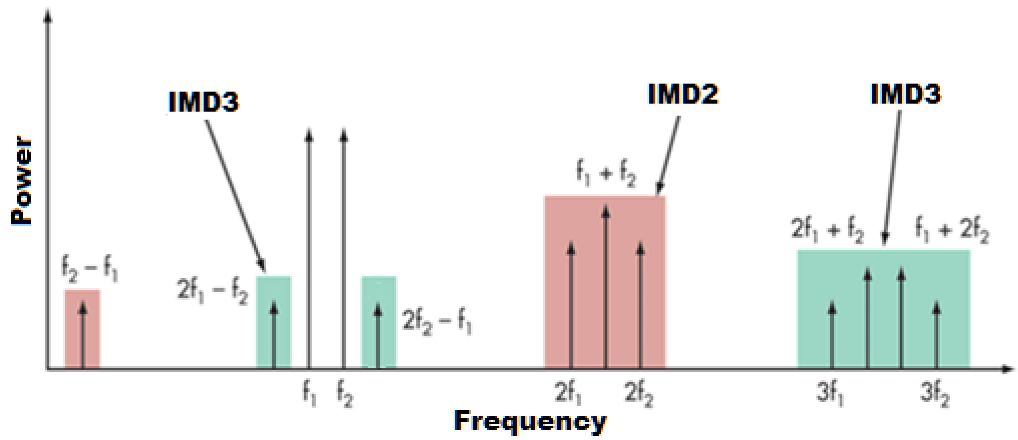

Figure 4.12 – Spurious Response of a Non-linear Device [36].

In nonlinear amplifiers, spurious signals are due to the non-linear distortion of the input RF signal. This distortion results in both the harmonics of RF tones and the cross-modulation frequencies of the input RF tones.

In up-converter mixers, spurious signals are due to the harmonic mixing of intermediate frequency (IF) and local oscillator (LO) input signals. For single-tone IF and LO signals, the spurious signal frequencies are the N × IF plus M × LO harmonic products, where N and M are integers. For multi-tone IF and LO signals, the spurious-signal frequencies include not only the primary N × IF and M × LO harmonic products for each IF tone combined with each LO tone individually, but also the cross-modulation products between multiple IF tones and LO tones.

The up-converter mixer spurious-signal generation is typically defined in the RF & Microwave industry by means of inter-modulation product table (.imt) files. The inter-modulation product table file, shown in Figure 4.13, is used to define a mixer's spurious-signal generation properties as a function of IF and LO tone mixing order, as well as of IF and LO signal power levels.

```
BEGIN  IMTDATA
!  Intermodulation table for double balanced TGC2510-SM

!  Signal Level (dBm)   LO Level (dBm)

! Reference levels have been adjusted for use with Sput_Track_prj

#        -10                 6
!   M x LO ( Horizontal )   N x Signal (Vertical )

%    0    1    2    3    4    5    6    7    8    9    10   11   12   13   14   15

     99   23   -17  25   99   99   99   99   99   99   99   99   99   99   99   99
     56   0    8    26   99   99   99   99   99   99   99   99   99   99   99
     28   33   32   62   99   99   99   99   99   99   99   99   99   99
     48   43   66   71   99   99   99   99   99   99   99   99   99
     99   99   99   99   99   99   99   99   99   99   99   99
     99   99   99   99   99   99   99   99   99   99   99
     99   99   99   99   99   99   99   99   99   99
     99   99   99   99   99   99   99   99   99
     99   99   99   99   99   99   99   99
     99   99   99   99   99   99   99
     99   99   99   99   99   99
     99   99   99   99   99
     99   99   99   99
     99   99   99
     99   99
     99
END
```

Figure 4.13 – Inter-modulation Product Table for Triquint TGC2510-SM Up-Converter Mixer.

Spurious domain emissions resulting from harmonic and inter-modulation products can be predicted using commercial CAD tools that implement similar harmonic balance analysis methods as described in [24]. Figure 4.14 shows the Tx Sub-Array configuration and excitation source parameters for simulation of spurious domain emissions.

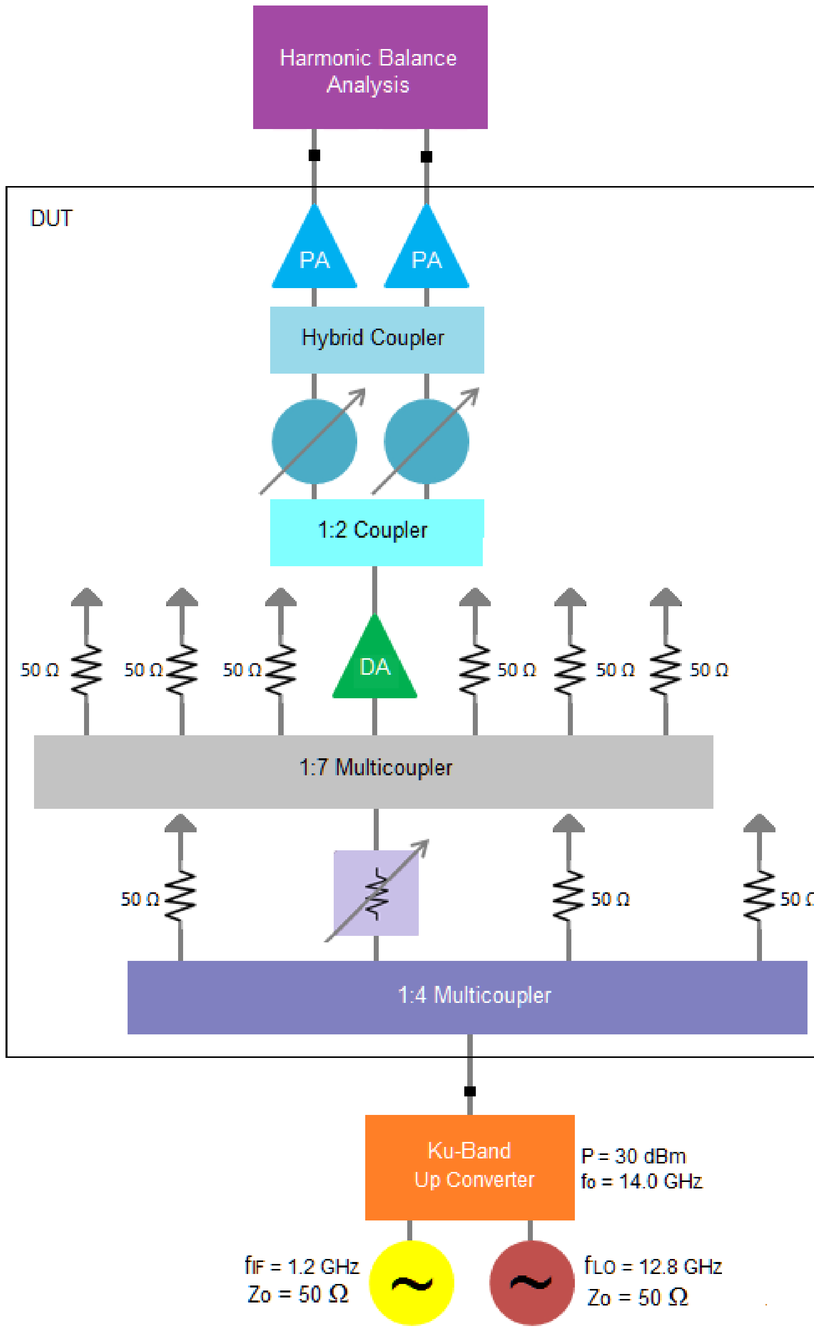

Figure 4.14 – Tx Sub-Array Configuration for Simulation of Spurious Domain Emissions.

Figure 4.15 shows the predicted Tx Sub-Array spurious domain emissions for a test case with LO frequency equal to 12.8 GHz, IF frequency equal to 1.2 GHz, elevation scan angle equal to 0°, polarization tilt angle equal to 0° and RF input power level equal to 30 dBm. The predicted spurious emission levels are used to estimate spurious emission attenuation in Section 5.3.

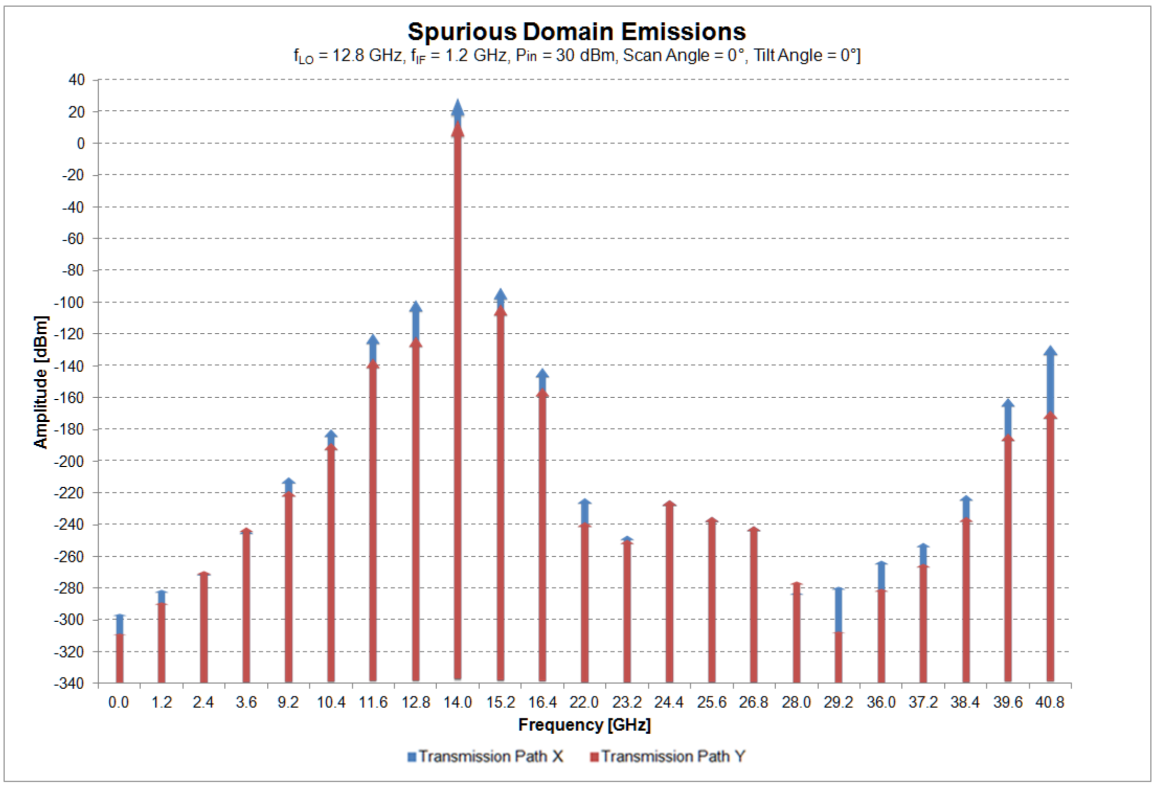

Figure 4.15 – Tx Sub-Array Spurious Domain Emissions for a Test Case with LO frequency Equal to 12.8 GHz, IF Frequency Equal to 1.2 GHz, Elevation Scan Angle Equal to 0°, Polarization Tilt Angle Equal to 0° and RF Input Power Level Equal to 30 dBm.

4.4 OUT OF BAND EMISSIONS

Non-linear effects in microwave transmitter components produce harmonics and inter-modulation products that cause spectral re-growth in the presence of a modulated waveform. This phenomenon spreads the spectrum of the modulated waveform causing interference issues in adjacent radio frequency channels as shown in Figure 4.16.

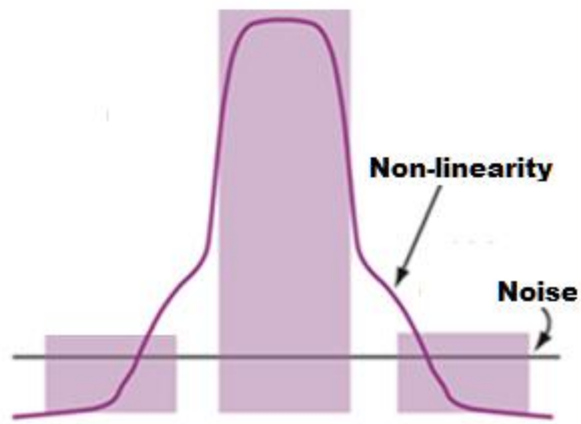

Figure 4.16 –Adjacent Channel Interference from Spectral Re-growth [37].

The specification in [35] defines out of band the (OoB) emissions as emissions on a frequency or frequencies immediately outside the necessary bandwidth which results from the modulation process, but excluding spurious emissions. Any emission outside the necessary bandwidth which occurs in the frequency range separated from the assigned frequency of the emission by less than 250% of the necessary bandwidth of the emission will generally be considered an emission in the OoB domain. However, this frequency separation may be dependent on the type of modulation, the maximum symbol rate in the case of digital modulation, the type of transmitter, and frequency coordination factors.

For example, in the case of some digital, broadband, or pulse modulated systems, the frequency separation may need to differ from the 250% factor.

The modulation waveforms implemented in UAV beyond line of sight satellite communications links are described by NATO in the "Interoperable Data Links for Imaging Systems" specification, STANAG 7085. The STANAG 7085 specification provides general requirements and directives for the implementation of the U.S. common data link (CDL) system. The U.S. common data link system is a family of full duplex, jam resistant, spread spectrum, point to point microwave communications links developed by U. S. government and used in imagery and signals intelligence collection systems.

Table 4.1 found in the unclassified document [48] summarizes the most relevant waveform parameters regarding the waveforms included in the CDL specification. The CDL waveforms might be replicated by assuming the modulation scheme and forward error correction (FEC) rate (R_c) that produce the corresponding bit rate (R_b) and bandwidth (B) values shown in Table 4.1.

CDL Waveform	Bit Rate (Mbps)	Bandwidth (MHz)
BR-0.2	0.2	0.8
BR-0.4	0.4	1.6
BR-2.0	2	8
BR-10.71A	10.71	21.4
BR-10.71B	10.71	21.4
BR-21.42	21.42	42.8
BR-44.73	44.7368	89.5
BR-137A	137.088	137.1
BR-137B	137.088	146.3
BR-137C	137.088	137.1
BR-137D	137.088	146.3
BR-274A	274.176	274.2
BR-274B	274.176	292.6
BR-274C	274.176	274.2
BR-274D	274.176	292.6

Table 4.1 – CDL Waveforms.

According to [12] CDL uses offset quadrature phase shift keying (OQPSK) modulation schemes for all three modes of its reverse link. For the implementation of OQPSK waveforms, a time offset (δ) equal to one half of symbol duration (T_s) is introduced in $\mathrm{Q(t)}$. Hence, the expression from Eq. 3.17 takes the form shown in Eq. 4.13.

Eq. 4.13

$$s(t) = \sqrt{\frac{2E_s}{T_s}}\left[h(t)\,\mathrm{I(t)}\cos(2\pi f_c t) - h(t)Q\left(t - \frac{T_s}{2}\right)\sin(2\pi f_c t)\right]$$

where T_s can be calculated using the expressions in Eq. 4.14

Eq. 4.14

$$T_s = \frac{1}{R_s}$$

and Eq. 4.15

Eq. 4.15

$$R_s = \frac{R_b}{R_c \log_2 M}$$

where R_s is the symbol rate out of the encoder and M is the order of the *M-ary* phase shift keying modulation scheme.

In this case, the baseband shaping filter $h(t)$ is described by the impulse response of a root raised cosine (RRC) filter found in [38] and shown in Eq. 4.16.

Eq. 4.16

$$h(t) = \frac{\left(\frac{4\beta t}{T_s}\right)\cos\left[\frac{\pi t(1+\beta)}{T_s}\right] + \sin\left[\frac{\pi t(1-\beta)}{T_s}\right]}{\frac{\pi t}{T_s}\left[1 - \left(\frac{4\beta t}{T_s}\right)^2\right]}$$

The RRC filter roll-off (β) can be calculated using the expression in Eq. 4.17.

Eq. 4.17

$$\beta = \left(\frac{B}{R_s} - 1\right)$$

The main advantage of phase and frequency modulation systems over amplitude modulations systems, is that it has a constant envelope. Hence it is not sensitive to fluctuations in amplitude. As long as the phase changes are gradual, amplitude variations in PSK are smooth and more or less maintain a constant envelope from one state to the other. In QPSK waveforms, each phase state (symbol) represents two bits of a bit sequence. Up to 4 different phase states (symbols) are used to produce the modulation. The theoretical spacing between these phase states (symbols) is equal to 90°. However, when two bits change simultaneously, then the phase experiences a change of 180°. This 180° phase change causes the envelope to invert producing out of band and/or spurious frequency components in the QPSK spectrum.

When rectangular pulses are passed through the pulse shaping filter (i.e. RRC filter), these frequency components are attenuated. However, this also causes heavy fluctuations in the envelope of the modulated waveform. OQPSK is used to prevent the OoB envelope fluctuations and spurious frequency components. The implementation of OQPSK modulation limits the maximum phase change performed in QPSK modulated waveforms. In OQPSK, the I and Q bits are offset by half a symbol period (i.e one bit period). This ensures that both bits in a symbol won't change their state simultaneously, limiting the maximum phase change to 90° and preventing any OoB spurious frequency components.

The OoB emissions resulting from spectral re-growth can be predicted using commercial CAD tools that implement similar envelope analysis methods as described in [24]. Figure 4.17 shows the Tx Sub-Array configuration and excitation source parameters for simulation of out of band emissions.

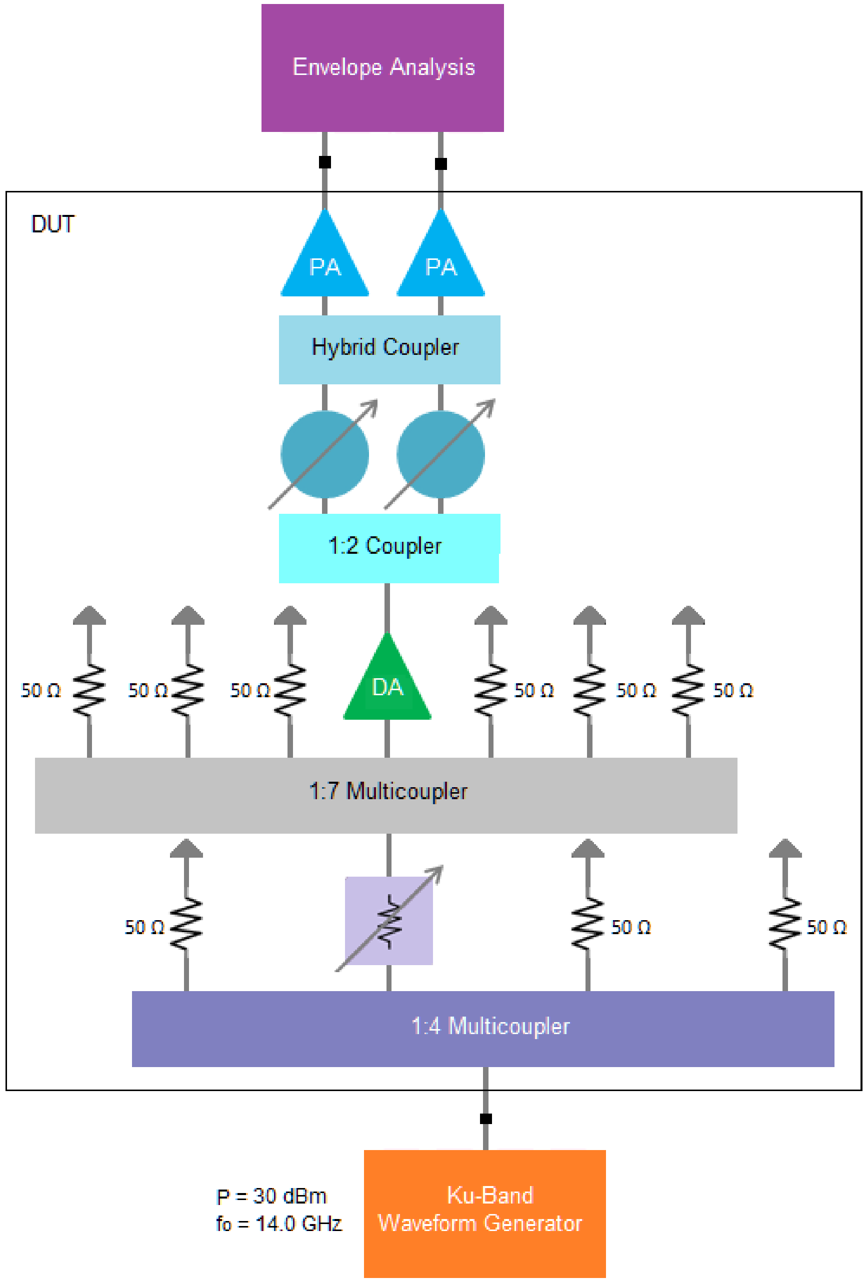

Figure 4.17 – Tx Sub-Array Configuration for Simulation of Out of Band Emissions.

Table 4.2 shows the modulation waveform parameters for simulation of OoB emissions. A 32,767 bit pseudorandom test pattern with NRZ data format is used to model the arbitrary baseband signal according to ITU's Recommendation O.150 in [39].

Waveform	BR-10.71
Modulation Scheme	OQPSK
Bit rate (Mbps)	10.71
I(t) PN Sequence Taps	16385
I(t) PN Sequence Seed	9837
Q(t) PN Sequence Taps	16385
Q(t) PN Sequence Seed	4829
FEC Rate	1/2
RRC Filter Roll-Off	1
Bits per Symbol	2
Symbol Rate (Mbps)	10.71
Occupied Bandwidth (MHz)	21.42

Table 4.2 – Waveform Parameters for Simulation of Out of Band Emissions.

Figure 4.18 shows the predicted Tx Sub-Array symbol trajectory for a test case with a 10.71 Mbps pseudo random bit sequence,OQPSK modulation scheme, FEC rate equal to 1/2, RRC filter roll-off equal to 1, elevation scan angle equal to 0°, polarization tilt angle equal to 0°, frequency of operation equal to 14.0 GHz and RF input power level equal to 30 dBm. Even with pulse shaping filtering in place it is not difficult to observe the constant envelope character of the simulated OQPSK modulated waveform. The symbol trajectory approaches a well defined circular shape due to the relaxed RRC filter roll-off factor.

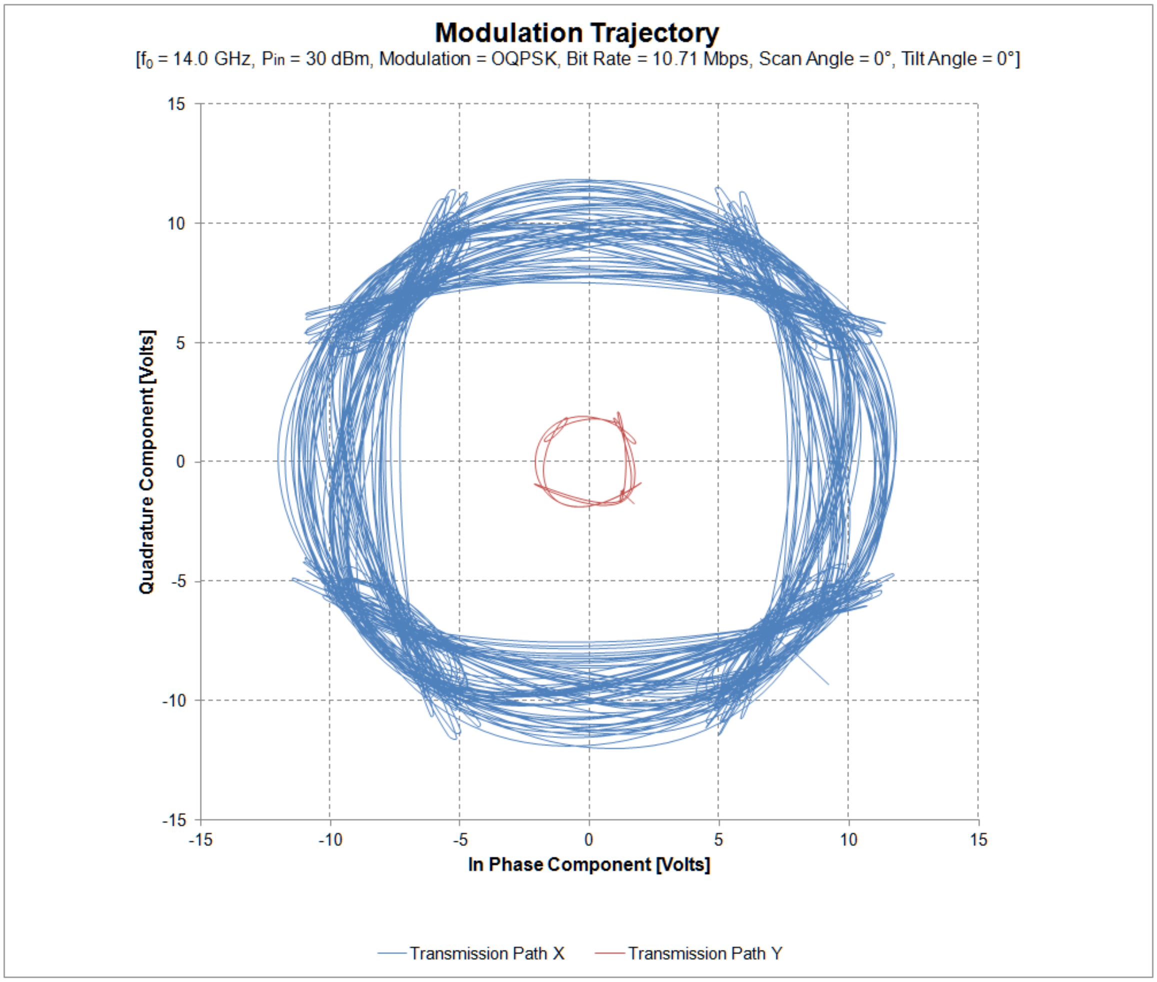

Figure 4.18 – Tx Sub-Array Modulation Trajectory for a Test Case with a 10.71 Mbps Pseudo Random Bit Sequence ,OQPSK modulation scheme, FEC Rate Equal to 1/2, RRC Filter Roll Off Equal to 1, Elevation Scan Angle Equal to 0°, Polarization Tilt Angle Equal to 0°, Frequency of Operation Equal to 14.0 GHz and RF Input Power Level equal to 30 dBm.

Figure 4.19 shows the predicted Tx Sub-Array out of band emissions for a test case with a 10.71 Mbps pseudo random bit sequence, OQPSK modulation scheme, FEC rate equal to 1/2, RRC filter roll-off equal to 1, elevation scan angle equal to 0°, polarization tilt angle equal to 0°, frequency of operation equal to 14.0 GHz and RF input power level equal to 30 dBm. The predicted OoB emission levels are used to estimate OoB emission attenuation in Section 5.4.

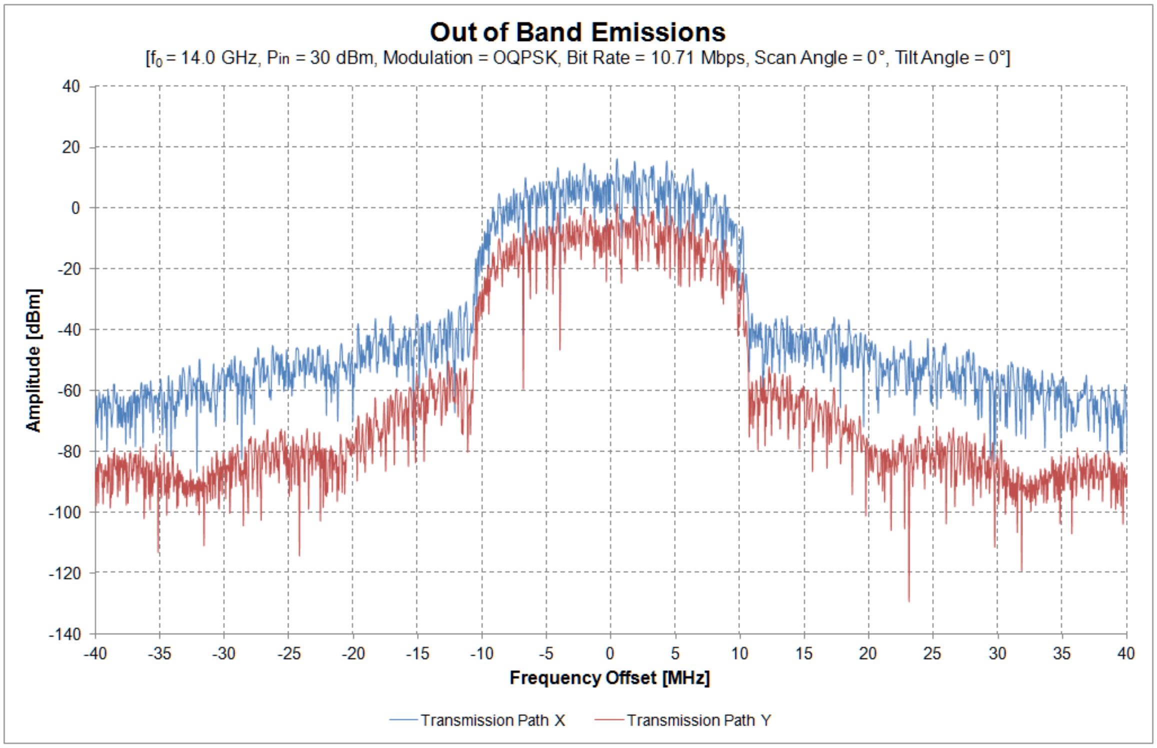

Figure 4.19 – Tx Sub-Array Out of Band Emissions for a Test Case with a10.71 Mbps Pseudo Random Bit Sequence, OQPSK modulation scheme, FEC Rate Equal to 1/2, RRC Filter Roll Off Equal to 1, Elevation Scan Angle Equal to 0°, Polarization Tilt Angle Equal to 0°, Frequency of Operation Equal to 14.0 GHz and RF Input Power Level equal to 30 dBm.

4.5 MODULATION ACCURACY

Modulation accuracy is one of the most significant performance indicators regarding transmitted signal integrity in modern wireless telecommunication systems. Inter-symbol interference, close-in phase noise, carrier leakage, I/Q modulator imbalance, non-linear distortion, gain ripple, frequency error and in-band noise are factors that have direct influence on transmitter's modulation accuracy.

The modulation accuracy is usually characterized in terms of the constellation error vector magnitude (EVM) shown in Figure 4.20.

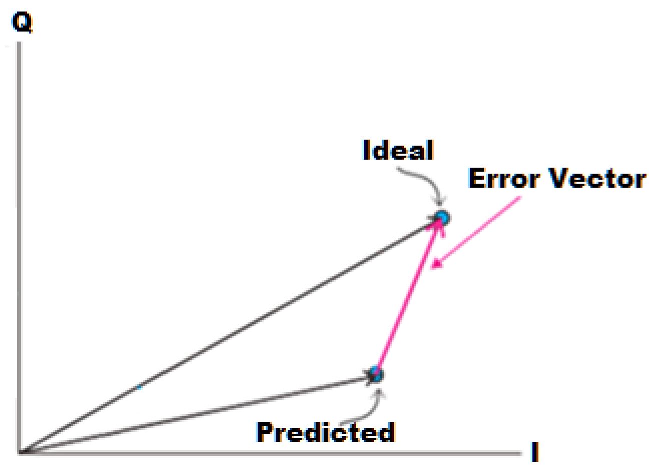

Figure 4.20 – Constellation Error Vector Magnitude [40].

The error vector magnitude is defined by [41] as a measure of the error in the modulated signal constellation, taken as the root mean square of the error vectors over the active subcarriers, considering all symbols of the modulation scheme. It is usually expressed as a percentage value related to the reference vectors of the ideal signal constellation.

In a more practical sense [42] defines the relative root mean square error vector magnitude (EVM_{RMS}) as shown in Eq. 4.18

Eq. 4.18

$$EVM_{RMS} = \sqrt{\sum_{k \in K} |E(k)|^2 \Big/ \sum_{k \in K} |S(k)|^2}$$

where $E(k)$, the error vector, is measured and calculated for each instant k, $S(k)$ is the ideal transmitter signal observed through the measurement filter at instant k determined by Eq. 4.19

Eq. 4.19

$$k = floor(t/T_s)$$

where T_s corresponds to the symbol time.

The symbol error vector magnitude at symbol k is defined as shown in Eq. 4.20

Eq. 4.20

$$EVM(k) = \sqrt{\frac{|E(k)|^2}{\frac{\sum_{k \in K} |S(k)|^2}{N}}}$$

where N is the number of elements in the set K. $EVM(k)$ is the vector error length relative the root average energy of the useful part of one burst. The EVM can be simulated using commercial CAD tools that implement similar envelope transient analysis, or envelope analysis methods as described in [24] and [43]. Table 4.2 shows the modulation waveform parameters for simulation of constellation EVM. Figure 4.21

shows the Tx Sub-Array configuration and excitation source parameters for simulation of constellation EVM.

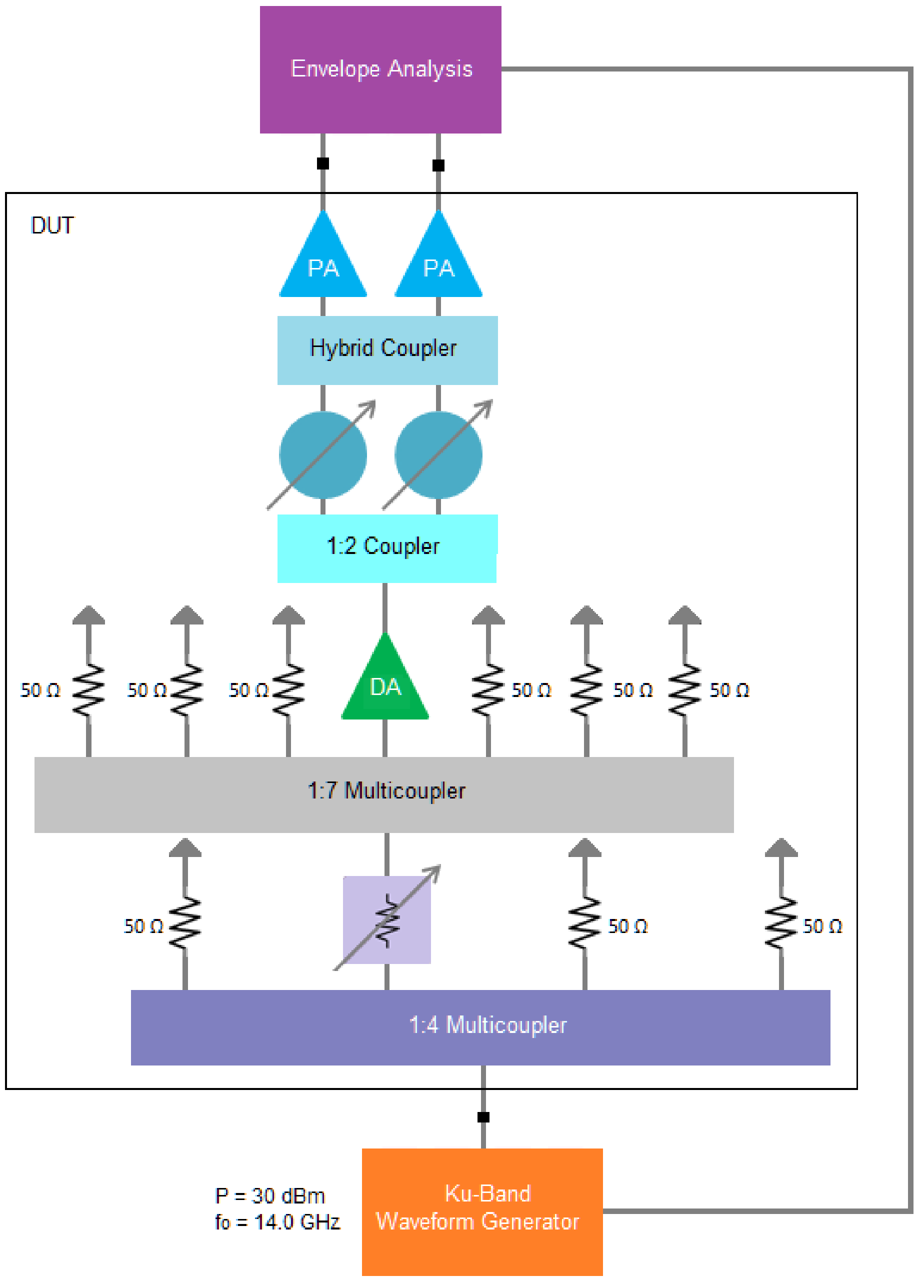

Figure 4.21 – Tx Sub-Array Configuration for Simulation of Constellation Error Vector Magnitude.

Figure 4.22 shows the predicted Tx Sub-Array modulation constellation for a test case with a 10.71 Mbps pseudo random bit sequence, OQPSK modulation scheme, FEC rate equal to 1/2, RRC filter roll-off equal to 1, elevation scan angle equal to 0°, polarization tilt angle equal to 0°, frequency of operation equal to 14.0 GHz and RF input power level equal to 30 dBm. Even with pulse shaping filtering in place it is not difficult to observe the constant envelope character of the simulated OQPSK modulated waveform. The modulation constellation approaches a well defined and balanced square shape with minimal dispersion but still with some ISI due to the relaxed RRC filter roll-off factor.

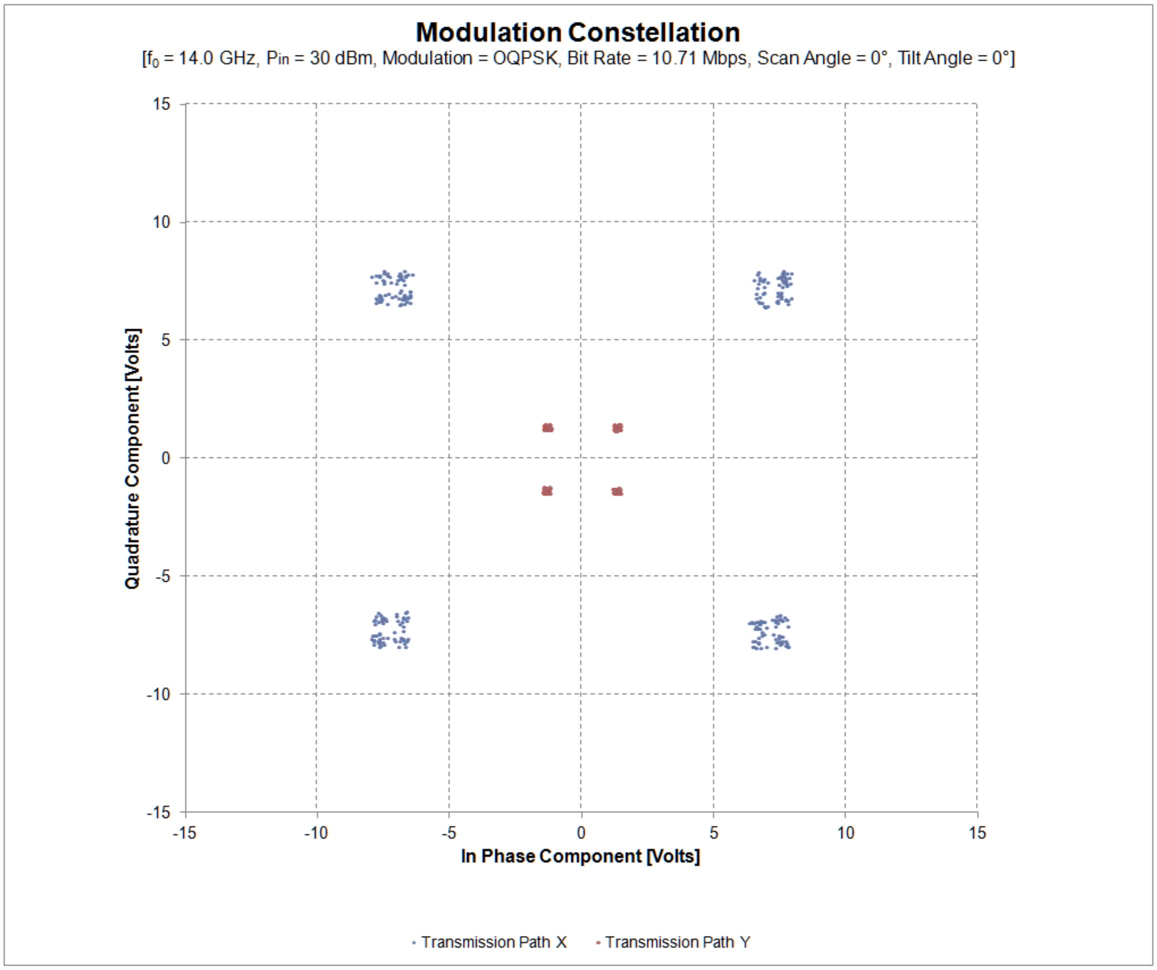

Figure 4.22 – Tx Sub-Array Modulation Constellation for a Test Case with a10.71 Mbps Pseudo Random Bit Sequence, OQPSK modulation scheme, FEC Rate Equal to 1/2, RRC Filter Roll Off Equal to 1, Elevation Scan Angle Equal to 0°, Polarization Tilt Angle Equal to 0°, Frequency of Operation Equal to 14.0 GHz and RF Input Power Level equal to 30 dBm.

Figure 4.23 shows the predicted Tx Sub-Array root mean square error vector magnitude for a test case with a 10.71 Mbps pseudo random bit sequence, OQPSK modulation scheme, FEC rate equal to 1/2, RRC filter roll-off equal to 1, elevation scan angle equal to 0°, polarization tilt angle equal to 0°, frequency of operation equal to 14.0

GHz and RF input power level equal to 30 dBm. The predicted EVM values are used to estimate the probability of bit errors in Section 5.5.

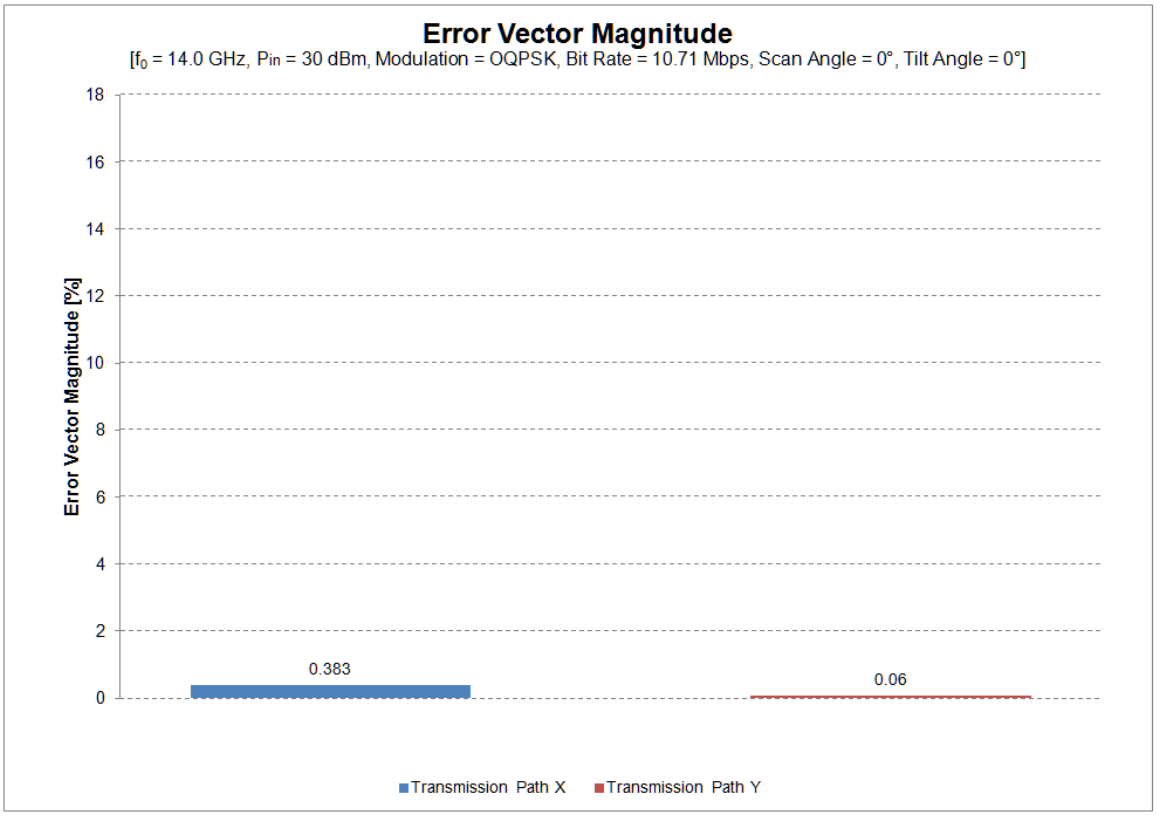

Figure 4.23 – Tx Sub-Array Error Vector Magnitude for a Test Case with a 10.71 Mbps Pseudo Random Bit Sequence, OQPSK modulation scheme, FEC Rate Equal to 1/2, RRC Filter Roll Off Equal to 1, Elevation Scan Angle Equal to 0°, Polarization Tilt Angle Equal to 0°, Frequency of Operation Equal to 14.0 GHz and RF Input Power Level equal to 30 dBm.

4.6 POLARIZATION ACCURACY

The polarization of a transverse electromagnetic plane wave describes the locus traced by the tip of its time - harmonic electrical field vector at a plane in space that is orthogonal to its direction of propagation. Figure 4.24 shows an elliptical polarization locus in the XY plane.

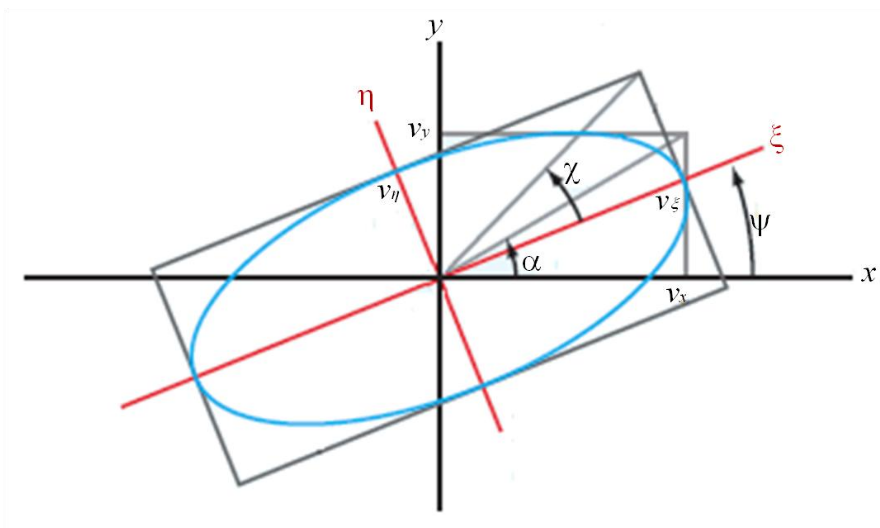

Figure 4.24 – Elliptical Polarization Locus in the XY Plane [44].

A transverse electromagnetic plane wave is said to be elliptically polarized if the locus traced by the tip of its time - harmonic electrical field vector approaches the shape of an ellipse as shown in Figure 4.25.

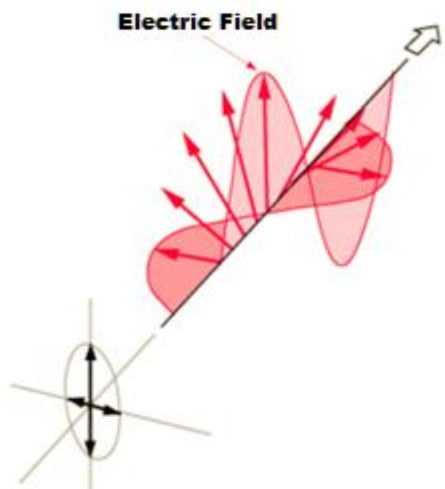

Figure 4.25 – Elliptically Polarized Wave [45].

Some specific circumstances may cause the elliptical locus traced by the tip of the time - harmonic electrical field vector to degenerate into a shape that resembles a straight line. In this case the wave is said to be linearly polarized as shown in Figure 4.26.

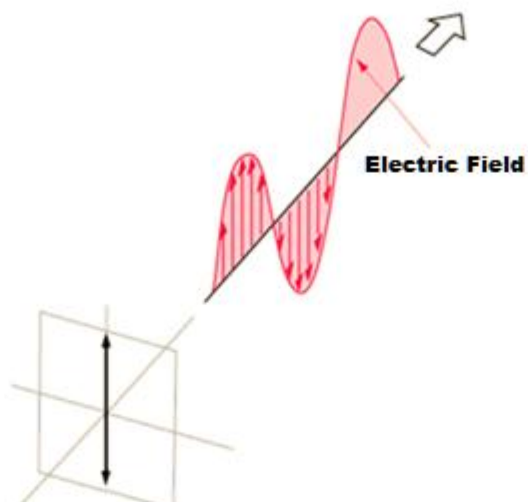

Figure 4.26 – Linearly Polarized Wave [45].

The shape of the polarization locus, its sense of rotation and its tilt angle are determined by the time - harmonic electric field vector component amplitude ratio (v_y/v_x) and the phase difference (δ) defined in Eq. 4.21

Eq. 4.21

$$\delta = \left(\phi_y - \phi_x\right) \cong \left(\phi_{y_0} - \phi_{x_0}\right)$$

where ϕ_y is the phase of the vector component in the direction of the y axis in $radians$, ϕ_x is the phase of the vector component in the direction of the x axis in $radians$, ϕ_{y_0} is the phase shift of transmission path y in $radians$ and ϕ_{x_0} is the phase shift of transmission path x in $radians$.

Polarization diversity is usually implemented to minimize the effects of multipath fading in modern wireless communications systems. However, satellite communication links suffer the additional effects of Faraday rotation due to ionospheric propagation, amplitude modulation due to satellite spin and sudden changes in aircraft navigation.

The implementation of adaptive polarization diversity techniques might help to mitigate most of these effects to increase the probability of link availability and its perceived quality of service. Moreover, the implementation of polarization diversity techniques provides an alternative solution to mitigate the ASI generated by transmissions to and from satellites operating on similar frequency ranges.

In this case, adaptive linear polarization is achieved implementing simultaneous control of the elevation scan angle and the polarization tilt angle. The phase shift ϕ_{x_0} is set in terms of the target elevation scan angle using Eq. 4.22

Eq. 4.22

$$\phi_{x_0} = \left(\frac{2 \cdot \pi \cdot f_0}{c}\right) \cdot d \cdot sin(\theta_0)$$

where f_0 is the frequency of operation in Hz, c is the speed of light in vacuum in m/s, and d is the distance between adjacent phased array antenna elements in m and θ_0 is the target elevation scan angle in $radians$ [6].

Likewise, the phase shift ϕ_{y_0} is set in terms of the target polarization tilt angle in $radians$ (ψ_0) as shown in Eq. 4.23.

Eq. 4.23

$$\phi_{y_0} = \phi_{x_0} + \frac{\pi}{2} - 2 \cdot \psi_0$$

Table 4.4 shows the Tx Sub-Array phase shifter settings required to achieve tilt angles of selected polarization states.

Elevation Scan Angle (θ)	Polarization Tilt Angle (ψ)	Phase Shift in X (ϕ_x)	Phase Shift in Y (ϕ_y)
0°	0°	0°	90°
0°	22.5°	0°	45°
0°	45°	0°	0°
0°	67.5°	0°	315°
0°	90°	0°	270°
0°	112.5°	0°	225°
0°	135°	0°	180°
0°	157.5°	0°	135°

Table 4.3 – Tx Sub-Array Phase Shifter Settings for Selected Polarization States.

Nevertheless, phase compensation procedures are performed in advance in order to mitigate the impact of phase errors on the polarization accuracy of selected polarization states. In this case, a manual phase compensation procedure is implemented. The manual phase compensation procedure assumes a fixed phase state in the phase shifter of Transmission Path X and then tests several adjacent phase states in the phase shifter of Transmission Path Y until the error between the actual and target polarization tilt angles achieves its minimum value.

The polarization loci of selected polarization states can be simulated performing multi-port S-parameter analysis procedures described in [32] and small-signal, linear, AC analysis. Figure 4.27 shows the Tx Sub-Array configuration and excitation source parameters for simulation of polarization accuracy.

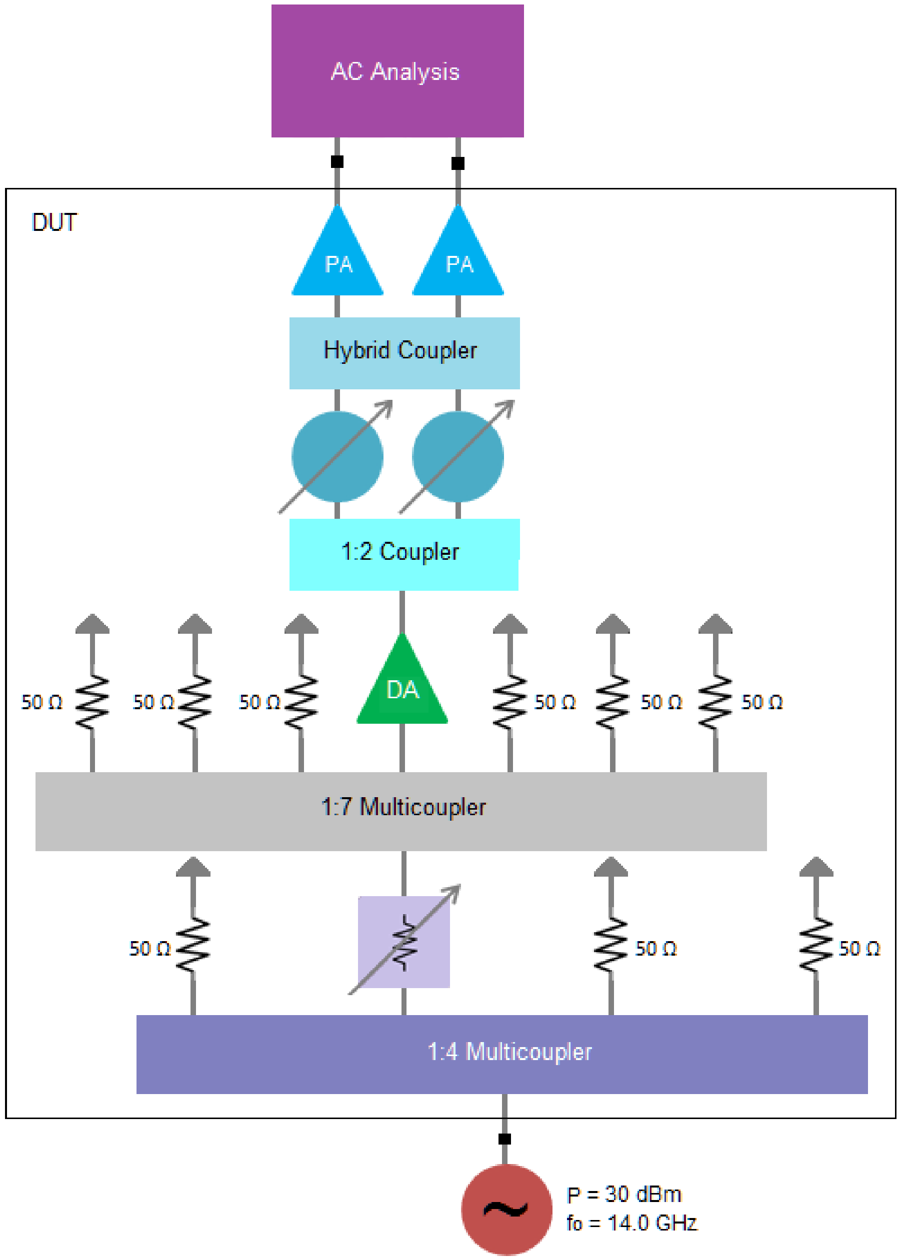

Figure 4.27 – Tx Sub-Array Configuration for Simulation of Polarization Accuracy.

Figure 4.28 shows the predicted Tx Sub-Array polarization loci for selected polarization states with elevation scan angle equal to 0°, frequency of operation equal to

14.0 GHz and RF input power level equal to 30 dBm. From these results it can be easily observed that the predicted tilt angles of all simulated polarization states are very close to their corresponding target tilt angles. However, the polarization loci don't exhibit the expected linear behavior for the majority of the simulated polarization states. This implies degradation of the polarization axial ratio performance in those specific polarization states. Further, analysis and discussion of this problem are performed in Section 5.6.

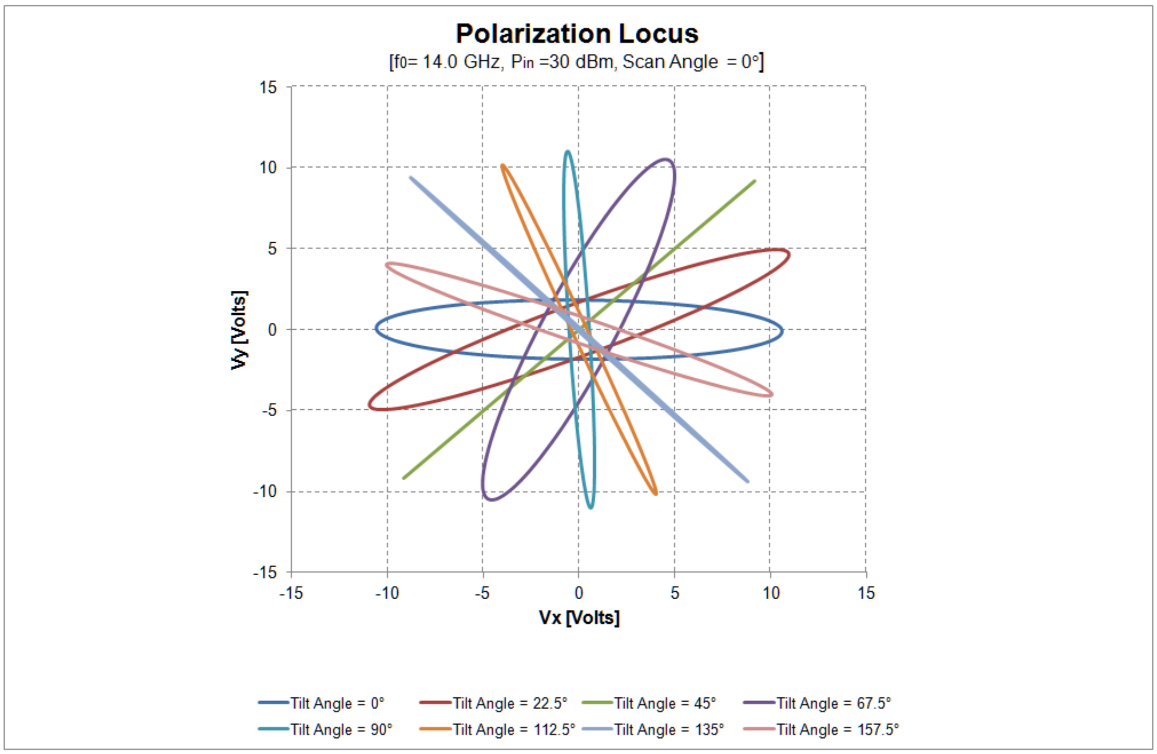

Figure 4.28 – Tx Sub-Array Polarization Loci for Selected Polarization States with Elevation Scan Angle Equal to 0°, Frequency of Operation Equal to 14.0 GHz and RF Input Power Level equal to 30 dBm.

Figure 4.29 shows the predicted Tx Sub-Array polarization component output power levels for selected polarization states with elevation scan angle equal to 0°, frequency of operation equal to 14.0 GHz and RF input power level equal to 30 dBm. From these results it can be easily observed that amplitude errors (i.e. impedance mismatch losses) might be the cause of the elliptical loci displayed by most of the simulated polarization states. Further, analysis and discussion of this problem are performed in Section 5.6.

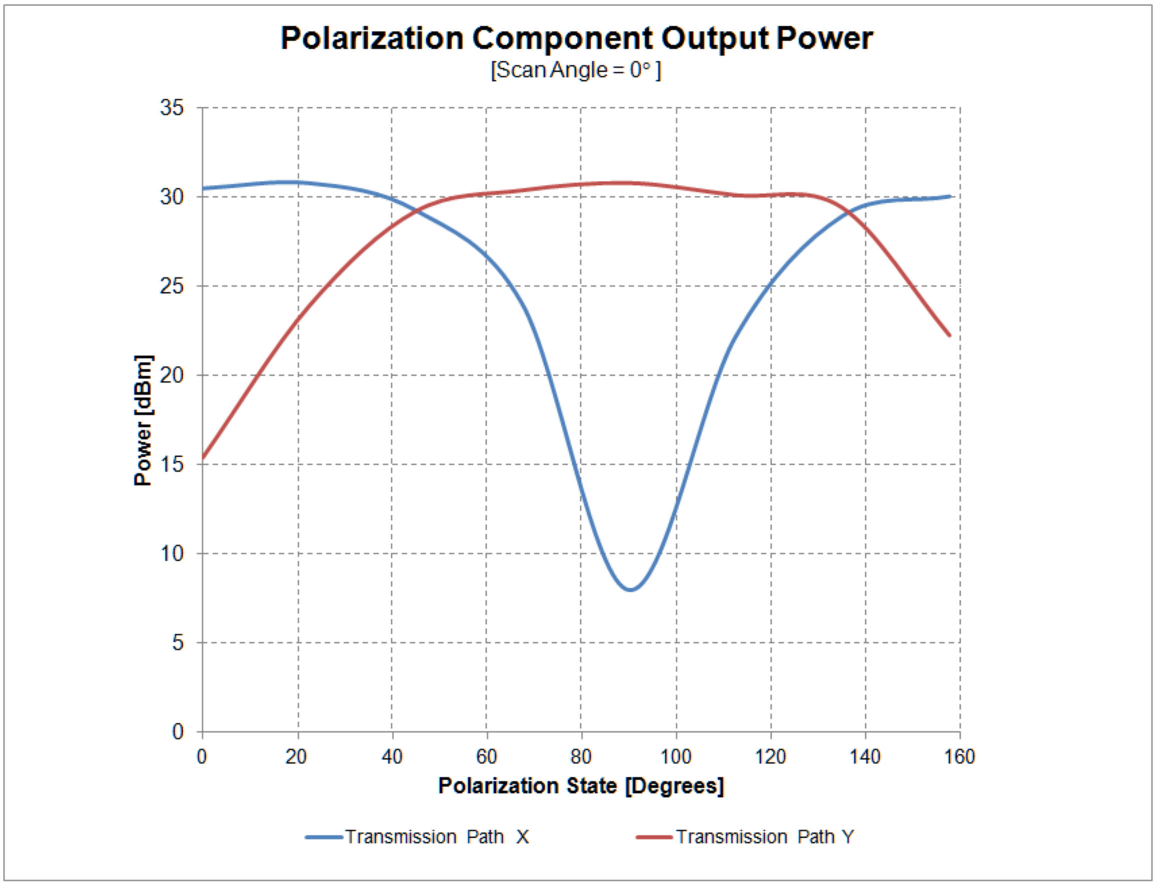

Figure 4.29 – Tx Sub-Array Polarization Resultant Output Power Levels for Selected Polarization States with Elevation Scan Angle Equal to 0°, Frequency of Operation Equal to 14.0 GHz and RF Input Power Level equal to 30 dBm.

5 DISCUSSION

5.1 FREQUENCY RESPONSE

MIL-STD-188-164B specifies in [46] that the amplitude variations of the transmission uplink function at the input to the antenna feed should not exceed ± 2.0 dB when operating at maximum linear power over the range of frequencies from 13.75 GHz to 14.5 GHz. Figure 5.1 shows the predicted Tx Sub-Array gain ripple for a test case with elevation scan angle equal to 0° and polarization tilt angle equal to 0°. The results from Figure 4.3 were analyzed to obtain these values.

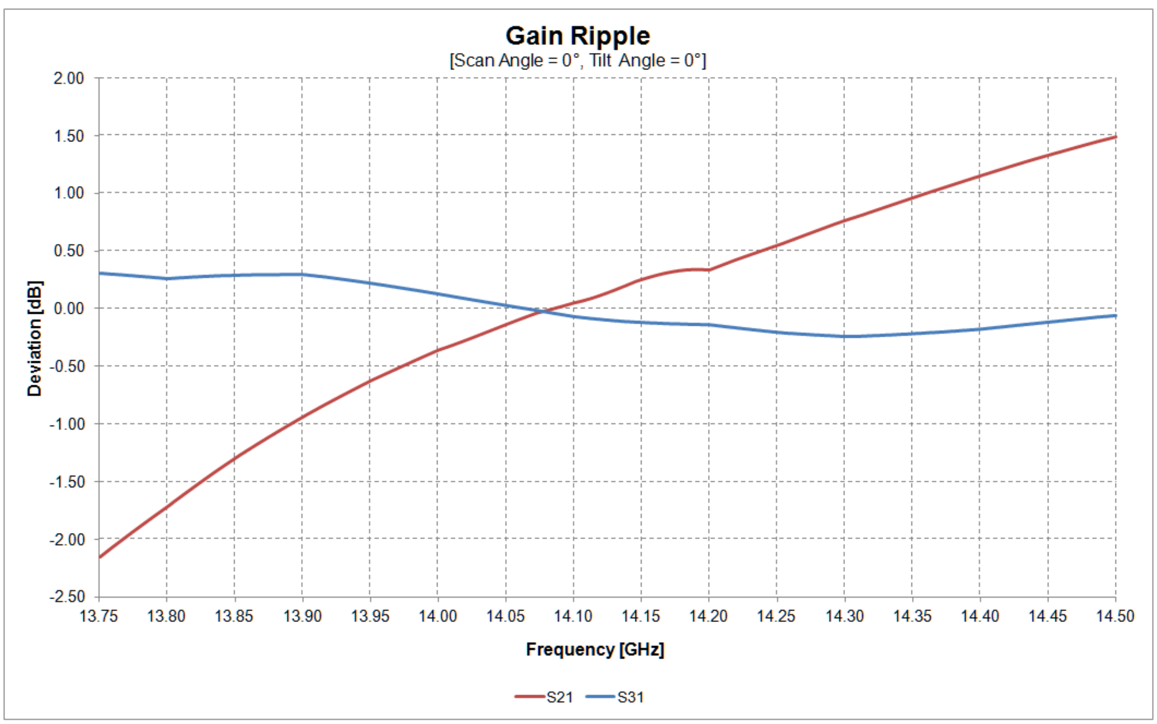

Figure 5.1 – Tx Sub-Array Gain Ripple for a Test Case with Elevation Scan Angle Equal to 0° and Polarization Tilt angle Equal to 0°.

The predicted gain ripple values partially comply with MIL-STD-188-164B specification regarding the amplitude variations of the transmission uplink function. The transmission path represented by the S_{21} parameter fails to comply the requirement at the lower 17.4 MHz of the frequency range from 13.75 GHz to 14.5 GHz.

Conversely, [46] specifies that departure from phase linearity of the transmission function shall not exceed $\pm 22.918°$ over any 36-MHz of instantaneous bandwidth when operating at any point up to the maximum-linear power. Figure 5.2 shows the Tx Sub-Array linear phase deviation for a test case with elevation scan angle equal to 0° and polarization tilt angle equal to 0°.

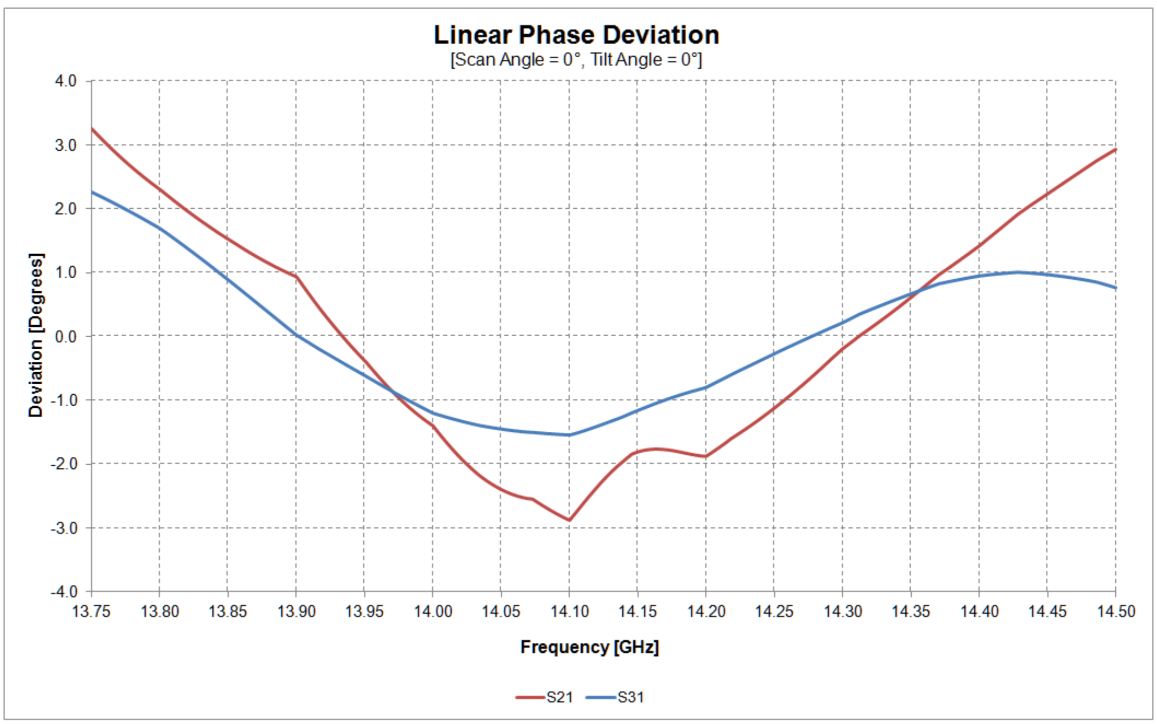

Figure 5.2 – Tx Sub-Array Linear Phase Deviation for a Test Case with Elevation Scan Angle Equal to 0° and Polarization Tilt angle Equal to 0°.

The predicted linear phase deviation values comply with MIL-STD-188-164B specification regarding departure from phase linearity.

5.2 LINEARITY

The practical implementation of complex quadrature modulation schemes requires inclusion of baseband pulse shaping filters to mitigate the effects of inter-symbol interference (ISI). The peak to average power ratio of the filtered waveform depends on the frequency response of these baseband pulse shaping filters. Hence, the filtered waveforms tend to have higher peak to average power ratio.

The higher the peak to average power ratio of a waveform the higher the degree of linearity required in microwave transmitter equipment to mitigate spectral re-growth and adjacent channel interference issues. Hence, the peak to average power ratio is commonly used to determine the required signal power back-off to provide enough linearity for the transmission of a specific modulation waveform.

For instance, the average 1 dB compression point value predicted in section 4.3 is 32.86 dBm. Since the peak power level of a waveform is limited by the output 1 dB compression point power level, it follows that the higher the peak to average power ratio of a waveform, the lower the average signal power level as shown in Eq. 5.1.

Eq. 5.1

$$P_{Avg_{dBm}} = P_{1dB_{dBm}} - PAPR$$

Table 5.1 shows the predicted Tx Sub-Array average output power level values for the CDL waveform with OQPSK modulation under consideration.

Waveform	Modulation Scheme	Bit Rate [Mbps]	RRC Filter Roll-Off	FEC Rate	P_{1dB} [dBm]	PAPR [dB]	P_{Avg} [dBm]
BR-10.71	OQPSK	10.71	1	1/2	32.86	2.11	30.75

Table 5.1 – Tx Sub-Array Average Output Power for the CDL Waveform with OQPSK Modulation.

The predicted average signal power value for the CDL waveform using OQPSK modulation scheme complies with the 30.35 dBm output power requirement calculated with Eq. 3.11..

5.3 SPURIOUS DOMAIN EMISSIONS

According to [47] the spurious domain generally consists of frequencies separated from the centre frequency of the emission by 250% or more of the necessary bandwidth of the emission. As the radio regulations (RR) forbid any radio service to cause harmful interference outside its allocated band, transmitter frequencies should be determined so that out-of-band emissions do not cause harmful interference outside the allocated band in accordance with RR No. 4.5.

The spurious domain emission limits for Category A services in [47] specify the minimum attenuation level as shown in Eq. 5.2

Eq. 5.2

$$Attenuation\ (dBc) = 43 + 10 \cdot \log_{10} P$$

where P is the mean power level at the antenna transmission line in Watts.

Conversely, [46] specifies that the $EIRP$ of extraneous emissions measured over any 10 kHz bandwidth shall be no greater than 37 dBm or -60 dBc, or whichever is larger considering the transmission of CW signal at the maximum-linear power level of the transmitter equipment.

Furthermore, [46] specifies that the level of all harmonics of the transmit carriers shall not exceed -60 dBc when measured at maximum linear power. Figure 5.3 shows the predicted Tx Sub-Array spurious domain emissions attenuation levels for a test case with LO frequency equal to 12.8 GHz, IF frequency equal to 1.2 GHz, elevation scan angle equal to 0°, polarization tilt angle equal to 0° and RF input power level equal to 30 dBm.

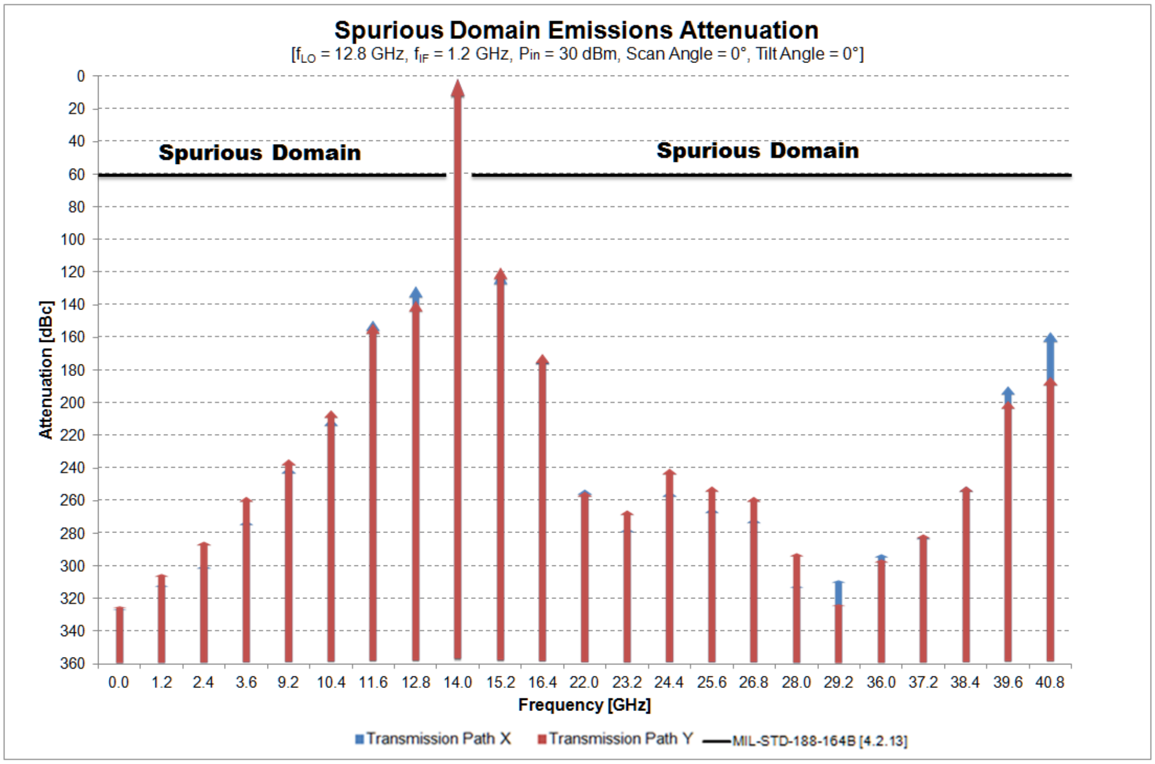

Figure 5.3 – Tx Sub-Array Spurious Domain Emissions Attenuation Levels for a Test Case with LO frequency Equal to 12.8 GHz, IF Frequency Equal to 1.2 GHz, Elevation Scan Angle Equal to 0°, Polarization Tilt Angle Equal to 0° and RF Input Power Level Equal to 30 dBm.

The predicted spurious domain emissions attenuation values comply with MIL-STD-188-164B specification regarding extraneous and harmonic emission limits.

5.4 OUT OF BAND EMISSIONS

ITU-R SM.1541-6 recommendation in [35] specifies that any emission outside the necessary bandwidth which occurs in the frequency range separated from the assigned frequency of the emission by less than 250% of the necessary bandwidth of the emission will generally be considered an emission in the out of band domain. However, this frequency separation may be dependent on the type of modulation, the maximum symbol rate in the case of digital modulation, the type of transmitter, and frequency coordination factors. For example, in the case of some digital, broadband, or pulse modulated systems, the frequency separation may need to differ from the 250% factor.

The allowed out of band emissions limits are typically specified as spectrum emission masks or as adjacent channel power ratio levels. For instance, the CDL Ku-band emission spectrum mask described in [48] is shown in Figure 5.4.

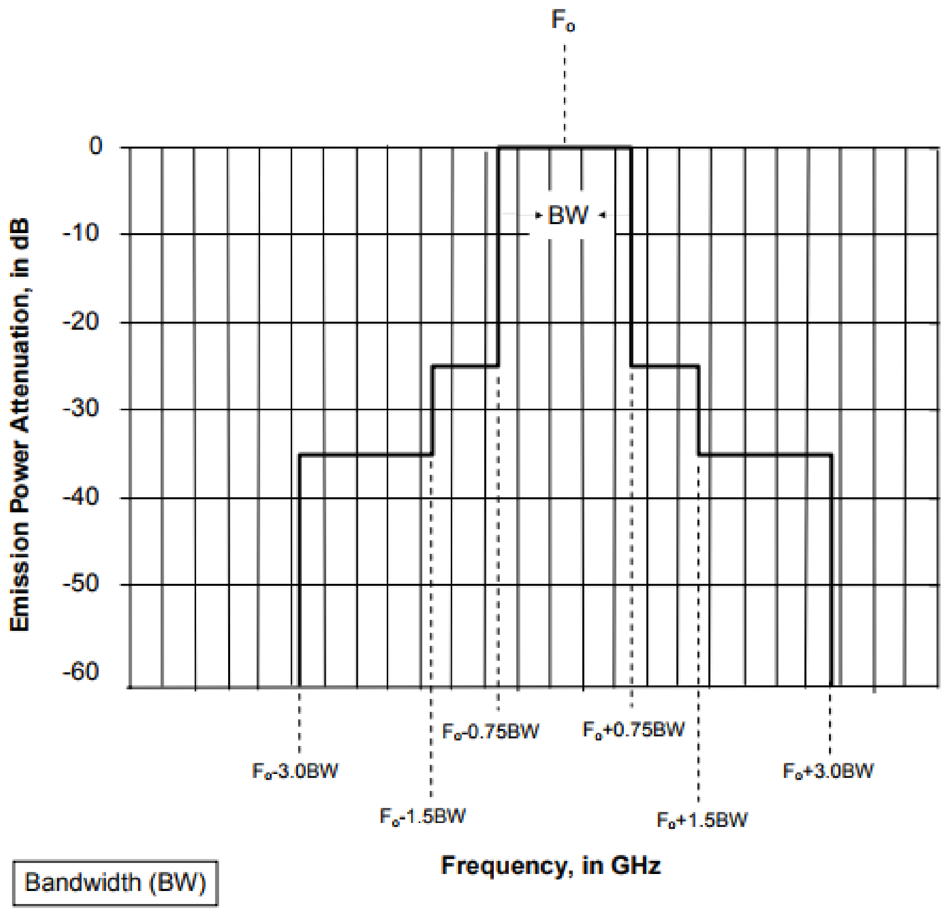

Figure 5.4 – CDL Ku-Band Emissions Spectrum Mask [48].

Likewise, Figure 5.5 shows the recommended out of band emissions attenuation for aeronautical-mobile transmitters other than aeronautical telemetry and exempted systems described in [35].

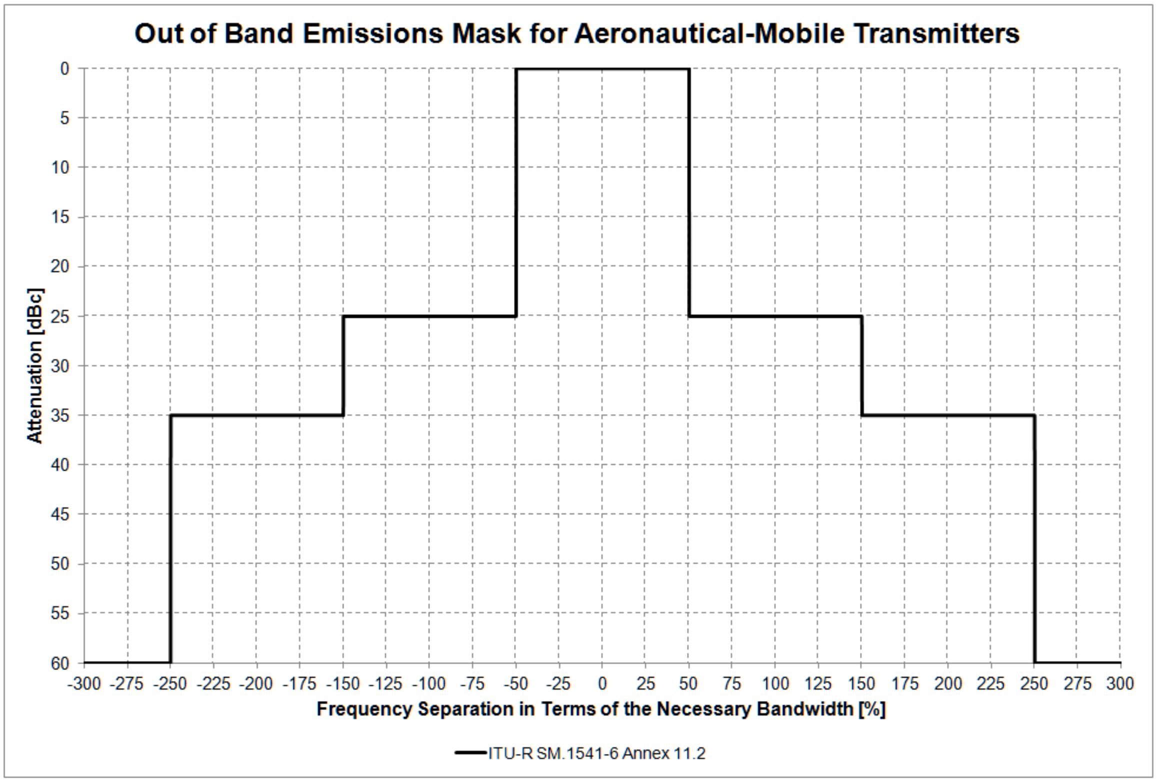

Figure 5.5 – Out of Band Emissions Mask for Aeronautical-Mobile Transmitters Other Than Aeronautical Telemetry and Exempted Systems from ITU-R SM.1541-6 (Annex 11.2).

A comparison between the emission masks in Figure 5.4 and Figure 5.5 reveals that the CDL mask is less stringent by allowing higher emission levels at frequency offsets that are ±50 to ±75 % and ± 250 to ±300 % away from the operating frequency.

Hence, the out of band emissions attenuation for aeronautical-mobile transmitters other than aeronautical telemetry and exempted systems recommended in ITU-R SM.1541-6 (Annex 11.2) is used to verify OoB emissions performance of the Tx Sub-Array.

Figure 5.6 shows the predicted Tx Sub-Array out of band emissions attenuation for a test case with a 10.71 Mbps pseudo random bit sequence, OQPSK modulation scheme, FEC rate equal to 1/2, RRC filter roll-off equal to 1, elevation scan angle equal to 0°, polarization tilt angle equal to 0°, frequency of operation equal to 14.0 GHz and RF input power level equal to 30 dBm. The predicted OoB emissions attenuation values comply with ITU-R SM.1541-6 (Annex 11.2) specification regarding aeronautical-mobile transmitters other than aeronautical telemetry and exempted systems. Furthermore, the margin achieved is larger than 20 dB over the spectrum adjacent to the necessary bandwith. Since all bits of the pseudorandom test pattern are transmitted using NRZ format they have exactly the same peak power. Furthermore, OQPSK is also a constant envelope modulation scheme as explained in Section 4.4. Hence, the only way to achieve such margin degradation are changing the RRC filter parameters, changing the modulation scheme or operating the amplifiers with input power levels beyond the required design values to cause amplifier saturation. All of these changes would impact the $PAPR$ of the modulated waveform.

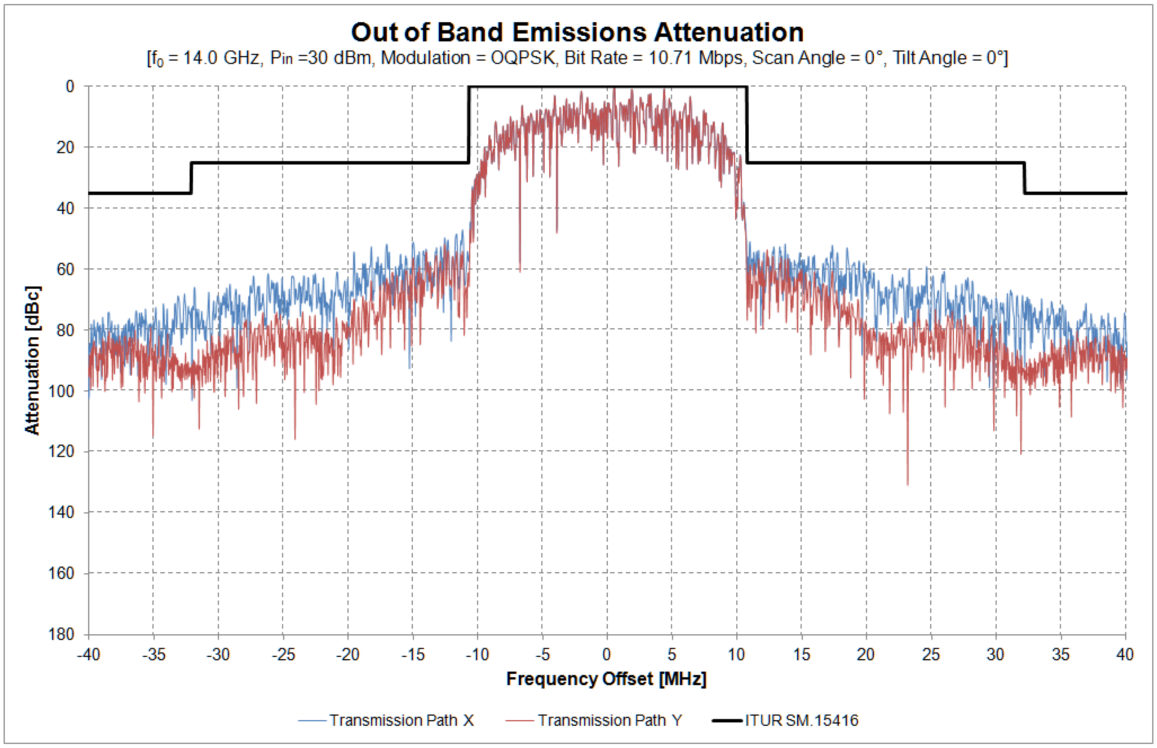

Figure 5.6 – Tx Sub-Array Out of Band Emissions Attenuation for a Test Case with a 10.71 Mbps Pseudo Random Bit Sequence, OQPSK modulation scheme, FEC Rate Equal to 1/2, RRC Filter Roll-Off Equal to 1, Elevation Scan Angle Equal to 0°, Polarization Tilt Angle Equal to 0°, Frequency of Operation Equal to 14.0 GHz and RF Input Power Level Equal to 30 dBm.

5.5 MODULATION ACCURACY

The performance requirements of modern satellite communication links are frequently specified in terms of their bit error rate (BER) or bit error probability (P_b). The BER of a digital communications link is the likelihood of receiving a transmitted bit incorrectly as defined in Eq. 5.3:

Eq. 5.3

$$BER = \frac{incorrectly\ received\ bits}{transmitted\ bits}$$

According to [49] the bit error rate of satellite communication links used for exploitation of UAV sensor data must be around 10^{-3} to 10^{-5} due to higher data correlation (i.e. MPEG-2 images) while the BER of command and control links must be around 10^{-6} to 10^{-9} to guarantee high reliability when flying over civil areas or during takeoff and landing procedures. Intelsat's "Satellite Link Budget" recommendation in [50] specifies the BER around 10^{-7} for legacy communication systems and around 10^{-9} for native IP links. Likewise, the recommendation in [51] specifies that acceptable bit error rates must be around 10^{-6} if communications security $(COMSEC)$ is implemented and around 10^{-8} if communications security is not implemented.

The analysis performed in [38] demonstrates that the bit error probability of OQPSK signals can be calculated with the expression in Eq. 5.4

Eq. 5.4

$$P_b = Q\left(\sqrt{2 \cdot \frac{E_b}{N_o}}\right) = \frac{1}{2} \cdot erfc\left(\sqrt{\frac{E_b}{N_o}}\right)$$

where E_b is the energy per bit and N_o is the noise power spectral density.

Figure 5.7 shows the bit error probability curve for OQPSK modulation scheme.

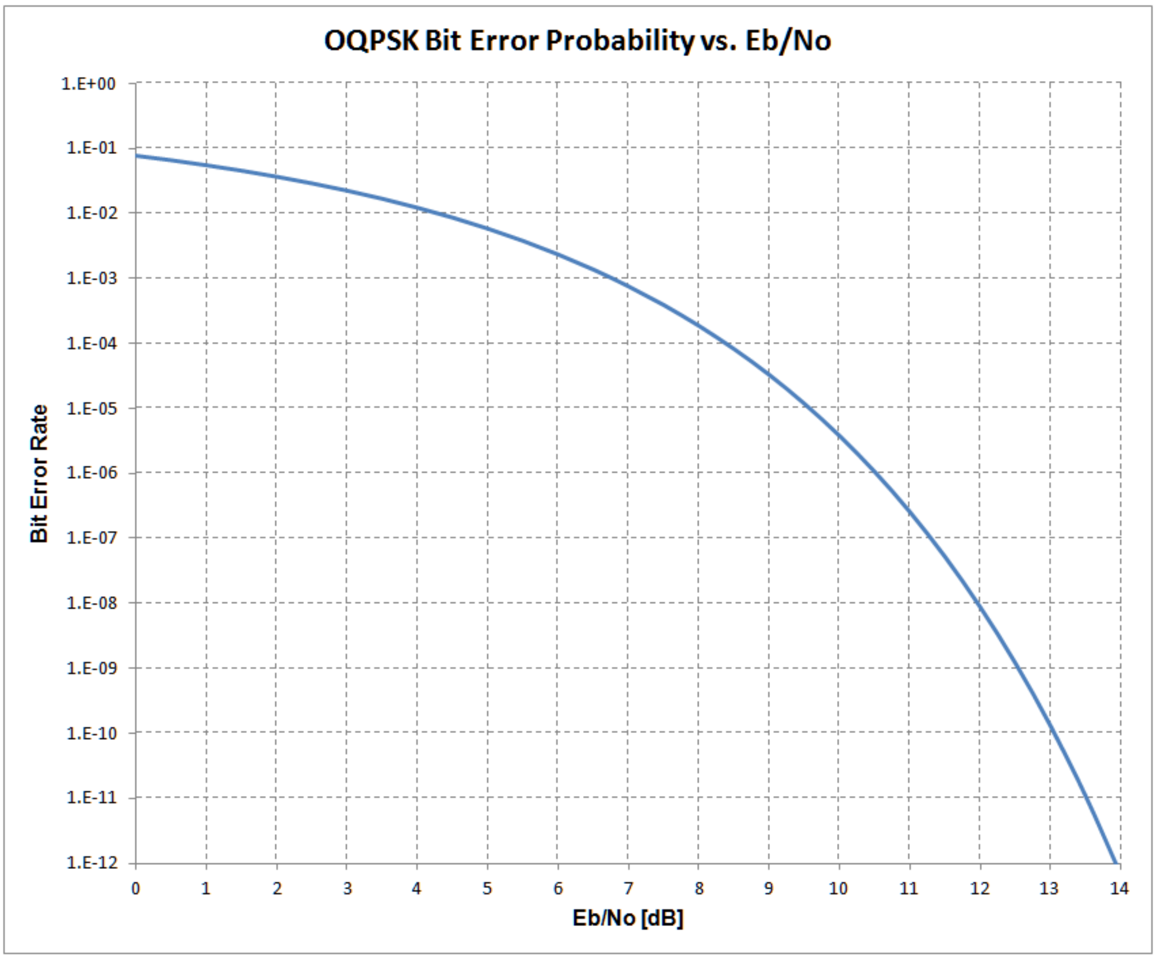

Figure 5.7 – Bit Error Probability Curve for OQPSK modulation scheme.

The signal to noise power ratio (SNR) parameter in [52] is expressed in terms of the bit energy to noise power density ratio (E_b/N_o) as shown in Eq. 5.5

Eq. 5.5

$$SNR = \frac{E_b}{N_o \cdot B \cdot T_b} = \frac{E_s}{N_o \cdot B \cdot T_s} = \frac{E_b \cdot \log_2 M}{N_o \cdot B \cdot T_s}$$

where B is the bandwidth of the complex envelope of the modulated waveform, T_b is the bit time, E_s is the energy per symbol, M is the order of the PSK digital modulation and T_s is the symbol time.

Furthermore, Eq. 5.5 and Eq. 5.6 can be combined to express the bit error probability (P_b) in terms of the signal to noise power ratio (SNR) as shown in Eq. 5.6.

Eq. 5.6

$$P_b = \frac{1}{2} \cdot erfc\left(\sqrt{\frac{E_b}{N_o}}\right) = \frac{1}{2} \cdot erfc\left(\sqrt{SNR \cdot \frac{B \cdot T_s}{\log_2 M}}\right)$$

Conversely, Eq. 5.7 shows the relationship between the error vector magnitude (EVM) and the signal to noise power ratio (SNR).

Eq. 5.7

$$SNR = \frac{1}{EVM^2}$$

Hence, the EVM can be related to the bit error probability of the modulated waveform through the signal to noise power ratio term in Eq. 5.6 and Eq. 5.7.

The Eq. 5.8 shows the relationship between the bit error probability (P_b) and the EVM.

Eq. 5.8

$$P_b = \frac{1}{2} \cdot erfc\left(\sqrt{\frac{E_b}{N_o}}\right) = \frac{1}{2} \cdot erfc\left(\sqrt{\frac{1}{EVM^2} \cdot \frac{B \cdot T_s}{\log_2 M}}\right)$$

The maximum system error vector magnitude $\left(EVM_{system\_max}\right)$ allowed to achieve a given maximum bit error probability (P_{b_max}) can be estimated using Eq. 5.9.

Eq. 5.9

$$EVM_{system\_max} = \sqrt{\frac{B \cdot T_s}{\left[erfc^{-1}\left(2 \cdot P_{b\_max}\right)\right]^2 \cdot \log_2 M}}$$

Table 5.2 shows the estimated maximum system error vector magnitude values assuming the target maximum bit error probability equal to 10^{-9}.

Waveform	Modulation Scheme	Bit Error Probability	Eb / No [dB]	SNR [dB]	EVM_{system_max} [%]
BR-10.71	OQPSK	1.E-09	12.550	12.550	23.579

Table 5.2 – Maximum System Error Vector Magnitude.

According to [26] the error vector magnitude due to non-linearity of a transmitter can be estimated using the expression in Eq. 5.10

Eq. 5.10

$$EVM_{lin} = 10^{\left[\frac{2 \cdot P_S - 2 \cdot OIP_3 + 6 + 10\log_{10}\left(\frac{3}{8}\right)}{20}\right]}$$

where P_s is the transmitter's saturation output power and OIP_3 is the output third order intercept point.

Assuming that non-linearity is the only contributor to Tx Sub-Array modulation symbol errors then the expression in Eq. 5.11 can be used to estimate the maximum error vector magnitude caused by the Tx Sub-Array $\left(EVM_{\_tx\_sub\_array\_max}\right)$.

Eq. 5.11

$$EVM_{\_tx\_sub\_array\_max} = EVM_{lin}$$

Table 5.3 shows the estimated maximum Tx Sub-Array error vector magnitude value assuming a bit error probability (P_b) equal to 10^{-9}.

Ps [dBm]	OIP3 [dBm]	EVM_lin [%]	EVM_tx_sub_array_max [%]
32.86	42.07	14.65	14.65

Table 5.3 – Maximum Tx Sub-Array Error Vector Magnitude.

The maximum CDL transmitter error vector magnitude $\left(EVM_{\_cdl\_transmitter\_max}\right)$ allowed to achieve a given bit error probability can be estimated using Eq. 5.12.

Eq. 5.12

$$EVM_{\_cdl\_transmitter\_max} = \sqrt{\left(EVM_{\_system\_max}\right)^2 - \left(EVM_{\_tx\_sub\_array\_max}\right)^2}$$

Table 5.4 shows the estimated maximum CDL transmitter error vector magnitude $\left(EVM_{\_cdl\_transmitter\_max}\right)$ values assuming the target maximum bit error probability $(\mathrm{P_b})$ equal to 10^{-9}.

Waveform	Modulation Scheme	Bit Rate [Mbps]	RRC Filter Roll-Off	FEC Rate	Bit Error Probability	EVM_system_max [%]	EVM_tx_sub_array_max [%]	EVM_cdl_transmitter_max [%]
BR-10.71	OQPSK	10.71	1	1/2	1.E-09	23.58	14.65	18.48

Table 5.4 – Maximum CDL Transmitter Error Vector Magnitude.

The worst case system error vector magnitude $\left(EVM_{\_system}\right)$ can be predicted using the expression in Eq. 5.13.

Eq. 5.13

$$EVM_{\_system} = \sqrt{\left(EVM_{\_cdl\_transmitter\_max}\right)^2 + \left(EVM_{\_tx\_sub\_array}\right)^2}$$

where $EVM_{tx\_sub\_array}$ is the Tx Sub-Array error vector magnitude predicted by the envelope analysis in section 4.5.

Table 5.5 shows the predicted worst case system error vector magnitude values assuming the target maximum bit error probability equal to 10^{-9}.

Waveform	Modulation Scheme	Transmission Path	EVM_cdl_transmitter_max [%]	EVM_tx_sub_array [%]	EVM_system [%]
BR-10.71	OQPSK	X	18.476	0.383	18.480
BR-10.71	OQPSK	Y	18.476	0.060	18.476

Table 5.5 – Worst Case System Error Vector Magnitude.

Furthermore, the actual bit error probability (P_b) can be predicted using the expression shown in Eq. 5.14.

Eq. 5.14

$$P_b = \frac{1}{2} \cdot erfc\left(\sqrt{\frac{E_b}{N_o}}\right) = \frac{1}{2} \cdot erfc\left(\sqrt{\frac{1}{\left(EVM_{\_system}\right)^2} \cdot \frac{B \cdot T_s}{\log_2 M}}\right)$$

Figure 5.8 shows the predicted bit error probability (P_b) for a test case with a 10.71 Mbps pseudo random bit sequence, OQPSK modulation scheme, FEC rate equal to 1/2, RRC filter roll-off equal to 1, elevation scan angle equal to 0°, polarization tilt angle equal to 0°, frequency of operation equal to 14.0 GHz and RF input power level equal to 30 dBm. The predicted average bit error probability (P_b) values for the 10.71 Mbps OQPSK waveform are 9.84×10^{-15} at Transmission Path X and 9.72×10^{-15} at Transmission Path Y. Both values comply with Intelsat's recommendation $(BER \leq 10^{-9})$ regarding native IP links in [50].

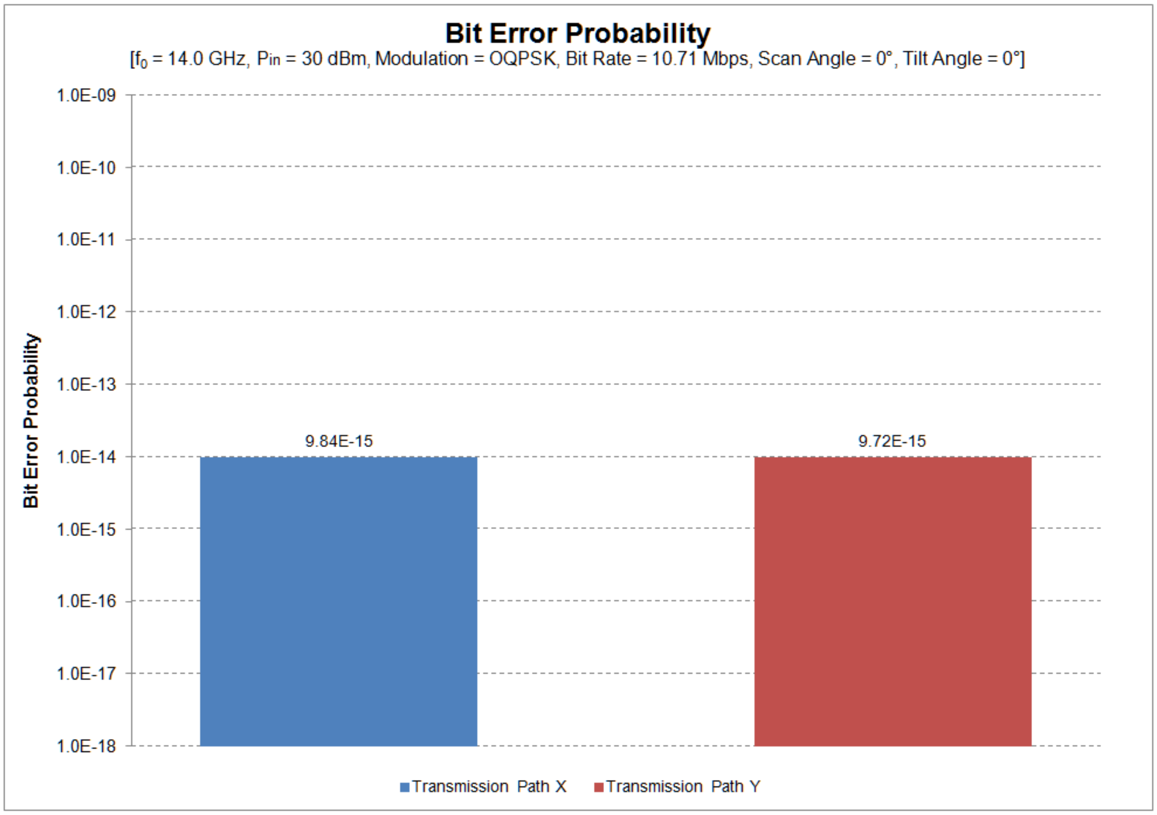

Figure 5.8 – Bit Error Probability for a Test Case with a 10.71 Mbps Pseudo Random Bit Sequence, OQPSK modulation scheme, FEC Rate Equal to 1/2, RRC Filter Roll-Off Equal to 1, Elevation Scan Angle Equal to 0°, Polarization Tilt Angle Equal to 0°, Frequency of Operation Equal to 14.0 GHz and RF Input Power Level Equal to 30 dBm.

5.6 POLARIZATION ACCURACY

In the most general sense the polarization of any transverse electromagnetic plane wave might be characterized using the same terms as for an ellipse. Hence, the axial ratio (AR) can be used to characterize shape of the polarization locus of any transverse electromagnetic plane wave.

The axial ratio of an ellipse is defined in Eq. 5.15 as the ratio between the amplitude of its major axis $\left(v_\xi\right)$ to the amplitude of its minor axis $\left(v_\eta\right)$ as shown in Figure 4.30.

Eq. 5.15

$$AR = \pm\frac{v_\xi}{v_\eta}$$

For instance, the shape of a linearly polarized locus is determined by an axial ratio that approaches infinity ($AR = \infty$) while the shape of a circularly polarized locus is determined by an axial ratio that approaches unity ($AR = 1$).

The shape of the polarization locus, its sense of rotation and its tilt angle are determined by the time - harmonic electric field vector component amplitude ratio (v_y/v_x) and the phase difference δ previously defined in Eq. 4.21. Both of these parameters are directly related to the performance of the proposed Tx Sub-Array design. Hence, it makes perfect sense to develop a simulation model that considers these parameters.

The expression in Eq. 5.16, derived from the set of equations in [44], defines axial ratio in terms of the time - harmonic electric field vector component amplitude ratio and the phase difference (δ).

Eq. 5.16

$$AR = \frac{1}{\tan\left(\frac{\sin^{-1}\left(\sin\left(2\tan^{-1}\left(\frac{v_y}{v_x}\right)\right)\sin(\delta)\right)}{2}\right)}$$

Likewise, the polarization tilt angle (ψ) can be estimated using the expression in Eq. 5.19.

Eq. 5.17

$$\psi = \frac{\frac{\pi}{2} - \delta}{2}$$

The antenna polarization specification in [46] requires the use of linear polarization with a minimum voltage axial ratio of $26\ dB$ for Ku-band systems using antennas with diameters smaller or equal to $2.5\ m$ for transmission in the direction of the satellite.

The axial ratio of selected polarization states can be estimated using Eq. 5.16 and the output voltage phasors from the linear AC analysis performed in section 4.6. Figure 5.9 shows the predicted Tx Sub-Array polarization axial ratio values for selected polarization states with elevation scan angle (θ) equal to 0°, frequency of operation equal to 14.0 GHz and RF input power level equal to 30 dBm. The predicted polarization axial ratio (AR) values partially comply with MIL-STD-188-164B specification $(AR \geq$

$26\ dB$) regarding linear polarization axial ratio for Ku-band systems using antennas with diameters smaller or equal to $2.5\ m$. The predicted average axial ratio (AR) value is $32.00\ dB$.

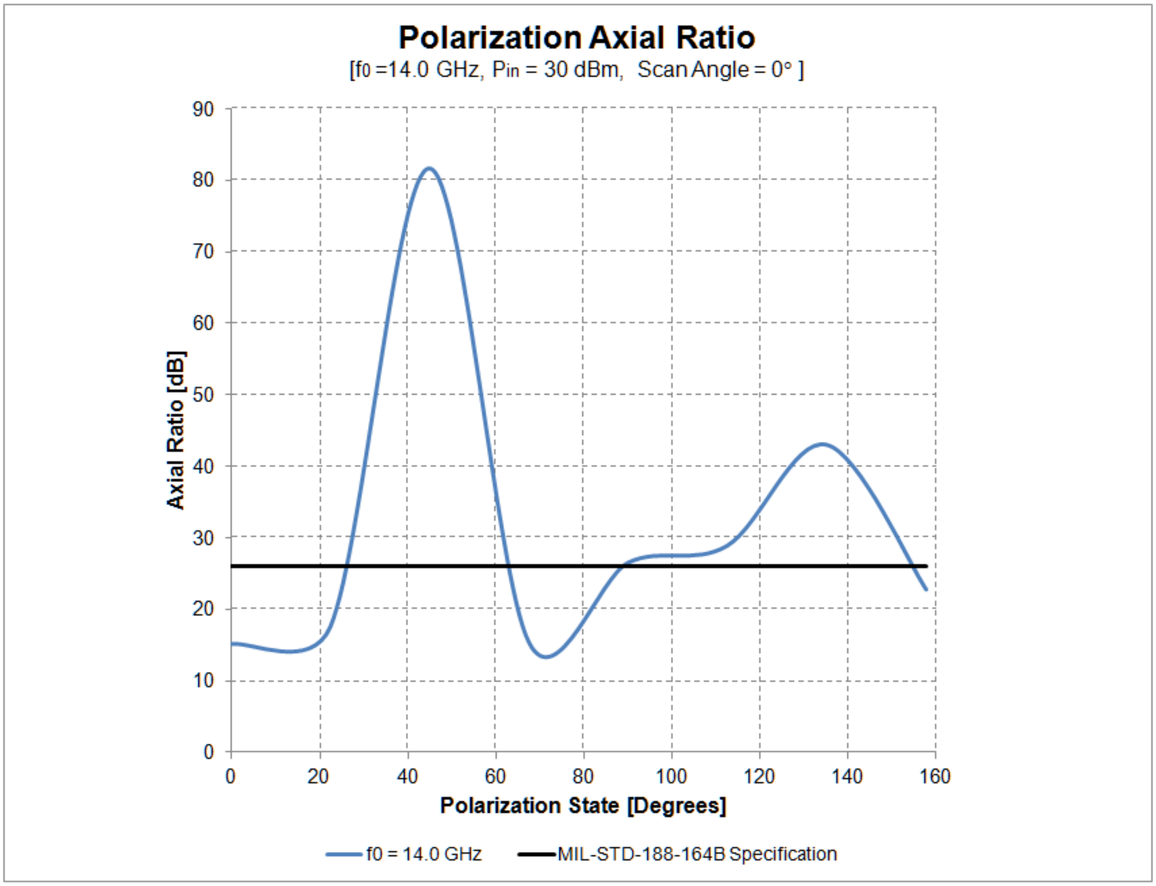

Figure 5.9– Tx Sub-Array Polarization Axial Ratio for Selected Polarization States with Elevation Scan Angle Equal to 0°, Frequency of Operation Equal to 14.0 GHz and RF Input Power Level Equal to 30 dBm.

Figure 5.10 shows the predicted Tx Sub-Array polarization tilt angle (ψ) values for selected polarization states with elevation scan angle (θ) equal to 0°, frequency of operation equal to 14.0 GHz and RF input power level equal to 30 dBm. The predicted tilt angle values reveal a highly linear behavior with maximum absolute tilt angle error of 3.10° and mean absolute tilt angle error of 0.99°.

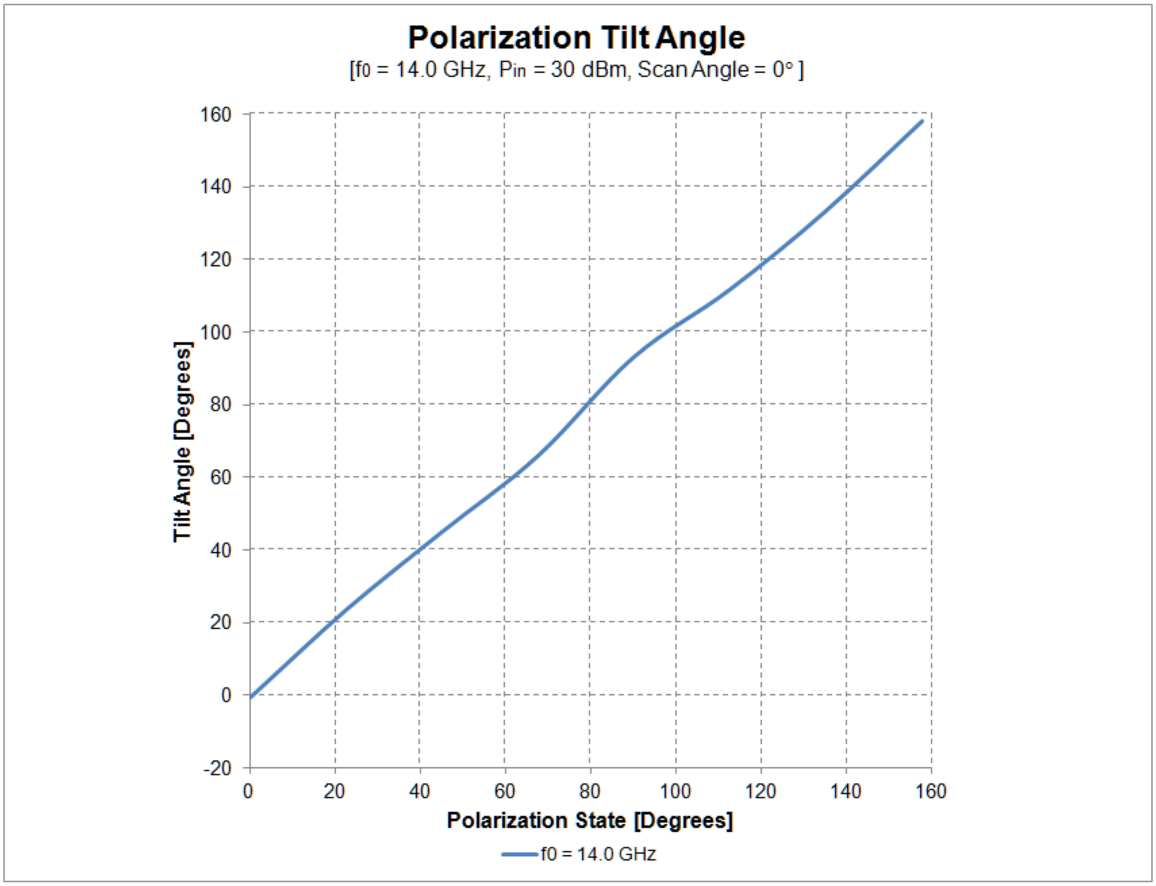

Figure 5.10 – Tx Sub-Array Polarization Tilt Angle for Selected Polarization States with Elevation Scan Angle Equal to 0°, Frequency of Operation Equal to 14.0 GHz and RF Input Power Level Equal to 30 dBm.

The polarization mismatch loss can be estimated using the predicted tilt angle error values and Eq. 5.20.

Eq. 5.18

$$PML_{dB} = -10\log_{10}\left(\left|\cos\left(\psi_{error}\right)\right|^{2}\right)$$

where PML_{dB} is the polarization mismatch loss in dB units and ψ_{error} is the polarization tilt angle error.

The predicted $polarization\ mismatch\ loss$, assuming the $maximum\ absolute\ tilt\ angle\ error$, is equal to $0.01\ dB$.

5.6.1 Polarization Accuracy Root Cause Analysis

A theoretical model might result really useful to understand the influence of amplitude and phase errors on polarization axial ratio of the proposed beamformer sub-array design. The expressions for the ideal time - harmonic electric field vector component ratio (v_y/v_x) and the ideal phase difference (δ) of the proposed beamformer design might be modified with an amplitude disturbance term $(1 - v_{error})$ and a phase disturbance term (ϕ_{error}) as shown in Eq. 5.17 and Eq. 5.18.

Eq. 5.19

$$\frac{v_y}{v_x} = \frac{\left|(1 - v_{error}) \cdot e^{j\left(\phi_{y_0} + \phi_{error} + \pi\right)} + e^{j\left(\phi_{x_0} - \frac{\pi}{2}\right)}\right|}{\left|(1 - v_{error}) \cdot e^{j\left(\phi_{y_0} + \phi_{error} - \frac{\pi}{2}\right)} + e^{j\left(\phi_{x_0} + \pi\right)}\right|}$$

Eq. 5.20

$$\delta = angle\left((1 - v_{error}) \cdot e^{j\left(\phi_{y_0} + \phi_{error} + \pi\right)} + e^{j\left(\phi_{x_0} - \frac{\pi}{2}\right)}\right) - angle\left((1 - v_{error}) \cdot e^{j\left(\phi_{y_0} + \phi_{error} - \frac{\pi}{2}\right)} + e^{j\left(\phi_{x_0} + \pi\right)}\right)$$

Likewise, Eq. 5.19 and Eq. 5.20 can replace their corresponding terms in Eq. 5.16 to obtain a theoretical model for analysis of the influence of amplitude and phase errors on polarization axial ratio. The theoretical curves in Figure 5.11 show that polarization axial ratio suffers severe degradation due to amplitude errors. The phase errors cause a much smaller degree of degradation that is just visible when the amplitude error term is equal to zero.

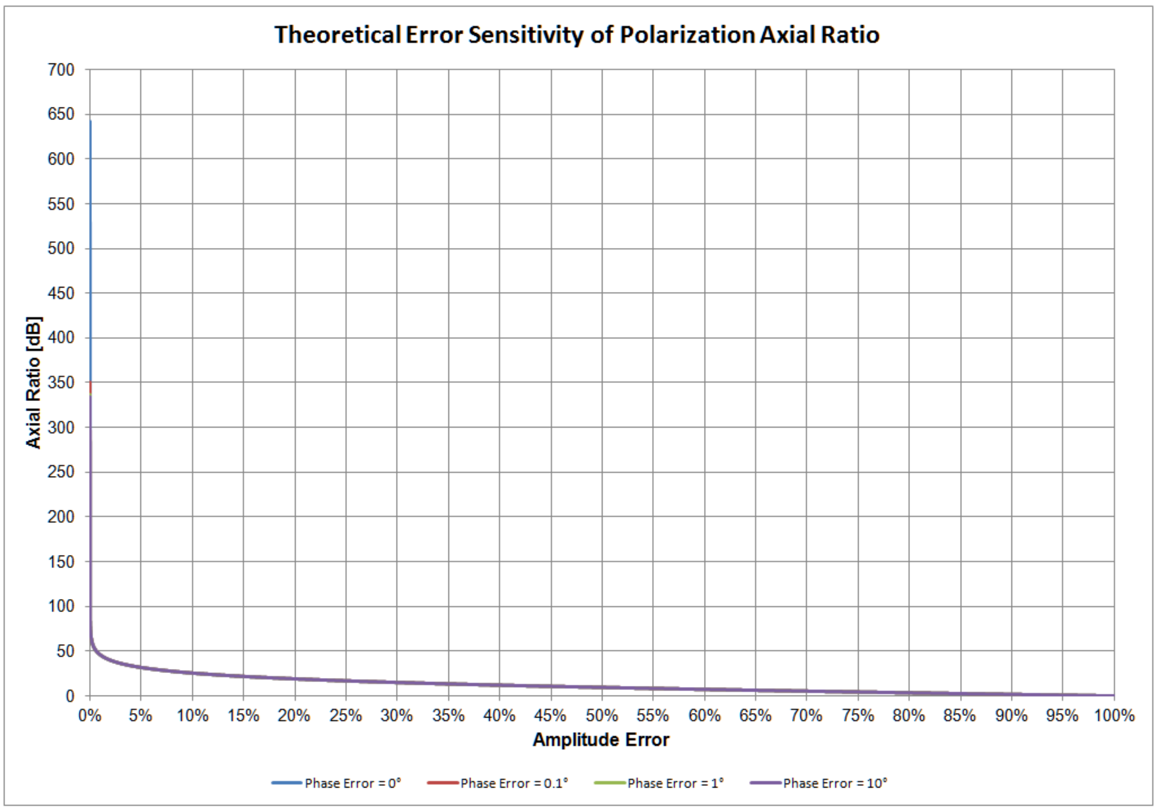

Figure 5.11 – Theoretical Error Sensitivity of Polarization Axial Ratio.

Amplitude errors are typically classified as insertion losses, insertion gains and/or impedance mismatch losses. The insertion losses are mainly caused by resistivity, surface roughness, and impurities of the conductors employed in the design and implementation of microwave circuits. Conversely, the impedance mismatch losses are caused by the differences in the impedances of connected ports between cascaded microwave circuit components. Figure 5.12 shows the magnitude of the amplitude imbalance between transmission paths due to amplitude errors through the Tx Sub-Array components.

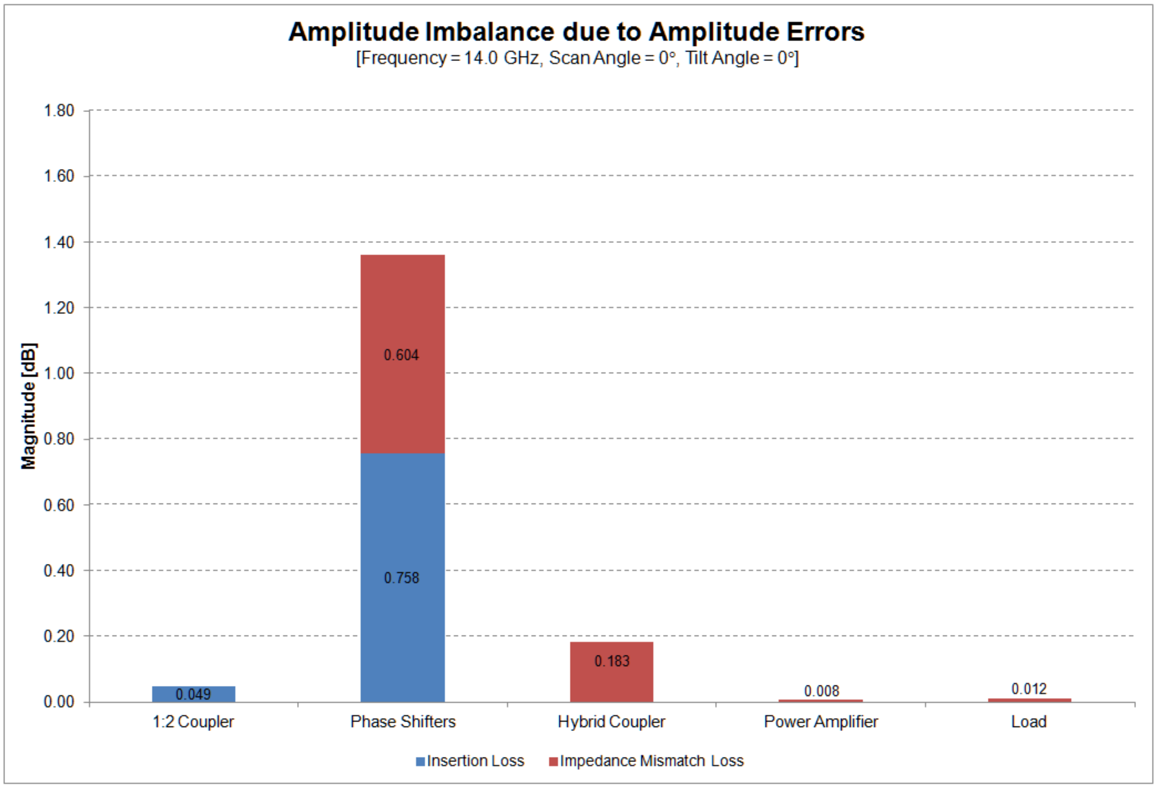

Figure 5.12 – Amplitude Imbalance due to Amplitude Errors through the Tx Sub-Array Components.

In this case, the highest extent of polarization axial ratio performance degradation was predicted at the interconnection between the output ports of the phase shifters and the input ports of the hybrid coupler. Hence, the implementation of amplitude compensation must be considered in future Tx Sub-Array design revisions. Figure 5.13 shows the degradation of polarization axial ratio performance through the Tx Sub-Array's components.

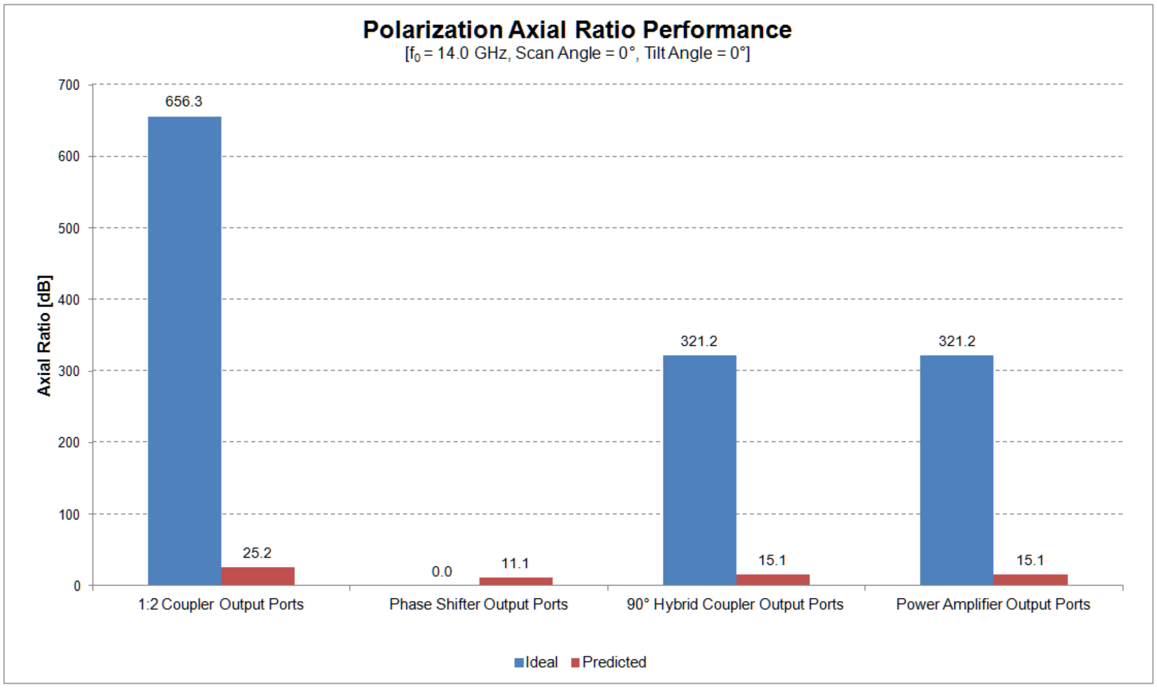

Figure 5.13 – Amplitude Imbalance due to Amplitude Errors through the Tx Sub-Array Components.

The implementation of amplitude compensation can be achieved by the inclusion of variable attenuators and/or variable gain amplifiers. Variable gain amplifiers introduce less noise than variable attenuators. However, variable gain amplifiers require re-design of power supply, digital control and thermal management solutions.

Also, variable gain amplifiers require certain power back-off to mitigate non-linear effects that might appear during the transmission of complex modulation waveforms used in Ku-band satellite communications links. Hence, variable attenuators are presented as the most practical solution for the implementation of amplitude compensation in future Tx Sub-Array design revisions. Figure 5.14 shows the recommended microwave circuit architecture for the Tx Sub-Array now with a variable attenuator in each of its transmission paths.

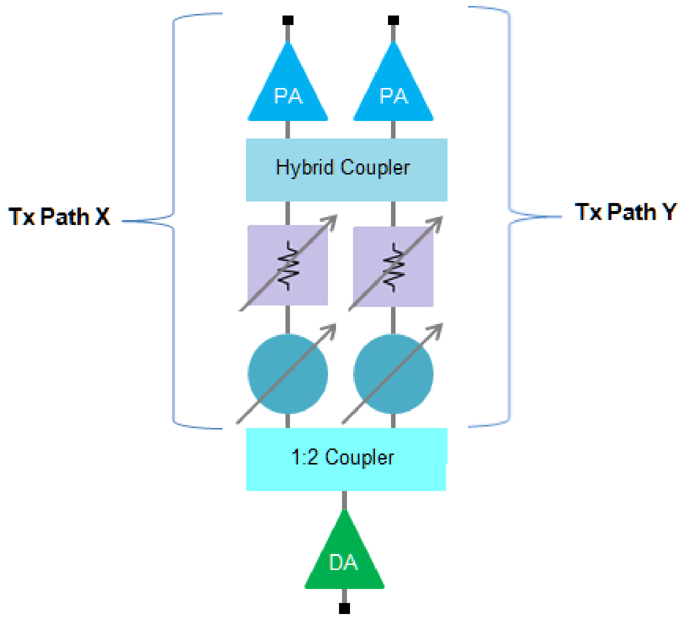

Figure 5.14 – Recommended Microwave Circuit Architecture for the Tx Sub-Array.

The addition of variable attenuators between phase shifters and hybrid couplers increases the length of the microwave circuuit layout by only 2.34 mm while it provides certain improvement to the impedance match issues caused by variable phase shifters. Figure 5.15 shows the microwave circuit layout for the recommended Tx BFN Module design.

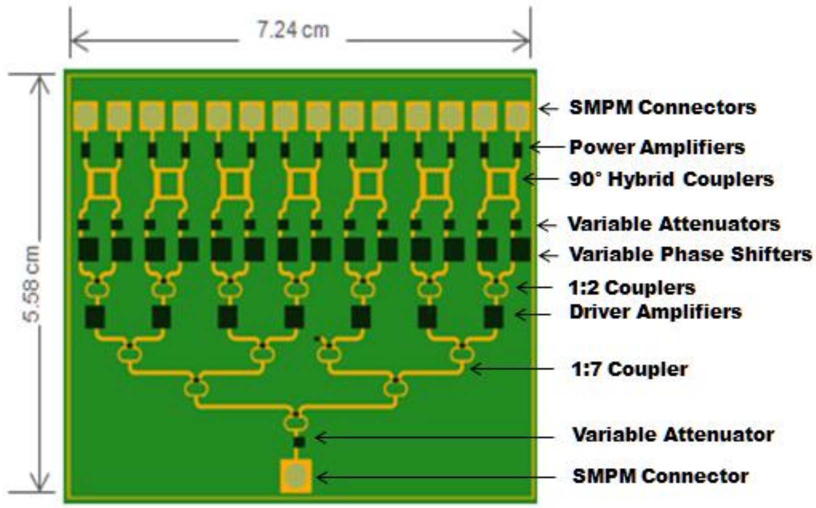

Figure 5.15 – Microwave Circuit Layout of the recommended Tx BFN Module design.

Figure 5.16 shows the newly predicted Tx Sub-Array polarization loci for selected polarization states with elevation scan angle equal to 0°, frequency of operation equal to 14.0 GHz and RF input power level equal to 30 dBm.

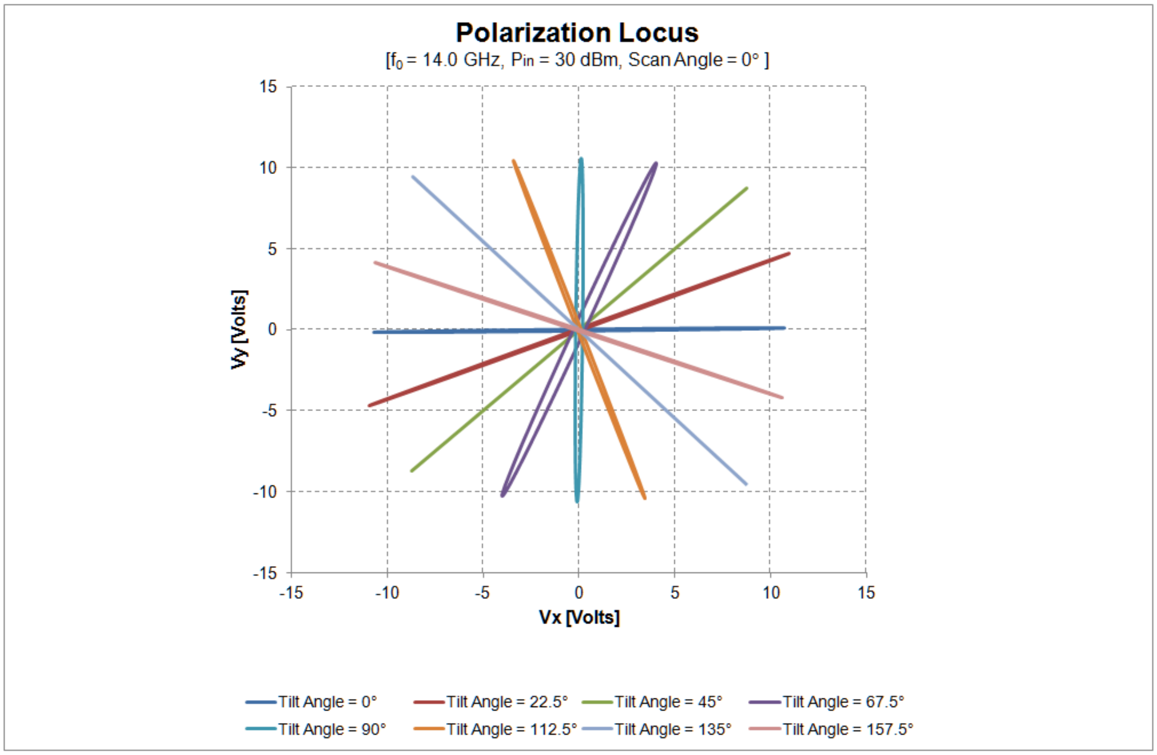

Figure 5.16 – Predicted Tx Sub-Array Polarization Loci for Selected Polarization States with Elevation Scan Angle Equal to 0°, Frequency of Operation Equal to 14.0 GHz and RF Input Power Level Equal to 30 dBm.

Figure 5.17 shows the newly predicted Tx Sub-Array axial ratio values for selected polarization states with elevation scan angle equal to 0°, frequency of operation equal to 14.0 GHz and RF input power level equal to 30 dBm.

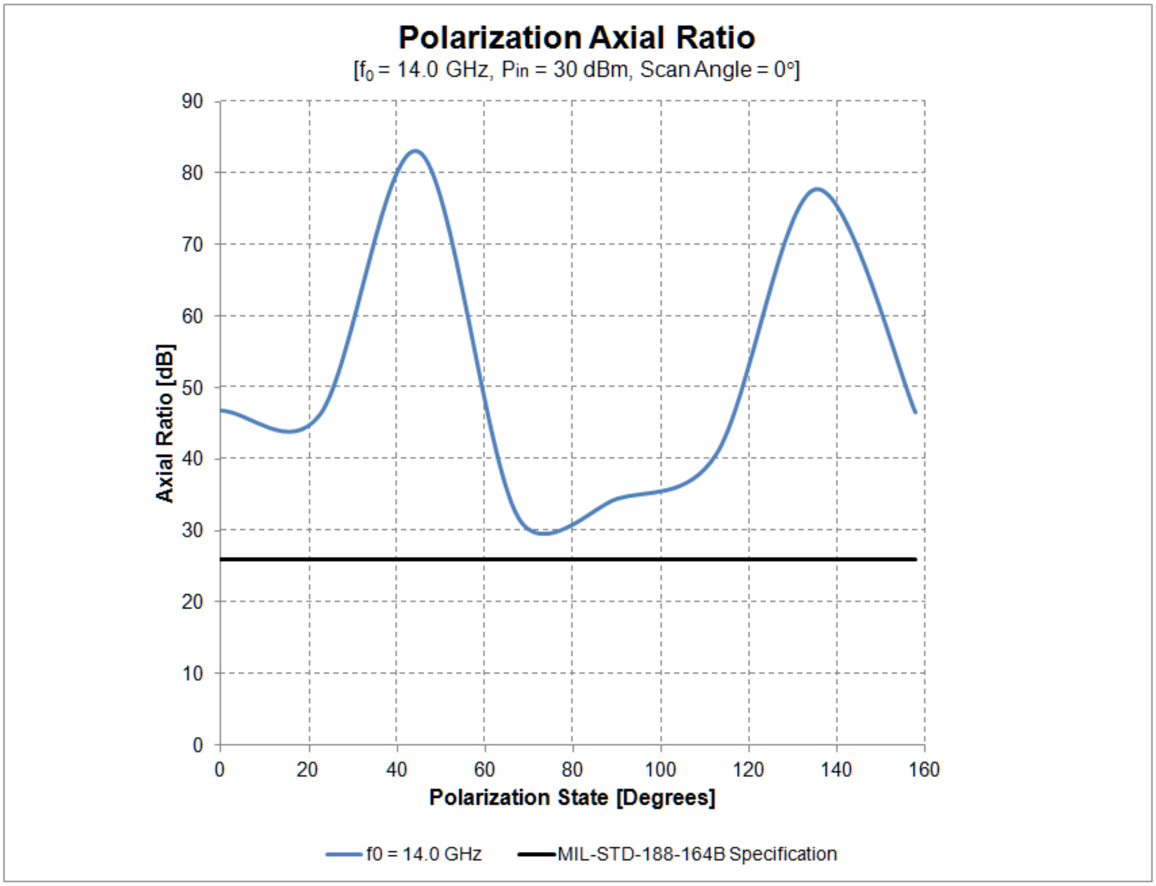

Figure 5.17 – Predicted Tx Sub-Array Axial Ratio for Selected Polarization States with Elevation Scan Angle Equal to 0°, Frequency of Operation Equal to 14.0 GHz and RF Input Power Level Equal to 30 dBm.

The newly predicted Tx Sub-Array polarization axial ratio values fully comply with MIL-STD-188-164B specification $(AR \geq 26\ dB)$ regarding linear polarization voltage axial ratio for Ku-band systems using antennas with diameters smaller or equal to 2.5 m. The newly predicted average axial ratio value is 51.60 dB.

Figure 5.18 shows the newly predicted Tx Sub-Array polarization tilt angle (ψ) values for selected polarization states with elevation scan angle equal to 0°, frequency of operation equal to 14.0 GHz and RF input power level equal to 30 dBm.

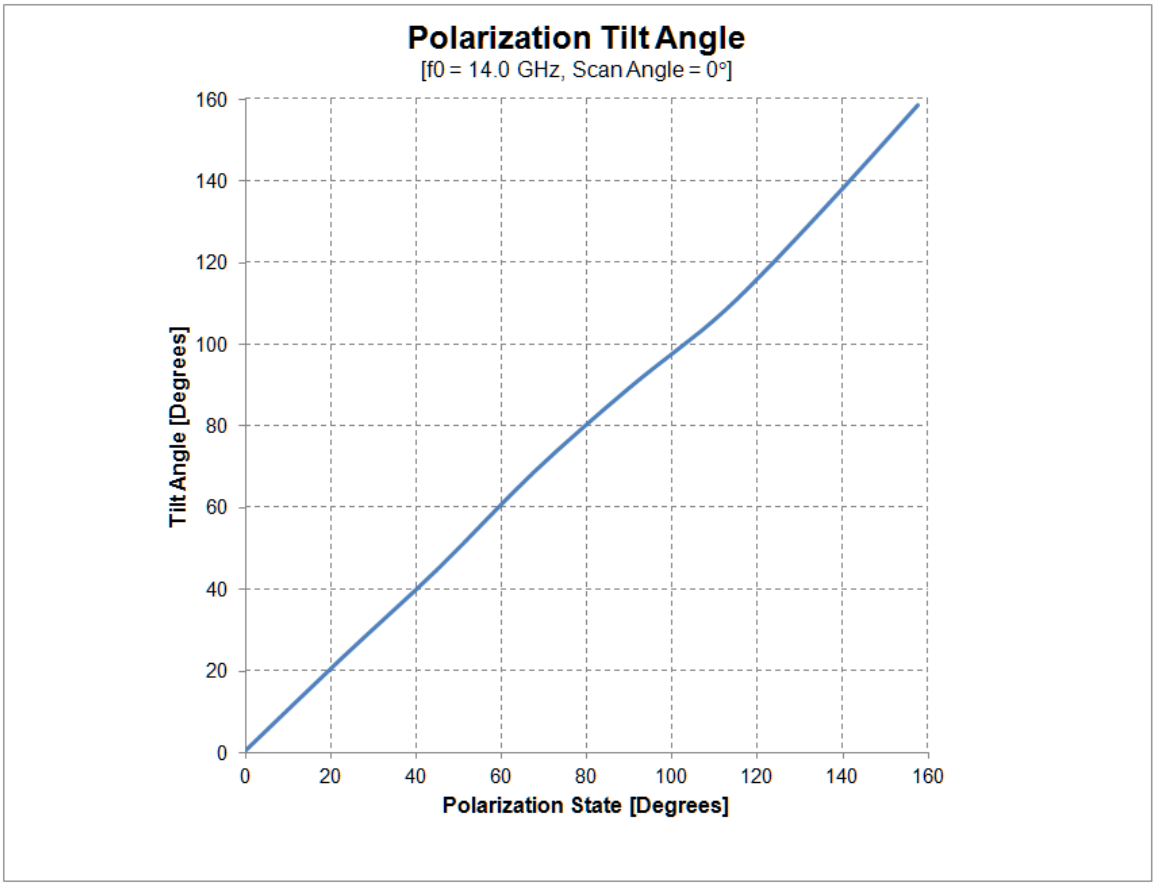

Figure 5.18 – Predicted Tx Sub-Array Polarization Tilt Angle for Selected Polarization States with Elevation Scan Angle Equal to 0°, Frequency of Operation Equal to 14.0 GHz and RF Input Power Level Equal to 30 dBm.

The newly predicted Tx Sub-Array tilt angle values reveal a highly linear behavior with $maximum\ absolute\ tilt\ angle\ error$ of 4.16° , *mean absolute tilt angle error* of 1.13° and *polarization mismatch loss* equal to 0.02 dB.

Conversely, Figure 5.19 shows the newly predicted bit error probability for a test case with a 10.71 Mbps pseudo random bit sequence, OQPSK modulation scheme, FEC rate equal to 1/2, RRC filter roll-off equal to 1, elevation scan angle equal to 0°, polarization tilt angle equal to 0°, frequency of operation equal to 14.0 GHz and RF input power level equal to 30 dBm.

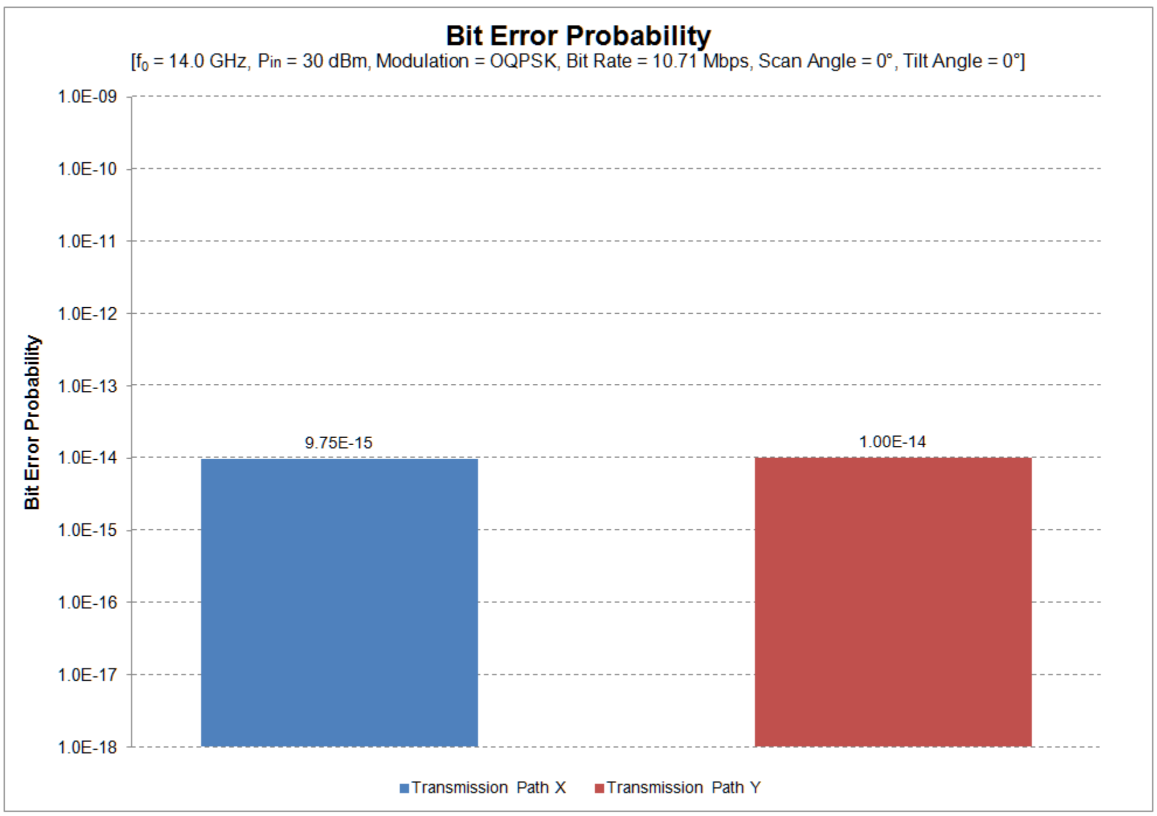

Figure 5.19 – Predicted Bit Error Probability for a Test Case with a 10.71 Mbps Pseudo Random Bit Sequence, OQPSK modulation scheme, FEC Rate Equal to 1/2, RRC Filter Roll-Off Equal to 1, Elevation Scan Angle Equal to 0°, Polarization Tilt Angle Equal to 0°, Frequency of Operation Equal to 14.0 GHz and RF Input Power Level Equal to 30 dBm.

The newly predicted average bit error probability values for the 10.71 Mbps OQPSK waveform are 9.75×10^{-15} at Transmission Path X and 1.00×10^{-14} at Transmission Path Y. No significant degradation of the average bit error probability is observed by the addition of variable attenuators to the Tx Sub-Array architecture while the performance of both transmission paths still comply with Intelsat's recommendation ($BER \leq 10^{-9}$) regarding native IP links in [50].

Dynamic control of variable attenuator states could be achieved with the implementation of the microwave power sensor interface circuit shown in Figure 5.20. The circuit is composed of two multiplexed analog to digital converters (ADCs) and two buffer operational amplifiers ICs. The main function of this circuit is to acquire and digitize the microwave power sensor signals generated by power amplifier MMICs of each Tx BFN Module. This feedback enables the required "closed loop" power control that continuously helps maximizing the polarization axial ratio of each Tx Sub-Array.

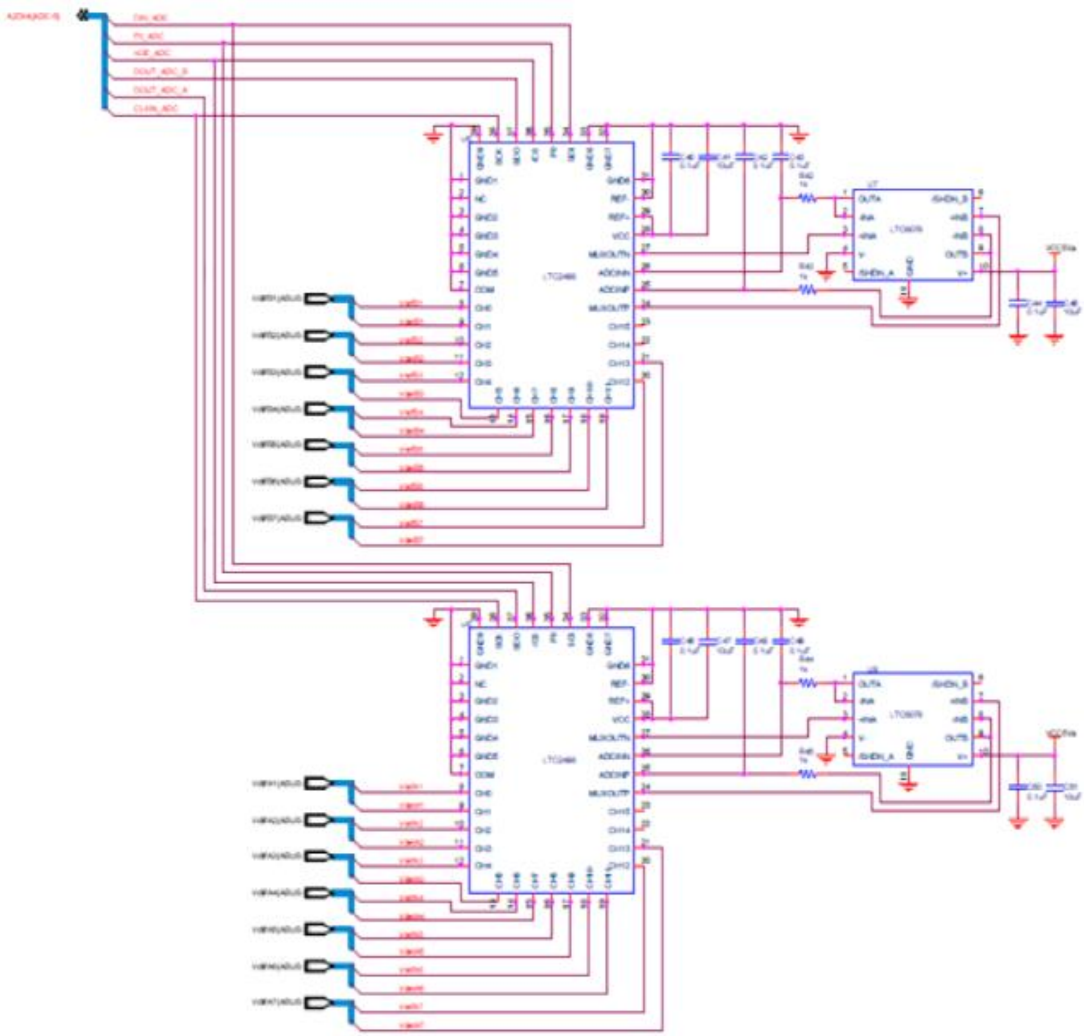

Figure 5.20 – Tx BFN Module Microwave Power Sensor Interface Circuit

6 CONCLUSIONS

The market outlook for upgrade, expansion and new acquisition of military UAS looks very optimistic. The expected market growth during the next eighteen years will open the door for the introduction and development of newer and more efficient antenna system technologies like flat panel hybrid steerable phased array antennas.

The proposed Tx Sub-Array design provides a fundamental unit cell that enables the development of a Ku band Tx BFN Module that minimizes the risks of fabrication errors, simplifies operation & maintenance tasks and provides roll-out flexibility for future Ku band phased array antenna system developments.

According to simulation results the overall performance of the proposed "Design of a Polarization Adaptive Beamforming Transmitter Sub-Array for Beyond Line of Sight Satellite Communications in Unmanned Aircraft Systems" meets relevant requirements of key commercial, military and industrial standard specifications available to the general public as unclassified or declassified information. This indicates that it is feasible to develop a Tx Sub-Array that meets the given set of technical requirements using "commercial off the shelf" MMICs and microstrip line structures.

However, it was also observed that the predicted polarization axial ratio performance partially complies with MIL-STD-188-164B standard specifications regarding amplitude variations of the transmission uplink function and linear polarization axial ratio for Ku-band systems using antennas with diameters smaller or equal to $2.5\ m$.

The theoretical model developed as part of this research project confirmed that the polarization axial ratio performance suffers severe degradation mainly caused by the introduction of amplitude errors. Also, it was observed that the introduction of phase errors caused a much smaller degree of degradation that was just visible when the amplitude error term was equal to zero.

The highest extent of polarization axial ratio degradation was predicted at the interconnection between the output ports of the phase shifters and the input ports of the hybrid coupler. Hence, variable attenuators were presented as the most practical solution to enable the required amplitude compensation to mitigate the effects of amplitude errors on gain ripple and polarization axial ratio performance.

Improved Tx Sub-Array's polarization axial ratio performance was observed after the introduction of variable attenuators between output ports of the phase shifters and the input ports of the hybrid coupler. For instance, the predicted average value increased from $32.00\ dB$ to $51.60\ dB$. Hence, full compliance with MIL-STD-188-164B standard specification regarding linear polarization voltage axial ratio for Ku-band systems using antennas with diameters smaller or equal to $2.5\ m$ was also achieved at all tested polarization states while no significant impact to the Tx Sub-Array's circuit layout or its modulation accuracy performance.

REFERENCES

[1] J. Glaneueski, M. Strout, "Unmanned Aircraft System (UAS) Service Demand 2015-2035: Literature Review and Projections of Future Usage, Version 0.1",Volpe National Transportation Systems Center, Cambridge, MA, 2013, pp. 1-9, 43-44, https://fas.org/irp/program/collect/service.pdf

[2] P. Finnegan, D, Cornell, "2016 World Military Unmanned Aerial Vehicle Systems Market Profile and Forecast", Teal Group Corporation, Fairfax, VA, 2016, http://www.tealgroup.com/index.php/pages/press-releases/47-teal-group-predicts-worldwide-military-uav-production-of-80-billion-over-the-next-decade-in-its-2017-uav-market-profile-and-forecast

[3] C. M. Hudson, E. K. Hall and G. D. Colby, "AISR Missions on Intelsat EpicNG Ku-Band," 2014 IEEE Military Communications Conference, Baltimore, MD, 2014, pp. 1351-1355, http://ieeexplore.ieee.org/document/6956944/

[4] Intelsat General Corporation,, "Intelsat General's Broadband Solution for Government Airborne Applications", 2014, pp. 1-6, https://www.intelsatgeneral.com/wp-content/uploads/files/Airborne%20Satellite%20COTM%20White%20Paper%20FINAL.pdf

[5] Tom Tschida, "NASA Photo: EC05-0090-19", NASA Dryden Flight Research Center Photo Collection, 2005, https://www.nasa.gov/centers/dryden/multimedia/imagegallery/Altair_PredatorB/EC05-0090-19.html

[6] M. Skolnik, "Introduction to Radar Systems, 3rd Edition", The McGraw-Hill Companies, Inc., New York, NY, 2001, pp.559-567

[7] Matthias Weib, "Digital Antennas", NATO, Research Establishment for Applied Science (FGAN), Research Institute for Higher Physics and Radar Techniques (FHR), Wachtberg, Germany, 2009, pp. 1-8, https://www.sto.nato.int/publications/.../RTO-EN-SET-133/EN-SET-133-05.pdf

[8] W. J. Lynn III , "Unmanned Aircraft System Airspace Integration Plan, Version 2.0", Department of Defense, UAS Task Force Airspace Integration Integrated Product Team, , 2011, pp. D1-D3, https://www.uvsr.org/Documentatie%20UVS/Publicatii-internationale/DoD_2011_UAS_Airspace_Integration_Plan.pdf

[9] Intelsat General Corporation, "Why Ku-band Makes the Most Sense for the DoD Over the Next Few Years", https://www.intelsatgeneral.com/wp-content/uploads/files/Ku-band%20flyer.pdf.

[10] J. Maj, "NATO Intelligence, Surveillance, and Reconnaissance (ISR) Interoperability Architecture (NIIA) Volume 1: Architecture Description, AEDP-2 (Edition 1)", 2005, pp.14-19,

https://www.uvsr.org/Documentatie%20UVS/Reglementari%20internationale/Alte%20documente/AEDP-02v1.pdf

[11] D. Curt Osterheld, “Common Data Link (CDL) Overview”, 7th International Data Links Symposium, L-3 Communications Washington Operations, 2007, pp. 24-36, http://www.idlsoc.com/Documents/Symposiums/IDLS2007/IDLS2007_CDL.pdf

[12] Department of Defense Joint Interoperability Test Command, “Common Data Link [CDLa]”, Global Security, 2008, http://www.globalsecurity.org/intell/systems/cdl.htm

[13] D.E. Whiteman; L.M. Valencia; R.B. Birr,”Ku- and Ka-Band Phased Array Antenna for the Space-Based Telemetry and Range Safety Project”, NASA Dryden Flight Research Center, Edwards,CA, 2005, pp. 1-10, https://ntrs.nasa.gov/archive/nasa/casi.ntrs.nasa.gov/20050215644.pdf

[14] M.P. Carney, J.C. Simpson “An Error Analysis of the Phased Array Antenna Pointing Algorithm for STARS Flight Demonstration # 2”, NASA Technical Report Server, 2005, pp. 1-8, https://ntrs.nasa.gov/archive/nasa/casi.ntrs.nasa.gov/20120003161.pdf

[15] D.A. Burkes, “Ground Support for the Space-Based Range Flight Demonstration 2”,NASA Dryden Flight Research Center, Edwards,CA, 2007, pp. 1-13, https://ntrs.nasa.gov/archive/nasa/casi.ntrs.nasa.gov/20070034158.pdf

[16] Intelsat ”Adjacent Satellite Interference in Mobile / VSAT Environments”, Intelsat General Corp, 2015, pp.1-5, https://www.intelsatgeneral.com/wp-content/uploads/2015/06/Adjacent-Satellite-Interference-in-Mobile-VSAT-Environments-March-20151.pdf

[17] H. Wang; H. Sun; Z. Lu; W. Wu, "Realization of Linear Polarization Reconfiguration for Mobile Satcom in Ku-band", 2013 IEEE International Conference on Microwave Technology & Computational Electromagnetics, Qingdao, 2013, pp. 236-238, http://ieeexplore.ieee.org/document/6812460/

[18] S. R. Nichols, “An Electronically Controlled Polarization Generator at Ka-band”, 2013 7th European Conference on Antennas and Propagation (EuCAP), Gothenburg, 2013, pp. 3599-3603, http://ieeexplore.ieee.org/document/6546980/

[19] S. Miller, J. Shapira, "Transmission Considerations for Polarization-Smart Antennas" IEEE VTS 53rd Vehicular Technology Conference, Spring 2001. Proceedings (Cat. No.01CH37202), Rhodes, vol.1, 2001, pp. 258-262, http://ieeexplore.ieee.org/abstract/document/944843/

[20] Simeoni, M., I. E. Lager, C. I. Coman, A. G. Roederer , “Implementation of Polarization Agility in Planar Phased Array Antennas by Means of Interleaved Sub-Arrays”, RADIO SCIENCE, vol 44, RS5013, 2009, pp. 1-12, http://ieeexplore.ieee.org/document/7775914/

[21] R. J. Mailloux, “Phased Array Antenna Handbook 2nd Edition”, Artech House, Inc., Norwood, MA, 2005, pp. 1-43

[22] ITU – R, “Handbook on Satellite Communications (HSC), 3rd Edition, International Telecommunication Union, Switzerland, 2002 , pp.249-252

[23] A.Luzzatto, G.Shirazi, “Wireless Transceiver Design, Mastering the Design of Modern Wireless Equipment and Systems”, John Wiley & Sons, Ltd, England,, 2007,pp.72-77, 95-100a]

[24] S. A. Maas, “Nonlinear Microwave and RF Circuits, 2nd Edition”, Artech House, Inc., Norwood, MA, 2003, pp. 119-212

[25] Matthew M. Radmanesh, “Radio Frequency and Microwave Electronics Illustrated”, Prentice Hall, Inc.,Upper Saddle River, NJ 07458, 2001, pp. 558-563

[26] J. W. M. Rogers, C. Plett, “Radio Frequency Integrated Circuit Design, 2nd Edition”, Artech House, Inc., Norwood, MA, 2010, pp. 18-29, 63-70

[27] D.M. Pozar, “Microwave Engineering, 4th Edition”, John Wiley & Sons, Inc., Hoboken, NJ, 2012, pp. 147-153, 317-376, 675

[28] Rogers Corporation, “RO4000® Series High Frequency Circuit Materials Data Sheet”, Advanced Connectivity Solutions, Chandler, AZ, 2015, pp. 1-4, https://www.rogerscorp.com/documents/726/acm/RO4000-Laminates---Data-sheet.pdf

[29] Janusz A. Dobrowolski, “Microwave Network Design Using the Scattering Matrix”, Artech House, Inc., Norwood, MA, 2010, pp. 28-32

[30] R. Garg, "Analytical and Computational Methods in Electromagnetics", Artech House, Inc., Norwood, MA, 2008, pp. 445-488

[31] A. Bondeson , T. Rylander, P. Ingelström, “Computational Electromagnetics”, Springer Science+Business Media, Inc., New York, NY, 2005, pp.153-188

[32] Z. Wu, ‘Software VNA and Microwave Network Design and Characterisation”, John Wiley & Sons, Ltd, England, 2007, pp. 33-37

[33] K.K. Johnson, “Optimizing Link Performance, Cost and Interchangeability by Predicting Residual BER: Part II - Nonlinearity and System Budgeting”, Microwave Journal Magazine, September 1, 2002 http://www.microwavejournal.com/articles/print/5567-optimizing-link-performance-cost-and-interchangeability-by-predicting-residual-ber-part-ii-nonlinearity-and-system-budgeting

[34] D.K. Misra, “Radio-Frequency and Microwave Communication Circuits Analysis and Design, 2nd Edition”, John Wiley & Sons, Inc., Hoboken, NJ, 2004, pp. 45-48

[35] ITU-R, "Recommendation SM.1541-6: Unwanted Emissions in the Out-of-Band Domain", International Telecommunication Union, Switzerland, 2015, pp. 2-6, 63-64, https://www.itu.int/dms_pubrec/itu-r/rec/sm/R-REC-SM.1541-6-201508-I!!PDF-E.pdf

[36] D. Hall, "Understanding Intermodulation Distortion Measurements", Communications Technologies, Electronic Design Magazine, October 9, 2013 http://electronicdesign.com/communications/understanding-intermodulation-distortion-measurements

[37] D. Hall, "Understanding IF Bandwidth In RF Signal Analyzers", Test & Measurement Technologies, Electronic Design Magazine, November 22, 2013, http://www.electronicdesign.com/test-amp-measurement/understanding-if-bandwidth-rf-signal-analyzers

[38] J.G. Proakis, M. Salehi, "Digital Communications, 5th Edition", The McGraw-Hill Companies, Inc., New York, NY, 2008, pp.675

[39] ITU, "Recommendation O.150: Digital Test Patterns for Performance Measurements on Digital Transmission Equipment", International Telecommunication Union, Switzerland, 1993, pp. 1-5, https://www.itu.int/rec/T-REC-O.150-199210-S

[40] Keysight Technologies, http://rfmw.em.keysight.com/wireless/helpfiles/89600b/webhelp/subsystems/digdemod/content/trc_error_vector_time.htm

[41] E. Dhalman, S. Parkvall, J. Sköld, "4G LTE/LTE-Advanced for Mobile Broadband", Academic Press, Burlington, MA, 2011, pp.367

[42] ETSI 3GPP, "Technical Specification ETSI TS 145 005 V13.1.0: Digital Cellular Telecommunications System (Phase 2+) (GSM); Radio Transmission and Reception (3GPP TS 45.005 Version 13.1.0 Release 13)", European Telecommunications Standard Institute, France, 2016, pp. 219, http://www.etsi.org/deliver/etsi_ts/145000_145099/145005/13.01.00_60/ts_145005v130100p.pdf

[43] F. Giannini, G. Leuzzi, "Nonlinear Microwave Circuit Design", John Wiley & Sons, Ltd, England, 2004, pp.43-45

[44] F.T. Ulaby, D.G. Long, "Microwave Radar and Radiometric Remote Sensing", University of Michigan Press, Ann Arbor, MI 2014, pp,. 41-45

[45] R. Nave, "HyperPhysics Intro", Georgia State University, Department of Physics and Astronomy, http://hyperphysics.phy-astr.gsu.edu/hbase/phyopt/polclas.html

[46] DoD, "MIL-STD-188-164B Department of Defense Interface Standard: Interoperability of SHF Satellite Communications Terminals", Defense Information Systems Agency, Fort Meade,

MD, 2012, pp. 17, 20, 34-35, http://everyspec.com/MIL-STD/MIL-STD-0100-0299/MIL-STD-188_164B_41602/

[47] ITU-R, "Recommendation SM.329-12: Unwanted Emissions in the Spurious Domain", International Telecommunication Union, Switzerland, 2012, pp. 5, 8-9, https://www.itu.int/dms_pubrec/itu-r/rec/sm/R-REC-SM.329-12-201209-I!!PDF-E.pdf

[48] A. Adegorusi, J. Timko, R. Mendolera, "Common Data Link EMC Analysis", Aeronautical Systems Center, Reconnaissance Systems Program Office, Sensors and Data Links, Department of Defense Joint Spectrum Center, Annapolis, MD, 2004, pp.2-2, https://info.publicintelligence.net/JSC-04-044.pdf

[49] S. Baiotti, "Advances in UAV Data Links: Analysis of Requirement Evolution and Implications on Future Equipment", RTO SCI Symposium on Warfare Automation: Procedures and Techniques for Unmanned Vehicles, Ankara, Turkey, 1999, pp. B10-3, http://www.dtic.mil/dtic/tr/fulltext/u2/p010327.pdf

[50] Intelsat, "Satellite Link Budget", International Telecommunications Satellite Organization, pp.27-29, http://www.itso.int/images/stories/Capacity-Building/Dakar-2015/LBA.pdf

[51] ASSC, "Study of the Application of the MPEG-2 Digital Video Compression Standard for Use in Uninhabited Aerial Vehicle Systems", Avionic Systems Standardization Committee, 2002, pp.18-19, https://www.scribd.com/document/86244605/Assc-Study-Application-Mpeg2-Digital-Video-Compression-Standard

[52] A. Goldsmith, "Wireless Communications", Cambridge University Press, New York, NY, 2005, pp. 172, 180

[53] A.Ludwig, "The definition of cross polarization", IEEE Transactions on Antennas and Propagation, Jan 1973,vol. 21, no.1, pp. 116-119, http://ieeexplore.ieee.org/document/1140406/

[54] K.P. Valavanis, P. Oh, L. A. Piegl, "Unmanned Aircraft Systems - International Symposium on Unmanned Aerial Vehicles, UAV'08," Springer, 2009, pp. 61-77

[55] R. C. Hansen, "Phased Array Antennas 2nd Edition," John Wiley & Sons, Inc., Hoboken, NJ, 2009, pp. 171-220

[56] Freeman, Roger L., "Radio System Design for Telecommunications (1–100 GHz),": John Wiley & Sons Ltd; New York, 1987, pp.221-438

[57] Ivancic, W.D., Sullivan, D.V., "Delivery of Unmanned Aerial Vehicle Data", 2010 Earth Science Technology Forum, Arlington, VA, June 22–24, 2010,pp.1-6, https://roland.grc.nasa.gov/~ivancic/papers_presentations/2010/ESTF2010-Paper-Efficient%20Delivery%20of%20UAV%20Data.pdf

[58] Wei Shi; Zuping Qian; Jun Zhou; Xinbo Qu; Yang Xiang; and Liu Hong; "A Small Ku-Band Polarization Tracking Active Phased Array for Mobile Satellite Communications," International

Journal of Antennas and Propagation, 2013, pp. 1-12, https://www.hindawi.com/journals/ijap/2013/747629/

[59] Tiezzi, F.; Vaccaro, S.; Llorens, D.; Dominguez, C.; Fajardo, M., "Ku-band Hybrid Phased Array Antennas for Mobile Satellite Communication Systems", 2013 7th European Conference on Antennas and Propagation (EuCAP) , April 2013, pp.1605-1608, http://ieeexplore.ieee.org/document/6546548/

[60] Ruiz, A.R.; Pellon, A.; Pena, M.A., "Low Profile Ku-Band Transmit/Receive Terminal ODU for Satellite Mobile Communications", Proceedings of the 5th European Conference on Antennas and Propagation (EUCAP), April 2011, pp.2358-2361, http://ieeexplore.ieee.org/document/5781907/

[61] Guodong Han; Biao Du; Wei Wu; Bing Yang, "A Novel Hybrid Phased Array Antenna for Satellite Communication on-the-Move in Ku-band", IEEE Transactions on Antennas and Propagation, April 2015, vol.63, no.4, pp.1375-1383 , http://ieeexplore.ieee.org/document/7004863/

[62] Schippers, H.; Verpoorte, J.; Jorna, P.; Hulzinga, A.; Meijerink, A.; Roeloffzen, C.; Heideman, R.G.; Leinse, A.; Wintels, M., "Conformal Phased Array with Beamforming for Airborne Satellite Communication," International ITG Workshop on Smart Antennas (WSA 2008), 26-27 Feb. 2008, pp.343-350

[63] A. Safaripour, S. M. Bowers, K. Dasgupta and A. Hajimiri, "Dynamic Polarization Control of Two-Dimensional Integrated Phased Arrays", in IEEE Transactions on Microwave Theory and Techniques, vol. 64, no. 4, 2016, pp. 1066-1077, http://ieeexplore.ieee.org/abstract/document/7422847/

[64] A. D. Panagopoulos, "Uplink Co-channel and Co-Polar Interference Statistical Distribution Between Adjacent Broadband Satellite Networks," Progress In Electromagnetics Research B, Vol. 10, 2008, pp. 177-189, http://www.jpier.org/PIERB/pierb10/12.08092902.pdf

APPENDICES

APPENDIX A – SCHEMATIC DIAGRAM

Tx BFN Module – System Architecture

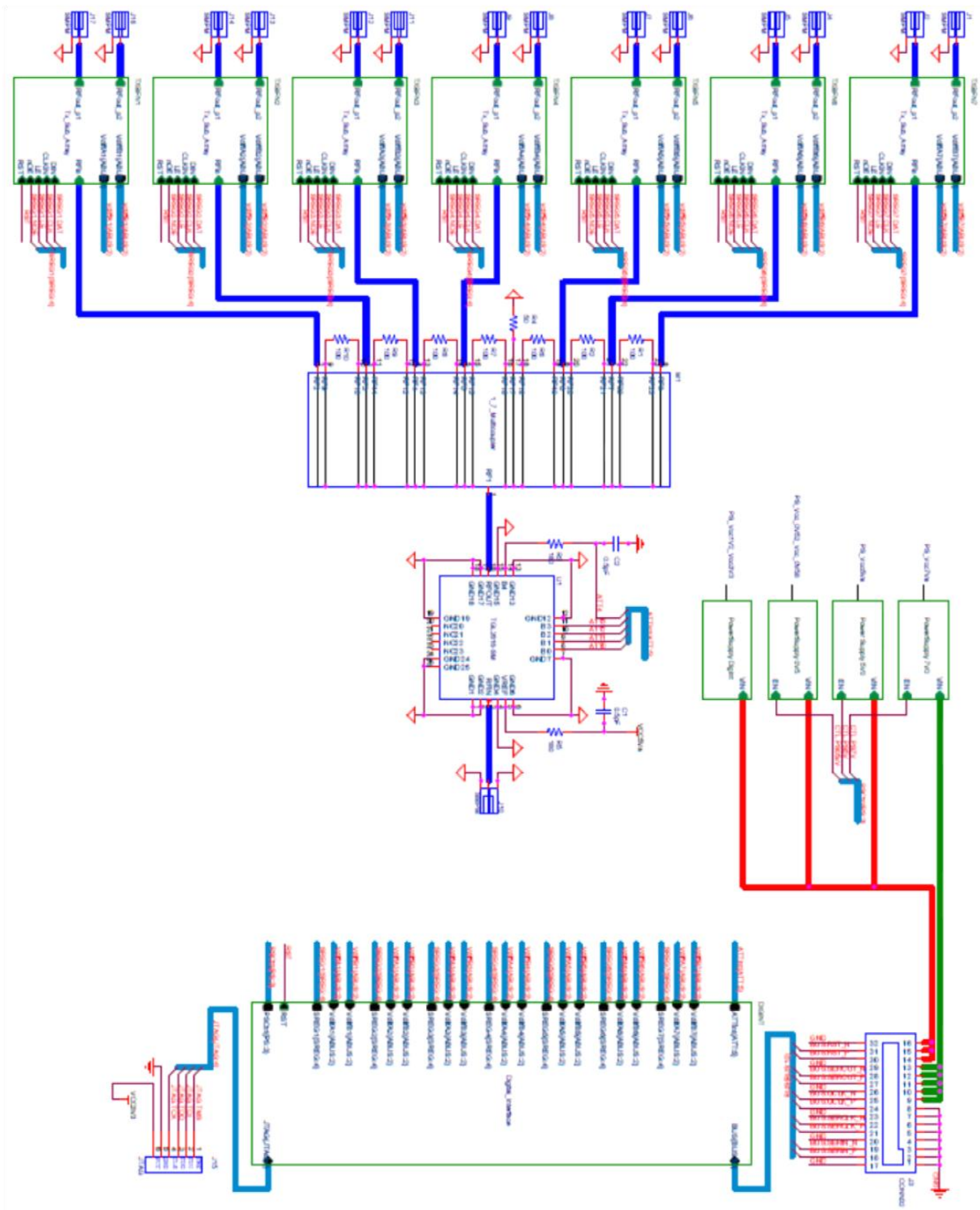

Tx Sub-Array - Microwave Circuit

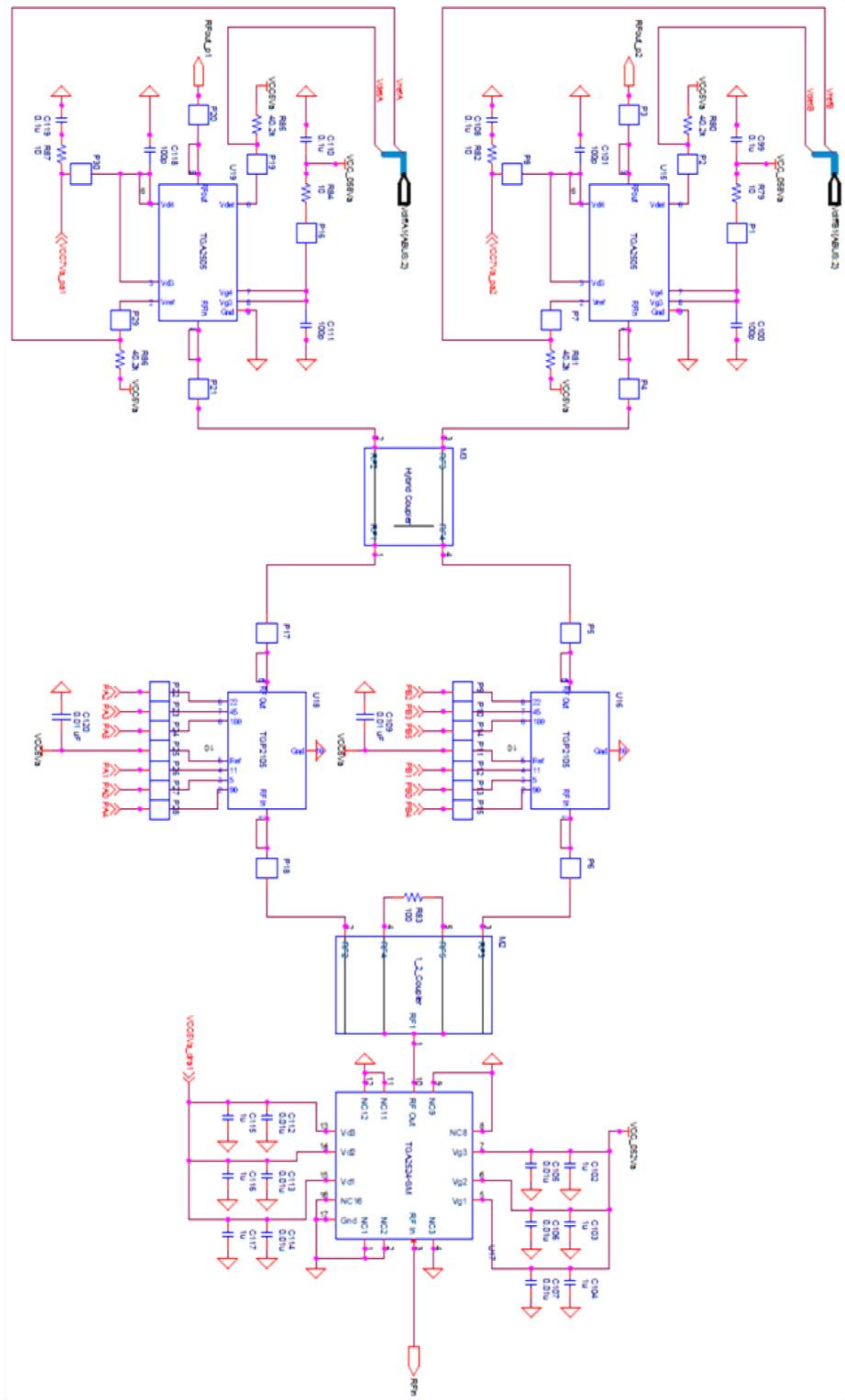

Tx Sub-Array – DC Power Load Switching Circuit

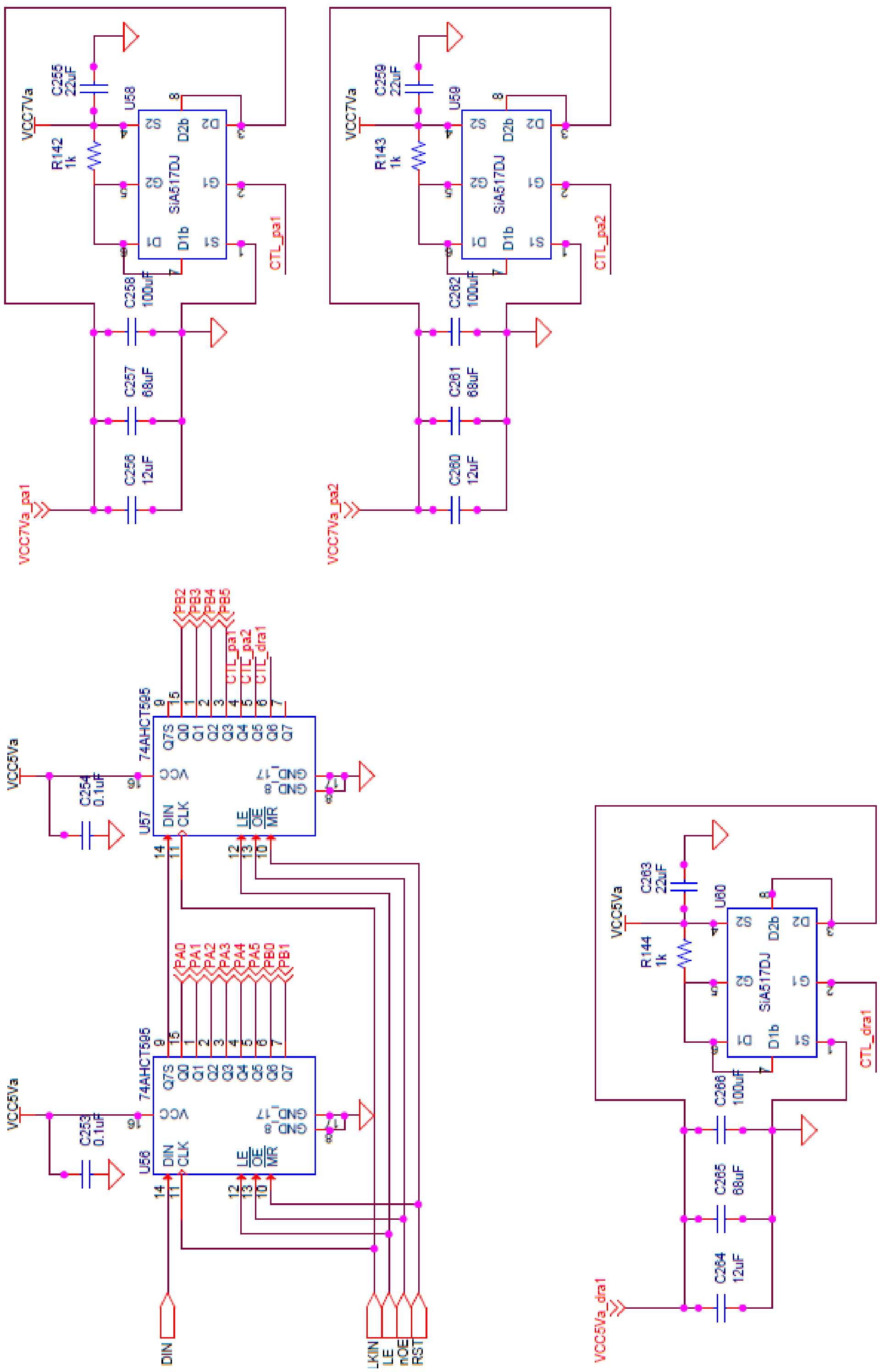

Tx BFN Module – Microwave Power Sensor Interface Circuit

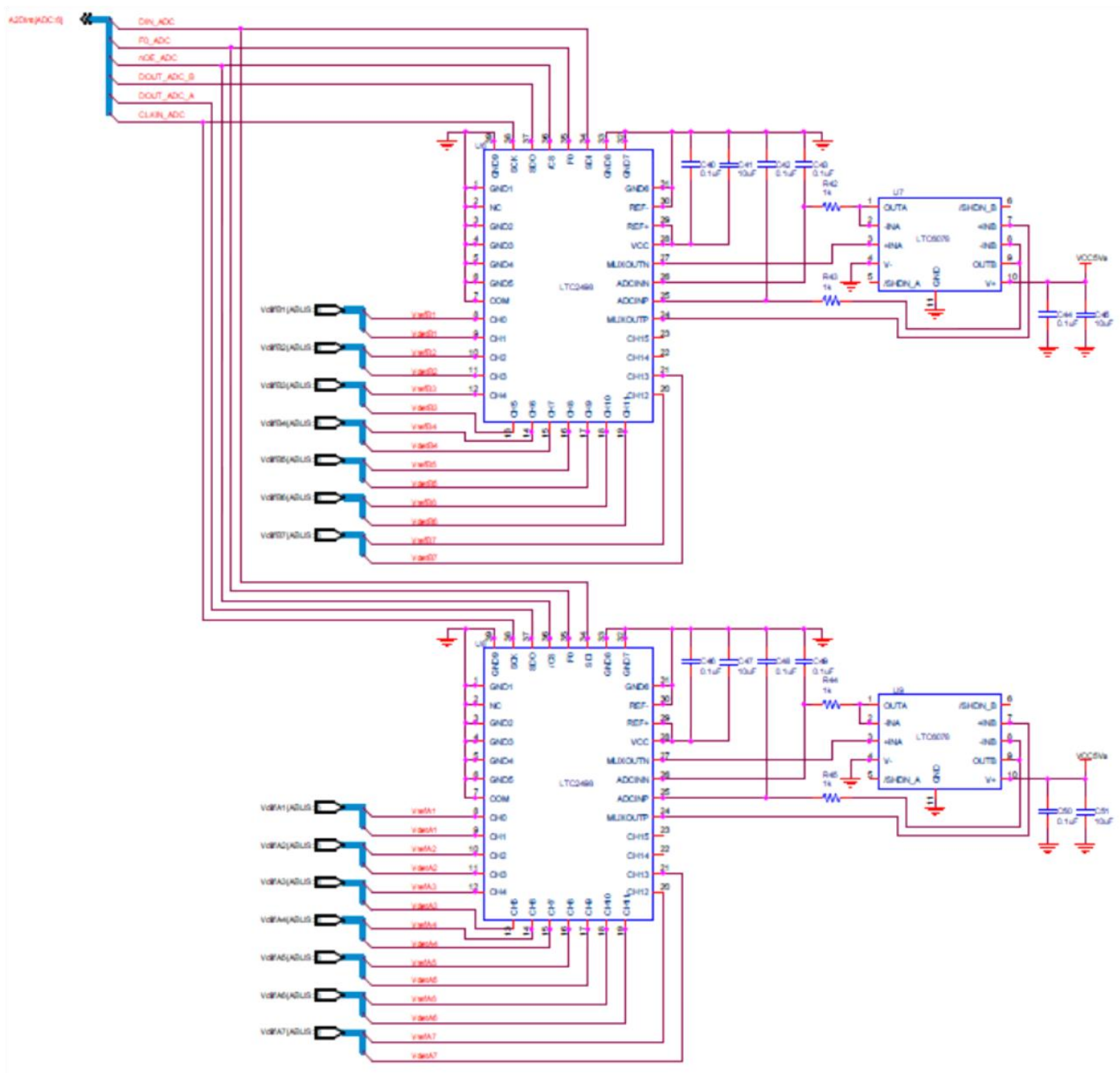

Tx BFN Module - +7.0 V DC Power Supply Circuit

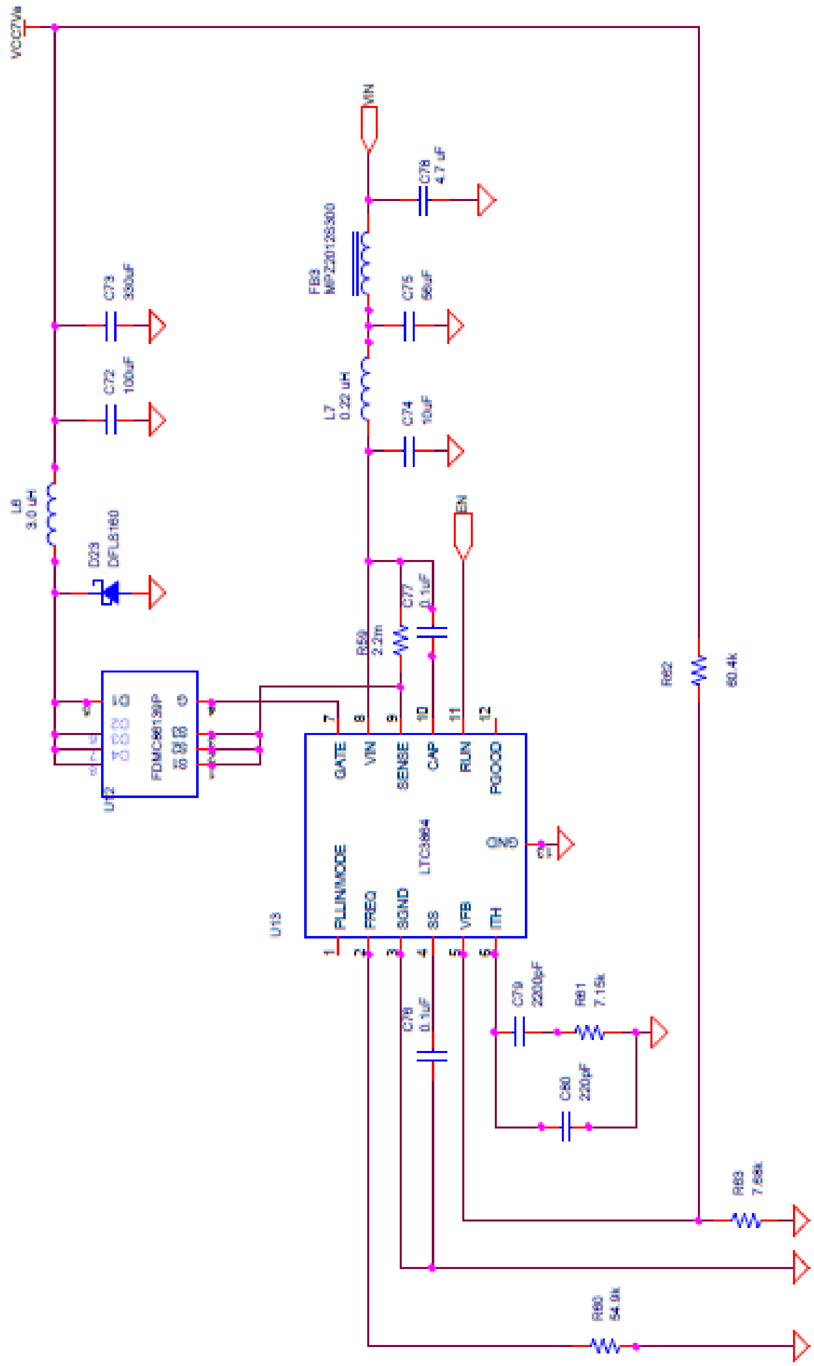

Tx BFN Module - -0.52 V/ 0.58 V DC Power Supply Circuit

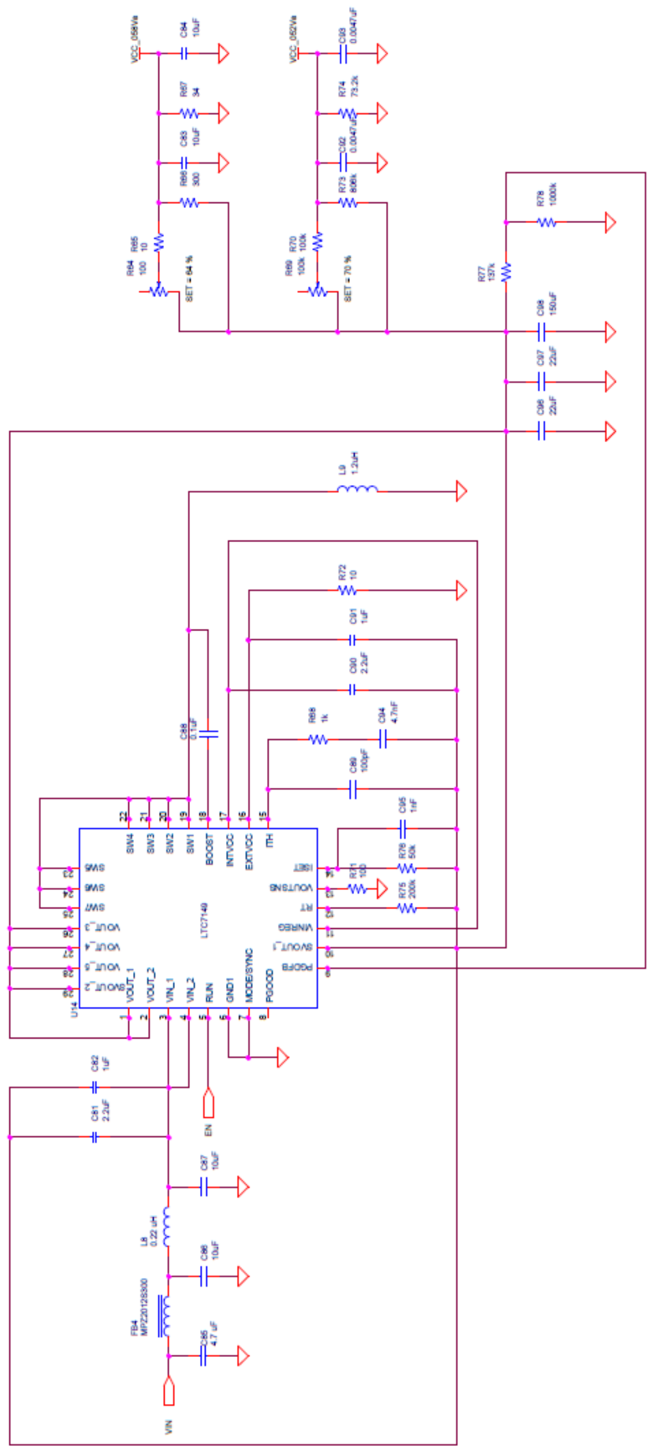

Tx BFN Module - +5.0 V DC Power Supply Circuit

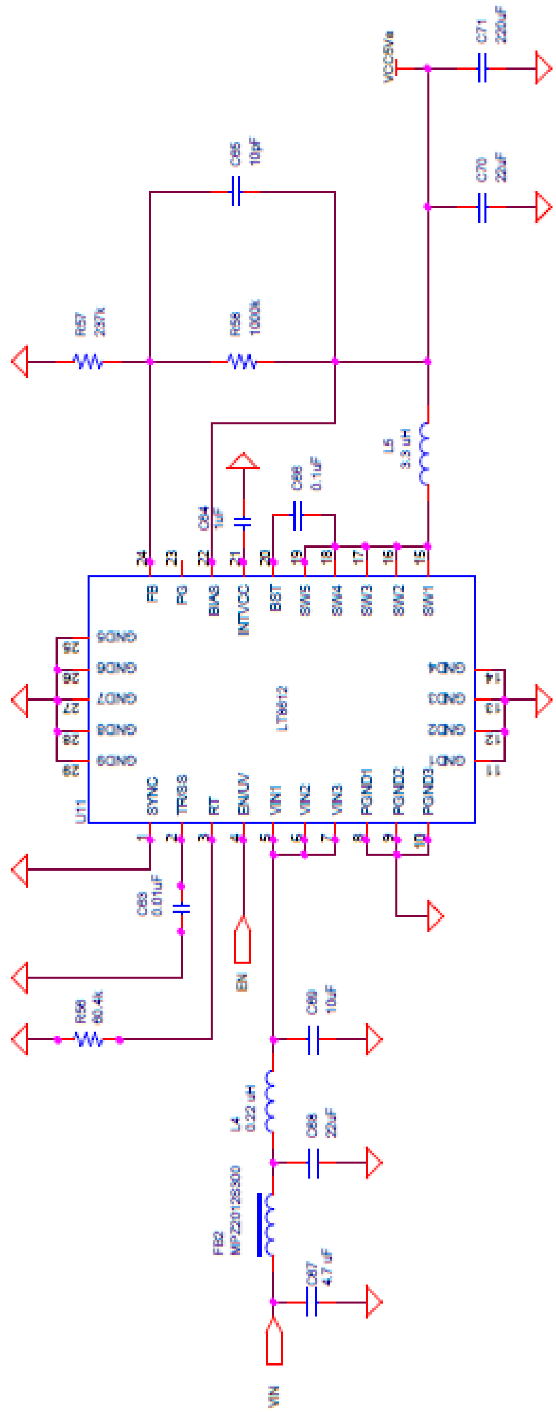

Tx BFN Module - +1.2 V/ +3.3 V DC Power Supply Circuit

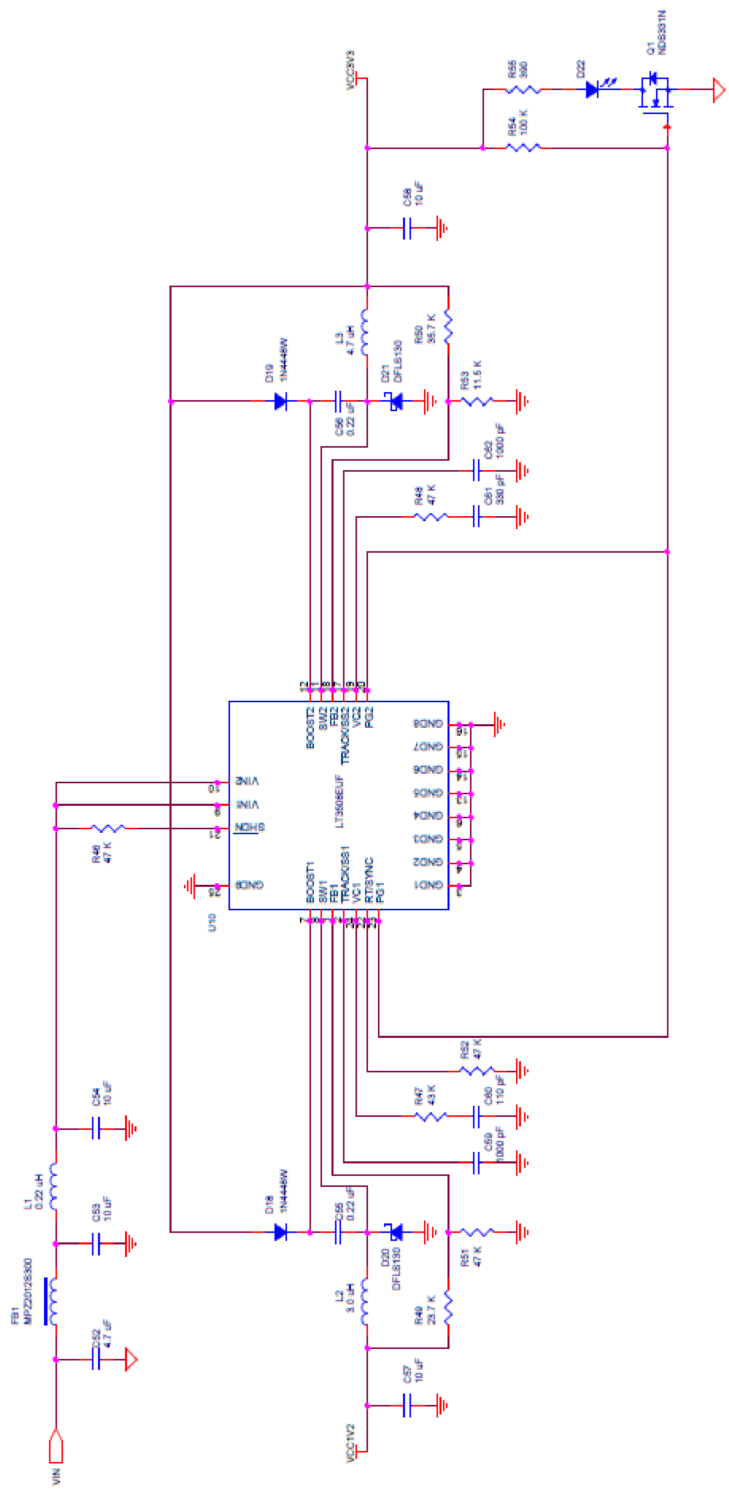

Tx BFN Module - Digital Control Interface Circuit

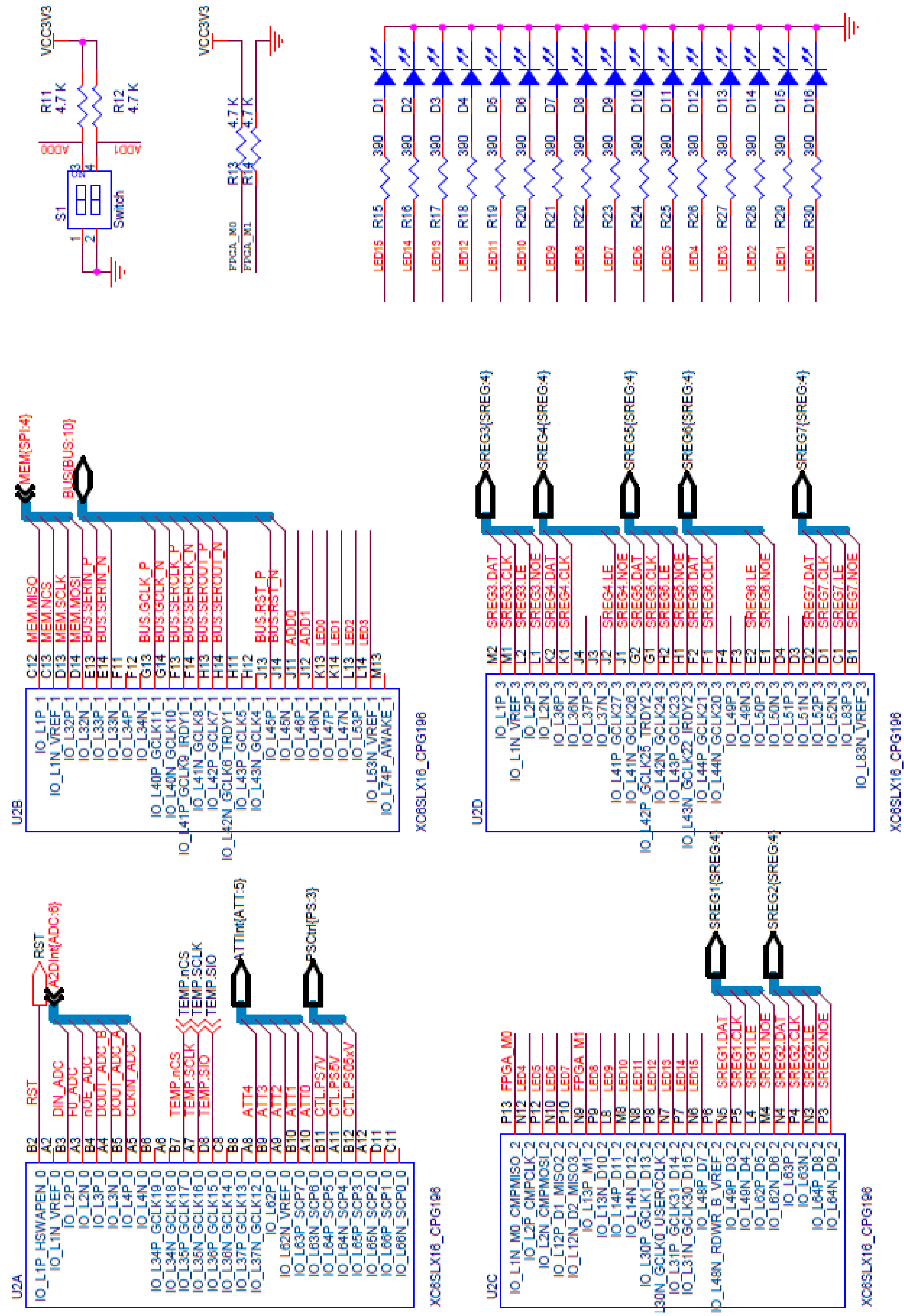

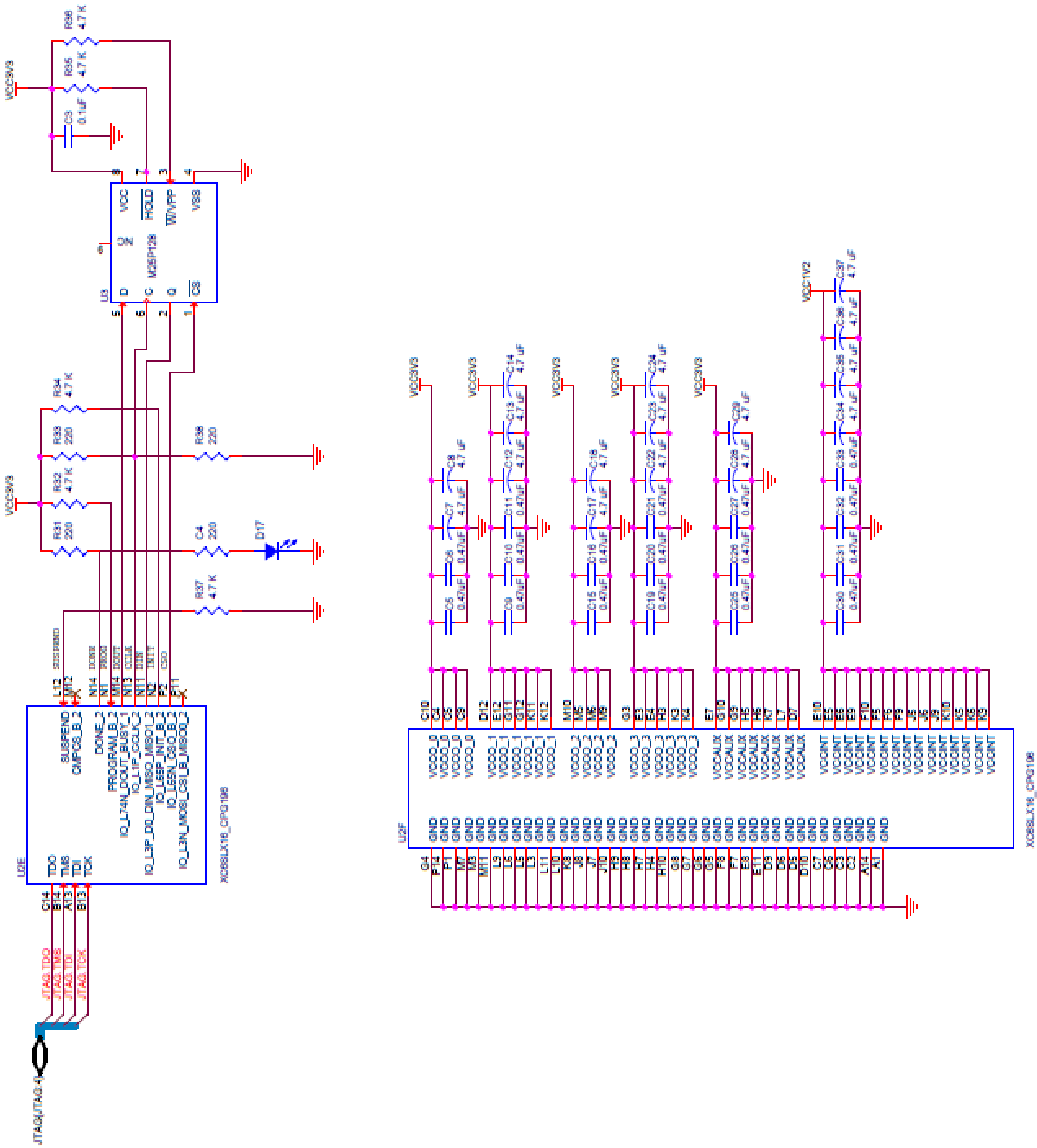
VCC3V3
VCC1V2
M25P128
U3
U2E
U2F
XC6SLX16_CPG196
JTAG(JTAG:4)

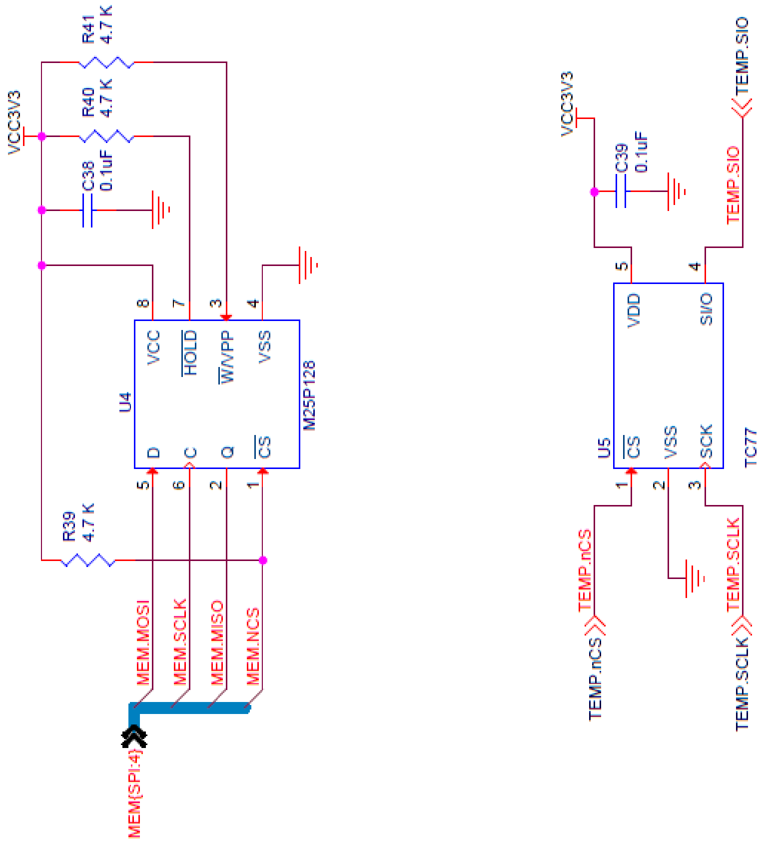

VCC3V3
R41
4.7 K
R40
4.7 K
C38
0.1uF
U4
VCC
HOLD
W/VPP
VSS
D
C
Q
CS
M25P128
R39
4.7 K
MEM.MOSI
MEM.SCLK
MEM.MISO
MEM.NCS
MEM(SPI:4)
VCC3V3
C39
0.1uF
U5
VDD
SI/O
CS
VSS
SCK
TC77
TEMP.SIO
TEMP.nCS
TEMP.SCLK

APPENDIX B – DC POWER LOAD SWITCH PERFORMANCE

Transient Analysis Results

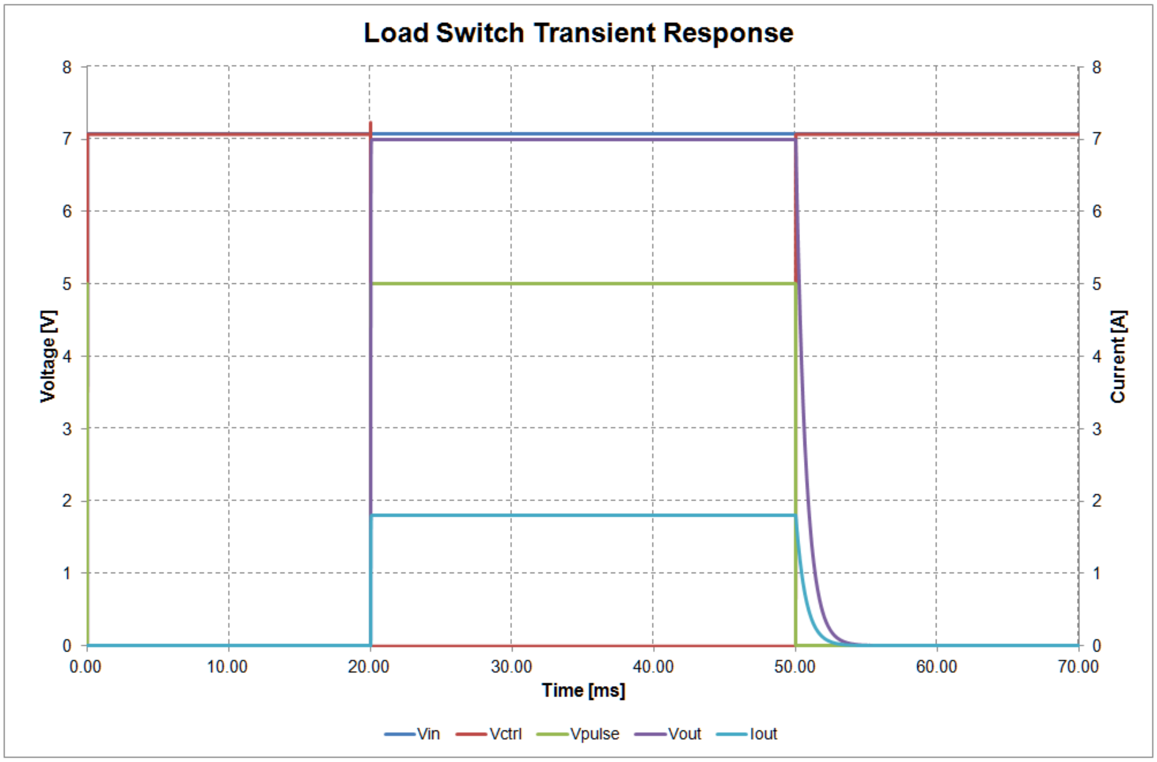

APPENDIX C – DC POWER SUPPLY PERFORMANCE

Transient Analysis Results

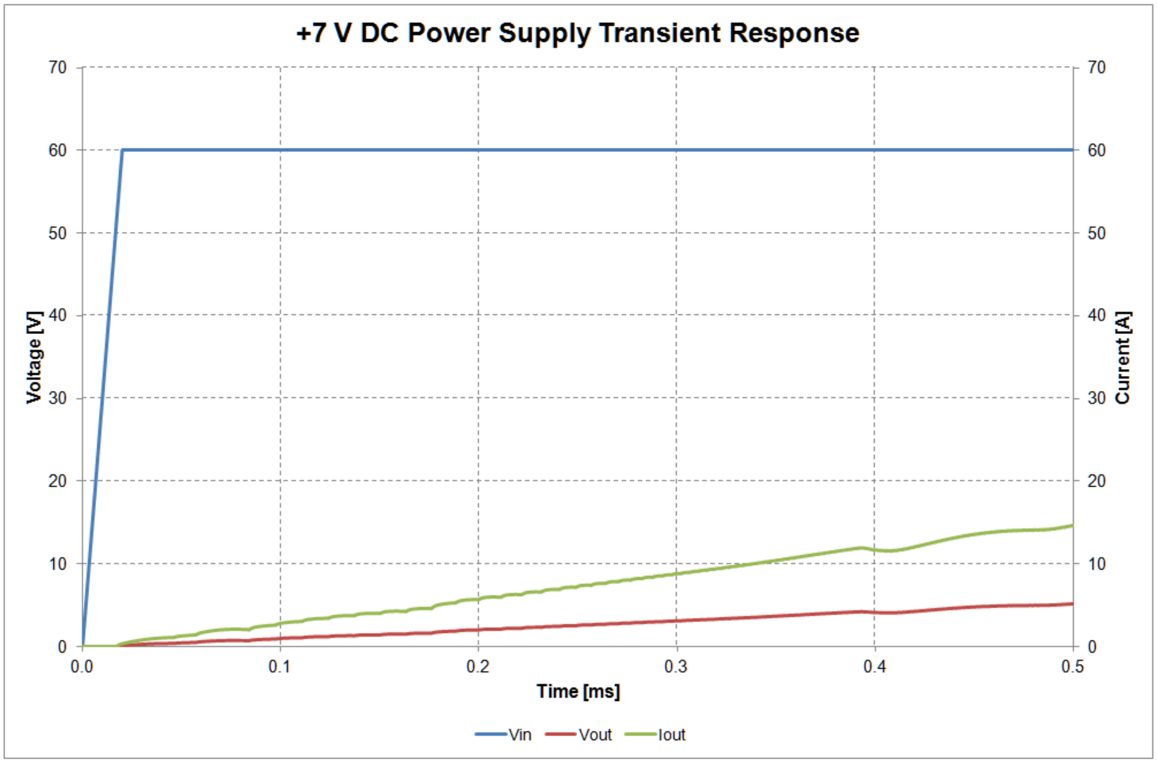

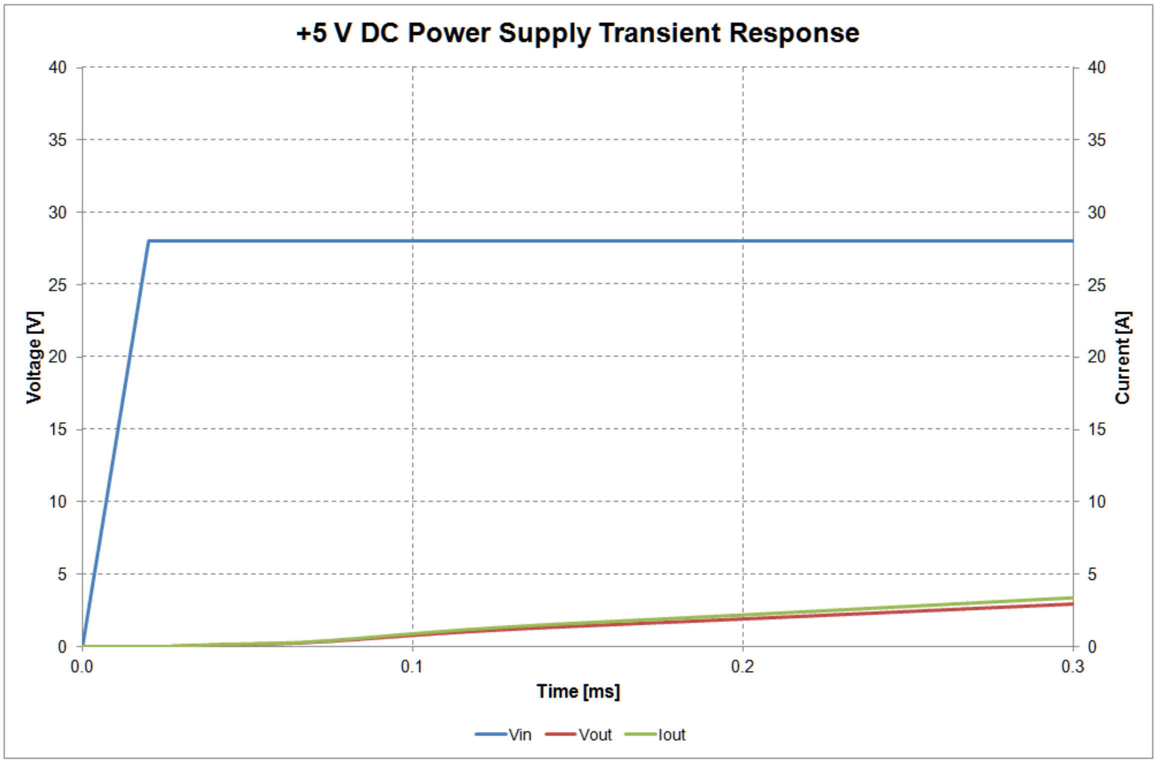

+5 V DC Power Supply Transient Response
Voltage [V]
Current [A]
40
35
30
25
20
15
10
5
0
0.0
0.1
0.2
0.3
Time [ms]
Vin
Vout
Iout

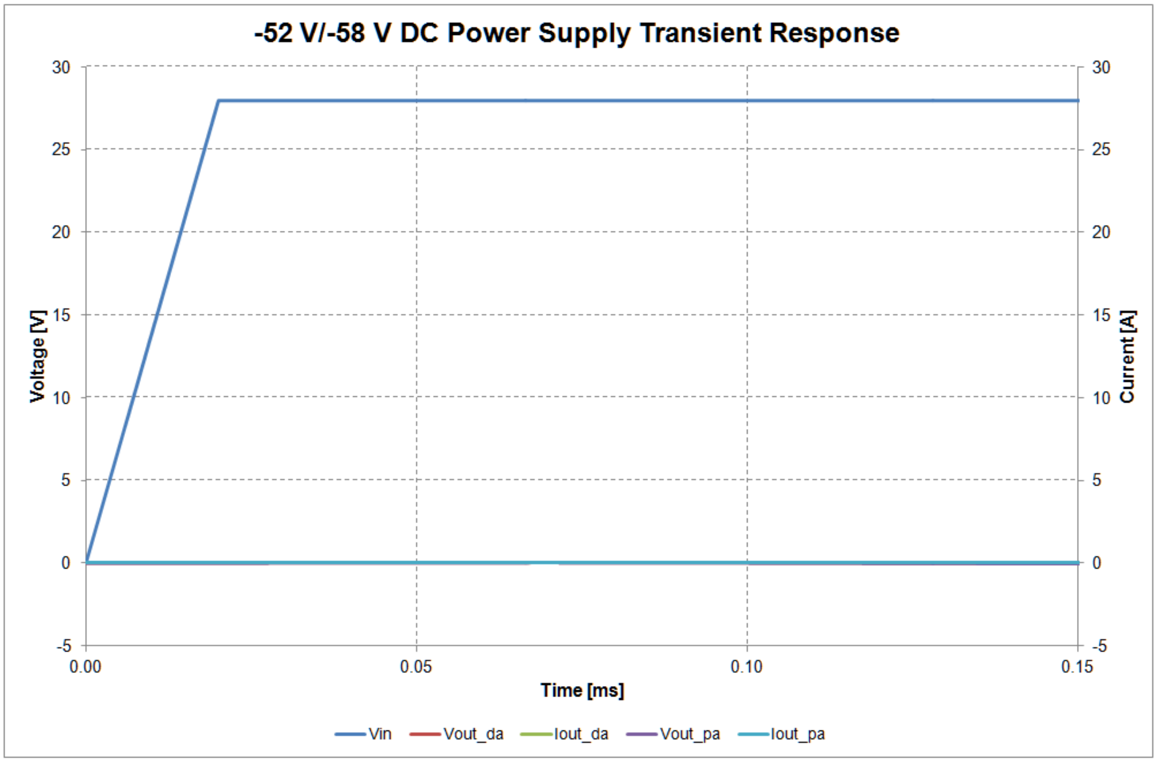

-52 V/-58 V DC Power Supply Transient Response
Voltage [V]
Current [A]
30
25
20
15
10
5
0
-5
0.00
0.05
0.10
0.15
Time [ms]
Vin
Vout_da
Iout_da
Vout_pa
Iout_pa

APPENDIX D – MATLAB PROGRAM CODES

```
%%%%%%%%%%%%%%%%%%%%%%%%%%%%%%%%%%%%%%%%%%%%%%%%%%%%%%%%%%%%%%%%%%%%%%%
% Author: E.Alvelo (Copyright E. Alvelo 2018)                         %
%                                                                     %
%                                                                     %
% This program determines the symbolic S parameter matrix and axial   %
% ratio expressions of a 3 port Tx Sub-Array model based on measured  %
% S parameter matrices of individual multiport microwave circuit      %
% components.                                                         %
%                                                                     %
%%%%%%%%%%%%%%%%%%%%%%%%%%%%%%%%%%%%%%%%%%%%%%%%%%%%%%%%%%%%%%%%%%%%%%%


clear all; close all; clc;

% Input variables

syms SA(S11,S12,S13,S21,S22,S23,S31,S32,S33); % 1:2 Coupler matrix.
syms SB(S44,S45,S54,S55); % Phase shifter Y matrix.
syms SC(S66,S67,S76,S77); % Phase shifter X matrix.
Syms SD(S88,S89,S810,S811,S98,S99,S910,S911,S108,S109,S1010,S1011,...
        S118,S119,S1110,S1111) % Hybrid Coupler matrix.
syms SE(S1212,S1213,S1312,S1313); % Power amplifier Y matrix.
syms SF(S1414,S1415,S1514,S1515); % Power amplifier X matrix.

% Program procedures

SA(S11,S12,S13,S21,S22,S23,S31,S32,S33) =
[S11,S12,S13;S21,S22,S23;S31,...
    S32,S33a];
SB(S44,S45,S54,S55) = [S44,S45;S54,S55a];
SC(S66,S67,S76,S77) = [S66,S67;S76,S77a];
SD(S88,S89,S810,S811,S98,S99,S910,S911,S108,S109,S1010,S1011,...
S118,S119,S1110,S1111) =
[S88,S89,S810,S811;S98,S99,S910,S911;S108,S109,S1010,...
S1011;S118,S119,S1110,S1111a];
SE(S1212,S1213,S1312,S1313) = [S1212,S1213;S1312,S1313a];
SF(S1414,S1415,S1514,S1515) = [S1414,S1415;S1514,S1515a];

See = [S11,0,0;0,S1313,0;0,0,S1515a];
Sei  =  [S12,S13,0,0,0,0,0,0,0,0,0,0;0,0,0,0,0,0,0,0,0,0,S1312,0;0,0,0,...
        0,0,0,0,0,0,0,0,S1514a];
Sie  =  [S21,0,0;S31,0,0;0,0,0;0,0,0;0,0,0;0,0,0;0,0,0;0,0,0;0,0,0;0,0,...
        0;0,S1213,0;0,0,S1415a];
Sii = [S22,S23,0,0,0,0,0,0,0,0,0,0;S32,S33,0,0,0,0,0,0,0,0,0,0;0,0,...
        S44,S45,0,0,0,0,0,0,0,0;0,0,S54,S55,0,0,0,0,0,0,0,0;0,0,0,0,...
        S66,S67,0,0,0,0,0,0;0,0,0,0,S76,S77,0,0,0,0,0,0;0,0,0,0,0,0,...
        S88,S89,S810,S811,0,0;0,0,0,0,0,0,S98,S99,S910,S911,0,0;0,0,0,...
        0,0,0,S108,S109,S1010,S1011,0,0;0,0,0,0,0,0,S118,S119,S1110,...
```

```
S1111,0,0;0,0,0,0,0,0,0,0,0,0,S1212,0;0,0,0,0,0,0,0,0,0,0,0,S1414a];
Gii  =  [0,0,1,0,0,0,0,0,0,0,0,0;0,0,0,0,1,0,0,0,0,0,0,0;1,0,0,0,0,0,0,...
        0,0,0,0,0;0,0,0,0,0,0,1,0,0,0,0,0;0,1,0,0,0,0,0,0,0,0,0,0;0,...
        0,0,0,0,0,0,0,0,1,0,0;0,0,0,1,0,0,0,0,0,0,0,0;0,0,0,0,0,0,0,...
        0,0,0,1,0;0,0,0,0,0,0,0,0,0,0,0,1;0,0,0,0,0,1,0,0,0,0,0,0;...
        0,0,0,0,0,0,0,1,0,0,0,0;0,0,0,0,0,0,0,0,1,0,0,0a];

Se = See + Sei * inv(Gii - Sii) * Sie;

Ay = simplify(Se(2,1),'Steps',5);
Ax = simplify(Se(3,1),'Steps',5);

% Output variables

AR = simplifyFraction(Ay/Ax) % Tx Sub-Array axial ratio.
```

```
%%%%%%%%%%%%%%%%%%%%%%%%%%%%%%%%%%%%%%%%%%%%%%%%%%%%%%%%%%%%%%%%%%%%%%
% Author: E.Alvelo (Copyright E. Alvelo 2018)                        %
%                                                                    %
%                                                                    %
% This program determines and plots the theoretical effect of        %
% amplitude and phase errors on Tx Sub-Array axial ratio.            %
%             %                  %                                   %
%%%%%%%%%%%%%%%%%%%%%%%%%%%%%%%%%%%%%%%%%%%%%%%%%%%%%%%%%%%%%%%%%%%%%%


clear all; close all; clc;

% Input variables.

scan_deg = 0; % Scan angle value in Degrees.
tilt_deg = 0; % Polarization tilt angle value in Degrees.
phase_error_deg = 0; % Phase error in Degrees.

% Program procedures.

amplitude_ratio = 0:.00001:1;
amplitude_error = 1 - amplitude_ratio;

amplitude_x = 1;
amplitude_y = amplitude_ratio;
phase_x = scan_deg*pi/180;


for m = 1:length(tilt_deg);
phase_y(m) = (phase_x + (pi/2) - 2*(tilt_deg(m)*pi/180)) - ...
             (phase_error_deg*pi/180);
for n = 1:length(amplitude_ratio);
ay(m,n) = (amplitude_y(n)*exp(-phase_y(m)*i))*(exp(pi*i)) + ...
          (amplitude_x*exp(phase_x*i))*(exp((-pi/2)*i));
ax(m,n) = (amplitude_y(n)*exp(-phase_y(m)*i))*(exp((-pi/2)*i)) +...
          (amplitude_x*exp(phase_x*i))*(exp(pi*i));
alpha0(m,n) = atan(abs(ay(m,n)/ax(m,n)));
delta(m,n) = angle(ay(m,n))-angle(ax(m,n));
Psi(m,n) = (atan(tan(2*alpha0(m,n))*cos(delta(m,n)))/2)*(180/pi);
Chi(m,n) = asin(sin(2*alpha0(m,n))*sin(delta(m,n)))/2;
R(m,n) = 1/tan(Chi(m,n));
AR_dB(m,n) = 20*log10(abs(R(m,n)));
end
end

% Output variables.

plot(amplitude_error,AR_dB); % Plot axial ratio in dB vs. errors.
```

```
%%%%%%%%%%%%%%%%%%%%%%%%%%%%%%%%%%%%%%%%%%%%%%%%%%%%%%%%%%%%%%%%%%%%%%
% Author: E.Alvelo (Copyright E. Alvelo 2018)                        %
%                                                                    %
%                                                                    %
% This program determines the required error vector magnitude of a   %
% transmitted waveform to achieve a specific bit error rate          %
% probability at the receiver.                                       %
%                                                                    %
%%%%%%%%%%%%%%%%%%%%%%%%%%%%%%%%%%%%%%%%%%%%%%%%%%%%%%%%%%%%%%%%%%%%%%


clear all; close all; clc;

% Input variables.

m = 4; % Modulation order.
bit_rate_mbps = 10.71; % Payload bit rate in Mbps.
filter_alpha = 1; % Root raised cosine filter roll off factor.
fec_rate = 0.5; % Forward error correction rate.
bit_error_probability = 10^(-9); % Target bit error rate.

% Program procedures.

bits_per_symbol = log2(m);
symbol_rate = (bit_rate_mbps/fec_rate)/bits_per_symbol;
occupied_bandwidth = (bit_rate_mbps*(1+filter_alpha)/fec_rate)/...
                      bits_per_symbol;
symbol_time = 1/symbol_rate;

ebno = (erfcinv(2*bit_error_probability))^2;
signal_to_noise_power_ratio = ebno*(log2(m)/(occupied_bandwidth*...
                              symbol_time));
evm_required_rx =
sqrt((occupied_bandwidth*symbol_time )/(ebno*log2(m)));


% Output variables

evm_required_rx_dB = -20*log10(evm_required_rx) % Required EVM in dB.
evm_required_rx_percentage = evm_required_rx*100 % Req. EVM percentage.
```

APPENDIX E – THERMAL ANALYSIS

Thermal Design Details

Heatsink type:	Extrusion
Part number:	Extrusion: 66427
Weight:	2.19452 kg
Heatsink dimensions:	309.96 mm wide x 127.0 mm long x 74.3 mm high
Material:	Aluminum
Finish:	Degreased
Length:	127 mm
Thermal Interface Impedance	0.07 in^2 °C/W

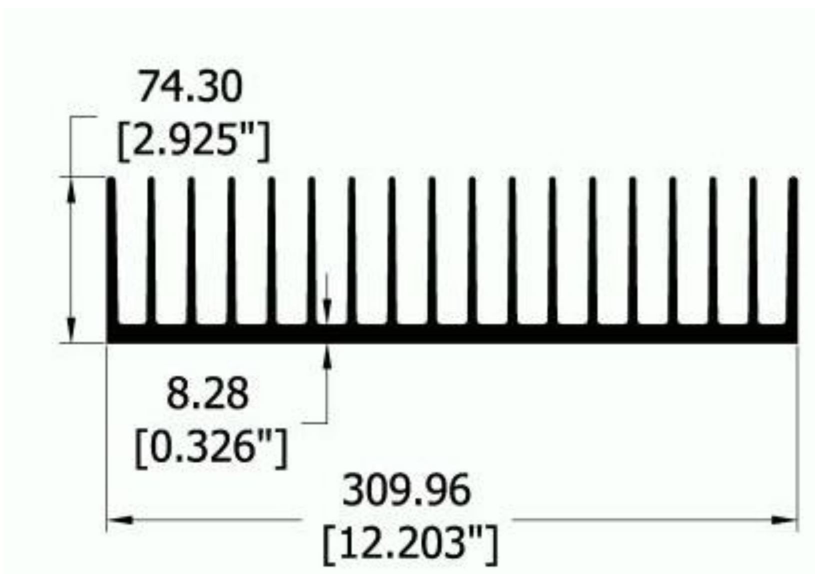

Environment

Ambient Temperature:	25.0 C
Altitude:	0.0 m

Hydraulic Design Details

Type of Flow:	Fixed velocity (push)
Fluid:	Air
Flow rate:	333.75 cfm

Total Pressure Drop: 23.872 Pa
Exit Temperature: 27.4 C

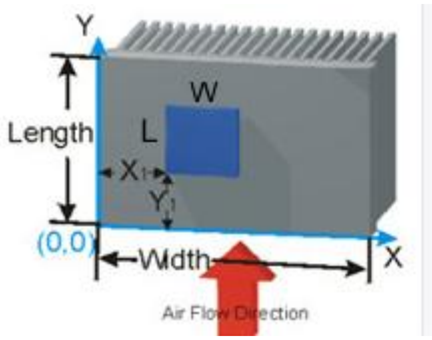

Thermal Design Results

Source Name	%sc	Pdiss (W)	Tsink-avg (° C)	Tsink-max (° C)	Tcase (° C)	Tjunction (° C)
RF_PA_1	0.00%	7.38	64.9	65	65	108
RF_PA_2	0.00%	7.38	65.5	65.7	65.7	108.8
RF_PA_3	0.00%	7.38	66.1	66.4	66.4	109.4
RF_PA_4	0.00%	7.38	66.9	67.1	67.1	110.1
RF_PA_5	0.00%	7.38	67.4	67.5	67.5	110.6
RF_PA_6	0.00%	7.38	67.4	67.7	67.7	110.7
RF_PA_7	0.00%	7.38	68.3	68.4	68.4	111.5
RF_PA_8	0.00%	7.38	68.8	68.9	68.9	111.9
RF_PA_9	0.00%	7.38	68.8	68.9	68.9	112
RF_PA_10	0.00%	7.38	68.7	69	69	112
RF_PA_11	0.00%	7.38	69.4	69.5	69.5	112.5
RF_PA_12	0.00%	7.38	69.3	69.4	69.4	112.5
RF_PA_13	0.00%	7.38	69	69.1	69.1	112.2
RF_PA_14	0.00%	7.38	69.7	69.9	69.9	112.9
RF_PA_15	0.00%	7.38	69.9	70.1	70.1	113.1
RF_PA_16	0.00%	7.38	69.9	70	70	113.1
RF_PA_17	0.00%	7.38	69.7	69.9	69.9	112.9
RF_PA_18	0.00%	7.38	70.1	70.3	70.3	113.3
RF_PA_19	0.00%	7.38	70.3	70.4	70.4	113.4
RF_PA_20	0.00%	7.38	69.7	69.9	69.9	112.9
RF_PA_21	0.00%	7.38	70	70.2	70.2	113.2

RF_PA_22	0.00%	7.38	70.4	70.5	70.5	113.6
RF_PA_23	0.00%	7.38	70.1	70.4	70.4	113.4
RF_PA_24	0.00%	7.38	70	70.2	70.2	113.2
RF_PA_25	0.00%	7.38	70.5	70.6	70.6	113.7
RF_PA_26	0.00%	7.38	70.4	70.5	70.5	113.6
RF_PA_27	0.00%	7.38	70	70.2	70.2	113.2
RF_PA_28	0.00%	7.38	70.1	70.3	70.3	113.3
RF_PA_29	0.00%	7.38	70.3	70.4	70.4	113.5
RF_PA_30	0.00%	7.38	70.1	70.2	70.2	113.2
RF_PA_31	0.00%	7.38	69.8	70	70	113
RF_PA_32	0.00%	7.38	70.3	70.4	70.4	113.5
RF_PA_33	0.00%	7.38	70.3	70.4	70.4	113.4
RF_PA_34	0.00%	7.38	69.8	69.9	69.9	113
RF_PA_35	0.00%	7.38	70	70.1	70.1	113.1
RF_PA_36	0.00%	7.38	70	70.1	70.1	113.2
RF_PA_37	0.00%	7.38	69.8	69.9	69.9	112.9
RF_PA_38	0.00%	7.38	69.3	69.5	69.5	112.5
RF_PA_39	0.00%	7.38	69.6	69.8	69.8	112.8
RF_PA_40	0.00%	7.38	69.7	69.8	69.8	112.8
RF_PA_41	0.00%	7.38	69.1	69.3	69.3	112.3
RF_PA_42	0.00%	7.38	69.1	69.3	69.3	112.3
RF_PA_43	0.00%	7.38	69.3	69.4	69.4	112.4
RF_PA_44	0.00%	7.38	68.8	69	69	112
RF_PA_45	0.00%	7.38	68	68.3	68.3	111.3
RF_PA_46	0.00%	7.38	68.4	68.5	68.5	111.5
RF_PA_47	0.00%	7.38	68.1	68.3	68.3	111.3
RF_PA_48	0.00%	7.38	67.5	67.7	67.7	110.8
RF_PA_49	0.00%	7.38	67.3	67.5	67.5	110.5
RF_PA_50	0.00%	7.38	67.2	67.3	67.3	110.4
RF_PA_51	0.00%	7.38	66.6	66.7	66.7	109.8
RF_PA_52	0.00%	7.38	65.5	65.8	65.8	108.8
RF_PA_53	0.00%	7.38	65.4	65.5	65.5	108.5
RF_PA_54	0.00%	7.38	64.6	64.8	64.8	107.8
RF_PA_55	0.00%	7.38	63	63.4	63.4	106.4
RF_PA_56	0.00%	7.38	62.3	62.3	62.3	105.4
RF_DA_1	0.00%	1.4	57.1	57.3	57.3	100.9
RF_DA_2	0.00%	1.4	57.6	57.8	57.8	101.5
RF_DA_3	0.00%	1.4	58	58.2	58.2	101.9
RF_DA_4	0.00%	1.4	58.5	58.7	58.7	102.4
RF_DA_5	0.00%	1.4	58.6	58.9	58.9	102.5
RF_DA_6	0.00%	1.4	59.1	59.4	59.4	103

RF_DA_7	0.00%	1.4	59.2	59.5	59.5	103.1
RF_DA_8	0.00%	1.4	59.5	59.7	59.7	103.4
RF_DA_9	0.00%	1.4	59.6	59.8	59.8	103.5
RF_DA_10	0.00%	1.4	59.7	59.9	59.9	103.6
RF_DA_11	0.00%	1.4	59.8	60.1	60.1	103.7
RF_DA_12	0.00%	1.4	59.7	59.9	59.9	103.6
RF_DA_13	0.00%	1.4	59.9	60.1	60.1	103.8
RF_DA_14	0.00%	1.4	59.7	60	60	103.6
RF_DA_15	0.00%	1.4	59.9	60.1	60.1	103.7
RF_DA_16	0.00%	1.4	59.7	59.9	59.9	103.6
RF_DA_17	0.00%	1.4	59.6	59.9	59.9	103.5
RF_DA_18	0.00%	1.4	59.6	59.8	59.8	103.4
RF_DA_19	0.00%	1.4	59.2	59.5	59.5	103.2
RF_DA_20	0.00%	1.4	59.2	59.5	59.5	103.1
RF_DA_21	0.00%	1.4	58.8	59	59	102.7
RF_DA_22	0.00%	1.4	58.7	59	59	102.6
RF_DA_23	0.00%	1.4	58.3	58.5	58.5	102.2
RF_DA_24	0.00%	1.4	57.9	58.1	58.1	101.8
RF_DA_25	0.00%	1.4	57.4	57.6	57.6	101.2
RF_DA_26	0.00%	1.4	56.6	56.9	56.9	100.5
RF_DA_27	0.00%	1.4	56	56.3	56.3	99.9
RF_DA_28	0.00%	1.4	55	55.3	55.3	98.9

Baseplate Temperature Profile

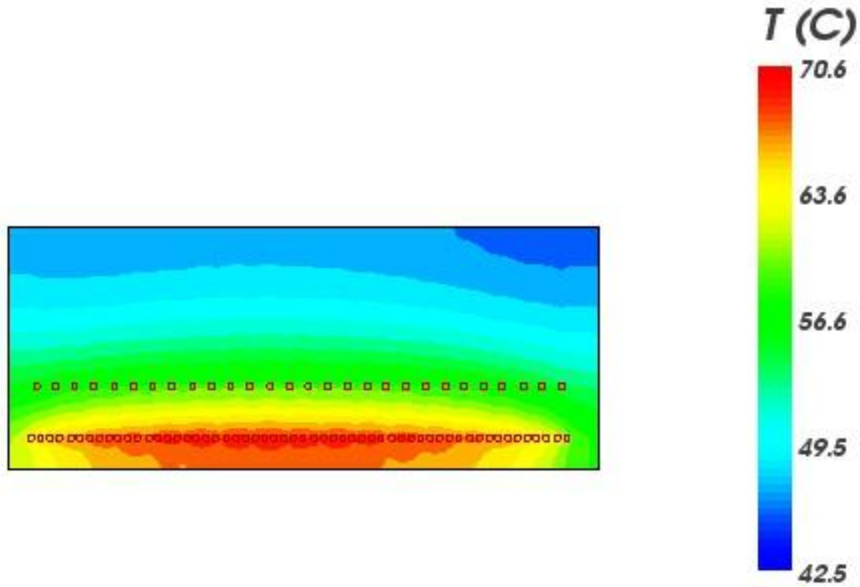

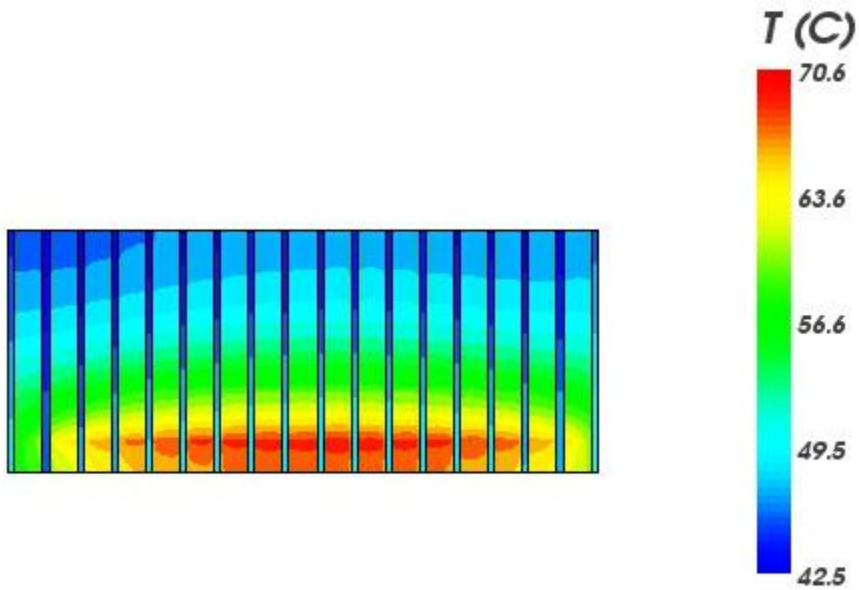

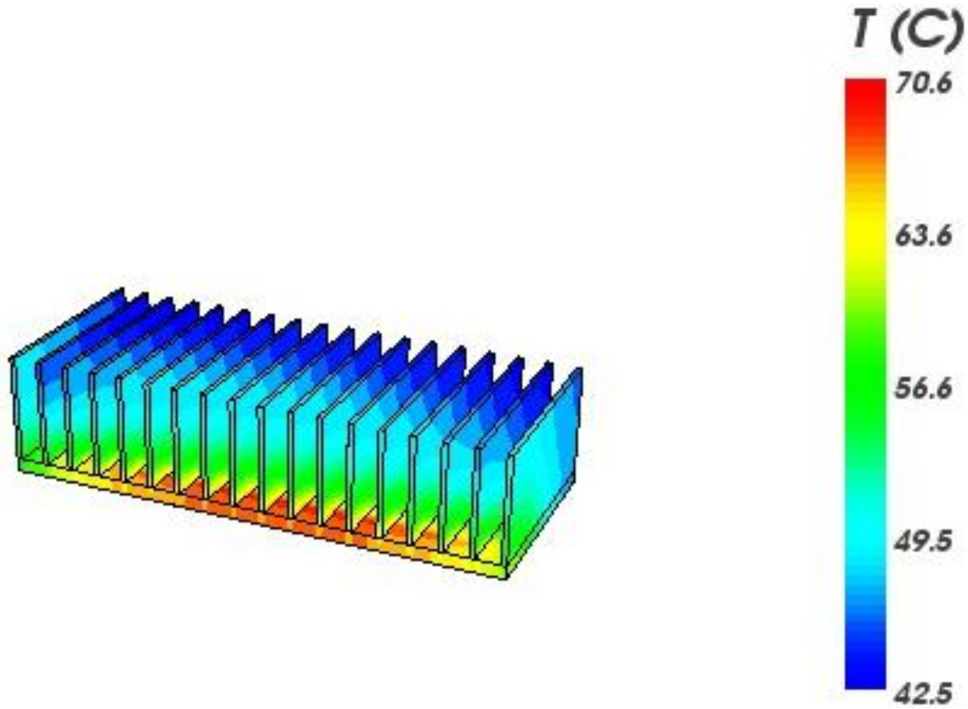
T (C)
70.6
63.6
56.6
49.5
42.5

APPENDIX F – TX AND RX MODULE OPERATION

The following figures were copied from unpublished presentation material prepared by Prof. Rafael H. Medina – Sanchez in relation to the “Hybrid Mechanical/ Electronic Steerable Antenna Array for SATCOM Terminals” currently developed by the University of Puerto Rico at Mayaguez.

Linear Polarization Waves

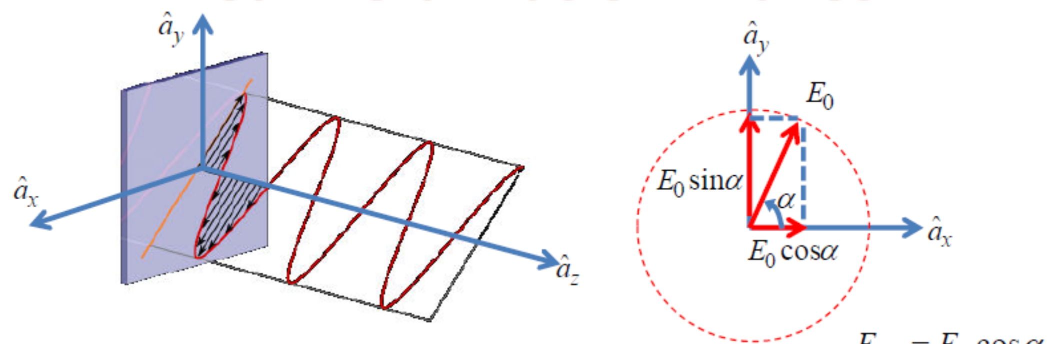

$$E_{x0} = E_0 \cos\alpha$$
$$E_{y0} = E_0 \sin\alpha$$

$$E(z,t) = \overline{E}_0 \cos(wt - kz + \beta)$$

$$\overline{E}_0 = \hat{a}_x E_0 \cos\alpha + \hat{a}_y E_0 \sin\alpha$$

$$E(z,t) = (\hat{a}_x E_0 \cos\alpha + \hat{a}_y E_0 \sin\alpha)\cos(wt - kz + \beta)$$

$$E(z,t) = \hat{a}_x E_0 \cos\alpha \cos(wt - kz + \beta) + \hat{a}_y E_0 \sin\alpha \cos(wt - kz + \beta)$$

$$E(z,t) = \hat{a}_x E_{x0} \cos(wt - kz + \beta) + \hat{a}_y E_{y0} \cos(wt - kz + \beta)$$

Polarization agile antennas

- **Element 1**

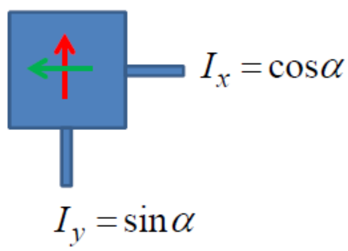

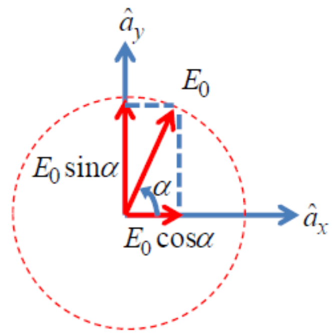

$$\overline{E}_0 = \hat{a}_x E_{x0} + \hat{a}_y E_{y0}$$

$$E_{x0} \approx I_x$$

$$E_{y0} \approx I_y$$

$$\overline{E}_0 = \hat{a}_x \cos\alpha + \hat{a}_y \sin\alpha$$

Polarization agile antennas

- **Element 2**

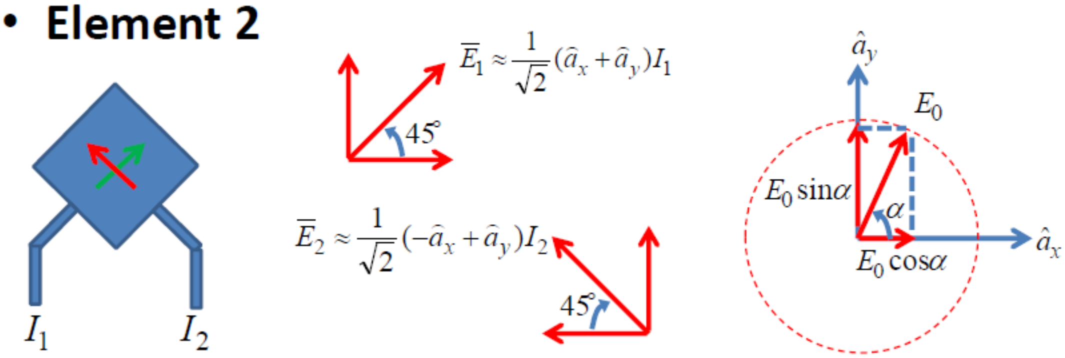

$$\overline{E}_0 = \overline{E}_1 + \overline{E}_2$$

$$\overline{E}_0 = \hat{a}_x \frac{1}{\sqrt{2}}(I_1 - I_2) + \hat{a}_y \frac{1}{\sqrt{2}}(I_1 + I_2)$$

$$\overline{E}_0 = \hat{a}_x \cos\alpha + \hat{a}_y \sin\alpha \qquad \begin{cases} (I_1 - I_2)/\sqrt{2} = \cos\alpha \\ (I_1 + I_2)/\sqrt{2} = \sin\alpha \end{cases}$$

Receive module operation

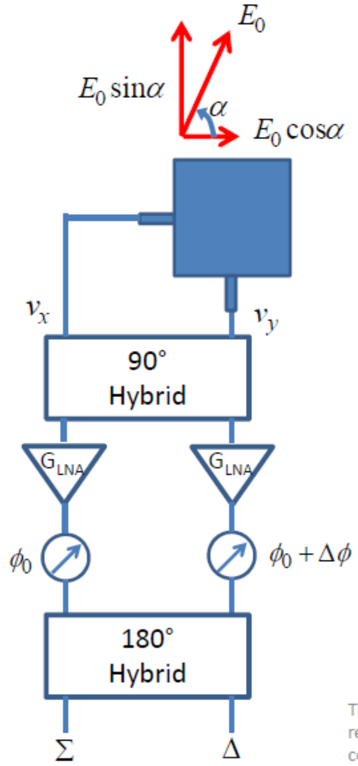

ϕ_0 = scan angle
$\Delta\phi_0$ = differential phase setting (control the slat angle)
v_x = Impressed voltage at horizontal polarization port
v_y = Impressed voltage at vertical polarization port
Σ = combined signal
Δ = difference signal

Receive module operation

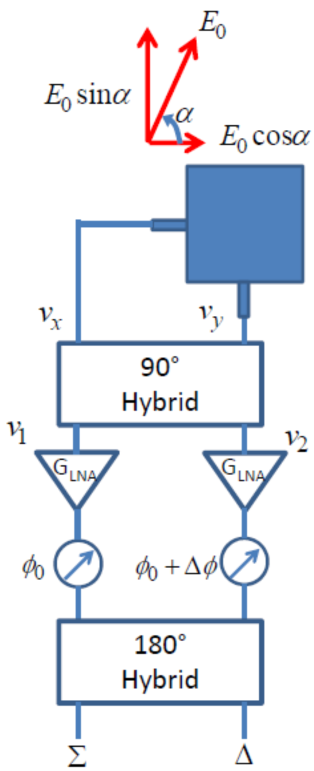

Impressed voltages

$$v_x \approx E_0 \cos\alpha$$
$$v_y \approx E_0 \sin\alpha$$

The output signals from the 90° hybrid are given by

$$v_1 = \frac{1}{\sqrt{2}}\left[v_x e^{-j90^\circ} + v_y{}^{-j180^\circ}\right]$$
$$\frac{1}{\sqrt{2}}\left[E_0 \cos\alpha e^{-j90^\circ} + E_0 \sin\alpha e^{-j180^\circ}\right] = \frac{E_0}{\sqrt{2}} e^{-j(\alpha+90^\circ)}$$

$$v_2 = \frac{1}{\sqrt{2}}\left[v_x e^{-j180^\circ} + v_y{}^{-j90^\circ}\right]$$
$$\frac{1}{\sqrt{2}}\left[E_0 \cos\alpha e^{-j180^\circ} + E_0 \sin\alpha e^{-j90^\circ}\right] = \frac{E_0}{\sqrt{2}} e^{j(\alpha+180^\circ)}$$

Receiver module operation

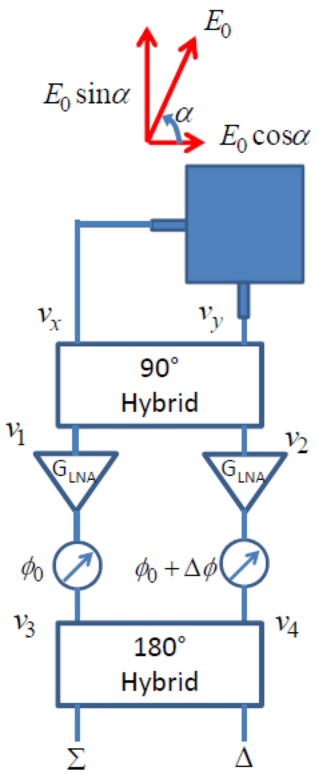

The signals at the output of the phase shifters are given as

$$v_3 = \sqrt{G_{LNA}} e^{j\phi_0} v_1 = \frac{1}{\sqrt{2}} \sqrt{G_{LNA}} E_0 e^{-j(\alpha + 90^\circ - \phi_0)}$$

$$v_4 = \sqrt{G_{LNA}} e^{j\phi_0 + \Delta\phi} v_2 = \frac{1}{\sqrt{2}} \sqrt{G_{LNA}} E_0 e^{j(\alpha + 180^\circ + \phi_0 + \Delta\phi)}$$

Receiver module operation

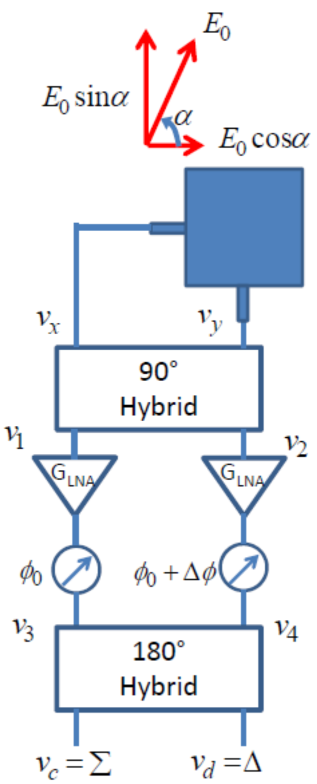

The combined signal at the output of 180° hybrid is

$$v_c = \frac{1}{\sqrt{2}}\left[v_3 e^{-j90^\circ} + v_4{}^{-j90^\circ}\right]$$

$$= \frac{1}{2}\sqrt{G_{LNA}}E_0 e^{-j90^\circ}\left[e^{-j(\alpha+90^\circ-\phi_0)} + e^{j(\alpha+180^\circ+\phi_0+\Delta\phi)}\right]$$

$$= \frac{1}{2}\sqrt{G_{LNA}}E_0 e^{j(\phi_0-135^\circ+\frac{\Delta\phi}{2})}[e^{-j(\alpha+45^\circ+\frac{\Delta\phi}{2})} - e^{j(\alpha+45^\circ+\frac{\Delta\phi}{2})}]$$

$$= \frac{1}{2}\sqrt{G_{LNA}}E_0 e^{j(\phi_0-135^\circ+\frac{\Delta\phi}{2})}[-j2\sin(\alpha+45^\circ+\frac{\Delta\phi}{2})]$$

$$= \sqrt{G_{LNA}}E_0 \sin(\alpha+45^\circ+\frac{\Delta\phi}{2})e^{j(\phi_0+135^\circ+\frac{\Delta\phi}{2})}$$

v_c is maximum when

$$\alpha + 45^\circ + \frac{\Delta\phi}{2} = 90 \;\Rightarrow\; \Delta\phi = 90^\circ - 2\alpha$$

$$v_c = \sqrt{G_{LNA}}E_0 e^{j(\phi_0+180^\circ-\alpha)}$$

Question: α?

Receiver module operation

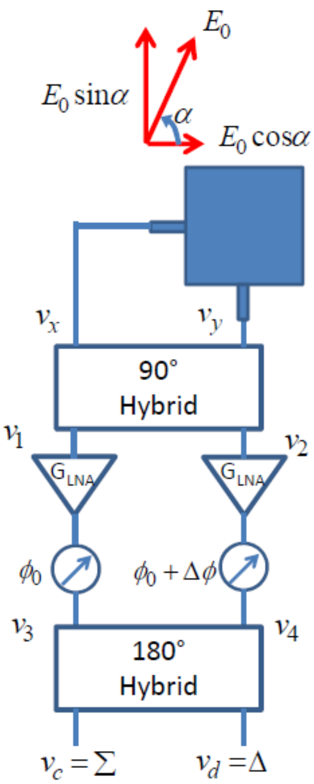

The difference signal at the output of 180° hybrid is

$$v_d = \frac{1}{\sqrt{2}}\left[v_3 e^{-j270^\circ} + v_4{}^{-j90^\circ}\right]$$

$$= \frac{1}{2}\sqrt{G_{LNA}}E_0\left[e^{-j(\alpha-\phi_0)} + e^{j(\alpha+90^\circ+\phi_0+\Delta\phi)}\right]$$

$$= \frac{1}{2}\sqrt{G_{LNA}}E_0 e^{j(\phi_0+45^\circ+\frac{\Delta\phi}{2})}[e^{-j(\alpha+45^\circ+\frac{\Delta\phi}{2})} + e^{j(\alpha+45^\circ+\frac{\Delta\phi}{2})}]$$

$$= \frac{1}{2}\sqrt{G_{LNA}}E_0 e^{j(\phi_0+45^\circ+\frac{\Delta\phi}{2})}[2\cos(\alpha+45^\circ+\frac{\Delta\phi}{2})]$$

$$= \sqrt{G_{LNA}}E_0 \cos(\alpha+45^\circ+\frac{\Delta\phi}{2})e^{j(\phi_0+45^\circ+\frac{\Delta\phi}{2})}$$

v_d is zero when v_c is maximum ($\Delta\phi = 90^\circ - 2\alpha$)

$v_d = 0$

Question: α?

Finding α

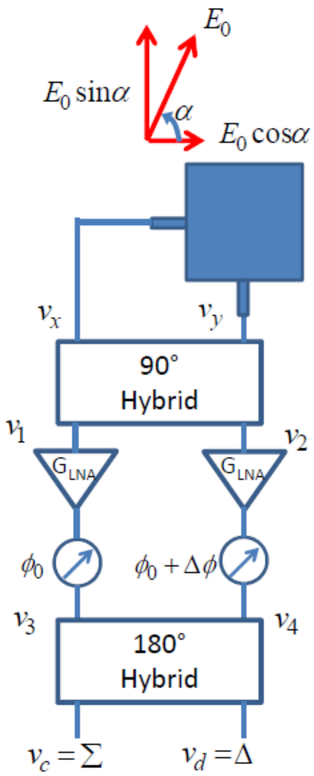

α is obtained from the ratio

$$\left|\frac{v_d}{v_c}\right| = \frac{\cos(\alpha + 45^\circ + \frac{\Delta\phi}{2})}{\sin(\alpha + 45^\circ + \frac{\Delta\phi}{2})} = \cot(\alpha + 45^\circ + \frac{\Delta\phi}{2})$$

$$= \tan(45^\circ - \alpha - \frac{\Delta\phi}{2})$$

Solving for α, it yields

$$\alpha = \tan^{-1}\left|\frac{v_d}{v_c}\right| + 45^\circ - \frac{\Delta\phi}{2}$$

Typically, we can find α using $\Delta\phi = 0$

$$\alpha = \tan^{-1}\left|\frac{v_d}{v_c}\right| + 45^\circ$$

Receive module operation (using element 2)

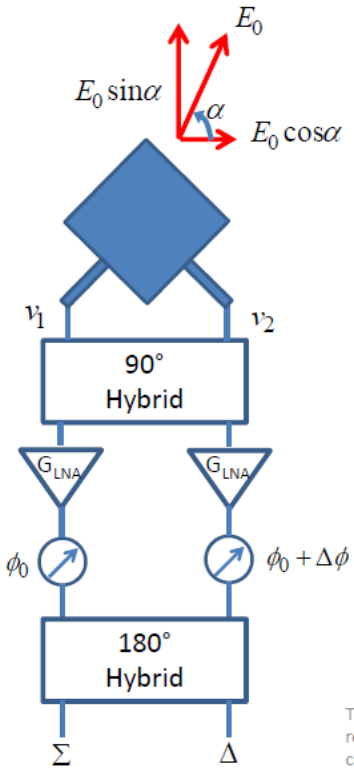

Impressed voltages at the antenna terminals

$$v_1 = \hat{a}_{v_1} . \hat{a}_{E_0}$$

$$= \left(\frac{\hat{a}_x}{\sqrt{2}} + \frac{\hat{a}_y}{\sqrt{2}}\right) . (\hat{a}_x E_0 \cos\alpha + \hat{a}_y E_0 \sin\alpha)$$

$$= \frac{E_0}{\sqrt{2}} (\cos\alpha + \sin\alpha)$$

$$v_2 = \hat{a}_{v_2} . \hat{a}_{E_0}$$

$$= \left(-\frac{\hat{a}_x}{\sqrt{2}} + \frac{\hat{a}_y}{\sqrt{2}}\right) . (\hat{a}_x E_0 \cos\alpha + \hat{a}_y E_0 \sin\alpha)$$

$$= \frac{E_0}{\sqrt{2}} (-\cos\alpha + \sin\alpha)$$

Receive module operation (using element 2)

$$v_1 = \frac{E_0}{\sqrt{2}}(\cos\alpha + \sin\alpha)$$

$$v_2 = \frac{E_0}{\sqrt{2}}(-\cos\alpha + \sin\alpha)$$

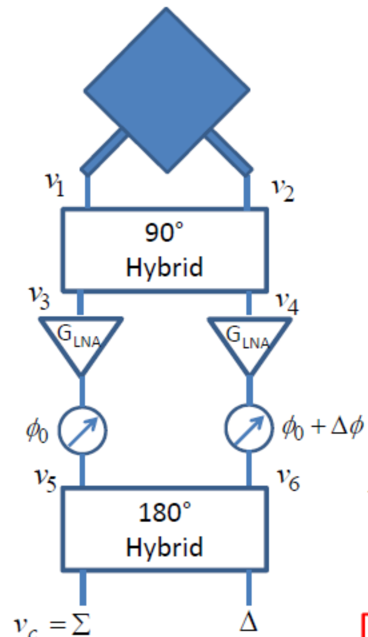

$$v_3 = \frac{E_0}{\sqrt{2}} e^{-j(\alpha + 45^\circ)}$$

$$v_4 = \frac{E_0}{\sqrt{2}} e^{j(\alpha + 225^\circ)}$$

$$v_5 = \frac{\sqrt{G_{LNA}}\,E_0}{\sqrt{2}} e^{-j(\alpha + 45^\circ - \phi_0)}$$

$$v_5 = \frac{\sqrt{G_{LNA}}\,E_0}{\sqrt{2}} e^{j(\alpha + 225^\circ + \phi_0 + \Delta\phi)}$$

$$v_c = \sqrt{G_{LNA}}\,E_0 \cos(\alpha + \frac{\Delta\phi}{2} + 135^\circ) e^{j(\phi_0 + \frac{\Delta\phi}{2})}$$

$$\boxed{\begin{aligned} &\Delta\phi = 90^\circ - 2\alpha \\ &v_c = \sqrt{G_{LNA}}\,E_0 e^{j(\phi_0 - \alpha + 45^\circ)} \end{aligned}}$$